HAL
open science

influence of the dielectric substrate on the electronic band structure in a monolayer of tmdc

Karl Kloss

To cite this version:

Karl Kloss. influence of the dielectric substrate on the electronic band structure in a monolayer of tmdc. Physics [physics]. Université Grenoble Alpes [2020-..], 2022. English. NNT : 2022GRALY045 . tel-03852818

HAL Id: tel-03852818

https://theses.hal.science/tel-03852818v1

Submitted on 15 Nov 2022

HAL is a multi-disciplinary open access archive for the deposit and dissemination of scientific research documents, whether they are published or not. The documents may come from teaching and research institutions in France or abroad, or from public or private research centers.

L'archive ouverte pluridisciplinaire **HAL**, est destinée au dépôt et à la diffusion de documents scientifiques de niveau recherche, publiés ou non, émanant des établissements d'enseignement et de recherche français ou étrangers, des laboratoires publics ou privés.

THÈSE

Pour obtenir le grade de

DOCTEUR DE L'UNIVERSITÉ GRENOBLE ALPES

École doctorale : PHYS - Physique
Spécialité : Physique de la Matière Condensée et du Rayonnement
Unité de recherche : Institut Néel

Influence du substrat diélectrique sur la structure de bandes dans une monocouche de TMDC

Influence of the dielectric substrate on the electronic band structure in a monolayer of TMDC

Présentée par :

Karl KLOSS

Direction de thèse :

Maxime RICHARD Directeur de Recherche, CNRS	Directeur de thèse
Julien RENARD Chargé de Recherche, CNRS	Co-encadrant de thèse
Olivier RENAULT Ingénieur HDR au CEA, CEA-LETI	Co-directeur de thèse

Rapporteurs :

YANNICK FAGOT-REVURAT
Professeur des Universités, UNIVERSITE DE LORRAINE
KAROL HRICOVINI
Professeur émérite, CY CERGY PARIS UNIVERSITE

Thèse soutenue publiquement le **30 juin 2022**, devant le jury composé de :

DEBORA PIERUCCI Chargé de recherche, CNRS DELEGATION ILE-DE-FRANCE SUD	Examinatrice
THIERRY OUISSE Professeur des Universités, GRENOBLE INP	Président
YANNICK FAGOT-REVURAT Professeur des Universités, UNIVERSITE DE LORRAINE	Rapporteur
KAROL HRICOVINI Professeur émérite, CY CERGY PARIS UNIVERSITE	Rapporteur

Invités :

Table of Contents

Résumé **6**

Abstract **6**

Introduction **7**

1 Introduction to monolayers of transition metal dichalcogenides (ML-TMDCs) **12**
1.1 Semiconducting TMDCs and their optoelectronic properties 13
1.1.1 2D-Materials in Optoelectronics: Monolayers of Transition Metal Dichalcogenides 13
1.1.2 The crystal structure of TMDCs 13
1.2 The band structure of monolayer TMDCs 15
1.2.1 Unit cell and Brillouin zone 15
1.2.2 Tight-binding approximation 15
1.2.3 Orbital composition of the band structure 17
1.2.4 Comparison of theoretical and experimental band structures and parameters 18
1.3 The influence of the band structure on the optoelectronic properties in ML-TMDCs 23

2 Introduction to principles of Photoemission and ARPES for the analysis of electronic structures **27**
2.1 Instrumental aspects of ARPES 28
2.1.1 The photoelectric effect and photoemission spectroscopy 28
2.1.2 Angle-resolved photoemission spectroscopy (ARPES) 30
2.1.3 Sample and instrumental requirements for ARPES on 2D-materials . 32
2.1.4 Requirements for light sources to study 2D-Materials with ARPES . 33
2.1.5 Energy- and momentum resolution of an ARPES setup 34
2.1.6 Techniques for spatially resolved ARPES on ML-TMDCs 35
2.1.7 Our ARPES instrument: Functionality of the NanoEsca PEEM apparatus 36
2.1.8 Energy filtering in the hemispherical analyzer 40
2.2 Theory of photoemission in ARPES experiments 43
2.2.1 Photo-ionizaton cross section 43
2.2.2 The theory of the photoemission process in the 3-step model 43
2.2.3 The Work Function of a semiconductor and its relation to Fermi Level Shifts 47

3 Fabrication of ML-TMDC samples for kPEEM **50**

3.1 Goals and challenges in fabrication of ML-TMDC-structures for kPEEM . . 51
3.2 Modern techniques for the development of ML-TMDC-structures for ARPES 51
3.2.1 Sizeable monolayers 52
3.2.2 Substrates 52
3.3 Mechanical exfoliation from bulk crystals 52
3.4 Standardized monolayer identification using an optical microscope 54
3.5 All-dry viscoelastic stamping 54
3.6 Laser lithography and metal evaporation for microscopic markers 57

4 The influence of the substrate onto the electronic band structure in monolayer WSe_2 60
4.1 The influence of the dielectric environment on the electronic structure in ML-TMDCs 61
4.1.1 Influence of the substrate is typical for monolayer-TMDCs 61
4.1.2 Dielectric screening of the substrate and its influence on the band structure from a theoretical POV 61
4.1.3 Typical substrates used for ARPES and their interactions with ML-TMDCs 62
4.1.4 ARPES studies on other substrates 67
4.1.5 Summary and conclusion 68
4.2 Measurements of ML-WSe_2 at the NanoEsca PEEM setup 70
4.2.1 Sample preparation 70
4.2.2 kPEEM raw data of ML-WSe_2 on different substrates 70
4.3 Our approach for the treatment and analysis of k-PEEM photointensity spectra 74
4.3.1 Finding equivalent k-space positions 74
4.3.2 Averaging over equivalent k-space positions 75
4.3.3 Background removal and EDC fitting 77
4.3.4 Nearly free electron band dispersion, dispersion correction and summation of equivalent EDCs 80
4.4 Band structure parameters of ML-WSe_2 and the influence of the dielectric substrate 84
4.4.1 Measured band structure parameters as a function of the substrate's dielectric constant 84
4.4.2 The role of the orbital character in charge screening of ML-TDMCs by the substrate 89
4.4.3 Supplementary effects aside charge screening and conclusion 90
4.5 Analysis of substrate-induced strain in ML-WSe_2 by Raman spectroscopy . 92
4.5.1 A short introduction on Raman spectroscopy 92
4.5.2 Linearly polarized Raman to measure biaxial strain in ML-WSe_2 . . 92
4.5.3 The effect of biaxial strain on ML-WSe_2 95
4.6 Work Function Determination of ML-WSe_2 on different substrates 97
4.6.1 Spatially-Resolved Work Function Measurement using EF-PEEM . . 97
4.6.2 Magnitude of charge transfer from substrate to ML-WSe_2 and implications for the band structure 98

Conclusion and Outlook 100

5 Résumé du travail en français 103
5.1 Introduction aux monocouches des métaux de transition dichalcogenures . . 103
5.2 Principes de la photoémission et de l'ARPES 109

5.2.1 Principe de photoémission, effet photoélectrique et cinématique de la photoémission . . . 109
5.2.2 Principe d'ARPES . . . 110
5.2.3 Notre dispositif expérimental: le NanoEsca I . . . 111
5.2.4 Théorie de la photoémission . . . 113
5.2.5 Influence de la géometrie expérimentale sur l'élément de matrice de photoionisation . . . 116
5.3 Fabrication d'échantillons de monocouches de TMD pour mesure en kPEEM 118
5.4 L'impact du substrat diélectrique sur la structure électronique d'une monocouche en TMD . . . 120
5.4.1 Notre approche pour le traitement et l'analyse des spectres de photointensité en kPEEM . . . 122
5.4.2 Description des résultats . . . 126
5.4.3 Relation entre les paramètres de la structure de bandes et la constante diélectrique statique du substrat . . . 127
5.4.4 Mesures Raman pour vérifier la présence de stress mécanique . . . 131
5.4.5 Mesures de travail de sortie . . . 131
5.4.6 Conclusions et perspectives . . . 133

Bibliography **135**

List of figures **152**

List of tables **162**

5.5 Appendix . . . 164

Abstract

Dans la famille des matériaux 2D, les monocouches de dichalcogénures de métaux de transition, et en particulier, MoS_2, $MoSe_2$, WS_2, WSe_2, sont des semi-conducteurs aux propriétés optoélectroniques exceptionnelles. Ces propriétés sont dues à leur épaisseur nanométrique et aux conséquences qui en résultent sur leur structure de bandes. Cette influence offre une opportunité unique de contrôler les propriétés optoélectroniques de ces matériaux en modifiant simplement leur environnement diélectrique. Dans ce travail, nous examinons expérimentalement cette influence en exposant une monocouche de WSe_2 à différents substrats. Nous utilisons l'exfoliation mécanique et une technique de stamping pour produire différents échantillons de monocouches de WSe_2 sur des substrats de différentes constantes diélectriques. À l'aide d'une technique de photoémission appelée k-space Photoelectron Emission Microscopy (kPEEM), nous mesurons la structure de bandes électronique d'une monocouche de WSe_2 déposée sur ces différents substrats. Un travail d'analyse numérique nous permet d'extraire quantitativement les caractéristiques essentielles de la structure de bandes. Nous constatons en effet que ces caracteristiques dependent du substrat, via un mécanisme d'écrantage diélectrique induit par le substrat sur les états electroniques de le monocouche situés à quelque nanomètre de distance. Nous constatons nottament que nous pouvons modifer sensiblement l'énergie de la bande de valence en K et en Γ, qui jouent un role clé dans les propiétés optoélectroniques du matériau. Nous discutons cet effet à la lumière des travaux théoriques récents et excluons d'autres mécanismes qui pourraient être responsables de la modification de la structure de la bande, tels que la contrainte mécanique et le transfert de charge.

Keywords: Monocouches, TMD, diélectrique, écrantage, contrainte, dopage

Abstract

In the family of 2D materials, transition metal dichalcogenide monolayers, and in particular, MoS_2, $MoSe_2$, WS_2, WSe_2, are semiconductors with exceptional optoelectronic properties. These properties are due to their nanometric thickness and the resulting consequences on their band structure. This influence offers a unique opportunity to control the optoelectronic properties of these materials by simply modifying their dielectric environment. In this work, we experimentally examine this influence by exposing a WSe2 monolayer to different substrates. We use mechanical exfoliation and a stamping technique to produce different samples of WSe2 monolayers on substrates of different dielectric constants. Using a photoemission technique called k-space Photoelectron Emission Microscopy (kPEEM), we measure the electronic band structure of a WSe_2 monolayer deposited on these different substrates. A numerical analysis work allows us to quantitatively extract the essential characteristics of the band structure. We indeed note that these characteristics depend on the substrate, via a dielectric screening mechanism induced by the substrate on the electronic states of the monolayer located at a few nanometer distance. We note in particular that we can significantly modify the energies of the valence band in K and in Γ, which play a key role in the optoelectronic properties of the material. We discuss this effect in light of recent theoretical work and rule out other mechanisms that might be responsible for altering the band structure, such as mechanical strain and charge transfer.

Keywords: Monolayers, TMDC, dielectric, screening, strain, doping

Introduction

We are living an age of exponential technological growth. If a hundred years ago, people marvelled at the invention of the radio for the grand public, we can now access the combined knowledge of humanity through our smartphones. This development will undoubtedly continue for the foreseeable future. This technological revolution would not be possible without the underlying electronics and optoelectronics, the part of electronics responsible for light-matter-interaction.

But this hunger to implement more technologies comes at a cost: materials needed for electronics must be extracted, purified and refined in a long and energy-consumptuous process to provide for new devices. The mining for these materials has a direct and lasting detrimental impact on the health of the workers, their communities and the adjacent environment. On a global scale, the extraction, processing and transport of these materials emits huge masses of carbon dioxides driving global warming to new records. Lastly, the reliance on these materials has serious strategic implications for all countries: the disruption of supply-chains during the COVID pandemic has shown just how dependent international trade has become on very few suppliers. Considerations to bring back critical industries to western countries are expressed by political leaders.

Monolayers of TMDCs as candidates for new optoelectronic devices and the influence of the substrate

One promising answer to these issues is the use of two-dimensional materials (2D materials). The remarkable property about 2D materials is their extreme thinness of a few atoms. In 2007, André Novoselov and Konstantin Geim were awarded the nobel prize for the discovery and experiments on the two-dimensional version of graphite, graphene. Graphene is a 2D material that is flexible, transparent and can be a good conductor under the right circumstances. Numerous other two-dimensional materials have been discovered and examined since then, such as the insulating hexagonal boron nitride or black phosphorus. If each of these 2D materials brings their own physical properties, combining them into so-called van-der-Waals structures is a way to create completely new electronic systems.

In this vast family of 2D-materials, monolayers of transition metal dichalcogenides (ML-TMDCs) are the most promising candidates traded for optoelectronic devices. A TMDC bulk or multilayer crystal in 2H-Polymorphism possesses an indirect band gap. When thinned down to the monolayer, the TMDC crystal acquires a direct band gap. This drastic change in the *band structure* of the monolayer TMDC crystal enhances the light-matter interaction in these monolayers. Many optoelectronic properties of monolayers of TMDCs crucially depend on their *band structure*. If one controls the band structure, one thus determines the optoelectronic properties of the monolayer.

Generally, an electron in a crystal is sensitive to its immediate surroundings and will interact with such. This interaction is expressed by the quantum energy levels of the electron in the crystal, i. e. the band structure. In the multilayer form the surrounding environment of the electron is a three-dimensional periodic crystal. In the two-dimensional form the immediate surrounding outside of the monolayer is often modelled as vacuum, which triggers the indirect-to-direct band gap transition as discussed above. Modelling the exterior of the crystal as vacuum works well in many cases, but in reality, the monolayer will be in contact with another material, the so-called substrate. The electron is influenced by the substrate as part of its new environment and interact with it. Could the choice of

substrate be a way to influence its band structure?

In this work, we thus look at the *influence of the substrate on the band structure of monolayers of TMDC*. We limit ourselves to *dielectric* substrates which are semi-conducting or insulating.

Outline of this work

In chapter 1 we introduce monolayers of TMDCs as an optoelectronic material and review the role of the band structure: we start out from the crystal structure and derive the basic symmetries of the TMDC crystal. The band structure is based on these symmetries and we compare theoretical calculations of the band structure with experimental results. We then show how the exceptional optoelectronic properties emerge from very simple band structure properties. We conclude that by tuning the underlying band structure we can directly control the optoelectronic properties of the monolayer.

In chapter 2 we introduce the current techniques of measuring a ML-TMDC based on Angle-Resolved Photoemission Spectroscopy (ARPES): μ-ARPES, nanoARPES and k-space Photoelectron Emission Spectroscopy (kPEEM). These techniques are based on the photoelectric effect and we show how the band structure, i. e. the relationship between an electron's energy and its **k**-vector can be retrieved using either technique. We revisit the state of the art of ARPES for monolayers of TMDCs, advantages and disadvantages of either technique. We detail the inner workings of our setup, the NanoEsca I, which is capable of k-space Photoelectron Emission Microscopy on a small area and explain how band structures are measured. We review theoretical elements on ARPES in the framework of the three-step-model, an intuitive approach to understand the entire process of photoemission in ARPES and its relationship to the band structure.

In chapter 3 we detail our fabrication methods: We summarize current techniques for the creation of monolayer-based TMDC systems and weigh pros and cons of either technique for our study. We describe our technique in which we use mechanical exfoliation and stamping on a dedicated setup. We explain the workflow of this technique in order to create monolayers of TMDCs on different substrates.

In chapter 4, we begin by stating our problematic: the influence of dielectric substrates on the band structure of monolayers of TMDCs. The mechanism of dielectric screening of the substrate onto the band structure has been considered by several groups with diverging findings. Experimentally, monolayers of TMDCs have been analysed by ARPEs on a number of different substrates (graphite, hBN, gold, silicon, STO, TiO_2, GaN and in suspension), but the influence of the dielectric substrate has not been sufficiently quantified and the results are conflicting. We have found no systematic and coherent study which compares the effect of a dielectric substrate and attempt to identify the underlying mechanism. This is the main goal of this research work.

This lack of studies is in part due to the poor signal-to-noise ratio on some dielectric substrates. Certain authors were not able to measure the full set of band structure parameters. Facing the same issue on several substrates, we devise a methodology to significantly enhance the signal-to-noise ratio. We successfully extract a full set of band structure parameters on all our substrates and relate these to the static dielectric constants of the substrate. We find a significant, but non-trivial (non-monotonic) correlation between the static dielectric constant of the substrate and one band structure parameter.

In order to verify that the observed influence is due to dielectric screening, we experimentally check the influence of other possible mechanisms that can potentially impact the

band structure. In the following subsections we check for the presence of strong biaxial strain by linearly polarized Raman spectroscopy and find no significant presence of biaxial strain. Another mechanism would be a transfer of charges from the substrate to the monolayer. While we see a significant change in the work function of the monolayer on different substrates.

From these findings we conclude that dielectric screening of the substrate is responsible for the observed band structure changes. This should pave the way to control optoelectronic properties of the ML-TMDC via choice of substrate.

1

Introduction to monolayers of transition metal dichalcogenides (ML-TMDCs)

1.1 Semiconducting TMDCs and their optoelectronic properties

1.1.1 2D-Materials in Optoelectronics: Monolayers of Transition Metal Dichalcogenides

In the light of upcoming optoelectronic applications, the family of transition metal dichalcogenides (TMDCs) have emerged as promising candidates for future optoelectronic devices. Examples are molybdenum disulfide (MoS_2), molybdenum diselenide ($MoSe_2$), tungsten disulfide (WS_2) and tungsten diselenide (WSe_2). TMDCs are made up of single layers, so-called **monolayers**, which can be extracted from the bulk crystal. While there are many other monolayers in the transition metal dichalcogenide family, the four mentioned, have been extensively studied using various theoretical and experimental methods. From now on, we will refer to monolayers of the four (MoS_2, $MoSe_2$, WS_2, WSe_2) (as $1H_c$-polymorphism) as monolayers of TMDCs (ML-TMDCs).

Objective of this work and overview

As monolayers, and more specifically as $1H_c$-polymorphism, these four TMDCs posess some exceptional optoelectronic properties despite their extreme thinness of only 3 atoms. The optoelectronic properties of these ML-TMDCs are determined in large part by their particular electronic band structure. If one can achieve control over the band structure, one can thus tune these optoelectronic properties. Different methods such as mechanical stress on the monolayer [5, 118] or doping [17] are discussed in the literature to change the underlying band structure. Recently, a third way, the dielectric screening of charges in the monolayer by the substrate has been anticipated to change the ML-TMDC band structure [185]. The focus of this work is thus to understand the effect of a dielectric substrate on the band structure of a ML-TMDC.

In the following sections of this chapter we describe the crystal structure and symmetries of bulk TMDCs and its $1H_c$-monolayers. The information about the crystal structure is needed for band structure calculation. We present the tight-binding-approximation as an exemplary method for band structure calculations in ML-TMDCs [20, 93, 146, 177]. Moreover, we detail the orbital composition of the valence band maximum in ML-TMDCs. We then proceed to compare the theoretical calculations to experimentally measured band structures. To conclude we show how the band structure is responsible for many of the optoelectronic properties of ML-TMDCs.

1.1.2 The crystal structure of TMDCs

We have based the explanations in this paragraph on [77, 81] unless otherwise cited. In this introduction to TMDCs, we will present the structure of transition metal dichalcogenides (TMDCs) without limiting ourselves to MoS_2, $MoSe_2$, WS_2 and WSe_2. A single molecule of a TMDC has the chemical formula MX_2 where M is a transition metal (e. g. Mo, W, Re, Nb) and X a chalcogen (e. g. S, Se, Te). In panel a) of figure 1.1 we show the different crystal configurations for bulk TMDCs. In a bulk TMDC, these single molecules crystallize into stacked layers. Within one layer, a sheet of transition metal atoms in the same plane is being sandwiched by sheets of chalcogen atoms. Chalcogens and transition metal atoms form covalent bonds.

While the covalent bonds constitute very attractive strong forces within a layer, multiple stacked layers are kept together by weaker van-der-Waals forces. The transition metal atom can have trigonal prismatic or octahedral coordination. The stacking between the

layers can also differ: Typical stacking configurations are 1T, 2H or 3R. Here, the number in front indicates the number of layers within one unit cell, whereas the letter stands for **t**etrahedral, **h**exagonal or **r**hombohedral structure shown in panel a) of figure 1.1. In panel b) of figure 1.1 we show two bulk configurations of a $2H$-TMDC with a transition metal in gold and the chalcogen atoms in blue. The 2H-polymorphisms can be distinguished as $2H_a$, $2H_b$ and $2H_c$ with stacking type [AbA CbC] for $2H_A$ and [CaC AcA] for $2H_c$ as shown in panel b) of figure 1.1. $2H_b$ appears for non-stoichiometric configurations where an excess metal atom is found in the gap between the layers. Examples for the $2H_a$ polytype are NbS_2, $NbSe_2$, $NbTe_2$, TaS_2, $TaSe_2$ and $TaTe_2$. For $2H_b$ are $Nb_{1+x}Se_2$ and $Ta_{1+x}Se_2$ and for $2H_c$ are MoS_2, $MoSe_2$, WS_2, WSe_2 and $MoTe_2$ [77]. Sometimes, the term 1H is used to designate monolayers extracted from $2H$-TMDCs [82, 83].

The in-plane lattice constant a ranges from 3.16 Å ($MoSe_2$ or WS_2 to 3.299 Å ($MoSe_2$), whereas the out-of-plane lattice constant c ranges from 12.28 Å (MoS_2) to 12.986 (Wse_2)Å [77, 81].

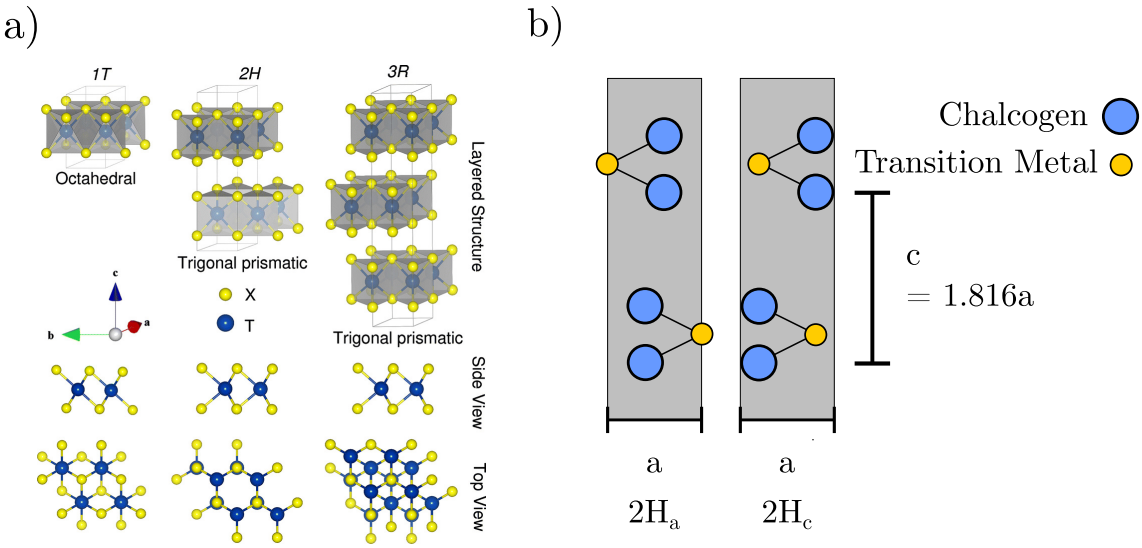

*Figure 1.1 – **a)** The crystal structure of a TMDC in 1T, 2H and 3R-polymorphism. In the first row, a side view of the layered structure, the second row a side, and third row a top view of the monolayer. The metal atom coordination (trigonal prismatic or octahedral) is indicated. The number of the polymorphism (1, 2, 3) refers to the number of layers in the unit cell, the letter stands for **t**etrahedral, **h**exagonal or **r**homohedral structure. Taken from [81] **b)** Unit cells of 2H-TMDCs in the H_a and H_c-configuration. Here, the blue dots represent chalcogen atoms whereas the gold dots represent transition metal atoms. Taken and adapted from [77]. The lattice parameters c (out-of-plane) and a (in-plane) are related by $c = 1.816 \times a$ [167].*

1.2 The band structure of monolayer TMDCs

1.2.1 Unit cell and Brillouin zone

We have based the explanations in the following paragraphs on [137] unless otherwise cited. Panel a) of FIGURE 1.2 shows the basis atoms of a ML-TDMC unit cell. The transition metal atom (gold) is at the origin of the coordinate system, whereas the chalcogen atoms (blue) are placed at the basis vectors

$$\delta_{\pm} = d\left(0, \frac{a}{\sqrt{3}}, \pm\frac{a}{2\sqrt{3}}\right) \tag{1.1}$$

where a is the in-plane lattice constant of the ML-TMDC and d the distance between transition metal and chalcogen atom. In the two-dimensional plane the ML-TMDC crystallizes in a hexagonal form as shown in panel b) of FIGURE 1.2. The unit cell is marked by dashed gray lines and is hexagonal. The Bravais lattice vectors for the hexagonally symmetric crystal plane are

$$\mathbf{R}_1 = (a, 0, 0) \tag{1.2}$$

$$\mathbf{R}_2 = \left(\frac{a}{2}, \frac{\sqrt{3}a}{2}, 0\right) \tag{1.3}$$

Using the condition of reciprocity $2\pi\delta_{ij} = \mathbf{R}_i \cdot \mathbf{K}_j$ one can thus deduce the corresponding reciprocal lattice vectors

$$\mathbf{K}_1 = \frac{4\pi}{\sqrt{3}a}\left(\frac{\sqrt{3}}{2}, -\frac{1}{2}, 0\right) \tag{1.4}$$

$$\mathbf{K}_2 = \frac{4\pi}{\sqrt{3}a}(0, 1, 0) \tag{1.5}$$

In reciprocal space the hexagonal symmetry of the crystal lattice is conserved and leads to a hexagonal Brillouin zone shown in panel c) of FIGURE 1.2. In this Brillouin zone, one can find the following points fo high symmetry

$$\Gamma = (0, 0, 0) \tag{1.6}$$

$$K = \left(\frac{2\pi}{3a}, \frac{-2\pi}{\sqrt{3}a}, 0\right) \tag{1.7}$$

$$K' = \left(\frac{4\pi}{3a}, 0, 0\right) \tag{1.8}$$

$$M = \left(\frac{\pi}{a}, \frac{-\pi}{\sqrt{3}a}, 0\right) \tag{1.9}$$

which are invariant under a rotation of 120°.

1.2.2 Tight-binding approximation

In order to calculate the band structure of ML-TMDCs, different formalisms are available such as Density Functional Theory [17, 78, 97, 149] or $\hat{k} \cdot \hat{p}$-theory [9, 78, 79]. A full theoretical review on these formalisms is beyond the scope of this work. Here, we present the tight-binding approximation as one way to calculate band structures of ML-TMDCs [20, 93, 146, 177]

We have based the explanations in the following paragraphs on [137] unless otherwise cited. The assumption of the tight-binding method is that the electrons are strongly bound to

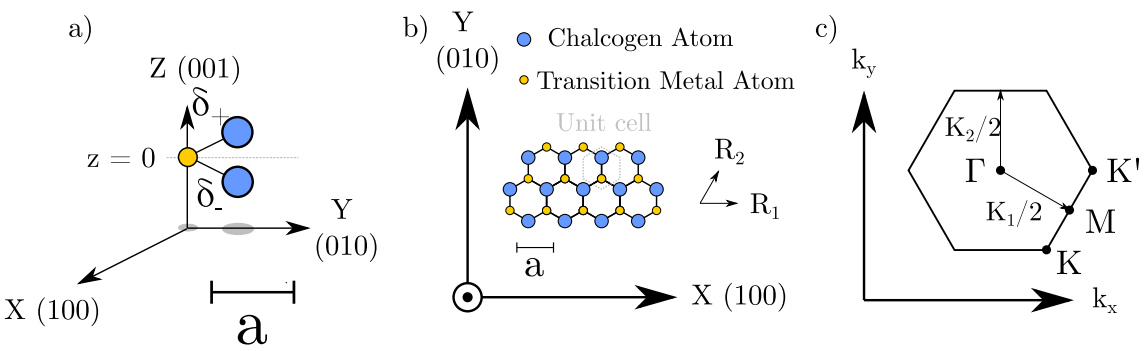

FIGURE *1.2* – ***a)*** *Unit cell of* $1H_c$*-*MX_2 *with a transition metal atom M and two chalcogen atoms X at lattice constant a. The chalcogen atoms (blue) are separated from the transition metal atom (gold) by the vectors* $\delta_\pm$ *as defined in the text.*
b) *Top view on the* $1H_c$*-*MX_2*-structure with real space lattice vectors* R_1 *and* R_2*. The hexagonal unit cell is marked by a gray dashed line.*
c) *Resulting planar hexagonal Brillouin zone with reciprocal lattice vectors* K_1 *and* K_2 *and the points of high symmetry* Γ*, K, K' and M as defined in the text. All figures adapted from [137].*

their respective atomic nuclei and only weakly interact with other electrons/nuclei. For an isolated atom a set of atomic orbitals is given by $\{\phi_l(\mathbf{r}-\mathbf{t}_k)\}$. Here, l is an index which runs over all possible electron valence orbitals. $\mathbf{t}_k$ denotes $\mathbf{t}_1 = 0, \mathbf{t}_2 = \delta_-, \mathbf{t}_3 = \delta_+$ which are the basis vectors of the transition metal and the two chalcogen atoms inside the unit cell as seen in panel a) of FIGURE 1.2. For an electron wave function χ_{lk} which depends on the orbital function l at atomic site k one can write the Bloch sum which comprises one electron valence state l at one lattice site i

$$\chi_{lk}(\mathbf{k},\mathbf{r}) = \frac{1}{\sqrt{N}} \sum_{\mathbf{R}}^{N} e^{i\mathbf{k}\cdot\mathbf{R}} \phi_l(\mathbf{r}-\mathbf{t}_k-\mathbf{R}) \tag{1.10}$$

and $\mathbf{R}$ runs over all N lattice vectors. This function satisfies the Bloch theorem

$$\chi_{lk}(\mathbf{k},\mathbf{r}+\mathbf{R}) = e^{i\mathbf{k}\cdot\mathbf{R}} \chi_{lk}(\mathbf{k},\mathbf{r}) \tag{1.11}$$

for an arbitrary lattice vector $\mathbf{R}$. The electron eigenfunctions are linear combinations of χ_{lk}

$$\Psi_{n\mathbf{k}}(\mathbf{r}) = \sum_{lk} c_{nlk}(\mathbf{k}) \chi_{lk}(\mathbf{k},\mathbf{r}) \tag{1.12}$$

where the coefficients $c_{nlk}(\mathbf{k})$ with the band index n are to be determined by this method. Using the time-independent Schrödinger equation the eigenproblem becomes

$$\sum_{lk} c_{nlk}(\mathbf{k}) \left[\langle \chi_{mj} | \hat{H} | \chi_{lk} \rangle - E_n(\mathbf{k}) \langle \chi_{mj} | \chi_{lk} \rangle \right] = 0 \tag{1.13}$$

Another way to write is as matrices:

$$\sum_{lk} c_{nlk}(\mathbf{k}) \left[M_{mjlk} - E_n S_{mjlk} \right] = 0 \longleftrightarrow M \cdot \mathbf{c} = E_{\mathbf{k}} \cdot S \cdot \mathbf{c} \tag{1.14}$$

In order to find the energies of the bands, one has thus to solve for $E_{n\mathbf{k}}$. The elements of S are called overlap matrix elements and the elements of M are called transfer integrals.

The overlap matrix elements are written as

$$S_{mjlk} = \langle \chi_{mj} | \chi_{lk} \rangle = \frac{1}{N} \sum_{\mathbf{R},\mathbf{R}'} e^{i\mathbf{k}\cdot(\mathbf{R}-\mathbf{R}')} \langle \phi_m(\mathbf{r}-\mathbf{t}_k-\mathbf{R}') | \phi_l(\mathbf{r}-\mathbf{t}_k-\mathbf{R}) \rangle \tag{1.15}$$

The expression for the overlap matrix elements can be simplified by putting $\mathbf{R} = 0$ and $1/N \sum_{R'} = 1$

$$S_{mjlk} = \sum_{\mathbf{R}} e^{i\mathbf{k}\cdot\mathbf{R}} \langle \phi_m(\mathbf{r}-\mathbf{t}_k) | \phi_l(\mathbf{r}-\mathbf{t}_k-\mathbf{R}) \rangle \tag{1.16}$$

The transfer matrix elements are written by

$$M_{mjlk} = \sum_{\mathbf{R}} e^{i\mathbf{k}\mathbf{R}} \langle \phi_m(\mathbf{r}-\mathbf{t}_k) | \hat{H} | \phi_l(\mathbf{r}-\mathbf{t}_k-\mathbf{R}) \rangle \tag{1.17}$$

Orbitals of different quantum numbers ml are assumed to be orthogonal if they are centered at the same atom. This means that only diagonal elements of M_{mjlk} are non-zero (on-site energies). Further, one assumes interaction only between orbitals which are next-neighbors such that

$$M_{mjlk} = \epsilon_l \delta_m \delta_{ij} \delta(\mathbf{R}) + \sum_{\mathbf{R}=\mathbf{d}_{ij}+\mathbf{t}_k-\mathbf{t}_k} e^{i\mathbf{k}\cdot\mathbf{R}} \langle \phi_m(\mathbf{r}-\mathbf{t}_k | \hat{H} | \phi_l(\mathbf{r}-\mathbf{t}_k-\mathbf{R}) \rangle \tag{1.18}$$

1.2.3 Orbital composition of the band structure

In order to carry out band structure calculations one needs to know about the electron valence orbitals that participate in the bands. In tight-binding this knowledge is necessary to define the set of atomic orbital $\{\phi_l(\mathbf{r}-\mathbf{t}_k)\}$ needed in equation (1.15) for equation (1.17) and equation (1.15) [93, 137, 177].

Cappelluti et al. [20] have carried out density function theory (DFT) band structure calculations on ML-MoS_2 as a representative case for all ML-TDMCs. They find that ≪ The four conduction bands and the seven valence bands are mainly constituted by the five 4d orbitals of Mo [5d of W] and the six (three for each layer) 3p orbitals of S [4p of Se], which sum up to the 93% of the total orbital weight of these bands. ≫ [20]. Based on these findings, Silva et al. [149] have carried out DFT calculations to determine the orbital contributions of the Mo, $4d_{z^2}$, 4_{xy} We $5d_{z^2}$, $5d_{xy}$, S $3p_{xy}$, $3p_z$ and Se $4p_{xy}$, $4p_z$. We show the values of these contributions for the valence band maximum at K/K' and Γ in table 1.1.

According to table 1.1 the orbital composition of the valence band at K/K' and Γ is qualitatively and even quantitatively similar for all ML-TMDCs. At K/K' the band is mostly (≈ 75%) composed of d_{xy} orbitals from the transition metal atom and to a smaller extent (≈ 20%) made of p_{xy} from the chalcogen atoms. d_{z^2} and p_z make only negligible contributions at K/K'. This is in stark contrast to Γ, where d_{z^2} of the transition metal (p_z of the chalcogen atoms) make up about 70% (30%) of the valence band maximum. At Γ the d_{xy} and p_{xy} orbitals have negligible contributions.

TMDC	Orbital	K/K'	Γ	TMDC	Orbital	K/K'	Γ
MoS_2	d_{z^2}	0.0	0.66	**WS_2**	d_{z^2}	0.0	0.64
	d_{xy}	0.76	0.0		d_{xy}	0.74	0.0
	p_{xy}	0.20	0.0		p_{xy}	0.21	0.0
	p_z	0.0	0.28		p_z	0.0	0.28
$MoSe_2$	d_{z^2}	0.0	0.71	**WSe_2**	d_{z^2}	0.0	0.69
	d_{xy}	0.78	0.0		d_{xy}	0.73	0.0
	p_{xy}	0.18	0.0		p_{xy}	0.20	0.0
	p_z	0.0	0.23		p_z	0.0	0.23

TABLE *1.1 – Orbital composition of the valence band maximum (VBM) at K/K' and Γ as calculated by DFT from [149] for ML-MoS_2, $MoSe_2$, WS_2 and WSe_2. d-orbitals belong to the transition metal atom, p-orbitals stem from the two chalcogen atoms. For all ML-TMDCs holds that the valence band maximum at K/K' is made up of mostly d_{xy} and p_{xy} orbitals, whereas at Γ mostly d_{z^2} and p_z contribute.*

1.2.4 Comparison of theoretical and experimental band structures and parameters

With the knowledge about the crystal symmetry , the orbital composition and the numerical methods such DFT, $\hat{k} \cdot \hat{p}$ or tight-binding, one can calculate the electronic band structure of a of $1H$-TMDC. How do these calculations hold up in the face of experimentally determined band structures ? We thus compare some representative theoretical works to band structures determined by by Angle-Resolved Photoemission Spectroscopy (ARPES). ARPES can only measure occupied states, usually below the band gap in the absence of doping [121, 181]. We thus focus this review on the valence bands.

First, we make a qualitative comparison between experiment and theory: In FIGURE 1.3 we show band structure as measured by ARPES left of panel a) to d) and right theoretical band structure calculations by [149] using density function theory (in grey) and the tight-binding approach (red). For all ML-TMDCs, a local maximum can be found at Γ, whereas the global maximum is found at K/K'. The maximum of the valence band can be seen at K/K' for all ML-TMDCs, a necessary conditions for a direct band gap at K. This aligns with the theoretical calculations which anticipate a direct band gap at K/K' for all ML-TMDCs.

Below the valence band maximum at K/K' one finds a split-off bands a few hundreds of meV below for all ML-TMDCs. This split-off band arises due to the strong spin-orbit coupling in ML-TMDCs [93, 149]. This spin-orbit splitting of the bands and the spin-polarization has been analysed in spin-resolved ARPES: in FIGURE 1.4 we show spin-resolved photoemission spectra of the electrons at K and K' from [112]. At the K-point, the upper spin-split band has the spin index $|s\rangle = |+1/2\rangle$ and the lower $|s\rangle = |-1/2\rangle$. These sign switch at K'. Aside from the sign switch of the spins, the energies of the bands remain the same from K to K'. We will therefore treat K and K' as equivalent points of high symmetry, denoted by ≪ K/K' ≫.

For a more quantitative comparison we compare theoretical and experimental values of band structure parameters in TABLE 1.2 and TABLE 1.3. First, we will look at the effective masses m_e of the *upper* and *lower* spin-split band at the valence band edge at the K-point. Here, *upper band* refers to the band closer to the vacuum level/Fermi level, *lower* band

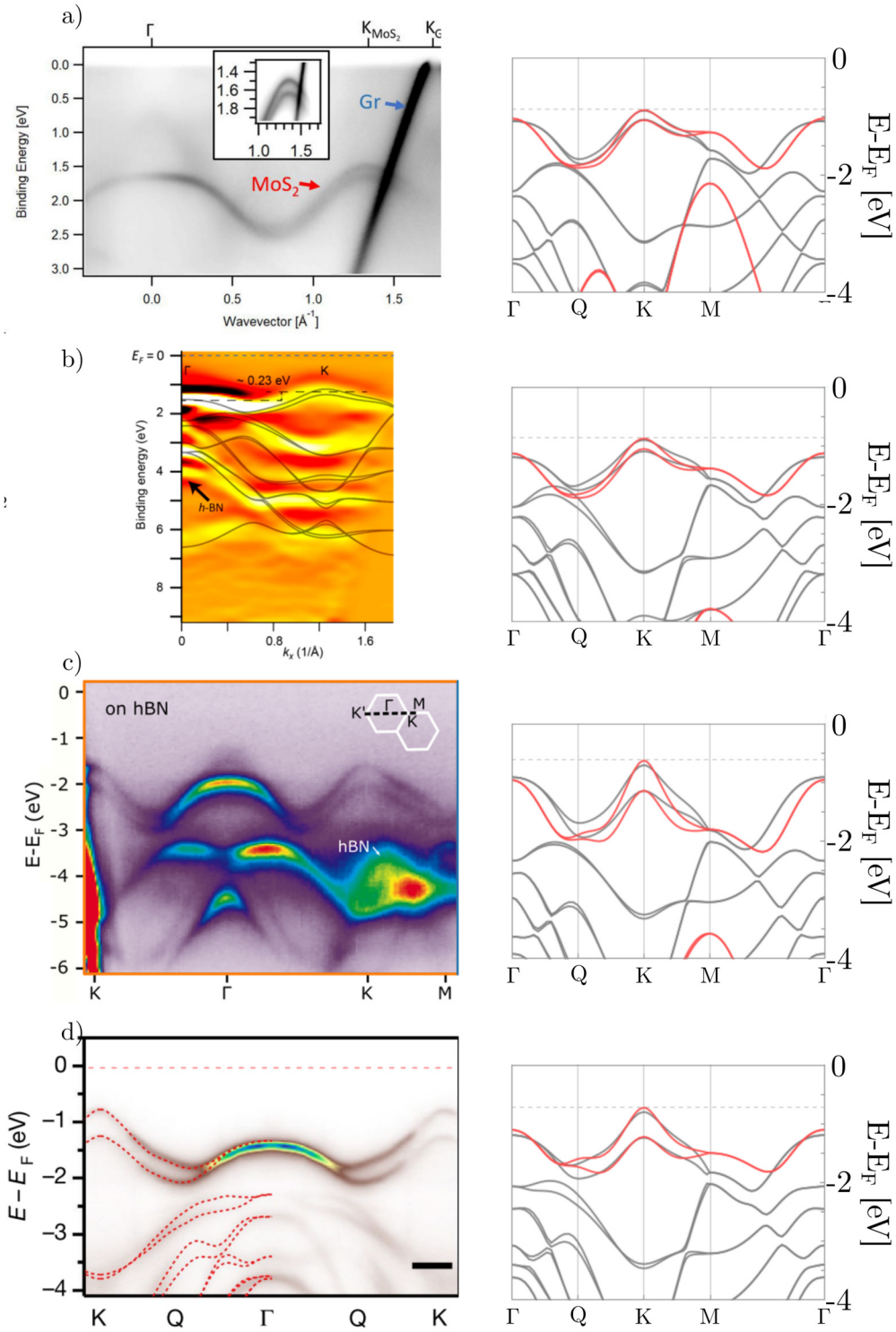

FIGURE 1.3 – ***a)-d)*** *Band structure measurements by ARPES on ML-TMDCS (left side; multiple authors) and corresponding theoretical band structures from [149] (on the right side) by DFT (in grey) and tight-binding calculations (red).*
MoS_2 on graphene [36], $MoSe_2$ on hBN [25], WS_2 on hBN [164], WSe_2 on hBN [121]. We have mirrored the calculations of [149] to correspond to the experimental graphs. For all ML-TMDCs there is good qualitative agreement between the theory and the experimental band structures. A local maximum of the valence band can be found at Γ, the global maximum of the valence band is found at K/K' with a split-off band.

further away from the vacuum level/Fermi level. Binding energies are generally measured in respect to the Fermi level $E - E_F$ where E_F is the Fermi. Further, one measures the spin-orbit splitting between the two bands at the valence band maximum at K/K' Δ_{SOC}. At Γ one can measure the effective mass of the band at the valence band edge. The binding energy of the valence band edge at K $E_{bin,K}$ and Γ $E_{bin,\Gamma}$ in relation to the Fermi level is measured, too. We will refer to the difference of the two as $E_{\Gamma K} = E_{bin,\Gamma} - E_{bin,K}$.

The ARPES measurements find a spin splittings Δ_{SOC} in the hundreds of meV at K/K'. The numerical values of these spin-splittings are reproduced very well by theoretical calculations. Differences regarding Δ_{SOC} between theory and experiments are only in the few tens of meV. The spin-splitting is highest for WSe_2 and lowest for MoS_2.

The effective mass of the band at Γ range from ≈ -2 $to - 3$ $m_{e,0}$ for all ML-TMDCs. At K/K' they are a lot lighter, ranging from ≈ -0.4 $m_{e,0}$ to ≈ -1 $m_{e,0}$. The effective mass of the lower spin-split band is higher or equal to the effective mass at the upper spin-split bands, for all ML-TMDCs. Deviations between theory and experiment are in the 0.1 $m_{e,0}$ for all ML-TMDCs.

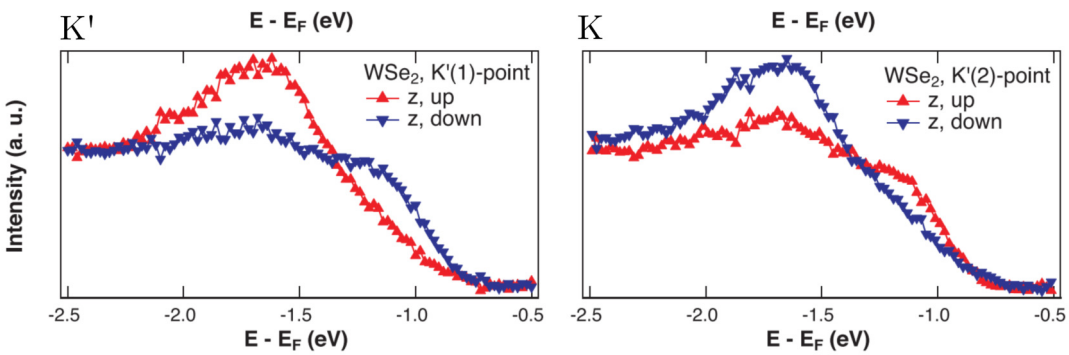

FIGURE *1.4 – Spin-polarized photoemission spectra at K' (left) and K right showing the different spin-split states for ML-WSe_2 at approximately $E - E_F = -1.2$ eV and -1.7 eV. The sign of the spin switches from K to K', but the energies of the bands remain the same. Taken and adapted from [112]*

The difference between the valence band maximum at K/K' and Γ $E_{\Gamma K}$ is in the hundreds of meV as expected for a direct band gap at K/K'. But the values can deviate in the hundreds of meV even amongst different experimental values.

In conclusion, we have seen that there is good qualitative agreement between theoretical and experimental band structures. The global maximum of the valence band maximum at K/K' and the spin-orbit splitting are reproduced by the theory. Quantitatively, the theory approximates well the experimental values for effective masses and spin-orbit splitting. For $E_{\Gamma K}$ it is difficult to find an agreement because there is no consensus on this value for a ML-TMDC in the experimental literature.

	MoS_2		$MoSe_2$	
	Theory	Exp.	Theory	Exp.
m_e Upper band at K[$m_{e,0}$]	-0.54 [78]; -0.54 [78]	-0.57 ± 0.03 [65]; -0.7 ± 0.1 [121]	-0.59 [78]; -0.6 [78]	-0.5 ± 0.1 [121]
m_e lower band at K [$m_{e,0}$]	-0.61 [78]; -0.61 [78]	-0.84 ± 0.08 [65]	-0.7 [78]; -0.7 [78]	
m_e at Γ [$m_{e,0}$]	-2.6 [78]; -2.45 [78]	-2.7 ± 0.1 [111]; -2.4 ± 0.3 [62]; -2 ± 0.35 [63]; -1.85 ± 0.22 [63]; -2.41 ± 0.05 [72]	-3.94 [78]; -3.49 [78]	-3.07 ± 0.08 [33]; -0.82 ± 0.01 [33]
Δ_{SOC} [eV]	0.148 [78]; 0.148[78]; 0.148 [93]	0.145 ± 0.004 [111]; 0.149 ± 0.004 [65]; 0.144 ± NA [36]; 0.17 ± 0.04 [121]	0.186 [78]; 0.184 [78]; 0.184 [93]	0.18 ± NA [112]; 0.18 ± NA [181]; 0.22 ± 0.03 [121]
$E_{\Gamma K}$ [eV]	0.07 [78]; 0.46 [78];	0.3 ± NA [41]; 0.36 ± 0.06 [15]; 0.3 ± NA [65]; 0.31 ± NA [111]; 0.14 ± 0.04 [121]	0.342 [78]; 0.329 [78]	0.23 ± NA [33]; 0.48 ± 0.03 [121]

TABLE *1.2 – Band structure parameters as measured by ARPES (expt.) and from theoretical calculations (theory) for ML-MoS_2 and ML-WS_2. The band structure parameters are the effective masses m_e of the upper and lower spin-split band at K/K', the effective mass of the band at Γ, the spin-orbit splitting at K/K' Δ_{SOC} and the difference between the upper spin-split band at K/K' and Γ. m_e is the electron rest mass.*

	WS_2		WSe_2	
	Theory	Exp.	Theory	Exp.
m_e Upper band at K[$m_{e,0}$]	-0,35 [78]; -0.36 [78]	-0.57 ± 0.09 [32]; -0.4 ± 0.02 [32]; -0.48 ± 0.05 [164]; -0.5 ± 0.1 [121]; -0.48 ± 0.05 [164]	-0.36 [78]; -0.36 [78]	-0.529 ± NA [184]; -0.42 ± 0.05 [121]; -0.35 ± 0.01 [84]
m_e lower band at K [$m_{e,0}$]	-0.49 [78]; -0.5 [78]	-0.78 ± 0.1 [164]; -0.64 ± 0.1 [164]	-0.54 [78]; -0.54 [78]	-0.532 ± NA [184]; -0.49 ± 0.05 [84]
m_e at Γ [$m_{e,0}$]	-2.18 [78]; -2.15 [78]	-2.55 ± 0.05 [164]; -2.45 ± 0.05 [164]	-2.87 [78]; -2.7 [78]	-2.344 ± NA [184]; -3.5 ± 1.8 [173]
Δ_{SOC} [eV]	0.429 [78]; 0.425 [78]; 0.43 [5]	0.425 [78]	0.466 [78]; 0.462 [78]; 0.466 [93]; 0.47 [5]	0.46 ± NA [184]; 0.47 ± NA [112]; 0.469 ± 0.008 [118]; 0.485 ± 0.01 [121]
$E_{\Gamma K}$ [eV]	0.252 [78]; 0.269 [78]	0.51 ± NA [158]; 0.26 ± NA [160]; 0.182 ± NA [44]; 0.24 ± 0.005 [66]; 0.28 ± 0.01 [164]; 0.28 ± 0.01 [164]; 0.39 ± 0.02 [121]	0.496 [78]; 0.506 [78]	0.68 ± NA [184]; 0.62 ± 0.01 [121]; 0.8 ± 0.1 [124]; 0.21 ± 0.01 [173]; 0.892 ± 0.02 [84]

TABLE *1.3* – *Same table as* TABLE *1.2 but for ML-$MoSe_2$ and ML-WSe_2. m_e is the electron rest mass.*

1.3 The influence of the band structure on the optoelectronic properties in ML-TMDCs

We have based the explanations in the following paragraphs on [165] unless otherwise cited. Optoelectronics in ML-TMDCs are governed by the optical excitation and recombination of coupled electron-hole pairs called **excitons**. Despite the extreme thinness of ML-TMDCs, the excitonic physics lead to some astounding optoelectronic properties: To name a few examples, ML-WS_2 which is encapsulated in layers of hBN can absorb almost 100% of light at its lowest exciton energy [39]. In ML-MoS_2 the quantum yield of photoluminescence is close to unity after a special chemical treatment of the monolayer [4]. These exceptional features of ML-TMDCs are in great part determined by their distinct band structure. In this section, we give a brief theoretical description of excitons in ML-TMDCs based on the Wannier-Mott and the 2D hydrogen model. We then show how some of these distinct optoelectronic properties follow from the previously discussed band structures parameters.

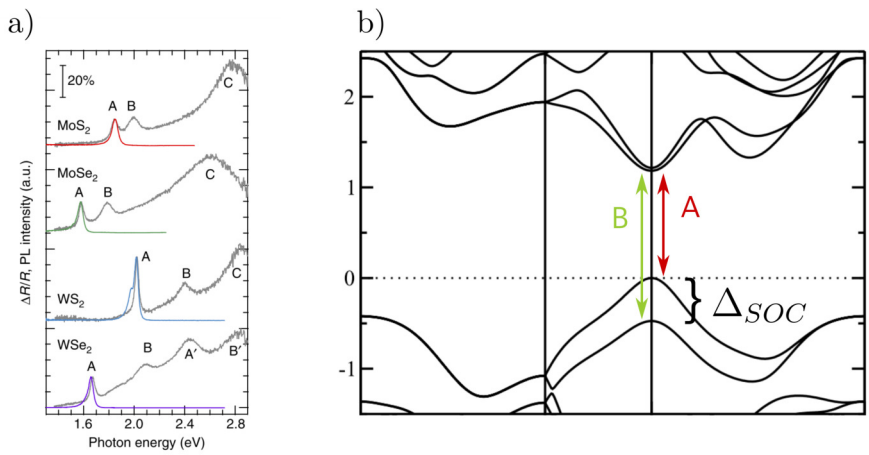

FIGURE 1.5 – ***a)*** *Photoluminescence (colored) and differential reflectance spectra on monolayers of MoS_2, $MoSe_2$, WS_2 and WSe_2 taken from [80]. The authors have indicated the transitions of the A, B and C exciton. For ML-WSe_2 two peaks labelled A' and B' are marked by the authors. Their origin was not elucidated, the background partially attributed to the C exciton seen in the other ML-TMDCs.* ***b)*** *Band structure of ML-WSe_2 taken and modified from [17]. The red and green arrow indicate the bound electron (hole) states in the conduction (valence) band which participate in forming an exciton. Because of the large spin-orbit splitting, the energy of the B exciton is ≈ 0.5 eV higher than of the A exciton, as can be seen for ML-WSe_2 in panel a).*

A1s exciton, exciton binding energy and relation to the effective masses

During excitation of an electron described by the state $|e\rangle = |s_e, \tau_e, \mathbf{k}_e\rangle$ from the valence band to the conduction band, a hole described by $|h\rangle = |s_h, \tau_h, \mathbf{k}_h\rangle$ is created in the valence band. Here, $s_e, \tau_e, \mathbf{k}_e$ ($s_h, \tau_h, \mathbf{k}_h$) designate the spin number, valley index and $\mathbf{k}$-vector of the electron (hole). The resulting exciton wave function includes electron and hole states and can be written as

$$|\Psi_{exc}\rangle = \sum_{e,h} C_{exc}(\mathbf{k}_e, \mathbf{k}_h)\, |e; h\rangle \tag{1.19}$$

with coefficients C_{exc} to be determined.

During this electronic excitation the total energy, momentum and spin are conserved. For photon energies close to the optical band gap, a photon carries the momentum $\mathbf{p}_{ph} = \hbar\mathbf{k}_{ph}$

which is negligibly small at energies of the band gap value $h\nu$ (around 2 eV) [165]. This means that the transition is *direct* in momentum, i. e. $\mathbf{k}_{e,i} - \mathbf{k}_{e,f} \approx 0$ for the electron from its initial to its final state. This in turn means that the energetically lowest excitation will be created at the direct band gap, which resides at K/K' in ML-TMDCs.

The nature of the band gap, direct or indirect, is parametrized by the difference between the valence band at Γ and K/K', called $E_{\Gamma K}$. A positive $E_{\Gamma K}$ means that the valence band maximum at K/K' is has a lower binding energy than at Γ. Without the direct band gap at K/K', the exciton creation/recombination would be a lot less efficient. This can be seen when comparing bilayer TMDCs, with an indirect band gap, to monolayer TMDCs, with the direct band gap [103].

The lowest excited exciton state is called **A exciton**. In panel b) of FIGURE 1.5 we show the band structure of ML-WSe_2 by [17]. The electronic states of the electron (in the conduction band) and the hole (in the valence band) which participate in forming the A exciton are indicated by a red double arrow. The recombination of the A exciton can be seen as a peak in all photoluminescence measurements in panel a) of FIGURE 1.5.

This energy of the excitonic transition as seen in photoluminescence measurements is hundreds of meV lower than the free particle band gap at K/K' [51, 124, 138]. The difference between the energy of the A exciton and the free particle band gap at K/K' is called the **exciton binding energy** E_{bin}. If the exciton is energetically excited above its binding energy, it will dissociate in free electron and hole. In other direct band gap semiconductors, for instance GaAs quantum wells, the exciton binding energy is on the order of 10 meV [108] such that excitons can easily be dissociated at room temperature. In ML-TMDCs they remain bound even at room temperature because of the high binding energies which we will quantify in the next step.

The magnitude of this binding energy in ML-TMDCs can be related to its distinct band structure. The relative motion of the bound electron-hole pair can be approximated in the framework of a two-dimensional hydrogen atom. In analogy, one can then use the quantum numbers (n, m), the principal and magnetic quantum number, to describe the relative motion of the charges. The energetically lowest exciton state for $(n, m) = (1, 0)$, often referred to as the 1s state in analogy to the hydrogen atom, has the highest binding energy. For $n \to \infty$ electron and hole dissociate and become free carriers. One can find an estimation for the binding energy of the 1s exciton state if we apply the eigen-energies of the 2D hydrogen model to the exciton in two dimensions:

$$E_{bin} = E(n = \infty) - E(n = 1) \approx \frac{4 \cdot E_{Ryd} \cdot \mu}{m_e \cdot \epsilon_{eff}^2} \tag{1.20}$$

where E_{Ryd} is the Rydberg energy, $m_{e,0}$ the electron rest mass, ϵ_{eff} the effective dielectric screening constant of the environment and the reduced mass μ in the center-of-mass picture of electron and hole. The reduced mass μ can be estimated by the effective masses of electron m_e and hole m_h in their respective valleys. These values are approximately -0.5 m_e (cf. TABLE 1.2 and TABLE 1.3) such that $\mu \approx -0.25 m_e$. $\epsilon_{eff} \approx 5$ in ML-TMDCs. This in turn gives a binding energy on the order of 500 meV. We see that the effective masses and as such, the curvature of the band structure, significantly determine the binding energy of the excitons.

B1s exciton and its relation to the spin-orbit splitting

In photoluminescene measurements of panel a) in FIGURE 1.5 we only see the energetically lowest transition, i. e. the A exciton. However, another excitonic transition, labelled **B**

exciton (B1s exciton more specifically) can be found in differential reflectance spectra for all ML-TDMCs as seen in panel a) of FIGURE 1.5.

The origin of the B exciton with higher energy than the A exciton can again be understood by considering the band structure. During the creation or annihilation of an exciton via a photon, the spin of the bound electron must be conserved. Let's consider the exemplary case of ML-WSe_2 in panel b) of FIGURE 1.5. In the conduction band the two spin-split bands are close in energy on the order of few tens of meV for all TMDCs [94]. In the valence band, however, the spin-splitting is on the order of hundreds of meV[121]. An exciton can thus form by involving a hole from the higher spin-split band at K/K' (A exciton) or the lower spin-split band (B exciton) as indicated in panel b) of FIGURE 1.5. The B exciton will have an energy approximately higher by the spin-orbit splitting in the valence band at K/K'.

Neutral C exciton and its relation to band curvature

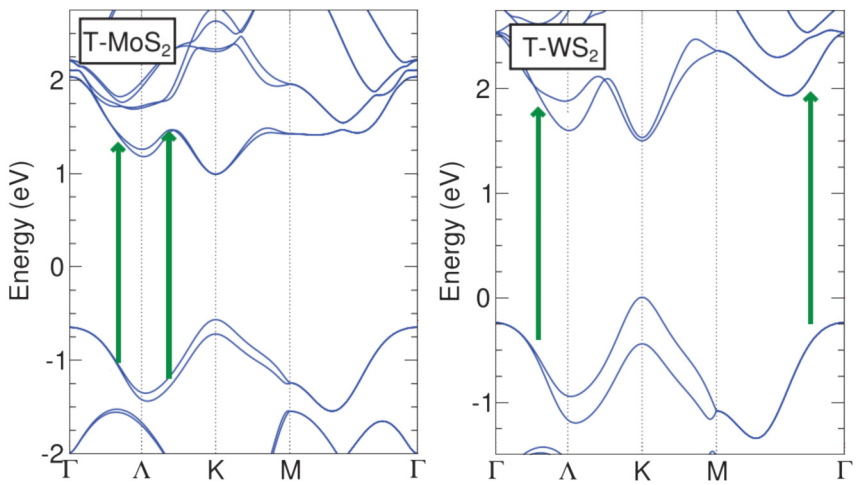

FIGURE *1.6 – Band structures calculated by [80]. The green arrows indicate electronic transition at parallel band curvatures where the joint density of states (jDOS) diverges. In differential reflectance spectra, the electronic transitions at the indicated areas contribute to the ≪ C exciton ≫ transition as seen in panel a) of* FIGURE *1.5.*

We have based the explanations in this paragraph on [7, 21, 80] unless otherwise cited. A third excitonic transition, labelled **C exciton**, can be found in the differential reflectance spectra in panel) of FIGURE 1.5. Notably, in the $\Delta R/R$ spectra, the C exciton peak has higher intensity than the A or B exciton. For ML-WSe_2 two peaks labelled A' and B' are marked by the authors [80]. Their origin was not elucidated, the background partially attributed to the C exciton seen in the other ML-TMDCs.

To understand the origin of the C exciton, we most understand the differential reflectance coefficient $\Delta R/R$. It can be written as [106, 122]

$$\frac{\Delta R}{R}(\nu) = \frac{4n}{n_0^2 - 1}\alpha(\nu) \tag{1.21}$$

where n is the refractive index of the flake, n_0 of the substrate and α is the absorption coefficient and ν the frequency of the absorbed/reflected photon.

The absorption coefficient, on the other hand, can be shown to be proportional to the joint density of states $j_{cv}(E)$[7]

$$\alpha(\omega) \propto j_{cv}(E) = \frac{2}{(2\pi)^3} \int_{E_c(\mathbf{k})-E_v(\mathbf{k})=E} \frac{1}{|\boldsymbol{\nabla}_{\mathbf{k}}(E_c(\mathbf{k}) - E_v(\mathbf{k})|} \, \mathrm{d}S \tag{1.22}$$

where $E_c(\mathbf{k})$ is the band dispersion the conduction band minimum and $E_v(\mathbf{k})$ at the valence band maximum at $\mathbf{k}$. A high joint density of states represents the ability of the system to excite an electron from an occupied state (in the valence band) to an unoccupied state (in the conduction band). The expression 1.22 becomes singular when

$$\boldsymbol{\nabla}_{\mathbf{k}} \left(E_c(\mathbf{k}) - E_v(\mathbf{k})\right) = 0 \tag{1.23}$$

In monolayer TMDCs this is the case at the K/K'-points where

$$\boldsymbol{\nabla}_{\mathbf{k}} E_c(\mathbf{k}) = \boldsymbol{\nabla}_{\mathbf{k}} E_v(\mathbf{k}) = 0 \tag{1.24}$$

We have seen that A and B exciton involve electron and hole states at the K/K-point. On the other hand, for ML-TMDCs one finds certain areas in the Brillouin zone at which the curvature between the valence band maximum and the conduction band minimum is almost parallel [21]. In these areas

$$\boldsymbol{\nabla}_{\mathbf{k}} E_c(\mathbf{k}) - \boldsymbol{\nabla}_{\mathbf{k}} E_v(\mathbf{k}) = 0 \tag{1.25}$$

which is called **band nesting** [21, 80]. Panel b) of FIGURE 1.6 shows a calculated band structure for ML-MoS_2 and ML-WS_2 from [21]. The arrows indicate electronic transitions between valence band and conduction band at which the joint density of states diverges. These transitions give rise to a high absorption at the energy close to the C exciton for all ML-TMDCs as shown in panel a) of FIGURE 1.5.

In conclusion, we have seen that the band structure has profound implications for the optoelectronic properties: curvatures/effective masses in different parts of the Brillouin zone, the direct band gap and the spin-orbit splitting at K/K' determine in large part the energies and intensities of A, B and C exciton. By tuning these band structure parameters, one can thus fundamentally influence the properties of excitons in ML-TMDCs.

2

Introduction to principles of Photoemission and ARPES for the analysis of electronic structures

2.1 Instrumental aspects of ARPES

In this chapter we will provide a review of our methods and the underlying fundamental theory on ARPES for ML-TMDCs. The section on instrumental aspects explains the basic principle of photoemission and Angle-Resolved Photoemission Spectroscopy (ARPES). The goal of ARPES is the measurement of the crystal's electronic band structure $E_{bin}(\mathbf{k})$. In the next sections, we illustrate the relationship between the measured vector $\mathbf{k}_{out}$ of a photoelectron and its kinetic energy E_{kin}, both in vacuum after photoexcitation. We relate these two to the binding energy E_{bin} and wave vector $\mathbf{k}_{in}$ of the photoelectron before photoexcitation. Today's ARPES systems are defined by their light source and the sampling and detection system. We explain why our light source, a gas-discharge lamp, is suitable for the analysis of ML-TMDCs. We summarize the state-of-the-art of modern sampling and detection systems, including recent developments, and explain in detail our own sampling and detection system: the NanoEsca I. The section on theoretical aspects summarizes the entire process of photoemission: the electron's probability of photoexcitation, traversal of the crystal and scattering events as well as emission at the surface. We rely on the 3-step-model which provides a good explanation of the underlying processes for the experimentalist. We relate these theoretical foundations to recent findings in ARPES on ML-TMDCs. Finally, we illustrate the process of work function measurement using photoemission.

2.1.1 The photoelectric effect and photoemission spectroscopy

Photoemission spectroscopy (PES) is based on the photoelectric effect discovered in 1887 by Heinrich Hertz and famously explained by Einstein later-on, earning him the phyics Nobel prize in 1921. We have based the explanations in the following paragraphs on [31, 55, 56, 150] unless otherwise cited.

In an improved version of the experiment by Hertz, metal cathodes of sodium or potassium are placed in a vacuum tube. These cathodes are then irradiated with light within the UV range. A closely placed anode collects charges emmitted from the metal cathode. When connecting cathode and anode one finds that a current flows between cathode and anode. A counter-voltage V is applied between anode and cathode. When the counter-voltage V is high enough, the current is cancelled out completely. Measuring the necessary counter-voltage determines the maximum kinetic energy of the electrons $E_{kin,max}$ emitted by the cathode

$$-e \cdot V = E_{kin,max} \tag{2.1}$$

where e is the elemental electron charge. It was then found that

$$E_{kin,max} = h\nu - \phi \tag{2.2}$$

where h the Planck constant, ν the frequency of the light used and ϕ a material specific parameter, the **work function** which we will further elaborate on (section 2.2.3).

Via the photoelectric effect, one can access an electron's binding energy E_{bin} inside a crystal and thus determine one variable of the electronic band structure. The knowledge provided by this experiment yielded the first measurement of photoemission spectra. Figure 2.1 shows a schematic density of states in a crystal $N(E)$ and the resulting photoemission spectrum $I(E_{kin})$ for a metal after photoexcitation of energy $h\nu$. Atomic core levels are reflected by single peaks in the photoemission spectrum, whereas the valence band is found as a broad, asymmetric peak. The lowest energy level that can be measured $E_{kin} = E_{vac}$ is offset to the Fermi level by the work function ϕ. This energy is usually referenced with respect to the Fermi level of the sample. In order to determine the Fermi level position, the spectrometer can be calibrated by a a clean noble metal surface.

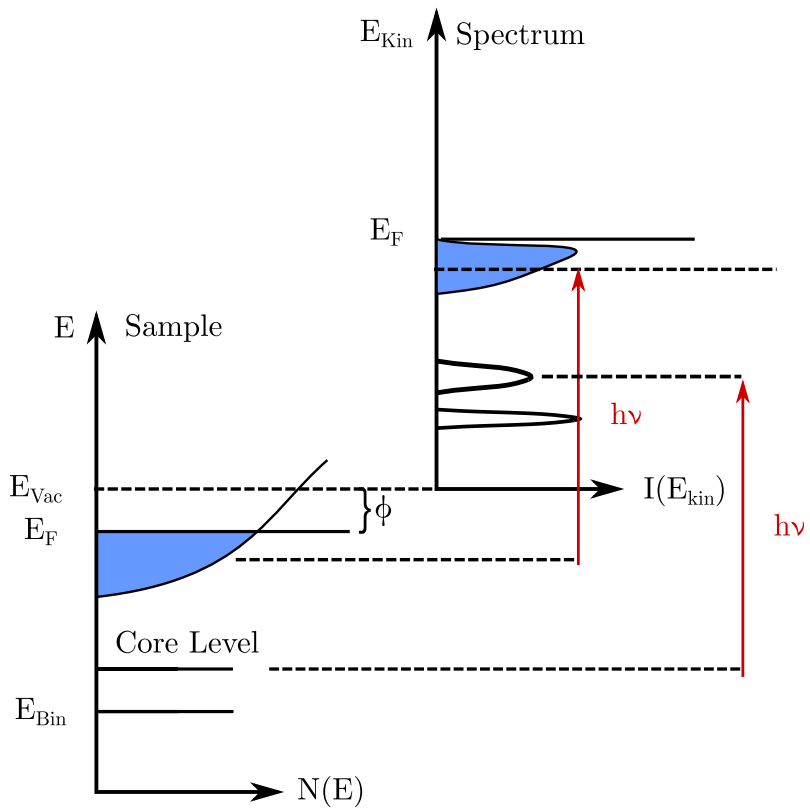

FIGURE *2.1 – Number of electrons as a function of internal energy $N(E)$ and the measured photointensity spectrum $I(E_{kin})$ as a function of kinetic energy E_{kin} after photoexcitation of energy $h\nu$. Core levels are mapped onto single peaks, the valence band is found as a broad band. Taken and adapted from [55].*

2.1.2 Angle-resolved photoemission spectroscopy (ARPES)

We have based the explanations in the following paragraphs on [31, 55, 56, 150] unless otherwise cited. The previous section explained how the binding energies of electrons inside a crystal could be determined using photoemission. In order to determine the band structure $E_{bin}(\mathbf{k}_{in})$, however, one must not only measure E_{bin} but also the wave vector $\mathbf{k}_{in}$ of the electron before photoexcitation inside the crystal. The relation between the two yields the band structure $E_{bin}(\mathbf{k}_{in})$. Measuring both E_{bin} and $\mathbf{k}_{in}$ is thus the goal in ARPES.

ARPES technique have evolved beyond simple band structure characterisation: Today, using different light polarizations, one can measure specific spin-states in *spin-resolved ARPES* [112, 134]. Another technique is *time-resolved* ARPES, using pump-probe experiments with pulsed light, electrons can be excited and this excited state then analyzed. This allows for instance the resolution of the otherwise empty conduction band [92], exciton momenta in the Brillouin Zone [100] or to resolve charge-transfer [91] between layers of a heterostructure.

For the analysis of band structures in ML-TMDCS we will conduct *spatially-resolved ARPES*. 2D-Materials and their heterostructures are typically microns in diameter. In spatially-resolved ARPES, one can analyze areas of a few μm to even 100s of nanometers in diameter. This allows to map the band structure as a function of position on the sample [23, 56]. There have been many developments, updates and new branches added to ARPES in the recent history which we will review in this chapter.

Kinematics of photoemission

Photoelectrons inside the crystal are subject to a different electrostatic potential than photoelectrons in vacuum measured by ARPES. In order to deduct the energy states inside the crystal from measured photoelectrons outside, one must thus consider how energy and momentum are conserved during the photoelectron's traversal of the crystal surface.

Upon illumination from a suitable light source with photon energy $h\nu$, electrons within the crystal are excited and energetically allowed to leave the crystal. The resulting kinetic energy E_{kin} and the components of the electron's wave vector $\mathbf{k}_{out}$ outside the crystal are given by

$$E_{kin} = h\nu - \phi - E_{bin} \tag{2.3}$$

$$k_{out,\parallel} = \frac{\sqrt{2m_{e,0}E_{kin}}}{\hbar} \cdot \sin(\theta) \tag{2.4}$$

$$k_{out,\perp} = = \frac{\sqrt{2m_{e,0}E_{kin}}}{\hbar} \cdot \cos(\theta) \tag{2.5}$$

where E_{kin} is the photoelectrons kinetic energy after excitation, ϕ the sample's work function and θ the angle with respect to the surface normal. E_{bin} is the photoelectron's binding energy with respect to the Fermi level, m the electron rest mass in vacuum. While $\mathbf{k}_{out}$ refers to the $\mathbf{k}$-vector of the photoelectron in vacuum and thus outside the crystal, one needs the value $\mathbf{k}_{in}$ after photoexcitation to retrieve the band structure. The parallel component of the photoelectron $\mathbf{k}$ is conserved during transmission through the surface, such that

$$k_{\parallel,out} = k_{\parallel,in} \tag{2.6}$$

This is not the case for the out-of-plane component $k_\perp$. However, since in our work we only consider 2D-materials, there is no dispersion in $k_\perp$-direction such that we do not

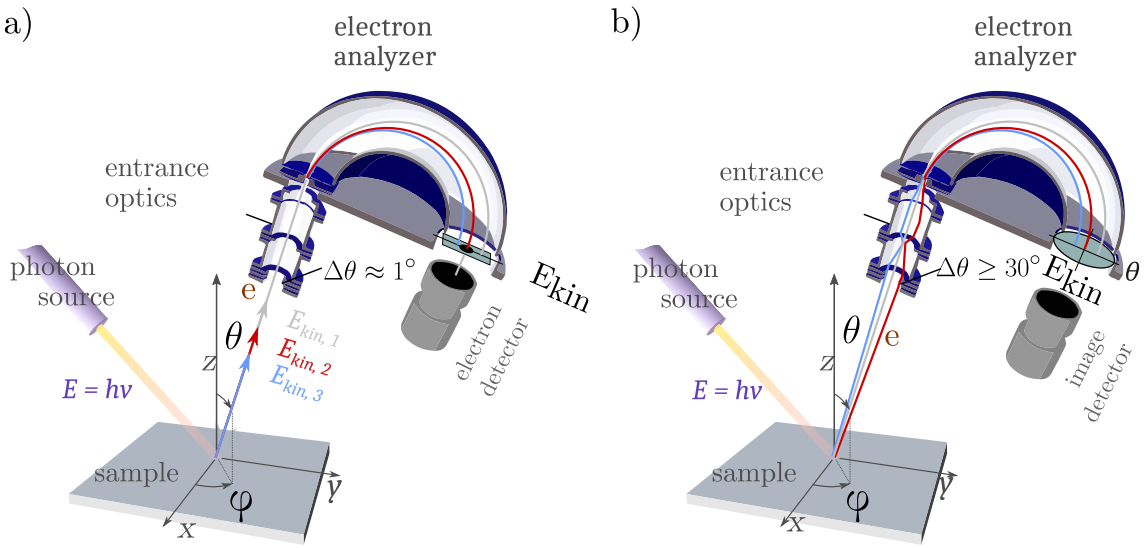

FIGURE *2.2 – The basic principle of an ARPES setup in the* ***a)*** *original and more advanced configuration* ***b)****. For both configurations the sample is illuminated by photons of energy $E = h\nu$ from a light source. The resulting photoelectrons are measured using the detection and imaging system as a function of their kinetic energy E_{kin} and their polar φ and azimuthal θ angle. In* ***a)*** *the electron analyzer disperses photoelectrons only by their kinetic energy E_{kin} along the radial axis for a fixed φ and θ. The slits at the entrance and exit of the analyzer determine the energy resolution. Photoelectrons are then measured by an electron detector. In* ***b)*** *photoelectrons are dispersed according to their θ and E_{kin} simultaneously. For clarity, we only show electrons of different θ, not E_{kin}. Both variables are recorded on a two-dimensional image detector. This allows faster measurement. All measured parameters E_{kin}, φ, θ are crucial to determine the band structure $E(\mathbf{k})$ of the electron before excitation. Taken and modified from Wikipedia* Spectroscopie photoélectronique résolue en angle, *19/11/2021 at 17:00*

have to consider the out-of-plane component. In bulk materials, the k_z or equivalently $k_\perp$-component must be considered as well, but the relation $E(\mathbf{k} = (k_x, k_y, k_z))$ is more complicated and usually requires further models and or approximation.

Faster scanning through 2D-detectors

We have based the explanations in the following paragraphs on [23, 56, 150] unless otherwise cited. Having understood the law of conservation for photoelectrons during photoemission, we now turn to the ARPES technique. In its simplest form, an ARPES setup is divided into four different components: the *light source*, the *entrance optics*, an *electron analyzer* and a *electron detection/imaging* system.

In panel a) of FIGURE 2.2 we show the *original* ARPES method. First, one sets the polar φ and azimuthal θ angle of the entrance optics's optical axis. The photoelectrons enter the entrance optics through a small aperture with a narrow acceptance angle $\Delta\theta \approx 1°$. The entrance optics maximize the electron collection. In the energy analyzer they are then dispersed by their kinetic energy E_{kin} along the radial axis. Photoelectrons of the desired kinetic energy are filtered by a small aperture and are detected by an electron detector.

As a result, one measures the kinetic energy of the exiting photoelectrons E_{kin} as a function of φ and θ. The kinetic energy can be related to the binding energy E_{bin} of the photoelectron in relation to the Fermi level before photoexcitation. φ and θ can be related to k_x and k_y of the electron before photoionization. Using the laws of energy and momentum-conservation one can then deduce the band structure $E_{bin}(\mathbf{k}_\parallel)$ for a 2D-material.

The configuration in a) however requires frequent rotation/tilt of the entrance optics to scan over all φ and θ. This is time-consuming and error-prone because the stability can be challenging during tilt/rotation. An advanced development is the use of two-dimensional image detectors as shown in panel b) of FIGURE 2.2. For a fixed φ, photoelectrons are collected through an aperture of a finite acceptance angle $\Delta\theta$. The electron analyzer disperses the photoelectrons not just by their kinetic energy on one axis, but also a range of θ which is on the orthogonal axis on the image detector screen. We thus have two axes for two variables. This allows to measure the Brillouin zone for a range of values in E_{kin} and θ at once and enables faster scanning.

Examples of this advanced ARPES technology with acceptance angles up to $\Delta = \pm 30°$ are the PHOIBOS 150 analyzer or $\Delta\theta \pm 15°$ for the Scienta R4000 electron analyzer [1].

The setup we have employed during our work takes this one step further: the entrance optics captures photoelectrons regardless of φ, θ and filters all electrons by energy. A photoelectron then holds 3 distinct information E_{kin}, φ, θ after exciting the crystal. We now have 3 variables to distinguish for 2 axes on the image detector. In order to explain this non-trivial measurement operation, we have taken great care in explaining the inner workings of our hemispherical (electron) analyzer in section 2.1.8.

2.1.3 Sample and instrumental requirements for ARPES on 2D-materials

We have based the explanations in this paragraph on [99, 126, 150] unless otherwise cited. Because of the extreme thinness of 2D-materials, the number of photoelectrons emitted in photoemission is low compared to bulk materials. This means that special care must

1. The PHOIBOS 150 https://www.specs-group.com/nc/specs/products/detail/phoibos-150-wal-2d-dld/ used by [1, 44] , Scienta R4000 https://www.aps.anl.gov/Sector-29/29-ID/ARPES used by [41, 64, 66, 67, 152, 160]

be taken to retrieve a sufficient signal-to-noise ratio in a photoemission experiment. The surface area of interest to be analyzed in ARPES can be of tens of micron in diameter down to sub-micron length. It has to be clean, i. e. free of contamination, and atomically flat, otherwise photoelectrons would randomly scatter at the surface. Since in ARPES, the photoelectron signal is integrated over many lattice unit cells, the signal would be blurred if the surface were inhomogeneous. To ensure the removal of residuals from the surface, samples are either sputtered or annealed before entering the analysis chamber. All ARPES experiments have to be conducted in ultra-high vacuum conditions (typically at 10^{-10} Torr). UHV conditions make sure that photoelectrons can exit the sample without scattering with air molecules. They also prevent the formation of water films on the surface that introduce further attenuations of the photoelectron signal. In some cases, sample fabrication techniques such as *molecular-beam epitaxy* (MBE) and *pulsed-laser deposition* (PLD) are coupled into a single UHV chamber with ARPES [70, 174], since all these techniques use UHV conditions. Combining these techniques within one vacuum-system ensures a seamless transfer from fabrication to measurement without running the risk of contaminating the sample in ambient conditions. These type of studies are called **in situ**.

2.1.4 Requirements for light sources to study 2D-Materials with ARPES

We have based the explanations in the following paragraphs on [56] unless otherwise cited. When choosing a suitable light source for an ARPES experiment on 2D-materials, different aspects need to be considered:

1. **Resolution and counting statistics**: Let $I = i \cdot 2\Delta E$ be the current of counted photoelectrons where i is the number of counted photoelectrons per unit time and interval of energy. ΔE is the energy resolution. We collect electrons in the energy range $[E - \Delta E, E + \Delta E]$. The better the setup's energy resolution, the smaller ΔE and the smaller the current of counted photoelectrons.
   In ML-TMDCs we want at least be able to resolve the spin-split bands with spin-orbit splitting at K. The value is $\Delta_{SOC} \approx 500$ meV for ML-WSe_2. The energy resolution is determined by the resolution of the spectrometer, the linewidth of the photon excitation and the temperature broadening and should be significantly lower than the spin-orbit splitting. At high resolution the photon flux of the optical excitation must be high enough such that the current of counted electrons I is sufficient.
2. **Matrix element effects and initial state selection**: The probability of exciting an electron from its initial state into a final photoelectron state is given by the matrix element. It is determined by the choice of wavelength, the polarization of the light, the experimental geometry (angles of crystal axis compared to angle of incident photon beam) and the orbital symmetry of the initial electron state. A detailed account of the underlying physics will be provided in section 2.2.2.
3. **Surface sensitivity**: The choice of wavelength determines the depth at which excited photoelectrons can be measured. The inelastic mean free path λ_{IMFP}, which we will explain in section 2.2.2, gives an estimation up to which depth a signal of unscattered photoelectrons can still be measured. For 2D-materials we are interested in maximizing the surface sensitivity on the order of $\approx 1-2$ nm. According to Seah and Dench this would imply the use of a photon excitation energy of $h\nu$ from 10 eV to 100 eV [114].
4. **Accessible momentum region**: The higher the energy of the photon excitation the larger the portion of the reciprocal space that can be detected in ARPES. Photoelectrons which have left the crystal can have a maximum parallel k-component of $k_{\parallel,out,max} = \sqrt{2m(h\nu - \phi)/\hbar}$. Because of the conservation of the parallel-component

$k_{\parallel,out} = k_{\parallel,in}$ this is also the maximum $k_{\parallel,in}$ that can be resolved. This means that $h\nu$ should be chosen such that at least the first Brillouin Zone can be resolved. For ML-TMDCs we take $k_{\parallel,max} \approx 1.3$ $\mathring{A}^{-1}$ and a work function of $\phi \approx 5$ eV. This yields a minimum photon energy of $h\nu \approx 11$ eV.

5. **Accessibility**: The light source should be available and allow measurements within a reasonable timeframe. This is important especially if many samples are to be analysed.

Currently, four different light sources are available for ARPES experiments. We have based the explanations in the following paragraphs on [23, 56, 150] unless otherwise cited.

— *Synchrotrons* can produce light ranging from VUV to hard X-Ray (few eV to $\propto$ 100 keV). Specialised optical setups allow to focus the photon excitation beam onto spots which are few microns to tens of microns in size. At the beamline 7.0.2 of the Advanced Light Source Synchrotron in Berkeley (USA), for instance, the photon excitation beam can be focussed on a spot of 10 μm in diameter [67, 159]. This is useful because flakes of ML-TMDCS usually are microns or tens of microns in diameter. Because of the high photon flux available at synchrotrons, the energy resolution is the highest for ARPES on ML-TMDCs. At the $\mu-$ARPES setup of MAESTRO synchrotron in Triestre (Italy), for instance, the resulting energy resolution is better than 20 meV [67].

  Synchrotron light thus provides excellent signal strength and allows a very high resolution down to few tens of meV in energy. Further, one can easily set a photon energy between $h\nu$ of 10-100 eV, which satisfies conditions 1 to 4. The only problem with synchrotrons is their accessibility: First, a proposal for an experiment has to be written which must be reviewed. Once the proposal is accepted, between 4 to 6 months go by until the experiment can be conducted. The timeframe for experimentation is also very limited (less than 5 days). This can be a problem if many different samples need to be compared in ARPES.

— *Laser sources* used for ARPES have an energy range from 6 to 11 eV. For the analysis of ML-TMDCs, they thus do not satisfy conditions 2 to 4. The photon beam emitted by a laser has, however, a very small linewidth ($\approx$ 1 meV) and lasers are available in many laboratories. Pulsed lasers have been used in time-resolved ARPES experiments [98, 100].

— *Gas-discharge lamps* have, like lasers, a naturally narrow linewidth of the signal $<$ 1 meV. Oftentimes noble gases and their dominant spectral lines are used, but they offer a larger variety of different photon energies in the necessary range (He-Iα at 21.22 eV, He-IIα 40.81 eV, Ne Iα at 16.85 eV and Ar I at 11.62 eV). Their photon energy is thus suitable for the analysis of ML-TMDCs. Unless the setup is adapted, the light of a gas-discharge lamp is unpolarized and continuous. A helium-run gas-discharge lamp is very suitable for our application as it is easy-to-use [150] even if the photon flux is lower than at the synchrotron. Gas discharge-lamps are table-top devices and are thus very accessible.

2.1.5 Energy- and momentum resolution of an ARPES setup

We have based the explanations in the following paragraphs on [56, 126, 150] unless otherwise cited. In order to measure features of the band structure, our experimental resolution must be sufficient. One important band structure feature is the spin-orbit splitting Δ_{SOC} which for ML-TMDCs is in the few hundreds of meV [121]. The total energy resolution of our ARPES setup must thus be significantly lower. It is determined by three aspects:

the linewidth of the photon excitation $h\Delta\nu$, the resolution of the analyzer ΔE_{ana} and the thermal broadening ($4k_BT$) such that the total resolution [56, 126]

$$\Delta E_{tot} = \sqrt{(h\Delta\nu)^2 + (\Delta E_{ana})^2 + (4k_BT)^2} \tag{2.7}$$

where k_B is the BOLTZMANN constant and T the temperature of the sample. For most ARPES-studies on 2D-materials the linewidth is ≈ 1 meV and thus negligible [56]. At cryogenic temperatures, k_BT also becomes negligible. The delimiting factor is then ΔE_{ana}. The resolution is set such that the accepted photocurrent is sufficiently high. At synchrotrons, where a high photon flux can be achieved, ΔE_{ana} can thus be set to very low values in the tens of meV [54, 67, 162]. For our study we use a helium gas discharge lamp with lower photon flux and we set the energy resolution of the analyzer no lower than 200 meV. The reciprocal length of a Brillouin zone is ≈ 1.3 $\mathring{A}^{-1}$. In order to measure dispersive features in $\mathbf{k}$, we thus need sufficient in-plane momentum resolution. It is determined by the acceptance angle $\Delta\theta$ and the azimuthal angle θ to the optical axis of the entrance optics[31]

$$\Delta k_{\parallel}^2 \leq \frac{2mE_{kin}}{\hbar^2} \cdot (\cos\theta \cdot \Delta\theta)^2 \tag{2.8}$$

where θ the angle to the optical axis of the electron analyzer relative to the sample. For most ARPES studies on ML-TMDCs this value ranges from < 0.01 $\mathring{A}^{-1}$ to ≈ 0.03 $\mathring{A}^{-1}$ [67, 121, 168]. The instrumental angular resolution $\Delta k_{\parallel}$ of our setup is estimated to be 0.03 $\mathring{A}^{-1}$. The effective angular resolution is $\approx 0.05\mathring{A}^{-1}$.

2.1.6 Techniques for spatially resolved ARPES on ML-TMDCs

Currently, two different approaches for spatially-resolved ARPES.

μ- or nano-ARPES

We have based the explanations in this paragraph on [23] unless otherwise cited. Synchrotron light is focussed onto a spot size of micron or sub-micron diameters [54, 57, 76, 121, 168]. By moving the sample a specific area of interest can be selected or an entire region iteratively scanned. Because of the small spot, this technique can be applied to samples where very small areas need to be analyzed ($\leq 1\mu m$ for instance for cleaved bulk crystals). When it comes to measuring the band structure of ML-TMDCs , these techniques routinely offer in-plane momentum resolutions of few $0.01\mathring{A}^{-1}$ [67, 121, 168] and energy resolutions in the few tens of meV [54, 67, 162] down to 14 meV [2].

Photoemission Electron Microscopy (PEEM)

We have based the explanations in this paragraph on [23, 56] unless otherwise cited. Instead of using a small spot size, a large area of the sample is illuminated with the light source which contains the field of view of the PEEM experiment. An electric potential difference of several kV's is applied between the sample and the PEEM column. The resulting electric field accelerates all photoelectrons towards the PEEM column which serves as an electron lens system. The column itself consists of electric lenses each with an image and a focal plane. The micron-size area of interest is selected with an iris in the image plane of the objective. Because all photoelectrons are recorded at once regardless of the respective $k_{\parallel}$, this enables an extremely fast acquisition. Furthermore, because the sample is not tilted or rotated, high stability during measurement can be guaranteed [23, 56].The

2. https://www.elettra.trieste.it/elettra-beamlines/spectromicroscopy.html

PEEM column itself cannot distinguish kinetic energies of the outgoing photo-electrons so it has to be combined with an energy filter. Hemispherical or time-of-flight analyzers are usually added to achieve energy-filtered PEEM (EF-PEEM). Resolutions reach typically about 100 meV in energy and 0.1 $\mathring{A}^{-1}$ in momentum [56] [3]. Recently, TUSCHE ET AL. demonstrated EF-PEEM with an energy resolution of down to 12 meV and a momentum resolution of $\Delta k_{\|} = 0.005\mathring{A}^{-1}$ [157].
One major advantages of EF-PEEM to nano- or μ-ARPES is its ability to quickly switch between real space and momentum mode allowing a quick selection of the analyzed area of interest in real space and subsequent band structure analysis. We explain this switching in section 2.1.7. We will refer to EF—PEEM in reciprocal space as **kPEEM**. Examples for kPEEM devices are NanoEsca II, METIS and FE-LEEM (low energy electron microscopy)/PEEM P90 of SPECS (SPECS GmbH, Berlin, Germany), and the ELMITEC PEEM/LEEM (ELMITEC Elektronenmikroskopie GmbH, Clausthal-Zellerfeld, Germany) [23, 56, 126].

	μ- or nanoARPES	**Our setup: kPEEM**
Light source	Synchrotron	Helium Lamp
Available energies	10 eV to keV [150]	21.22 eV (He I), 40.8 eV (He II)
$k_{\|}$ resolution	< 0.01 to 0.03 $\mathring{A}^{-1}$ [67, 121, 168]	≈ 0.03 $\mathring{A}^{-1}$
Energy resolution	tens of meV [54, 67, 162]	200 meV
Minimum crystal size for band structure analysis	down to ¡ 1 μm [54, 57, 76, 121, 168]	5 x 5 $(\mu m)^2$
Accessibility	poor	Lab-based, very available
Examples of ARPES on ML-TMDC based structures	ALS MAESTRO (USA) [67, 76, 140, 162], Diamond I05 Beamline (UK) [54, 57, 58] , SOLEIL (France) [52, 130], Elettra (Italy) [102, 121, 168]	PFNC of the CEA-LETI in Grenoble [72, 135] IRAMIS/SPEC/LENSIS at CEA-Saclay NanoESCA/Nanospectroscopy beamline at Elettra (Italy) University of Linköping, Sweden University of Bristol, UK

TABLE *2.1 – Comparison of currently used techniques for band structure analysis. Here, we compare μ- or nanoArpes with synchrotron light to our setup at the Plateforme Nanocaractérisation of the CEA-LETI in Grenoble.*

We have summarized the technical aspects of μ-or nanoARPES and our kPEEM setup in TABLE 2.1. Both of these techniques have been overtaken by a very recent upgrade of μ-ARPES at the Advanced Light Source synchrotron of Berkeley. New custom-made deflectors allow to scan the entire first Brillouin Zone without moving the sample [67, 159]. On the one hand this allows extremely fast acquisition such that an entire Brilloun Zone can be captured within minutes, on the other hand the sample remains stable during acquisition.

2.1.7 Our ARPES instrument: Functionality of the NanoEsca PEEM apparatus

Operation modes of the NanoEsca microscope

In this work we have carried out measurements with the NanoEsca PEEM setup of the CEA-LETI in Grenoble, at the Platform For NanoCharacterization (PFNC). The setup is issued and delivered by the Focus GmbH in Taunusstein, Germany. In total there are four different operating modes for the NanoEsca PEEM setup [43, 126]:

3. https://scientaomicron.com/Downloads/Brochures/ESPEC/NanoESCAII_SO_Brochure.pdf

— PEEM on secondary electrons without energy-filtering. This mode allows navigation on the sample and microscopic imagery without regard for the initial binding energy of the photoelectrons before excitation.

— EF-PEEM in real space: two-dimensional microscopy in real space either from core-level electrons (for chemical state analysis), from secondary electrons (for work function determination) or valence electrons (analysis of the valence band maximum).

— EF-PEEM in reciprocal space, also called *kPEEM*. This mode allows band structure measurement and analysis.

— Channeltron mode: an spectroscopic mode as in conventional photoemission spectroscopy. Here, the microscope enables a perfect control of the analysis area.

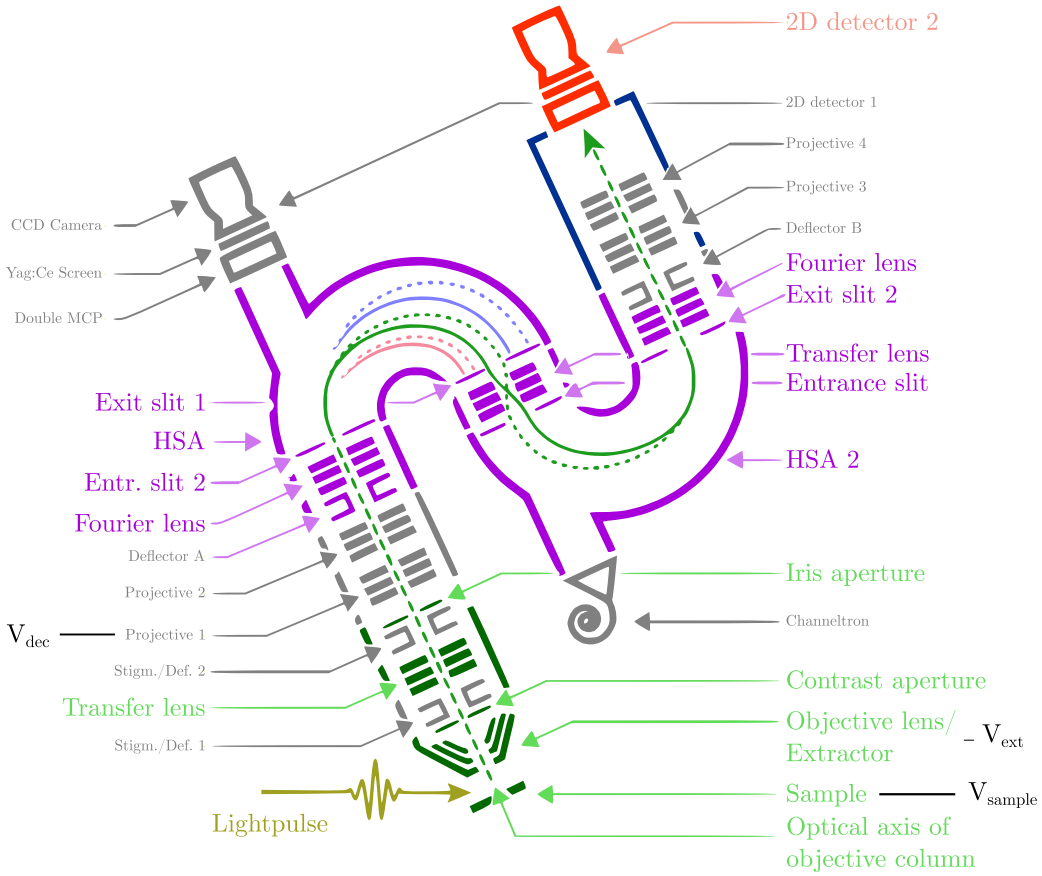

FIGURE *2.3 – Schematic of the NanoEsca I energy-filtered PEEM system as described in the text. The NanoEsca I consists of the PEEM objetive column, the double hemispherical analyzer (HSA) and its electron detection system. We have added the electrostatic potentials at the height of the V_{sample}, extractor anode V_{ext} and decelerating projective lens V_{dec}. Elements of the microscope which are relevant to our work are written in bold and colored. For completeness, we have also noted other elements in gray. Taken and modified from [126]*

In this work we have focussed on EF-PEEM in real space and reciprocal space (kPEEM) for the analysis of ML-TMDCs. This has allowed us to characterise the electronic structure of the ML-TMDCs in terms of their work function ϕ and band structure $E_{bin}(\mathbf{k})$. In the following we will explain the process of energy filtering in the NanoEsca which is crucial to determine E_{bin}. We also show how the NanoEsca corrects image aberrations and

switches from real space to momentum mode, allowing real space EF-PEEM and kPEEM within one measurement session. Eventually, we explain in detail the inner workings of the hemispherical (electron) analyzer and how it is able to energy-filter two-dimensional photoelectron images without tilts or rotations of the PEEM column.

Electrostatic potentials in the PEEM column for later energy-filtering

We have based the explanations in the following paragraphs on [43, 126] unless otherwise cited. The propagation of photoelectrons through the entire NanoEsca setup can be understood through FIGURE 2.3. The sample is illuminated by a photon source, a Helium discharge lamp in our case, with an energy of $h\nu = 21.22$ eV. Photoelectrons exiting the crystal surface are accelerated towards the objective lens through a strong electric field between the sample and the *extractor* anode [43, 126]. The potential difference between sample and extractor anode is 12 kV. This strong acceleration towards the PEEM column reduces the angular spread of the photoelectrons and in turn imaging (spherical) aberrations within the microscope. Photoelectrons that have left the crystal into vacuum carry a specific kinetic energy $E_{kin,out}$ after photoexcitation given by equation (2.3)

However, after acceleration through the extractor anode electrons in the PEEM column will have the new kinetic energy $E_{kin,col}$. If the microscope is used in PEEM-mode without energy-filtering, the sample potential V_{sample} is kept at ground $V_{sample} = 0$ and all photoelectrons are collected regardless of their kinetic energy. In energy-filtered mode, however, electrons of the former kinetic energy $E_{kin,out}$ are accelerated to an energy of $e \cdot V_{ext}$. This can be done by setting $e \cdot V_{sample} = E_{kin,out}$. In that case the new kinetic energy of the photoelectron with former kinetic energy $E_{kin,out}$ will just be

$$E_{kin,col} = E_{kin,out} + e \cdot (V_{ext} - V_{sample}) = e \cdot V_{ext} \tag{2.9}$$

where V_{ext} and V_{sample} are the electrostatic potentials of the sample and the extractor. The hemispherical analyzer, which we will explain in section 2.1.8, filters out all electrons of all electrons that enter with a kinetic energy $E_{kin} \notin [E_{pass} - \Delta E_{ana}, E_{pass} + \Delta E_{ana}]$. Here ΔE is the energy resolution of the analyzer.

For later energy-filtering, the photoelectrons at kinetic energy of $e \cdot V_{ext}$ must retarded to match the so-called pass energy E_{pass} of the hemispherical analyzer. This is achieved using a decelerating anode of potential V_{dec}

$$E_{pass} = E_{kin,col} - e \cdot V_{dec} - \phi_{hsa} = e \cdot V_{ext} - e \cdot V_{dec} - \phi_{hsa} \tag{2.10}$$

where V_{ext}, V_{dec} and ϕ_{hsa} are the electrostatic potential of the extractor anode and the decelerator anode and the work function of the hemispherical analyzer [126].

PEEM column for transfer of photoelectrons and image corrections

We have based the explanations in the following paragraphs on [40, 43, 126] unless otherwise cited. Photoelectrons which have reached the extractor enter the PEEM column. The role of the PEEM column is many-fold: it corrects image aberrations, provides a magnification of the electron image (telescopic mode) and allows fast switching from real space imagery into reciprocal imagery and vice versa.

In FIGURE 2.4 we see a cross-section of the PEEM column of the NanoEsca which illustrates a photoelectron's journey. We show the different electron trajectories, the initial photoelectron position on the sample and its outbound angle at the height of the sample: Once electrons have entered the column through the extractor, they pass through the

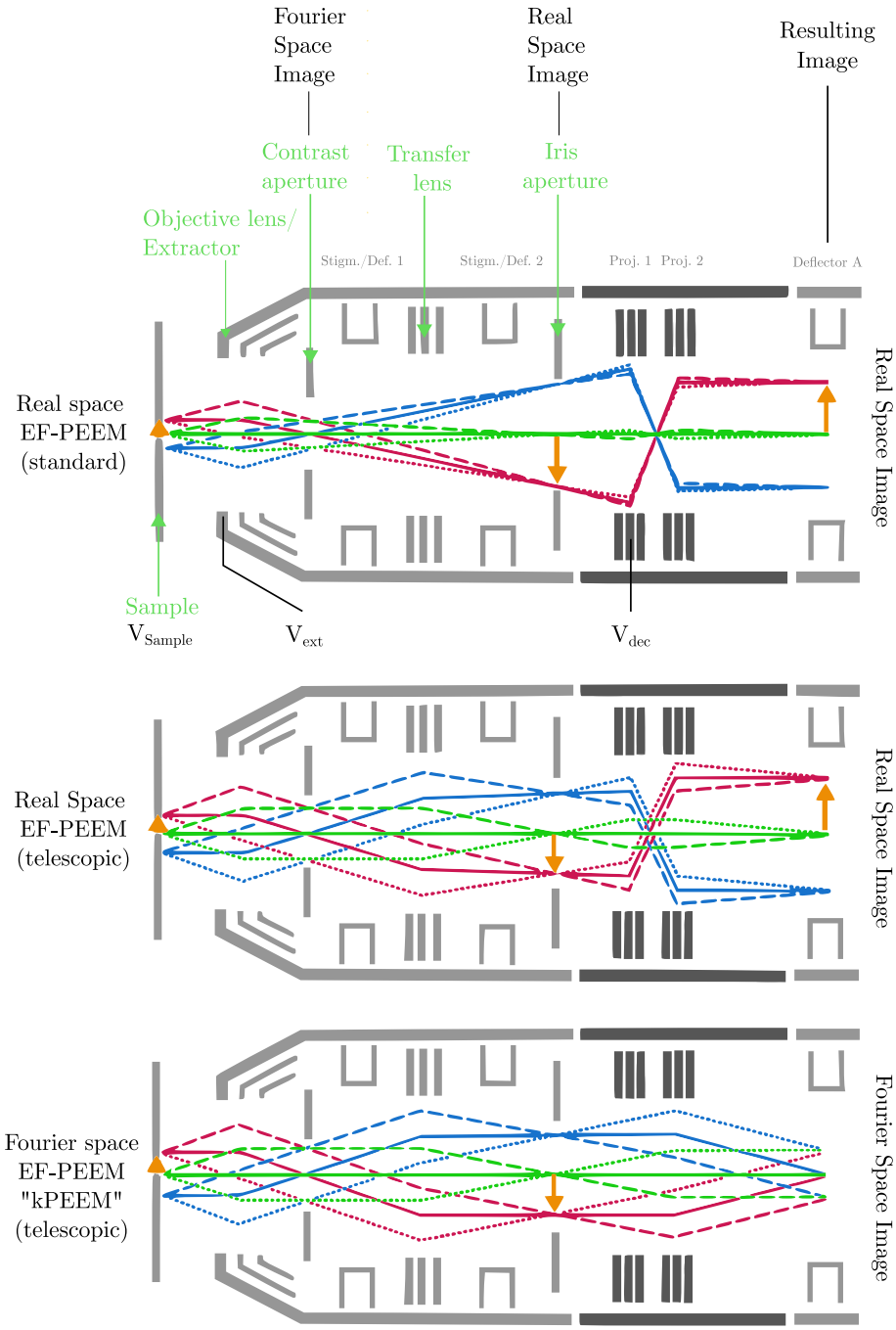

FIGURE *2.4 – Schematic of the NanoEsca I energy-filtered PEEM column as described in the text. We show the different modes and the trajectory of some photoelectron paths for real space EF-PEEM (standard), real space EF-PEEM (in telescopic mode) and Fourier Space EF-PEEM (kPEEM, in telescopic mode). For the latter two, the transfer lens is activated which moves the back fourier plane of the image. At the contrast aperture the image is always in reciprocal space, at the iris it is always in real space. We have noted the electrostatic potential at the sample V_{sample}, the extractor V_{ext} and the decelerating projective lens 1 V_{dec}. Elements of the microscope relevant to our work are written in bold and colored. For completeness, we have also noted other elements in gray. Taken from [126]*

contrast aperture (CA), deflectors/stigmators 1/2, transfer lens, iris aperture, projective lenses 1/2 and deflector A.

The PEEM column corrects image aberrations through the stigmators and deflectors: If the sample is not perfectly orthogonal in relation to the optical axis of the PEEM column, the real space image will suffer from an image aberration called **astigmatism**. Using the electrostatic octupole *stigmator/deflector 1/2* this aberration can however be corrected and the image centered.

The PEEM column also allows magnification of the image and switching from real space to reciprocal space: Let us consider FIGURE 2.4. The contrast aperture plane intersects with the back focal plane of the objective lens. The back focal plane is an angular diffraction plane. The iris aperture, on the other hand, intersects with the image plane of the projective lens 1. This means that the image at the plane of the contrast aperture will always be given in Fourier space, whereas the image at the iris aperture will always be given in real space. By changing the size of either aperture, one can thus limit the maximum image size in reciprocal or real space, respectively. For kPEEM, the contrast aperture is open to the maximum. By adjusting the transfer lens and the projective lenses, the projected image at the intermediate image plane of deflector A is either a real space image or the Fourier image. We thus record either real space images or reciprocal space images.

2.1.8 Energy filtering in the hemispherical analyzer

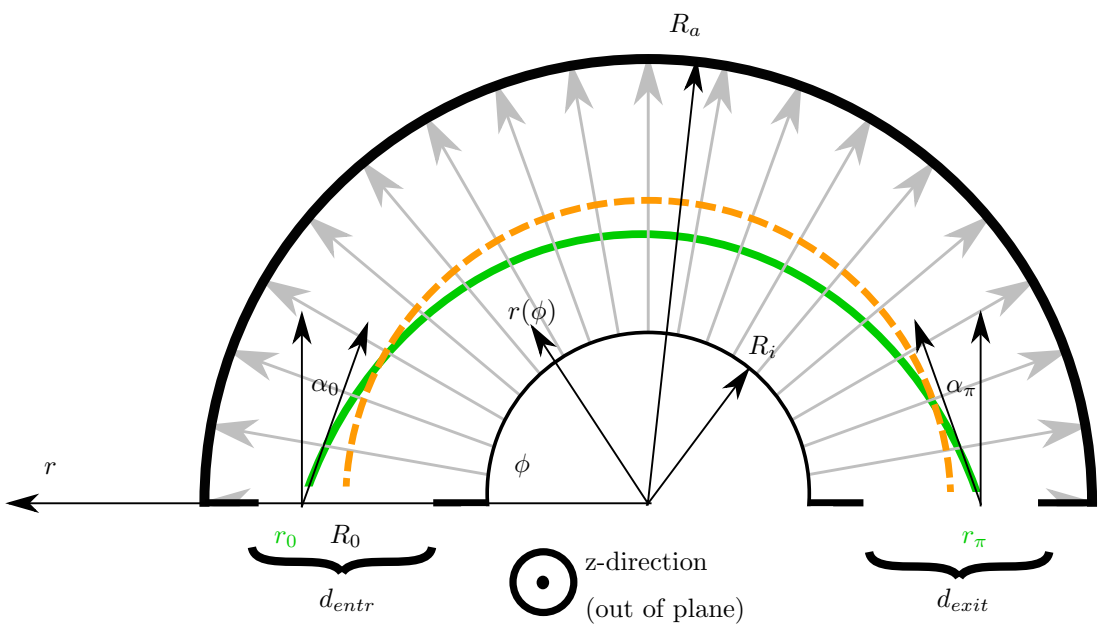

FIGURE 2.5 – *Schematic cross-section through a hemispherical analyzer along the dispersive (r, ϕ) plane. The grey lines indicate the direction of the electric field. The outter wall is of radius R_a whereas the inner wall is of radius R_i set at a higher electrostatic potential. An electron enters within the slit width d_{entr} at position r_0 under entrance angle α_0 (β_0, out-of-plane, not shown), follows the schematic trajectory in green (not exact) and leaves at position r_π at exit angle α_π ($\beta_p i$ not shown) within the slit width d_{exit}. Taken and adapted from [157]*

We have based the explanations in the following paragraphs on [126, 157] unless otherwise cited. As we have shown in the previous sections, photoelectrons of the considered kinetic

energy E_{kin} are shifted to the energy E_{pass}. The role of the hemispherical analyzer (HSA) is to filter out all other electrons.

Theoretically, energy resolutions of HSAs can go down to $\propto 100\mu$eV [150]. In practice, this resolution cannot be achieved for ARPES on ML-TMDC structures. Even with the high photon flux available at synchrotrons the signal becomes too feeble and routinely, lower resolutions are being used, with the best currently ≈ 14 meV at MAESTRO [4].

A cross-section of a HSA is shown in FIGURE 2.5. We use a cylindrical coordinate system (r, ϕ, z). The electric potential of the inner wall at radius R_i is lower than the one of the outer wall R_a, resulting in an electric field as indicated by the grey field lines of the potential $\varphi(r) \propto 1/r$. The centric radial direction therefore indicates the *dispersive direction* in the (r, ϕ)-plane, in which the electron trajectory is subject to change. Perpendicular to the dispersive direction is the (almost) *non-dispersive* direction along the z-coordinate.

At the beginning and the end of the HSA photoelectrons enter through an entrance and an exit slit of width d_{entr} and d_{exit} in the radial direction. A photoelectron may enter the HSA through the entrance slit centered at $r_0 = R_0$ and $z_0 = 0$ with a kinetic energy $E_{kin} = E_{pass}$ and angles $\alpha_0 = \beta_0 = 0$. Under these circumstances the electron enters perpendicularly to the entrance slit and will follow the circular orbit as indicated by the orange line. Finally, it exits perpendicularly to the exit slit again at $r = R_0$.

More generally, a photoelectron may enter the hemispherical analyzer with any radius r_0, z_0, entrance angles α_0 and perpendicularly β_0 and kinetic energy E_{kin} as long as they are not forbidden by slit width or some previous angle limitation in the microscope (contrast aperture). This photoelectron will then follow an elliptical orbit, shown by the green line, and leave at radius r_π at exit angle α_π. One finds for the entrance (0) and exit (π) values of angles (α, β) and position (r, z)

$$r_\pi = \left(\frac{2}{2 - \frac{r_0}{R_0} \frac{E_{pass}}{E_{kin}} \cdot \cos^2 \alpha_0} - 1 \right) \cdot r_0 \tag{2.11}$$

$$\alpha_\pi = -\alpha_0 \tag{2.12}$$

$$z_\pi = -z_0 \tag{2.13}$$

$$\beta_\pi = -\beta_0 \tag{2.14}$$

Energy resolution and non-isochromaticity of a hemispherical analyzer

We have based the explanations in the following paragraphs on [126, 157] unless otherwise cited. The electrons arriving at the plane of the exit slit are dispersed in radial direction according to their respective kinetic energy E_{kin}, α_0 and r_0 according to equation (2.11). Usually, one expects electrons leaving at $r_\pi = R_0$ to be at pass-energy $E_{kin} = E_{pass}$ and $\alpha_\pi = \beta_\pi = 0$. However, electrons of other kinetic energies E_{kin} and angles α_π can be mixed in as long as equation (2.11) is satisfied. This behaviour of the HSA limits the energy resolution. One can then show that for the energy resolution ΔE_{ana} for a conventional HSA

$$\frac{\Delta E_{ana}}{E_{pass}} = \frac{1}{2} \left(\frac{d_{entr} + d_{exit}}{2} + \alpha_{0,max}^2 \right) \tag{2.15}$$

where entrance slit width d_{entr} and exit slit width d_{exit} in radial direction and $\alpha_{0,max}$ is the maximum entrance angle possible at the entrance slit of the HSA. The NanoEsca I is made of two consecutive HSA with a transfer optic in between as shown in FIGURE 2.5. In

4. https://sites.google.com/a/lbl.gov/maestro/instrumentation/nanoarpes

the second HSA the dispersive effect, described by equation (2.11) is undone to recover a well-centered photoelectron beam.

Energy filtering of 2D photoelectron images in hemispherical analyzer

We have based the explanations in the following paragraphs on [126, 157] unless otherwise cited. If we are to energy-filter a 2D image, as is the case for EF-PEEM, mixing kinetic energies and spatial positions of photoelectrons is problematic. To circumvent this problem, one can transform the spatial information of a photoelectron (x, y) in angular coordinates (α, β) using a Fourier lens at the entrance and the exit of the HSA as shown in FIGURE 2.3. Having transferred spatial (x, y) into angular information (α, β) we know from equation (2.12) and equation (2.14) that $\alpha_\pi = -\alpha_0$ and $\beta_\pi = -\beta_0$ are conserved except for a sign flip. During the energy-filtering the spatial information is thus conserved and no longer mixed with electrons of other energies. Their angles (α, β) then reveal the original spatial information (x, y) after backtransformation through the exit Fourier lens.

Non-isochromaticity

We have based the explanations in the following paragraphs on [126, 157] unless otherwise cited. At the back fourier plane of the exit Fourier lens behind the HSA lies the two-dimensional image detector which will record the photointensity images. Because of the high number of pixels on the 2D image detector (at least hundreds in radial direction), the length of one pixel within radial direction $\mathrm{d}r$ will be very small. This implies that the accepted $\mathrm{d}\alpha_0$ becomes very small. For usual maximum entrance angles $\alpha_0 \approx 3°$, the value becomes negligible. This means that over one pixel, the energy spread ΔE due to α_0^2 aberration is insignificant. In that case equation (2.15) becomes

$$\Delta E = E_{pass} \cdot \frac{1}{2} \left(\frac{d_{entr} + d_{exit}}{2} \right) \tag{2.16}$$

However, over the entire 2D image detector the energy deviation in radial direction is significant. For photoelectrons with $r_0 - r_\pi = 0$ and $r_0 = R_0$ one then finds that the pass-energy changes as a function of pixel position (r) or equivalently angle (α) [156]

$$E_{pass}(\alpha_0) = \frac{1}{1 - \sin^2 \alpha_0} \cdot E_{pass}(\alpha_0 = 0) \approx (1 + \alpha_0^2) \cdot E_{pass}(\alpha_0 = 0) \tag{2.17}$$

This **non-isochromaticity** is important to be corrected in all real space PEEM images.

On the two-dimensional image detector some pixels are more sensitive than other due to ageing. This means that spectra of certain $\mathbf{k}$ will have have a lower total spectral weight $\int_{E_1}^{E_2} I(E', \mathbf{k})\, \mathrm{d}E'$. After measurement we normalize the photointensity spectra over their entire spectral weight

$$I_{norm}(E, \mathbf{k}) = \frac{1}{\int_{E_1}^{E_2} I(E', \mathbf{k})\, \mathrm{d}E'} I(E, \mathbf{k}) \tag{2.18}$$

where E_1 and E_2 delimit the measured energy range.

2.2 Theory of photoemission in ARPES experiments

2.2.1 Photo-ionizaton cross section

The probability of photoionization is determined by the **photoionization cross-section**. It describes the probability of a photon to be absorbed under photoemission of an electron in the solid crystal at a given polarization and wavelength. This cross-section depends on the type of orbitals involved and their geometry. If the wavelength of the optical excitation is beyond atomic scales (few nm), one uses the electron dipole approximation to calculate the photo-ionization cross-section. The photo-ionization cross-section depends on wavelength, electron orbitals and material. [16]. Tabulated values can be found in [16, 48, 144, 171].

2.2.2 The theory of the photoemission process in the 3-step model

In the process of photoemission, an electron initally occupies a quantum state within the crystal and is excited to a state in vacuum outside of the crystal through absorption of a photon. Additional quantum interactions of the electron, for instance with other crystal electrons or phonons, can take place during the process. Quantum mechanically this should be described by the formally rigorous **one-step model** where the entire photoexcitation process is described by one coherent quantum transition [109]. Another more intuitive, approximative approach, is the **3-step model** which we will use with the **sudden approximation**. We will develop this model based on the explanations of Damascelli and Moser [31, 113]. The three step-model treats the entire photoemission process in a phenomenological way as a product of three distinct steps:

1. An electron in the crystal is excited from its initial state under absorption of a photon.
2. The excited electron propagates towards the surface of the crystal and is potentially subjected to scattering events.
3. The electron traverses the crystal surface and escapes into vacuum.

Photoexcitation in the electron-dipole approximation

The goal of this model is to find an expression for the resulting photocurrent I_0 in a photoemission experiment which can be measured by ARPES. We can express the photocurrent as the negative electron charge times the transition rate of the photoexcitation quantum process using Fermi's Golden Rule. Here, the system assumes the initial state $|\Psi_i^N\rangle$ and is excited via the perturbation Hamiltonian $\hat{H}_{int}$ into the final state $\langle\Psi_f^N|$. N is the number of electrons in the system before excitation in the system. The photocurrent can then be expressed as

$$I_0 = -e \cdot \sum_{f,i} w_{f,i} = -e \cdot \frac{2\pi}{\hbar} \left| \langle \Psi_f^N | \hat{H}_{int} | \Psi_i^N \rangle \right|^2 \delta(E_f^N - E_i^N - h\nu) \tag{2.19}$$

where e the elemental charge, $w_{f,i}$ is the transition probability of photoexcitation of the system according to Fermi's Golden Rule from an initial (i) to a final (f) state, E_f^N and E_i^N the energy of the final and initial state respectively. The photon-electron interaction Hamiltonian can be written as

$$\hat{H}_{int} = \frac{e}{2mc} \Big(\mathbf{A}(\mathbf{r}) \cdot \hat{p} + \hat{p} \cdot \mathbf{A}(\mathbf{r}) \Big) \tag{2.20}$$

here $\mathbf{A}$ is the magnetic vector potential induced by the electric field of the incoming photon and $\hat{p}$ the momentum operator. In equation (2.20) we choose to gauge the scalar potential $\phi = 0$ at infinity and we drop terms beyond the linear approximation. This is not always valid, for instance in time-resolved ARPES the laser pulses have high intensity and higher-order terms must be considered. If the wavelength is long enough compared to a crystal unit cell, which is the case for our photon energy ($h\nu = 21.2\ eV \rightarrow \lambda \approx 60$ nm), one can assume $\nabla \mathbf{A} = 0$, that is, A does not change over one unit cell. This is called the **electron-dipole approximation**. In that case

$$\hat{H}_{int} = \frac{e}{2mc}\Big(\mathbf{A}(\mathbf{r}) \cdot \hat{p} + \hat{p} \cdot \mathbf{A}(\mathbf{r})\Big) \approx \frac{e}{mc}\mathbf{A} \cdot \hat{p} = \frac{2}{mc^2}\epsilon \cdot e^{i\mathbf{k}_{h\nu}\mathbf{r}}\hat{p} \tag{2.21}$$

where we have written ϵ as the polarization vector.

Participating electronic states and sudden approximation

We thus have found an expression for the interaction Hamiltonian, but we still need to define the initial and final state in equation (2.19). Here, one should consider that during photoexcitation a photoelectron is created which is removed from an N-electron system leaving behind an (N-1)-electron system. One can then write the wavefunction of the initial (i) and final state (f, m) of the entire system

$$\Psi_i^N = \mathcal{A}\phi_i^{\mathbf{k}_i}(\mathbf{r})\Psi_i^{N-1}(\mathbf{r}) \tag{2.22}$$

$$\Psi_{f,m}^N = \mathcal{A}\phi_f^{\mathbf{k}_f}(\mathbf{r})\Psi_{(f,m)}^{N-1}(\mathbf{r}) \tag{2.23}$$

where $\mathcal{A}$ is an operator that antisymmetrizes the wave function so it fulfills Pauli's exclusion principle. $\phi_{i/f}^{\mathbf{k}}$ are the initial/final state of the electron which we will define below. $\Psi_{i/(f,m)}^{N-1}$ is the initial/final state of the (N-1)-electron system. We note that there are multiple final states $\Psi_{(f,m)}^{N-1}$ available denoted by the index m. The total transition probability is then given by the sum over m of the scalar products.

By factorising the initial and the final state into the given form by equation (2.22) and equation (2.23) we implicitly assume the *sudden approximation*: the entire photoexcitation process happens so fast that during the excitation no other interactions, especially scattering processes, take place. In that case initial and final state can be factorised into an (N-1)-electron system wavefunction and a photoelectron wavefunction of the given form. High kinetic energy electrons leave the crystal quickly and justify such a model, at low kinetic energies, however, the rigorous one-step model has to be used.

If we enter this definition of initial and final state into the expression of the photocurrent from equation (2.19), we see that I_0 will be proportional to the following scalar products

$$\langle \Psi_{(f,m)}^N | \hat{H}_{int} | \Psi_i^N \rangle = \underbrace{\langle \phi_f^{\mathbf{k}_f}(\mathbf{r}) | \hat{H}_{int} | \phi_i^{\mathbf{k}_i}(\mathbf{r}) \rangle}_{M_{f,i}^{\mathbf{k}_i,\mathbf{k}_f}} \underbrace{\langle \Psi_{f,m}^{N-1}(\mathbf{r}) | \Psi_i^{N-1}(\mathbf{r}) \rangle}_{c_{(f,m),i}} \tag{2.24}$$

where we have defined the matrix elements $M_{i,f}^{\mathbf{k}_i,\mathbf{k}_f}$ and $c_{(m,i)}$. The first scalar product in equation (2.24) corresponds to the one-electron dipole matrix element, where the second scalar product describes the overlap integral between the initial state and the final state for the (N-1)-electron system. The total photocurrent can be found as the sum of transition probabilites from an initial to a final state $\omega_{(f,m),i}$ times the negative elementary charge e. This can be further divided into a sum over all possible final states given by the index m:

$$I_0(\mathbf{k}_f, \mathbf{k}_i, E_{kin}) = -e \cdot \sum_{f,i} w_{f,i} \tag{2.25}$$

$$= -e \cdot \frac{2\pi}{\hbar} \sum_{(f,m),i} \left| M_{i,f}^{\mathbf{k}_i,\mathbf{k}_f} \right|^2 \sum_m |c_{m,i}|^2 \delta(E_{kin} + E_m^{N-1} - E_i^N - h\nu) \tag{2.26}$$

for a set of possible final states $\langle \Psi_m^{N-1}|$ with index m. We thus see that on a photoemission spectrum the presence of an energy band will be reflected by δ-function like peaks. Determining the energy of these peaks will thus reveal the band position of the initial electron states in the band structure, the goal of ARPES.

Experimental geometry and implications for ARPES on ML-TMDCs

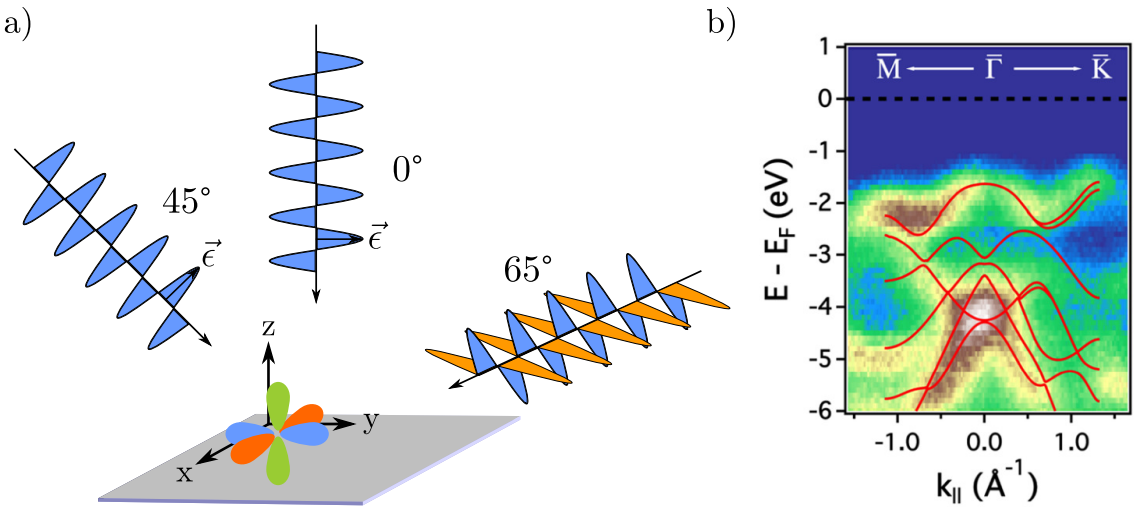

FIGURE 2.6 – *Electronic orbitals with in-plane character along x/y, (red, blue: for $d_{x^2-y^2}, d_{xy}$ and p_x, p_y) and out-of-plane along z (green: for d_{z^2} and p_z-orbitals). We show different experimental configurations of incident light, their angle and polarization.* ***b)*** *Disappearing signal at Γ for ARPES on ML-MoS_2 [62] because of the normal photon incidence.*

In the introduction (cf. section 1.2.3) we have discussed the orbital composition of the valence band edge of the band structure of ML-TMDCs. At Γ the Bloch states are composed of mainly d_{z^2} and p_z-orbitals whereas at K/K' the participating orbitals are $d_{x^2-y^2}, d_{xy}$ and p_x, p_y [95]. While the d_{z^2} and p_z-orbitals have an out-of-plane character (normal to the monolayer surface), the $d_{x^2-y^2}$, d_{xy} and $p_{x,y}$-orbitals have in-plane character. This has important implications for the experimental geometry of the ARPES study. Using the relation

$$\hbar \frac{\hat{p}}{m} = -i[\hat{x}, \hat{A}] \tag{2.27}$$

we can rewrite the interaction hamiltonian equation (2.21) and thus the matrix dipole element [31]

$$|M_{f,i}^{k_\parallel}|^2 \propto |\langle \phi_f^{\mathbf{k}} | \epsilon \cdot \hat{x} | \phi_i^{\mathbf{k}} \rangle| \tag{2.28}$$

Let us assume $|\phi_i^{\mathbf{k}}\rangle$ has in-plane-character (red and blue orbital in panel a) of FIGURE 2.6). In that case the z-component of $\hat{x}\,|\phi_i^{\mathbf{k}}\rangle$is vanishingly small. For a maximum matrix dipole element the polarization vector or maximum dot product $\epsilon \cdot \hat{x}$ respectively, ϵ must then

be parallel to the plane $\epsilon \parallel \mathbf{e}_z$. In the case of out-of-plane orbitals the case is exactly the opposite, here the polarization vector must be $\epsilon \perp \mathbf{e}_z$ in order to maximize the matrix dipole element.

The choice of this geometry is reflected by the literature: Jin et al. [62] have analysed ML-MoS_2 in ARPES using linearly polarized light. The incident optical excitation was normal to the surface as shown in panel a) of figure 2.6. This means that $\epsilon \perp \mathbf{e}_z$ and mostly states with an in-plane character were excited. In the study this is reflected by the recorded band structure: the photoemission signal is relatively strong at K/K' with its in-plane character orbitals and vanishes at Γ with its out-of-plane-orbitals. The disappearance of their signal is shown in panel b) of figure 2.6. Kim et al. [72] on the other hand, have analysed ML-MoS_2 in kPEEM with unpolarized light at 65° to the surface normal. At this angle of incidence and because of the unpolarized light, the out-of-plane components of the polarization vector ϵ are non-zero as shown in panel a) of figure 2.6. This means in turn that $\langle \mathbf{x}|\phi_i^{\mathbf{k}}\rangle$ becomes non-zero for out-of-plane electron orbitals and the photoemission probability for electrons at Γ becomes finite. Unlike Jin et al., the authors were then able to record a finite photoemission signal of the entire valence band edge from K/K' to Γ.

Whole photocurrent expression in ARPES for 2D-materials

We have based the explanations in this paragraph on [31] unless otherwise cited. In a real-life ARPES experiment on 2D-materials, the measured spectrum of photoelectrons, i. e. the **photocurrent** will be determined by a number of different factors. The following expression comprises both intrinsic effects which are inherent to the photoexcitation process as well as extrinsic effects such as scattering events as part of the three-step-model. Finite experimental resolution is incorporated, too. It gives thus a good model for the measured photointensity spectrum in 2D-materials [31]

$$I(\mathbf{k}_{\parallel,f}, \mathbf{A}) = \int \mathrm{d}E\, \mathrm{d}\tilde{\mathbf{k}}_{\parallel} \quad I_0(\tilde{\mathbf{k}}_{\parallel}, E_{kin}, \mathbf{A}) A(\tilde{\mathbf{k}}_{\parallel}, E) f(E) R(E_{kin} - E) Q(\mathbf{k}_f - \tilde{k}_{\parallel}) \tag{2.29}$$

$$+ B(E_{kin}) \tag{2.30}$$

where $\mathbf{k}_{\parallel,f}$ the in-plane component of the k-vector of the outgoing photoelectron, E_{kin} its kinetic energy and $\mathbf{A}$ the magnetic vector potential of the incident optical excitation. The different terms represent

- I_0 an expression for the photocurrent which can be developed in the dipole matrix formalism, as discussed above. This term contains information on the photon energy, polarization and ARPES geometry in relation to the selected electron orbitals.
- A the **one-particle spectral function** which contains information on the electronic band structure and lifetimes during photoexcitation [56]
- f the Fermi-dirac distribution This term guarantees that only occupied electron states can be excited.
- R a function representing the energy resolution of the experiment
- Q a function representing the momentum resolution of the experiment, both to be discussed in section 2.1.5
- B an extrinsic background signal. This can be due to the scattering events of electrons. Methods to identify and remove this extrinsic background signal will be discussed in detail in the next section.

Electron loss by scattering after photoexcitation and the photoemission background signal

During the propagation of the excited photoelectron to crystal surface, the electron may undergo scattering events. The **inelastic mean free path** λ_{IMFP} gives an indication as to the distance the electron can travel without scattering inelastically [56, 150]. While it depends greatly on both kinetic energy of the electron as well as the material, a universal curve has been proposed by Seah and Dench compiling hundreds of λ_{IMFP} measurements[114]. From IMFP measurements it can be found that generally, over all materials, the λ_{IMFP} is lowest in the range from 10 eV $< h\nu <$ 100 eV with $\lambda_{IMFP} \approx 5$ Å. This area is thus most interesting for surface analysis and 2D-Materials [56, 114, 150].

Inelastic scattering not only influences the measurable depth of a sample but also greatly influences the background signal: Electrons that scatter inelastically lose energy, their initial **k** and end up shifting to a seemingly higher binding energy on the measured photoemission spectrum [154]. These events lead to a background represented by the term $B(E_{kin})$ in equation (2.30). The difficulty lies then in discerning processes that are intrinsic to photoexcitation and such that can be purely attributed to inelastic scattering [38, 147, 154]. Electron scattering backgrounds are known well in X-Ray Photoemission Spectroscopy and several methods have been developped to remove unwanted scattering backgrounds [38, 136, 147, 148, 154].

Regarding ARPES on ML-TMDC-based samples, not only linear [67, 118, 182], but also higher polynomial [32, 65, 102] and so-called **Shirley backgrounds** [18, 184] have been used equally to remove backgrounds in EDCs at K for ML-TMDCs. In the mentioned studies no theoretical justification of the underlying electron scattering events was given. All these methods compel the author to make a choice about the shape of the background. We will describe our method of background removal in section 4.3.3.

2.2.3 The Work Function of a semiconductor and its relation to Fermi Level Shifts

Definition of the work function and use for 2D-Materials

Aside from the already mentioned band structure parameters (m_e, Δ_{SOC}, $E_{\Gamma K}$), there is another important parameter to describe the state of the monolayer, the work function ϕ. In its most general understanding, a crystal's *work function* ϕ is defined as [75, 175]

$$\phi = E_{vac} - E_F \tag{2.31}$$

where E_{vac} is the vacuum level and E_F the Fermi level of the crystal. We define the vacuum level as the energy level of an electron just outside the crystal potential and with zero kinetic energy [73, 107].

In bulk materials, one can distinguish between a bulk contribution to the work function and a surface contribution [73]. In 2D-materials this distinction falls flat however, because of the extreme surface-to-volume ratio. In general, surface effects can strongly alter the measured work function in a photoemission experiment through roughness [86, 107], crystal orientation of the surface [45, 107], atomic reconstruction [107], adsorbates [139], steps, [166] and alloying [141]. This makes work function analysis an interesting tool to study surface properties of a sample.

In the field of 2D-Materials the charactization of the work function is thus interesting in two ways: first, by knowing the work function of a material, the band alignment of a heterostructure can be estimated using the Anderson rule [26, 49, 85]. At the interface

between a metal and a semiconductor or between two semiconductors, the vacuum levels of either material must align. Further, the Fermi level has to be constant over the two materials. Far away from the interface the two Fermi level needs to match the intrinsic Fermi level of either bulk material.[5]. Secondly, because of the extreme thinness of 2D-materials surface effects are important to consider and the work function returns important information about the surface characteristics as shown above.

Photoemission as a means to measure the work function of 2D-materials

Many different techniques are available when it comes to measuring the work function of a material. We have based the explanations in the following paragraphs on [73, 107] unless otherwise cited. In thermionic emission spectroscopy, for instance, a tip-like sample of a material is heated such that the thermal energy of the electrons is high enough to surmount the work function energy necessary to leave the crystal. The photocurrent is determined as a function of temperature. But since the sample has to be heat resistant, this method is unsuitable for most 2D-materials.

For 2D-materials, the most popular techniques are **Photoemission Spectroscopy** (PES) and **Kelvin Probe Microscopy** (KPM). In Kelvin probe, a metallic AFM tip is within electron tunneling distance of the sample surface and both materials are electrically connected. In thermal equilibrium the Fermi levels of the two materials will then align and a *contact potential difference* between the two materials will drop accross the contact interface. This defines an initial capacitance between tip and sample. Upon varying the distance between the tip and the sample surface currents flow to adjust for the change in capacitance. These currents can be measured for instance by applying a counter-bias voltage and cancelling the current. Because of the small tip diameters Kelvin Probe has nano-meter scale resolution which is useful for measuring local work functions. However, it can only measure the *relative* work function in relation to the tip's work function, unless it is calibrated by an *absolute* work function method such as photoemission spectroscopy.

The NanoEsca setup allows measuring the absolute work function using a helium-discharge lamp ($h\nu = 21.22eV$ that is UV-light). It thus combines ultra-violett photoemission spectroscopy with the spatial resolution of PEEM. In FIGURE 2.7 one can see a prototypical angle-integrated photoemission spectra of a metal and a semiconductor. These show photoemission spectra as a function of kinetic energy of the photoelectrons after an excitation of the He-Iα spectral line at 21.22 eV. If a metal is used to calibrate the spectrometer, one can deduce the Fermi level from the highest kinetic energy $E_{kin,max}$ at which photoelectrons can still be detected. The kinetic energy of the photoelectrons can then be converted into the binding energy $E_{bin} = E - E_F$ which is referenced to the Fermi level. Because the energy $h\nu$ of the exciting light is finite, it can only lift electrons of a binding energy at $E_{Bin} > E_{vac} - h\nu$ out of the crystal. This manifests itself as a sharp photoelectron cut-off feature often called *secondary electron cut-off* (SECO) at the low kinetic energy side ($E_{kin,min}$) or equivalently high binding energy side (E_{SECO}) of the spectrum which can be seen in FIGURE 2.7. One can use it to determine the work function

$$\phi = h\nu - |E_F - E_{SECO}| = h\nu - |E_{kin,max} - E_{kin,min}| \tag{2.32}$$

where E_F the Fermi level, E_{SECO} the secondary cut-off feature, $E_{kin,max}$ the maximum kinetic energy and $E_{kin,min}$ the minimum kinetic energy. The second equality is valid only if photoelectrons up to the Fermi level are excited, for instance in metals.

5. This information was taken from an article by Herbert Kroemer in [104]

In the literature, different ways are suggested to determine the secondary-electron cut-off position. In the simplest case, a tangent line is extrapolated and the crossing with the baseline defines the cut-off position[8, 26]. Another way is to fit the cut-off feature using an error-function [105]. For the case of a gold sample, Patt has developed an even more sophisticated approach, where the fitting function for the SECO is a product of two functions: a) a step-edge function which is a convolution of a Gaussian to simulate finite energy resolution and an error function and b) a function simulating the expected photoemission spectrum for gold without cut-off feature [126].

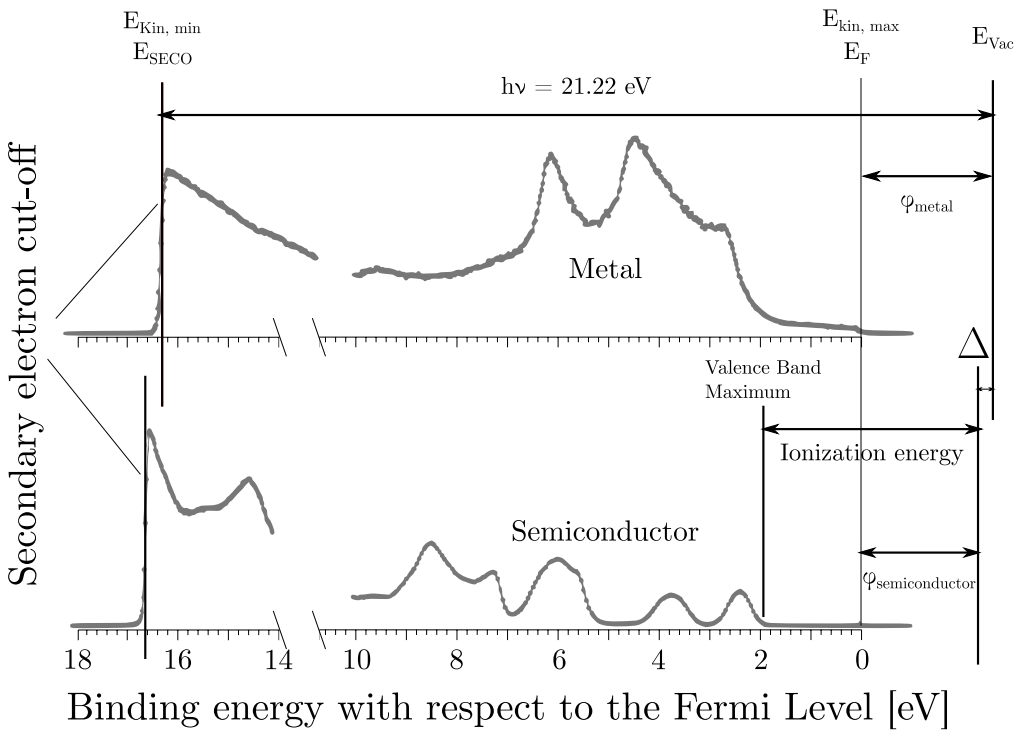

Figure 2.7 – *Photoemission spectra after excitation with the He-I α line at 21.22 eV for a typical metal and semiconductor. For the metal, the highest kinetic energy $E_{kin,max}$ that can be measured stems from photoelectrons that originate from the Fermi level E_F. The drop in photointensity at $E_{kin,max}$ then allows to calibrate the Fermi level position for semiconductors where the Fermi level is somewhere in the band gap. The lowest kinetic energy of photoelectrons is $E_{kin,min}$ measured by E_{SECO}. The exact materials were not specified by the authors. Δ refers to the work function difference between the metal and the semiconductor. The picture was modified.*
Taken under license from [73] [Creative Commons Attribution 4.0 International (CC BY 4.0)].

3

Fabrication of ML-TMDC samples for kPEEM

3.1 Goals and challenges in fabrication of ML-TMDC-structures for kPEEM

As we have outlined in section 4.1, the goal of this work is to study the effect of the dielectric substrate onto the electronic band structure of a ML-TMDC deposited thereon. We thus should fabricate a structure of a ML-TDMC on different substrates using suitable techniques. The experimental requirements demanded by ARPES, and more specifically our kPEEM setup (section 2.1.3), thus impose the following requirements onto our samples:

— **Sizable monolayers**: because our setup uses a helium gas-discharge lamp, the photointensity signal from the monolayer will be weak compared to ARPES at synchrotron facilities. The photointensity signal scales with the size of the selected area of interest. For a sufficient signal we need a large monolayer flake, at least 5 x 5 μm^2 in size.

— **Controlable monolayer position**: For specific substrates such as hBN-flakes, typically tens of μm in size, the monolayer needs to be deposited specifically on the hBN-flake within an accuracy of few μm.

— **Microscopic markers**: the maximum field of view in our ARPES experiment is limited to 150 μm. The contrast of the EF-PEEM image is further determined by the selected energy. At some energies the monolayer will be clearly visible, at others not. This is strongly determined by the underlying substrate. Large microscopic markers should guide us to the relevant monolayer structure.

— **Flexible choice of substrates**: The method for creation/deposition of the monolayer should not be limited to certain substrates.

— **Clean interfaces**: Because our goal is to analyse the interaction between the ML-TMDC and the substrate, the interface between the two should be free of contamination (water or other chemical products).

3.2 Modern techniques for the development of ML-TMDC-structures for ARPES

In the literature, mainly three different fabrication techniques have been employed in order to create ML-TMDC-systems for ARPES. *Molecular Beam Epitaxy* [15, 25, 102, 182], *Chemical Vapor Deposition* [2, 44, 66, 102], and *Mechanical Exfoliation* [62, 63, 84, 184].

In *Molecular Beam Epitaxy* (MBE) transition metals and chalcogens are evaporated from effusion cells onto a substrate where they react and coalesce into a monolayer. Two cases must be distinguished: *conventional MBE* and *van-der-Waals MBE*. In conventional MBE, the crystallographic symmetry and lattice parameter of the monolayer and the substrate surface must match closely for the epitaxial growth. This creates single crystals with a crystal orientation aligned parallel to the substrate's. In the latter, van-der-Waals materials such as hBN or graphite are used as growth substrates and the crystallographic matching is much less strict [27].

In *Chemical Vapor Deposition* (CVD) chemical precursors which contain either transition metal atoms or chalcogen atoms are sublimated, the gaseous precursors are transported

to the substrate by a carrier gas. On the substrate, the precursors react and nucleate to form the monolayer [10, 77].

In *Mechanical Exfoliation* followed by *all-dry viscoelastic stamping* monolayer flakes of TMDCs are extracted from a bulk crystal using scotch tape. These flakes can be exfoliated directly onto the target substrate or onto an intermediate substrate [22].

3.2.1 Sizeable monolayers

In terms of monolayer size, all techniques produce sufficiently large monolayer for analysis in kPEEM, i. e. larger than $5 \times 5\ \mu m^2$. CVD produces monolayers flakes of few μm in size [2, 44, 66] up to tens of μm [65, 131, 160]. Monolayer flakes produced in MBE, on the other hand, cover the entire epitaxial growth substrate [36, 111, 118, 182]. Since flakes of a few tens of μm in diameter are usually achievable, a sizeable monolayer flake grown by MBE is feasible for and has been demonstrated to work on our kPEEM setup [25].

3.2.2 Substrates

As described above, epitaxial growth in MBE requires the substrate to either closely match the lattice parameter/symmetry of the monolayer to grow or to use a van-der-Waals material as substrate. Further, MBE and CVD need adjusted growth recipes for the respective substrate. So far, MBE for the production of monolayers in ARPES has been achieved on graphene [36, 111, 118, 182] and Au(111) [53, 102]. CVD for monolayers in ARPES has been achieved for graphene [2, 15, 44, 66, 130, 131], SiO_2 [65] and Au(111) [15]. For ARPES monolayer-TMDCs have been transferred or directly exfoliated onto Si [62, 63, 84], hBN [100, 121], gold [183, 184] and TiO_2 and $SrTiO_3$ [161]. Generally, because of the strength of the van-der-Waals forces, there is no substrate that could not be exfoliated/transferred on, as long as the monolayer adheres to the substrate.

Once the monolayer has been deposited on an intermediate substrate, it can be transferred onto another substrate using the poly(propylene) carbonate (PPC)-based « pick-up » technique [74] or the PDMS-based « stamping » technique [22]. The PPC-based pickup technique allows to stack several monolayers of different materials with very clean interfaces [3, 61, 145]. However, this technique encapsulates the ML-TMDC in two hBN-layers of few nm, such that the photoelectron signal will be strongly attenuated. We thus opt for the PDMS-based stamping technique which allows transfer onto virtually any substrate. In order to free make sure our the interface between the ML-TMDC and the substrate is clean, we anneal our samples at 300° for at least 2h. Such a prolonged annealing has shown to almost completely remove polluants that contaminate the interface during transfer [59].

A combination of mechanical exfoliation and PDMS-based transfer seems the most viable method for this study: it creates large enough monolayers and can deposit the monolayer on virtually any position of any substrate.

3.3 Mechanical exfoliation from bulk crystals

In this section we explain the technique of mechanical exfoliation with the illustrations and photos of FIGURE 3.1. For our exfoliation, we use synthetic bulk crystals from « hq-graphene » and the National Institute of Material Sciences (NIMS) in Japan. The bulk crystal (1) of the TMDC is placed onto scotch tape . Preferably, one should use a crystal

with thickness below 1 mm and few mm's wide in lateral dimensions. We cover it with the other side of the scotch tape and pull this side off (2). This process is repeated, until a large argea of the scotch tape is covered by the crystal. An example of a successful exfoliation are the two densely covered scotch tapes (≪ good coverage ≫) in (3) where we also show an example of a losely covered scotch tape (≪ bad coverage ≫). This is the first stage when a monolayer can be produced, as shown by ≪ monolayer A ≫ in FIGURE 3.1. Sometimes, the bulk crystal has to be exfoliated on scotch tape a couple times before it becomes flat and thus suitable for proper exfoliation dimensions.

We then prepare a double layer of PDMS on a glass slide. The densely covered scotch tape is placed onto the PDMS and pulled off (4). For Graphene exfoliation, the scotch tape must be peeled off very carefully. For ML-TMDCs we have made the opposite observation. It should be pulled off quickly, within 1-2 seconds while the PDMS needs to stick to the glass stripe. This is the second stage when a monolayer can be created, as indicated by ≪ monolayer B ≫ in FIGURE 3.1. (5) shows PDMS on a glass stripe with visible bulky flakes. This is an indication that monolayers can be found on the PDMS. In the next step the monolayer needs to be identified and localized, before it can be transferred with an xyz-controllable stage (6). We describe our standardized technique for monolayer identification in the next section.

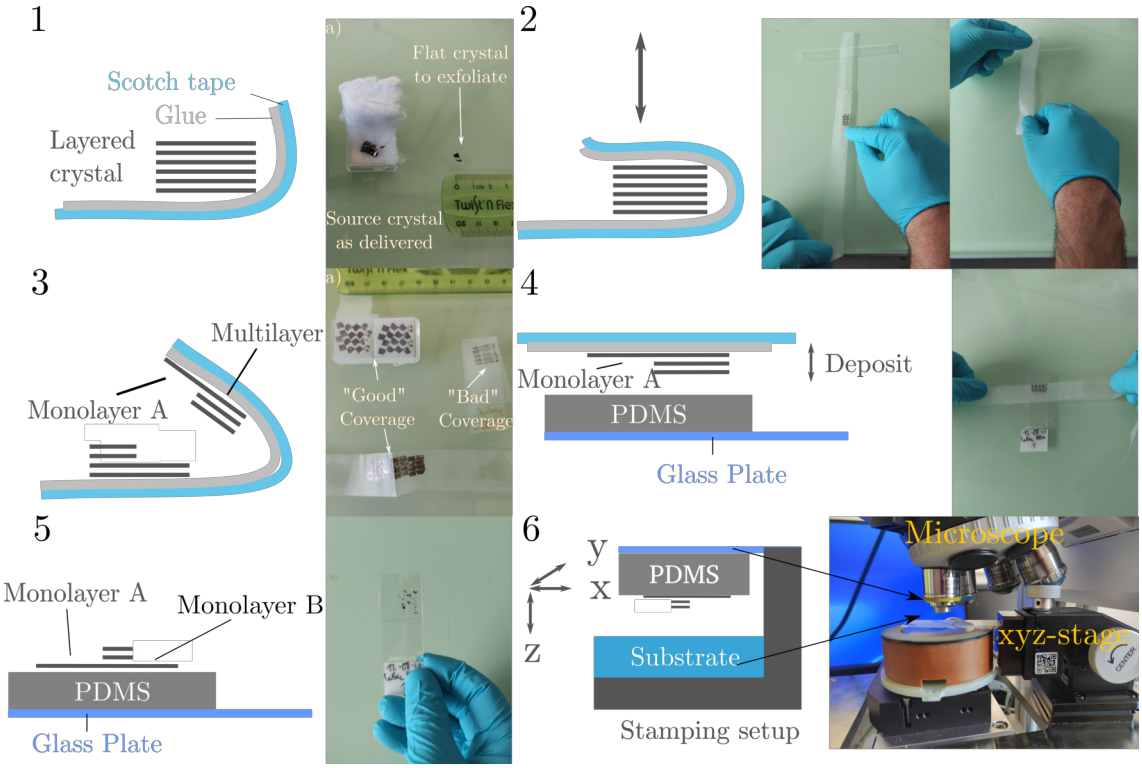

FIGURE 3.1 – *Complete steps from creation of a monolayer-TMDC flake via mechanical exfoliation to deposition using our stamping setup:* ***(1)*** *The bulk crystal is placed onto scotch tape and exfoliated through repeated covering and pulling* ***(2)****. In* ***(3)*** *we end up with mono- to multilayer flakes on the scotch tape which can then be deposited onto a transparent glass stripe covered with polydimethylsiloxane (PDMS)* ***(4)****. Having pulled off the scotch tape we obtain mono- and multilayer flakes on the PDMS* ***(5)****. The monolayer must now be localized under the microscope, before the glass slide can then be transferred. This is done using a microscope and an an xyz-controllable stage* ***(6)****.*

3.4 Standardized monolayer identification using an optical microscope

The process of mechanical exfoliation leaves flakes of TMDCs on the PDMS. These flakes usually have different shapes and thicknesses, from the monolayer to the multilayer or even bulk thickness. Whether or not a monolayer is produced during the process of exfoliation, is entirely arbitrary and beyond the control of the author. Statistically, however, at least some flakes will have monolayer thickness. In order to find a monolayer among the vast number of flakes within a reasonable timeframe, the applied technique has to be fast. There exists a number of different techniques that can prove monolayer thickness, for instance Atomic Force Microscopy [170], Raman [179] or photoluminescence spectroscopy [103], but these measurements would be extremely time-consuming if applied to many flakes.

A simple, more straight-forward approach is the identification of monolayer flakes under an optical microscope. In this technique, monolayers are discerned from multilayers by their optical contrast. Despite their extreme thinness, monolayers of MoS_2, $MoSe_2$, WS_2 and WSe_2 are visible under an optical microscope. Because of the strong oscillator strength of the excitonic transitions in ML-TMDCs, the absorbance can reach tens of % in visible range of light (1.5 to 3 eV) [87].

In panel a) of FIGURE 3.2 we show a WSe_2 flake with uncertain monolayer thickness. In panel b) FIGURE 3.2 we show a monolayer of WSe_2 whose monolayer property has been verified through other techniques than optical microscopy (e. g. AFM, Raman spectroscopy, ARPES). Because both pictures have been taken under different lighting conditions, the color of the flakes and the surrounding substrates are very different. This may be because the images stem from different microscopes or because the setup was not calibrated before pictures were taken. In order to confirm the possible monolayer properties of a) with the help of b), we have to make the images comparable. We can then use b) as a reference.

To do so, we measure the RGB-channels (red, green, blue) in the area delimited by the orange rectangle in either panel. RGB values are measured from 0 to 255 for red, green and blue. We adjust the channels such that green, blue and red align at 125, using ≪ Auto White Balance ≫ as well as ≪ Exposure time ≫. All these functions are readily provided by most graphics editing software and can also be carried out *a posteriori*. The resulting images in c) and d) now have a similarly colored background and the RGB-contributions align at 125. One can see that the color of the suspected monolayer matches with the color of the monolayer to confirm. We can thus use the flake as a monolayer in a) for stamping.

3.5 All-dry viscoelastic stamping

Having localized the monolayer, as described in the previous section, we remove unwanted parts of the PDMS with a scalpel and attach scotch tape for stability on the sides of the remaining PDMS. The resulting ≪ stamp ≫ is shown in panel a) of FIGURE 3.3. Because the glass stripe and the PDMS are transparent, we can identify the monolayer through the microscope in our ≪ stamping setup ≫. The setup includes an xyz-controllable stage as shown in panel 6) of FIGURE 3.1. Stage and/or monolayer are then moved such that the flake hovers above the desired position on the substrate. This is usually the center of the flake designated by microscopic arrow markers. The area in which the PDMS is in contact the substrate can be seen by a contrasted area delimited by a thin line, the so-called

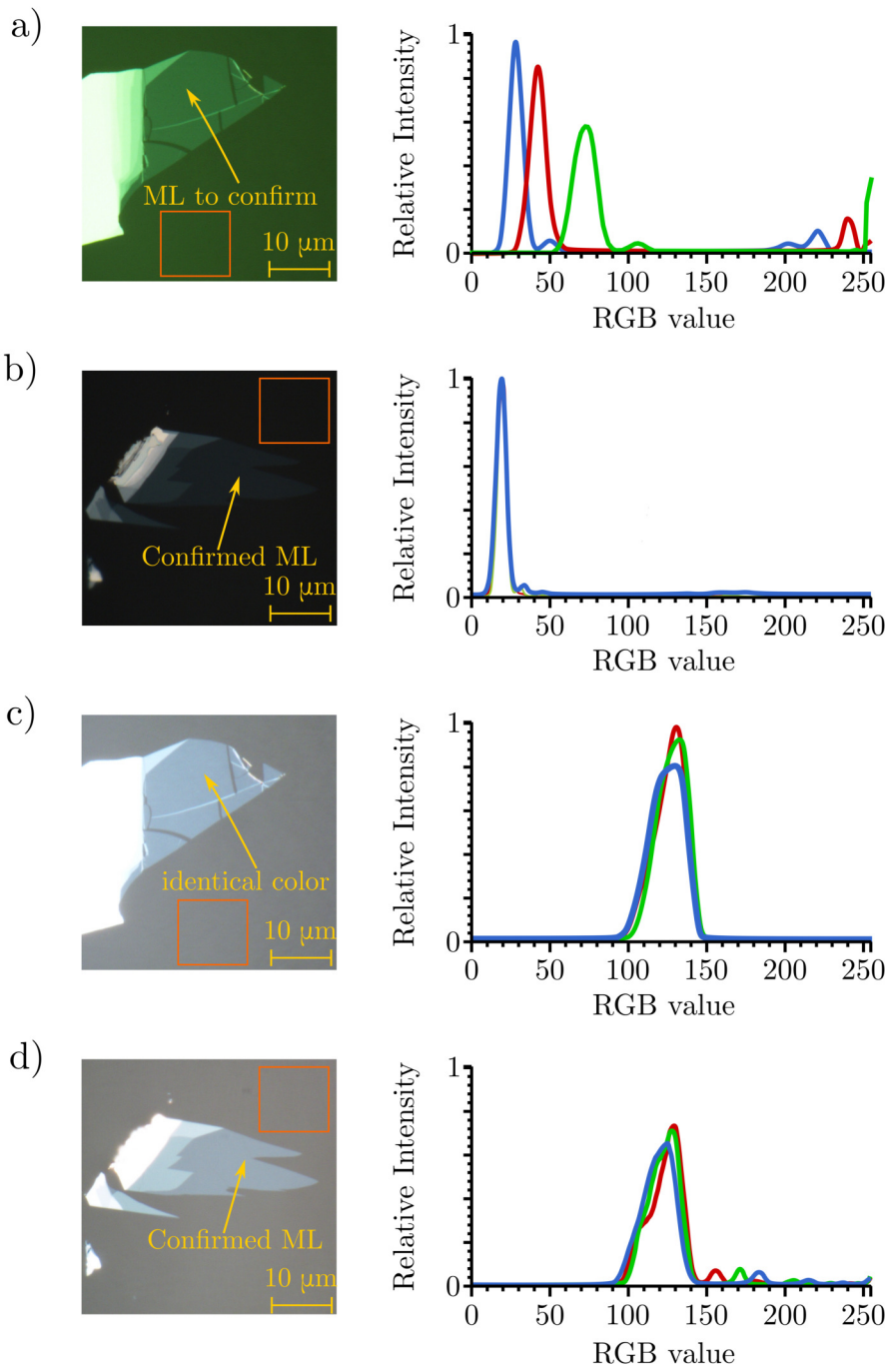

FIGURE *3.2 – Standardized procedure to confirm monolayer character of thin layer flakes under an optical microscope. In* ***a)*** *we show a possible monolayer as photographed under a microscope.* ***b)*** *shows a* WSe_2*-flake with confirmed monolayer thinness. Both pictures have been taken with different lighting conditions. In order to compare the two images, we use the green, blue and red channels histogramms provided in most microscopic photography or graphic editing software as shown next to the picture. These histogramms are created based on the areas without flakes, delimited by the orange rectangles. Using Automatic White Balancing and changing the exposure time we then calibrate the RGB-channels such that they align with a signal prototypical to* ***f)****. This procedure is applied for both flakes in* ***a)*** *and* ***b)****. The resulting images are shown in* ***c)*** *and* ***d)*** *where the suspected monolayer displays a similar color to the confirmed monolayer.*

« meniscus ». This area emerges because the diffractive properties of the PDMS-substrate interface are different to the diffractive properties of PDMS-air-interface. Upon slowly lowering the sample onto the stage or moving the stage up, respectively, the meniscus moves towards the monolayer flake. When the meniscus has bypassed the monolayer flake, we invert the process such that the meniscus moves again over the flake. Because the substrate is usually more adhesive than the PDMS, the monolayer flake then sticks to the substrate. We usually spent 10-20 minutes from the time the meniscus first touches the monolayer until it leaves the monolayer again. After stamping the samples are annealed at 300° for at least 2h to remove contaminants at the interface.

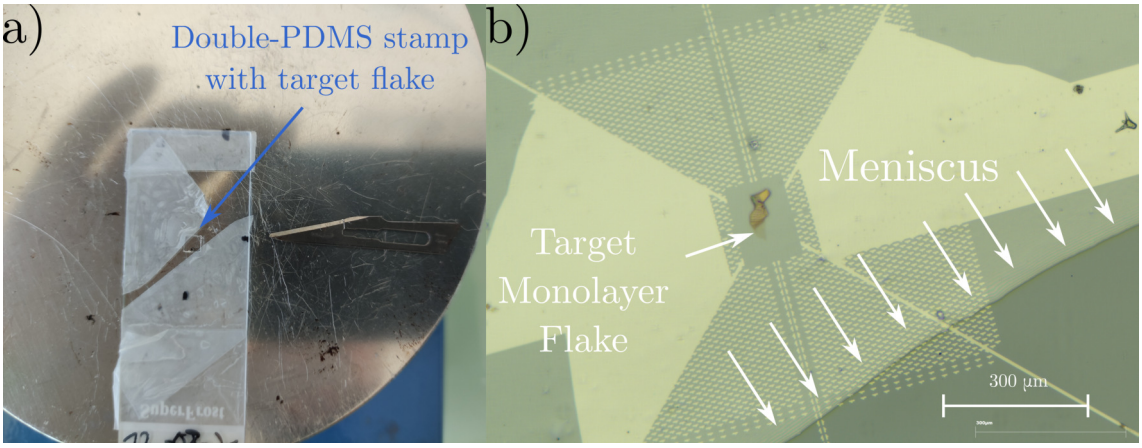

FIGURE *3.3* – ***a)*** *Fabricated stamp of double-layered PDMS with a target monolayer flake on top. Scalpel blade for size comparison.* ***b)*** *View under the microscope during lowering of the ML-TDMC-stamp. The monolayer flake is deposited in the target area demarked by microscopic arrow structures (microscopic markers). The dark area marks the contact surface between PDMS and substrate and is delimited by a fine line called « meniscus ». When the meniscus reaches the monolayer, said monolayer comes into contact with the substrate. Upon increasing the distance between substrate and PDMS glass stripe, the meniscus moves back and the monolayer remains on the substrate, provided the adhesive forces of the substrate are stronger than those of the PDMS.*

3.6 Laser lithography and metal evaporation for microscopic markers

In order to create microscopic markers for our substrates, we use laser lithography. FIGURE 3.4 shows the steps of development. The given substrate (1) is spin-coated with a laser lithography resine. This substrate is exposed to UV laser light which triggers a chemical reaction in the exposed part of the resin. A structure file with the areas to expose is shown in panel a) of FIGURE 3.5. The unexposed structures are then removed by a chemical photo developer (4). Eventually, using metal evaporation we deposit Ti and Au or Pt (5). Leaving the structure in acetone for overnight, removes all the remainder of the resine and only leaves the wanted structures (« lift-off »), which can be seen in panel b) of FIGURE 3.5 The details of the laser lithography recipe are:

— UV Resist : S1805

— Spinning parameters: speed 6000 rpm, acceleration 4000 rpm/s, time 30s

— Baking parameters: 115 °C for 1 min

— Exposure Dose: 15 mJ/cm^2 Development: Microposit Developer/DI water 1:1, 1 min dip followed by DI rinse and Nitrogen blowdry

— Metal deposition: Ti/Au 15 nm/35 nm at any rate

— Liftoff: Acetone dip at least 6 h, IPA rinse 1 min followed by Nitrogen blow-dry.

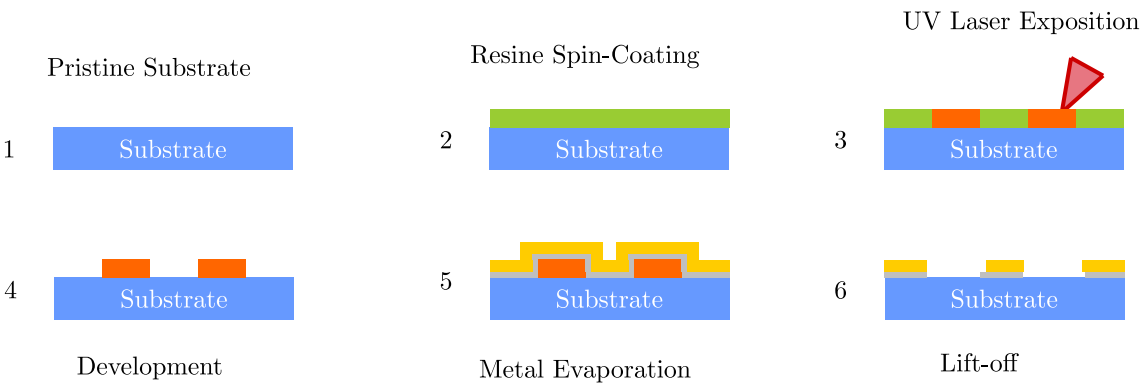

FIGURE *3.4* – ***1)*** *Pristine substrate.* ***2)*** *Deposition of an optical resine on top.* ***3)*** *Exposure to UV laser light according to the recipe in the text. The laser light induces a chemical reaction which makes the resine susceptible to being washed away by the presence of a developer liquid as shown in* ***4)****. In* ***5)*** *15 nm of Titanium and 30 nm of Gold or Platinum are evaporated onto the substrate. Using acetone* ***6)*** *the developped areas can be removed (« lift-off »).*

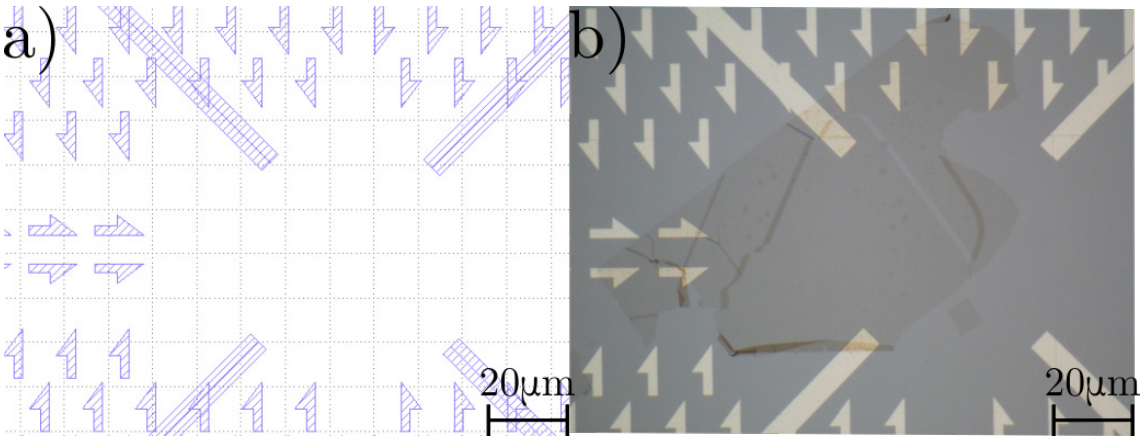

FIGURE *3.5* – ***a)*** *Microscopic markers for orientation as shown by computer lithography software.* ***a)*** *Microscopic markers structure with a deposited hBN-flake after finished laser lithography, development, evaporation and lift-off. The microscopic markers enable quick localization of the TMDC-based structure on the substrate despite the limited field of view of the kPEEM setup.*

4

The influence of the substrate onto the electronic band structure in monolayer WSe_2

4.1 The influence of the dielectric environment on the electronic structure in ML-TMDCs: What is the state of the art ?

4.1.1 Influence of the substrate is typical for monolayer-TMDCs

As we have seen in the introduction chapter (cf. section 1.3), the optoelectronic properties of ML-TDMCs are mainly determined by its band structure parameters: the effective masses m_e at the valence and conduction band of K and Γ, the spin-orbit splitting at K and the energy separation between the upper valence band at K (UVBM) and Γ called $E_{\Gamma K}$. The existence of the direct band gap, described by the parameter $E_{\Gamma K}$, enables the strong light-matter interaction. The high exciton binding energies E_B and the existence of a B1s exciton are linked to the effective masse and the spin-orbit coupling at K/K'. The C exciton and its high intensity in differential reflectance spectra is linked to the curvature of the bands close to Γ which are described by the effective mass at Γ and $E_{\Gamma K}$. This means that by controlling the band structure parameters one can effectively tune the optoelectronic properties of ML-TMDCs.

In the literature only few mechanisms are known which can change the band structure of a ML-TMDC:

— In ML-WSe_2 strong tensile strain on the order of several % is expected to decrease $E_{\Gamma K}$ by 100s of meV and can even lead to an direct-to-indirect band gap transition [118]. In WS_2 and WSe_2 strain of few % changes the effective mass at K on the order of 0.01 $m_{e,0}$ from -0.49 $m_{e,0}$ (WS_2) and -0.38 (WSe_2) of their values at 0% strain [5].

— p-doping on the order of $10^{14} e/cm^2$ is expected to lower $E_{\Gamma K}$ by hundreds of meV [17].

A third mechanism susceptible to change the band structure is the dielectric screening by the substrate which we will discuss in the following section.

4.1.2 Dielectric screening of the substrate and its influence on the band structure from a theoretical POV

The exact effect of dielectric screening of the substrate is under debate among theorists [151, 185]: Steinke et al. have calculated the band structure of ML-WS_2 as a function of the static dielectric constant of the substrate. For ML-WS_2 and a substrate with the static dielectric constant $\epsilon = 5(10)$ they find a reduction of the band gap of 300 (350) meV as compared to the vacuum case ($\epsilon = 1$). It is important to note that, according to their calculations, the dielectric effect only changes the magnitude of the band gap and not the curvature of the bands. Spin-orbit splitting, effective masses and $E_{\Gamma K}$ remain thus constant over all simulated substrates (for all ϵ). The shift of valence bands and conduction bands is thus ≪ rigid ≫.

Zibouche et al. compared calculations of the band structure of ML-MoS_2 on three different dielectric environments with different static dielectric constants ϵ: vacuum ($\epsilon = 1$), hBN with $\epsilon_{\text{hBN}} = 2.6$ and SiO_2 with $\epsilon_{SiO_2} = 3.9$. Similar to Steinke et al. they also found a band gap renormalization for different dielectric constants: the size of the quasiparticle band gap yielded: 2.72 eV in vacuum, 2.58 eV for a hBN substrate and 2.51 for a SiO_2 substrate. Beyond this band gap renormalization, which is measured as the difference between the valence band maximum and the conduction band minimum at K, Zibouche et al. found that the shape of valence and conduction band changes. For ML-MoS_2 in vacuum they found $E_{\Gamma K} = 0.23$ eV, for hBN $E_{\Gamma K} = 0.19$ and for SiO_2 they found $E_{\Gamma K} = 0.17$ eV. Thus for increasing static dielectric constant of the substrate in the order

of 1 to 5, $E_{\Gamma K}$ is decreased in the tens of meV. The hole masses m_e of the VBM at K increased slightly from $0.42m_{e,0}$ to $0.45m_{e,0}$ to $0.46m_{e,0}$ going from vacuum to hBN to SiO_2. The renormalization yields thus a « non-rigid » shift of valence and conduction bands.

Since every ML-TMDC needs to be deposited on a substrate with a certain static dielectric constant, the ability to change its band structure by choice of substrate seems a very simple and straight-forward way to tune its optoelectronic properties. For us, this raises the question if the effect of dielectric screening of the substrate onto the band structure has been discussed in the experimental literature, in particular:

1. Which substrates have been used for the analysis of ML-TMDCS in ARPES and why ?
2. How does the substrate influence the band structure parameters ?
3. Which interaction mechanisms have been identified ? Has dielectric screening of the substrate been considered ? If so, is the dielectric screening of rigid or non-rigid nature ?
4. Have different substrates been compared in their effect on the ML-TMDC band structure ?

In the following we will review studies by their chosen substrate and the analysed effects. We start with the most typical substrates before discussing studies with more rarely used substrates. Interaction effects with the substrate, changes in the band structure parameters and the question of dielectric screening will be reviewed for each substrate.

4.1.3 Typical substrates used for ARPES and their interactions with ML-TMDCs

In order to answer question one we have to understand the experimental limitations of ARPES: As described in the previous chapter ARPES experiments require atomically flat surfaces for a homogeneous photocurrent signal [31, 150]. Since the optical excitation ionizes the sample, it must be kept at a fixed potential difference to ground to avoid local charging effects. Such local charging effects can distort the trajectory of photoelectrons leaving the sample and blur the signal [143]. Because of these requirements, most ARPES studies have focussed on using the following substrates:

1. Gold, where the monolayer is often deposited or grown on a substrate of Au(111) crystal orientation [15, 32, 41, 65, 102, 111, 124, 184].
2. Graphene, in single-layer (SLG) [1, 2, 36, 44, 66, 110, 118, 130, 131, 176] , bilayer (BLG) form [112, 178, 181] or its bulk correspondent, graphite [18, 19, 128, 155, 164, 168]. We will refer to them as « graphene and peers ».
3. Multi-layer hBN crystals (monolayer to tens of nm thickness) [25, 64, 67, 121, 164].

Substrates of the first two categories are conductive enough such that their electrostatic potential can be fixed to prevent charging effects. When a bulk hBN crystal is used as a substrate, either a graphene contact can be added to ground the sample [121] or the monolayer flake touches both the hBN and the conductive substrate [67]. This trio of substrates make up the vast part of substrates used to analyse ML-TMDC band structures in ARPES. Let us look at the effect of these substrates on the ML-TMDC band structure of either of gold, graphene and peers and hBN.

Gold

TMDC-based monolayer systems on Gold can be created in two different ways: On the one hand, gold crystal surfaces in the Au(111) configuration have a hexagonal symmetry and

lattice parameter not too different from those of monolayer-TMDCs. This enables epitaxial growth of the ML-TMDC on the gold surface [15, 32, 41, 111]. On the other hand, gold can also be evaporated onto other substrates where it is amorphous. The ML-TMDC is then prepared through other means (mechanical exfoliation, CVD) and transferred onto the substrate surface [65].

A typical band structure for ML-MoS_2 on Au(111) can be seen as published by Bruix et al. [15] in figure 4.1. At K the spin-split bands of the valence band maximum (VBM) are energetically far from gold bands such that there is no hybridization. The situation is different at Γ where gold bands form a continuum. Such a continuum creates strong hybridization between the MoS_2 and gold orbital states and widely broadens the linewidth of the measured VBM in ARPES at Γ. For all studies on gold, a significant shift to higher binding energies of few 100s of meV has been observed compared to calculated free-standing bandstructures [15, 32, 65, 111]. Aside from this hybridization, a shift of the Fermi Level to the CBM is seen because of high electron transfer [15]. The shift of $E_{\Gamma K}$ in hundreds of meV and the hybidization with gold bands has been observed for other ML-TMDCs (WS_2, WSe_2) as well [32, 184]. In Bruix et al. [15] the influence of dielectric screening by the gold on the monolayer of MoS_2 was mentioned but not investigated .

Park et al. [124] compared ML-WSe_2 and ML-MoS_2 on gold to a sapphire substrate and find that the $E_{\Gamma K}$ changes. The $E_{\Gamma K}$ yields 0.06 eV(0.02) eV for ML-MoS_2 on gold (sapphire). For ML-WSe_2 it yields $E_{\Gamma K} = 0.02(0.26)$ eV on gold(sapphire).[1] The effect of the metallic substrate on $E_{\Gamma K}$ compared to the insulating substrate (sapphire) thus switches sign from ML-MoS_2 compared to WSe_2. This change was not commented on. [124].

Zhao et al. [184] also found that the band gap is renormalized at K to a value of 1.4 eV [184] when comparing with the value of 1.95 eV [181] measured by scanning tunneling spectroscopy in the literature. Further, they found that the measured spin-orbit splitting $\Delta_{SOC} = 460$ meV is reduced when compared to literature values of 475 meV on BLG [181] or 513 meV on SiO_2/Si[84]. The effective mass of the upper spin-split band at K was almost 50 % lower ($-0.529\ m_{e,0}$) for the upper band than another ARPES literature value $-0.35\ m_{e,0}$ [84]. Dielectric screening was mentioned as a possible reason for this discrepancy but not investigated.

Graphene and peers

In order to create monolayer or bilayer graphene substrates, 4H or 6H-terminated SiC(0001) substrates can be used. Single-layer Graphene (SLG) or bilayer graphene (BLG) on top of these substrates can be created by annealing the SiC [1, 2, 130, 131, 180] which can turn into freestanding Graphene (without covalent bonds) via hydrogen intercalation [1]. Monolayers of TMDs can then either be grown epitaxially on the graphene structure [112, 180], transferred from other sources [130, 131] or via chemical vapor deposition [1, 2, 66]. Thick flakes of graphite can be exfoliated from bulk crystals or cleaved [19, 155].

Generally, **monolayer** or **bilayer graphene** or **graphite** work as an atomically flat and conducting substrate and produce a strong homogeneous signal of the monolayer TMD band structure in ARPES. When undoped, the Fermi level in Graphene lies at the Dirac point.

1. We calculated these values for $E_{\Gamma K}$ from the values of the binding energies of the valence band maxima given in the text. $E_{\Gamma K}$ was not explicitly calculated by Park et al.[124].

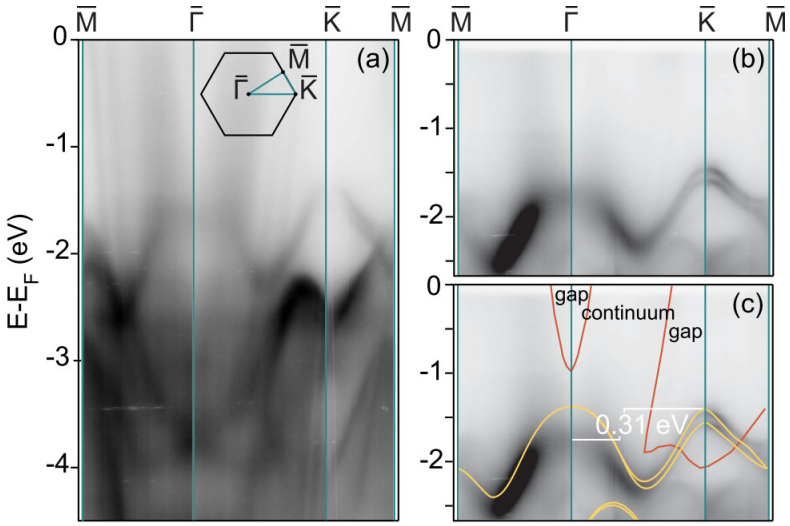

FIGURE *4.1* – *Measured ARPES bandstructures of MoS_2/Au(111) from* BRUIX ET AL. *[15] through the high symmetry points M, Γ and K of the Brillouin zone.* ***a)*** *and* ***b)*** *show the complete measured band structures at $h\nu = 70$ eV and $h\nu = 49$ eV excitation energy . In* ***c)*** *the authors show the data of b). The edges of the Au band continuums (orange lines) and the MoS_2 band structure of the theoretical MoS_2 band structure (yellow lines) have been superposed. « Gap » and « continuum » refer to the absence of bands from gold at K or to the band continuum of gold around the Γ-Point. At Γ strong hybridization between gold and MoS_2 bands blurrs the signal. The $E_{\Gamma K}$ between the VBM at K and the strongly hybridized band at K is ≈ 0.31 eV. Taken from [15].*

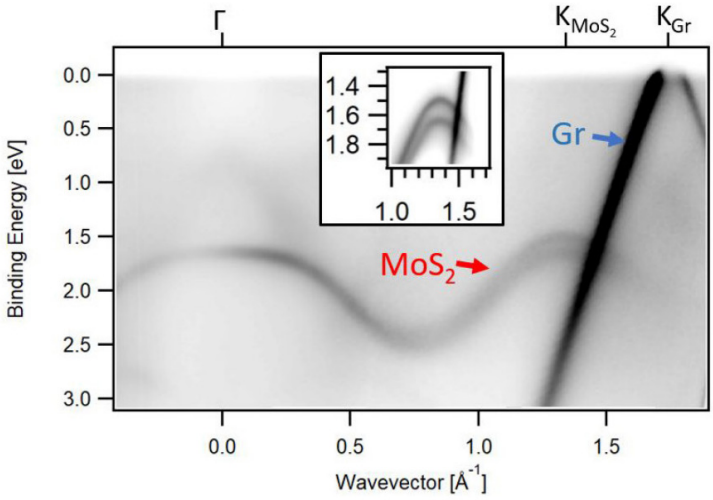

FIGURE *4.2* – *Measured band structure of monolayer MoS_2 on Graphene as measured by* EHLEN ET AL. *The annotation MoS_2 refers to the upper valence band edge of the MoS_2 bands, Gr refers to the graphene $\pi-$bands at K. No avoided crossings, indications of orbital hybridization, can be found between Graphene and MoS_2 bands close to K. K_{MoS2} and K_{Gr} refer to the K-Points of either MoS_2 or graphene layer. The Fermi level is situated at the Dirac point of Graphene. Taken from [36].*

When the crystal of the underlying graphene-like substrate and the ML-TMD are aligned, as can be the case if the monolayer TMD is grown on graphene via CVD [2], the highest band of graphene at the K_{Gr}-point of graphene will intersect with the VBM of the ML-TMD close to the K_{TMD}-point. Despite the proximity of the bands in energy, usually no hybridization is observed at lower binding energies, that is, up to -2 eV below the VBM of the ML-TMDC [2, 36, 44, 164]. This is due to the in-plane character of the electron orbitals of the TMDC-bands at K [186]. The superposition of the bands of graphene and a TMDC can be seen nicely in the FIGURE 4.2 of EHLEN ET AL. [36] where graphene bands intersect ML-MoS_2 bands close to K, but no avoided crossings are observed. However, at higher binding energies avoided crossings can be found as bands of the ML-TMDC and graphene hybridize as found by PIERUCCI ET AL. [130]. This is explained by the out-of-plane orbital character [29]. Because in undoped monolayer, bilayer graphene and graphite the Fermi level lies at the Dirac point, the occurence of n-doping of graphene can be determined if graphene bands are visible above the Dirac point and p-doping if the Dirac point is not visible. But the amount of charges is usually not quantified [1, 2, 118, 130].

MIWA ET AL.[111] determined the size of the band gap of ML-MoS_2 on gold at 1.39 ± 0.05 eV. They compared this value to the energy of the A1s exciton at 1.88 eV measured by [103]. It should be noted that the energy of the A1s exciton is usually lower than the size of the band gap, as explained in section 1.3. Nonetheless, the conclusion is valid that the band gap is significantly changed by hundreds of meV. This effect was attributed to dielectric screening of the gold substrate.

BUSSOLOTTI ET AL. found that the dielectric screening of HOPG does not influence the shape of the valence band in a ML-MoS_2 as compared to their own calculations [19].

hBN

Hexagonal boron nitride (hBN) is an insulating 2D-material with a wide band gap (5.4 eV [12]). Flakes of hexagonal boron nitride are atomically flat and thus provide a smooth surface for ARPES measurements. hBN flakes can be created by exfoliating hBN flakes from bulk crystals and subsequent transfer onto the target substrate [67, 121, 164]. This yields hBN flakes of several nanometer thickness [121]. Another way is to grow thin layers of hBN via CVD with subsequent growth of TMD-monolayers on top which makes monolayer hBN possible [25] . Generally, when studying the band structure of a ML-TMD/hBN structure in ARPES, the VBM of the ML-TMD and hBN do not intersect and are energetically separate due to the wide hBN band gap. One example measured by KATOCH ET AL.[67] is presented in FIGURE 4.3. When hBN and ML-TDMC crystals are aligned, the VBM of the ML-TMD at the K-Point is closest to the hBN-VBM at K, the so-called π-bands. At Γ one can see the local VBM of the ML-TMD and the VBM of the hBN σ-bands. The difference between the two materials' VBMs is greater at Γ than at K but even here the spacing remains greater than 500 meV for the case of monolayer hBN [25]. For bulk hBN the value is in the few eV [67, 164]. This strong separation in energy of the bands explains the absence of interlayer hybridization as witnessed by multiple studies [25, 67, 164].

CHEN ET AL. [25] considered ML-$MoSe_2$ on a monolayer of hBN grown on Rh(111). They calculated the so-called « compression factor » for the upper valence band [62] $(E_{max,meas} - E_{min,meas})/(E_{max,calc} - E_{min,calc})$ where $E_{max/min,meas}$ are the measured binding energy values of the maximum and the minimum of the highest band of the valence band and $E_{max/min,calc}$ are the corresponding calculated values. They found a band compression factor of 80 % when comparing with the calculations of JIN ET AL..

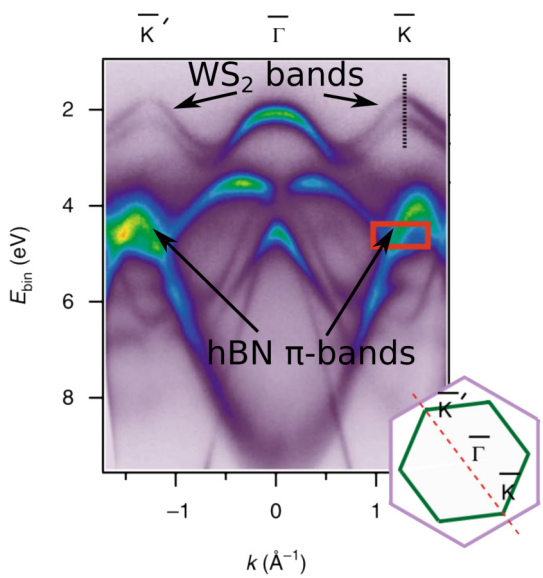

FIGURE *4.3 – Measured ARPES spectrum of ML-WS_2 on hBN. Taken and modified from [67]. The two hexagons indicate the cross-section through reciprocal space with the Brillouin zone of hBN (violet) and ML-WS_2 (green). At around $E - E_F = 2$ eV one can see the valence band edge of ML-WS_2, at around $E - E_F = 4$ eV the maxima of the hBN-π-bands. The valence band maxima of either ML-WS_2 and hBN are separated by roughly 2 eV and do not intersect.*

This means that the minimum and maximum of the highest band of the valence band move closer together in energy. Dielectric screening was mentioned as a possible reason for this compression but not discussed further.

Between hBN and graphite

WALDECKER ET AL. [164] considered the influence of graphite and hBN on a monolayer-flake of WS_2 which was deposited and overlaying both substrates. They found that while the band structure at VBM remained rigid in its form the choice of substrate induced a shift in binding energy of the VBM. The authors claim that this band shift is triggered by a band gap renormalization due to different static dielectric constants of hBN ($\epsilon = 4.5$) and graphite ($\epsilon = 9$). The values for spin-orbit splitting $\Delta_{SOC} = 0.43 \pm 0.02$ eV, effective masses $m_e = -0.48 \pm 0.05(-0.78 \pm 0.1)$ $m_{e,0}$ for the upper and lower spin-split bands at K and at Γ $m_e = -2.55 \pm 0.05$ $m_{e,0}$ remain thus equal for ML-WS_2 on hBN and graphite.

Conclusion

We have seen that out of experimental requirements (surface homogeneity, grounding of the sample, ability to grow monolayers) many studies have looked at ML-TMDC band structures on gold, graphene and peers, and hBN. In those studies that discuss the influence of dielectric screening it is difficult to discern from orbital hybridization, charge transfer or strain which occur simultaneously and have not been explicitly separated [15, 19, 25, 111, 124, 164].

4.1.4 ARPES studies on other substrates

ARPES studies have also analysed the band structure of ML-TMDCs on other substrates than the presented ones. Examples are Si with a native SiO_2 layer [62, 63, 84, 172, 173], doped TiO_2 [67, 160], doped $SrTiO_3$ [160], sapphire [124], GaN [52] and potassium-intercalated monolayers [37] have been analysed. Generally, the signal-to-noise ratio diminishes dramatically when rough substrates are used which makes it hard for studies to describe the effect of the substrate.

Silicon and monolayers in suspension

In some ARPES studies ML-TMDCs were analysed on Si terminated with a native SiO_2 layer (usually $\approx$ 1 nm in thickness) [62, 63, 84, 173]. Bands of the bulk Si substrate cannot be seen and no contributions of the amorphous native SiO_2 termination. Mainly two groups of authors have worked on this substrate: Jin, Yeh et al. have measured monolayer MoS_2 and WSe_2 on native SiO_2 terminated Si [62, 63, 172]. They experience a strong broadening of the band peaks in the photoelectron spectra. This was attributed to poor energy resolution (100 meV) and to the surface roughness of the substrate[62, 63, 172]. Jin et al. have also compared a monolayer of MoS_2 both on native SiO_2 terminated Si and suspended. The effective masses m_e at Γ and K are similar in both environments: at K the effective mass changes from $-0.43 \pm 0.02\ m_{e,0}$ to $-0.48 \pm 0.02\ m_{e,0}$ (Si to suspended) and at Γ from: $-2 \pm 0.35\ m_{e,0}$ to $-1.85 \pm 0.22\ m_{e,0}$ (Si to suspended) . Δ_{SOC} and $E_{\Gamma K}$ were not compared. Dielectric screening was not discussed [63].

Yeh et al. find that for ML-WSe_2 the effective mass at Γ is half as large ($-3.5 \pm 1.8\ m_{e,0}$ as they had calculated ($-7.1 \pm 0.2\ m_{e,0}$). Dielectric screening was mentioned as a reason but not investigated [173].

Jin et al. compared mechanically exfoliated to CVD-grown ML-MoS_2 on a doped Si substrate with native SiO_2 termination. They found that the shape of the valence band was significantly distorted as compared to the calculated shape. The compression factor was 80 % for exfoliated and 50 % for CVD-grown ML-MoS_2. This was attributed to substrate interaction but the exact mechanism was not specified [62].

Le et al. [84] transferred ML-WSe_2 onto silicon with SiO_2 termination. The measured effective masses of the upper spin-split band ($-0.35 \pm 0.01\ m_{e,0}$) and lower-spin-split band ($-0.49 \pm 0.05\ m_{e,0}$) match the authors' theoretical DFT calculations within the margin of error. The measured values of Δ_{SOC} (0.513 ± 0.01 eV) and $E_{\Gamma K}$ (0.892 ± 0.02 eV), however, surpass the theoretically predicted values by 10% and 47% respectively. Strain was discussed as a possible reason for the discrepancy in $E_{\Gamma K}$ and Δ_{SOC} from the theory. However, the authors could not match their experimental values of $E_{\Gamma K}$ and Δ_{SOC} with a corresponding lattice constant under the assumption of strain. For $E_{\Gamma K}$ the discrepancy was attributed to the orbital selectivity of the polarized optical excitation which is supposed to suppress photoemission signal from the valence band maximum at Γ. Dielectric screening was not discussed in the study.

GaN

On GaN Henck et al. found that the presence of a monolayer of MoS_2 shifts the VBM of GaN at Γ roughly 300 meV closer to the Fermi level, an indication for electrons transfer from GaN to MoS_2. Besides, no band structure values of MoS_2 were characterised and dielectric screening was not discussed [52].

Nb-$SrTiO_3$ and Nb-TiO_2

Ulstrup et al. [160] have compared the band structure of CVD-grown ML-WS_2 on niobium doped TiO_2 and niobium doped $SrTiO_3$ [160]. Despite a supposedly « smooth » surface on either substrate, a strong broadening of the signal can be seen. In the case of Nb−TiO_2 this was attributed to a spatial doping profile which shifts the bands as a function of location. On Nb−$SrTiO_3$ the broadened band structure was attributed to the coarse substrate due to the presence of both TiO_2 and SrO-terminations. While the ARPES signal almost vanishes for the bands at K on Nb−$SrTiO_3$ the authors claim that the valence bands shift upwards rigidly by 0.43 eV from STO to TiO_2 [160]. This shift was measured at Γ. On ML-WS_2/Nb−$SrTiO_3$ the authors were not able to resolve the spin-splitting at the K-Point such that band structure values could not be compared with Nb−TiO_2. The overall shape of the band structure agrees with theoretical predictions on both substrates, however. Because doping and dielectric screening both renormalise the band gap they could not be distinguished .

Katoch et al. observe a shift to lower binding energies of the ML-WS_2 valence band on doped TiO_2 as compared to hBN [67]. The shift was not quantified but said to be rigid. The authors were however unable to resolve the spin-split bands at K on TiO_2. They attribute this low SNR to surface roughness and charge impurities on TiO_2. No band structure values were compared and dielectric screening was not discussed [67].

4.1.5 Summary and conclusion

In conclusion, dielectric screening of the substrate onto the band structure is a mechanism that is frequently cited in the literature when substrate-related band structure modifications are discussed. But from the many ARPES studies that have been carried out, it is difficult to say how the dielectric environment changes the band structure. The following problems arise when consulting the literature on this issue:

1. **Ambiguity of interaction mechanisms**: Some studies mention the effect of dielectric influence by comparing measured band structures on a substrate to calculated band structures in a vacuum without separating it from other effects [19, 25, 62, 72, 173]. But the presence of a substrate alone can possibly change the band structure through other mechanisms as well such as strain [5, 118], charge transfer [17, 178, 184] or orbital hybridization [15, 111].
2. **Lack of consistent comparison studies**: Some studies compare their own band structure parameter values to experimental values found in the literature [19] or determined by completely other measurement types (for instance photoluminescence [111] or STS [184]) . This is problematic, however, because fabrication, experimental conditions and data analysis can be very different in studies of the same or different measurement types. Studies that compare substrates under the same controlled conditions using ARPES are rare and compare no more than two different dielectric environments, if any [63, 67, 160, 164].
3. **Poor signal quality on rough substrates**: Substrates need to be atomically flat, else the signal becomes very inhomogeneous and broadened [52, 62, 63, 67, 160]. These studies could not reliably determine a full set of band structure parameters (spin-orbit splitting, effective masses, $E_{\Gamma K}$) on such rough substrates.

In order to analyse the effect of dielectric screening onto the band structure of a ML-WSe_2 we therefore identify the following to compare:

1. Our study should make a comparison of the valence band structure on dielectric substrates, i. e. substrates with a band gap $E_g > 2$ eV must be used such that

charge transfer and hybridization with ML-TMDC is forbidden. Strain, as a possible mechanism, should be ruled out.

2. The study should encompass multiple dielectric environments and determine the full set of band structure parameters (spin-orbit splitting, effective masses and $E_{\Gamma K}$) in relation to the static dielectric properties of the substrate.

4.2 Measurements of ML-WSe_2 at the NanoEsca PEEM setup

We measured multiple samples of a ML-WSe_2 on different substrates using the NanoEsca I PEEM setup at the « Plateforme Nanocaractérisation » of the CEA-LETI in Grenoble. For one Si and and two hBN substrates we deposited ML-WSe_2 flakes from a synthetic WSe_2 source crystal from the National Institute of Material Sciences, Japan, (NIMS) directly on Si and on hBN. For all other samples, including a third hBN substrate, we used synthetic WSe_2 crystals from the manufacturer « hqgraphene ». As a deposition technique we used all-dry viscoelastic stamping using our specialised stamping setup at the plateforme « Nanofab » at the CNRS in Grenoble. We have explained this technique in section 3.2.

4.2.1 Sample preparation

In this section we describe the sample preparation by substrate:

— Si and hBN: 6 to 10 nm thick hBN flakes from Kenji Watanabe and Takahashi Taniguchi (NIMS) were deposited on Si(100) wafers by Siltronix. The thickness of the hBN flakes was controlled by Atomic Force Microscopy. These silicon wafers are terminated by a thin native (1 nm) SiO_2 layer.

— TiO_2: a film of 10 nm amorphous TiO_2 was deposited using atomic layer deposition. The precursor, Titanium(IV) tetraisoproxide (TTIP), was heated at 95 $°C$ while the deposition chamber was heated at 150°C. Pressure was kept at $2.8 \cdot 10^{-1}$ Torr. The static dielectric constant of our amorphous TiO_2 was measured by a micro-scale capacitive structure and determined at $\epsilon \approx 34$.

— STO: $SrTiO_3$ crystals of 1x1 cm size were bought from the substrate manufacturer Neyco (Vanves, France). We covered the entire surface of the substrate with 15 nm Ti and 35 nm gold except for a small square of 300 x 300 μm^2 size where we would later deposit the monolayer. This was done using metal evaporation and laser lithography as explained in section 3.2. In a final step, we removed the oxidized terminated surface by etching the samples in buffed hydrofluoric acid for 30s, the hydruofloric acid did not etch the titanium covered by gold, as verified by optical microscopy.

— SiO_2: 10 nm of SiO_2 were deposited on Si by Yoshiyuki YAMASHITA from the National Institute of Materials Sciences and measured by Olivier RENAULT at the NanoEsca.

All measurements were carried out using a helium discharge lamp whose most intense spectral line emits at $h\nu = 21.22$ eV. The measurements were carried out at room temperature $k_B T \approx 25$ meV. During measurement, the vacuum inside the preparation chamber was below 10^{-8} mbar. Before each measurement an annealing was carried out at 300° C for 2-4 h.

4.2.2 kPEEM raw data of ML-WSe_2 on different substrates

FIGURE 4.4 and FIGURE 4.5 show the raw photointensity data of our kPEEM measurement of ML-WSe_2 on five different substrates. For each substrate we show slices through the first Brillouin zone of ML-WSe_2 from K/K' to Γ. We also show energy distribution curves (EDCs), i. e. photoemission intensity spectra $I(\mathbf{k}, E)$, taken at $\mathbf{k} = \Gamma$ and $\mathbf{k} = K$ right next to the slices. In the slices and EDCs the photointensity was normalized as explained in section 2.1.8. After normalization, we have increased the photointensity of some EDCs by a factor ×2 or ×3 as shown in FIGURE 4.4 for better visibility. For the hBN substrate we only show the data from the sample with 0° twist angle.

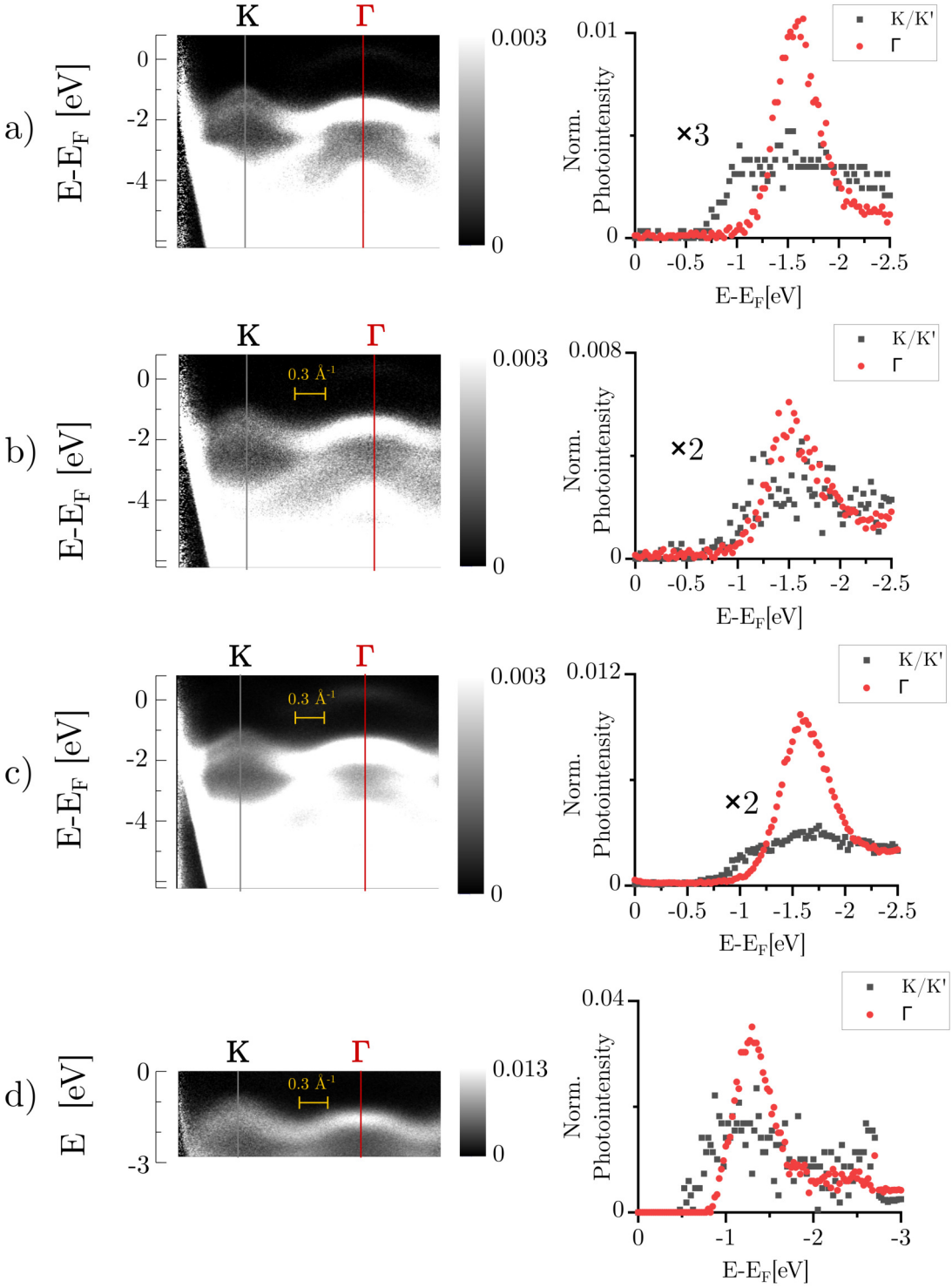

FIGURE 4.4 – *Raw photointensity data after normalization of our kPEEM measurements of ML-WSe_2 on a) hBN, b) silicon, c) amorphous TiO_2 and d) $SrTiO_3$. We describe the normalization in section 2.1.8. For each substrate, we show a slice through the Brillouin zone from K to Γ (left). We also show energy distribution curves taken at K and Γ (right). In some cases we have increased the photointensity spectra after normalization by a factor of ×2 or ×3. For each* $\mathbf{k}$ *the photointensity has been normalized over the integrated signal* $I_{norm}(E) = I(E,\mathbf{k})/\int I(E,\mathbf{k})\,\mathrm{d}E$. *In the case of $SrTiO_3$, which is insulating, our sample was electrically decoupled from the microscope such that we could not reliably determine the Fermi level position. For the hBN substrate we only show the data from the sample with* 0° *twist angle.*

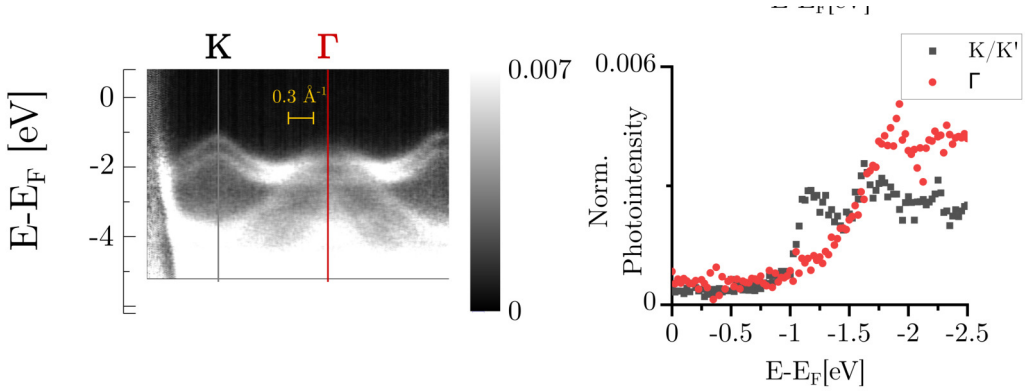

FIGURE *4.5* – *Same as* FIGURE *4.4 but for a substrate of SiO_2 as measured by Renault and fabricated by Yamashita.*

For the case of $SrTiO_3$, which is insulating, our sample was electrically decoupled from the microscope such that we could not reliably determine the Fermi level position. Over all measured band structures, we find the typical shape of ML-WSe_2 with a global valence band maximum at K/K' and a local maximum at Γ.

For hBN, which is a 2D material, we have measured three different samples. FIGURE 4.6 shows isoenergetic cuts through the Brillouin zone at energies of $E - E_F = -1.0$ eV and -2.9 eV. These energies lie roughly 100 meV below the valence band maxima at the K/K' point of ML-WSe_2 and hBN respectively. At **k**-points close to K/K' the energies chosen translate to areas of high photointensity in the isoenergetic photointensity slice. The center of these areas determine the position of the the K/K'-points. Connecting all K/K'-points for either material forms a hexagon for either material as shown right in FIGURE 4.6. This hexagon delimits the first Brillouin zone. Comparing the alignment angles of the Brillouin zones of either material (blue for hBN and orange hexagon for ML-WSe_2) allows us to retrieve the twist angle φ between the crystallographic axes of ML-WSe_2 and hBN for either sample. The twist angle is 5° for sample a) and 0° for sample b. For a third sample with a different source, we were not able to determine the twist angle. It is denoted ≪ 3. ≫.

Over all measured spectra we notice that at Γ the signal benefits from much higher signal-to-noise ratio than at K/K'. This is due to our experimental setup. As we have detailed in section 2.2.2, because the optical excitation beam enters at an angle of 65° to the sample normal, photoexcitation is generally favoured from orbitals with an out-of-plane character. This means that photoemission from d_{z^2}-orbitals and p_z orbitals will be strongest, the orbitals that contribute to the band at Γ [95]. Generally, the spin-splitting is not well resolved on almost all substrates except for SiO_2 and suffers from low signal-to-noise ratio. In the following section we therefore develop a methodology to extract band structure parameters despite the low signal-to-noise ratio.

We have added slices through the Brillouin zone from K over M to K' in the appendix (FIGURE 5.15).

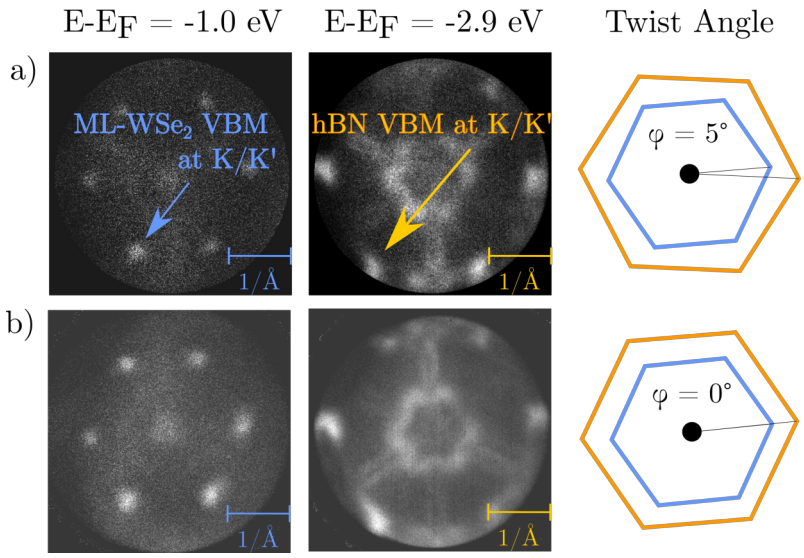

FIGURE *4.6* – *Isoenergetic slice of photoelectron intensity through the first Brillouin zone of ML-WSe_2 by kPEEM for two different samples* ***a)*** *and* ***b)****. Left column at $E - E_F = -1$ eV and middle column at $E - E_F = -2.9$ eV. The energies are chosen such that they lie roughly 100 meV below the valence band maximum at K/K' for ML-WSe_2 and hBN respectively. At these energies, the valence band maxima at K/K' of either material translate to small areas of high photointensity. The centers of these areas determine the approximate positions of the K/K'-points of either material. Comparing the angle between such two areas for either material allows us to determine the twist angle φ. The two hexagons in the right column thus indicate the extent of the first hexagonal Brillouin zones of either material. We find that in* ***a)****, there is a twist angle of* $5°$ *whereas in* ***b)*** *are roughly aligned at* $0°$.

4.3 Our approach for the treatment and analysis of k-PEEM photointensity spectra

Our goal is to reliably determine the important band structure parameters: the spin-orbit splitting Δ_{SOC}, the effective masses of upper and lower spin-split band m_e and the energy separation between the Γ and K-point $E_{\Gamma K}$. However, on some samples the EDCs at K show a low signal-to-noise ratio and broadened linewidth. On substrates which are not atomically flat this is a common occurance for ARPES studies of ML-TMDCs [52, 62, 63, 67, 160].

To extract the bands from the photointensity signal with the least possible ambiguity, we thus need to find a way to enhance the signal-to-noise ratio in the EDCs with the given dataset. In the following paragraph, we describe the physical justification of our approach before giving a detailed account of the methodology in the following sections.

In order to enhance the signal, we exploit two symmetries of the band structure in the Brillouin zone of a ML-TMDC. The first symmetry is the six-fold rotational symmetry of the Brillouin zone of ML-WSe_2. Without regard for the spin-valley-locking at K/K' (cf. section 1.2.4), the Brillouin zone of ML-WSe_2 is invariant under a rotation of 60°. Fitting an EDC at a given (k_x, k_y)-position should thus yields the same band positions as fitting after one or multiple 60° rotations of the Brillouin zone.

The second symmetry is the isotropy of the bands close to points of high symmetry: Let $\mathbf{X}$ be a point of high symmetry in the Brillouin zone of ML-WSe_2, i. e. the Γ-point or one of the six K/K'-points. Within a small area contoured around $\mathbf{X}$ the bands are approximately **isotropic** [79]: in this area, the position of the band peaks in the EDCs $I(\mathbf{k}, E)$ do not depend on the exact $\mathbf{k} = (k_x, k_y)$ but only on the difference $\Delta k = |\mathbf{k} - \mathbf{X}|$.

If $\mathbf{X}$ is one of the six K/K'-points, the above assumption is approximately valid in the range $\Delta k = |\mathbf{k} - \mathbf{X}| \leq 5\% \times \overline{\Gamma X}$ [78]. Here $\overline{\Gamma X}$ is the distance in reciprocal space from X to Γ. For a fixed energy, we propose to sum the intensities of all EDCs close to K or Γ which share the same $\Delta k = |\mathbf{k} - \mathbf{X}|$. Summing up these identical contributions should result in a strongly enhanced photointensity signal. In the following, we detail the necessary steps for this signal-to-noise enhancement using the example of ML-WSe_2 measured on hBN at twist angle 0°.

4.3.1 Finding equivalent k-space positions

In a first step, we determine the $\mathbf{k}$-positions of the six $\mathbf{X}$ = K/K'-points and the Γ-point in our photointenstity data. The left side of FIGURE 4.7 shows an isoenergetic photointensity spectrum $I(\mathbf{k}, E)$ for ML-WSe_2 measured on hBN roughly 100 meV below the later determined K-point and roughly 450 meV above the Γ-point. At these energies, the presence of the valence band maxima at the K/K'-points translates to small circular areas of high photointensity. We find the position of the K/K'-points by the method described in section 4.2. Conversely for the right side of FIGURE 4.7 and the Γ-point. To retrieve the six K/K'-points, we go up in energy until we see the initial dispersion of the bands.

In the isoenergetic plane, our data is discretized in pixels, such that the $\mathbf{k}$-positions of the $\mathbf{X}$-points are given in pixels. For the later calculation of the effective masses, we will have to find a reference value to convert the distances in k-space in pixel to $\mathring{A}^{-1}$. We thus take the distance between the positions of the K/K'-points $\mathbf{X}$ and the Γ-point $\mathbf{\Gamma}$ as $\overline{\Gamma X}$ for all six K/K'-points. We calculate the mean and standard deviation over these six values and thus retrieve the the distance $\overline{\Gamma K}$ and its uncertainty in pixel. To convert this value in $\mathring{A}^{-1}$, we remember the theoretical k-space length between Γ and K in a simple hexagonal

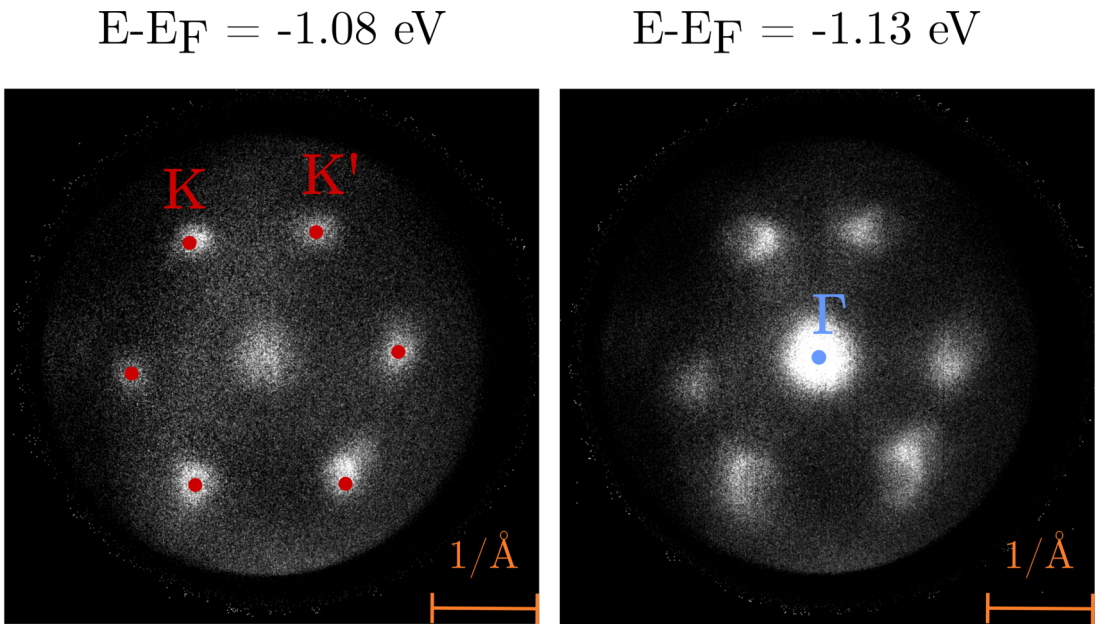

FIGURE *4.7 – Isoenergetic slice of a measured ML-WSe$_2$ on hBN at $E - E_F = -1.13$ eV for Γ (left) and $E - E_F = -1.08$ eV for K/K' (right) in kPEEM. The cuts are taken roughly 200 meV below the VBM at K. At these energies, the valence band maxima at K/K' of either material translate to small areas of high photointensity. The centers of these areas determine the approximate positions of the K/K'-points of either material. The determined K/K' and Γ points are indicated by red and blue dots.*

Brillouin zone from section 1.2.1

$$\overline{\Gamma K} = \frac{4}{3}\frac{\pi}{a} \tag{4.1}$$

where we take $a = 0.329 \pm 0.0005$ [69], the bulk in-plane lattice constant of WSe_2. This yields the following

$$\overline{\Gamma K} \approx 1.27 \mathring{A}^{-1} \tag{4.2}$$

which sets the k-scale of our dataset.

4.3.2 Averaging over equivalent k-space positions

In the previous step we have determined the $\mathbf{k} = (k_x, k_y)$ of the points of high symmetry K/K' and Γ. We now need to extract the EDCs which belong to equivalent k-space positions. KORMÁNYOS ET AL. have calculated the dispersion of the bands in ML-MoS_2 which we take as similar to ML-WSe_2. They estimate that at the VBM at $\mathbf{X}$ = K/K' the bands are isotropic for a distance of 5% of $\overline{\Gamma K}$ i. e. a distance in reciprocal space of $\Delta k = |\mathbf{k} - \mathbf{X}| \leq 0.06 \mathring{A}^{-1}$ [78].

Our kPEEM data $I(E, k_x, k_y)$ contains photointensity spectra as a function of energy E and $\mathbf{k} = (k_x, k_y)$. While the energy intervals are discretized by steps of 25 meV, the k-space positions in the (k_x, k_y)-plane are discretized in pixels and not continuous as stated in the previously. For a given Δk in pixels and a given K/K'-point in pixels, with coordinates $\mathbf{X}$, we can thus find an averaged intensity spectrum

$$I_{\mathbf{X}}(\Delta k, E) = \frac{1}{N(\Delta k)} \sum_{\substack{\mathbf{k}, \\ ||\mathbf{k}-\mathbf{X}|-\Delta k| \leq \delta k/2}}^{N(\Delta k)} I(\mathbf{k}, E) \tag{4.3}$$

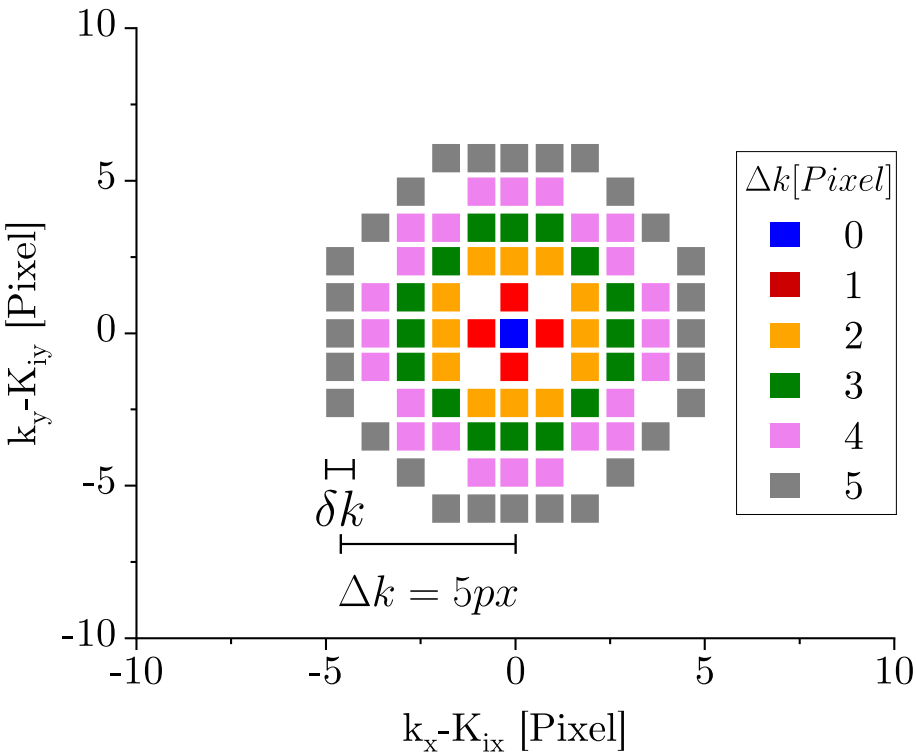

FIGURE *4.8 – Map of equivalent k-Space positions by pixel for different* $\Delta k = |\mathbf{k} - \mathbf{X}|$ *for a point of high symmetry* $\mathbf{X}$ *(K/K' or* Γ*): The center of the map is placed at one of the points* $\mathbf{X}$*.* δk *is the length of a pixel. For* $\Delta k = |\mathbf{k} - \mathbf{X}| \leq 5\% \times \overline{\Gamma K}$ *the bands are approximately isotropic as described in the text. Points of the same color are at the same* Δk *and indicate positions at which the energy distribution curve should have similar shape.*

here $N(\Delta k)$ is the number of spectra with $||\mathbf{k}-\mathbf{X}|-\Delta k| \leq \delta k/2$ around a given $\mathbf{X}$. δk is the length of one pixel in $\mathring{A}^{-1}$. FIGURE 4.8 represents a two-dimensional plane in reciprocal space where the origin $\Delta k = |\mathbf{k}-\mathbf{X}| = 0$ is fixed at a point of high symmetry K/K' or Γ. Each pixel is centered at a (k_x, k_y) position relative to the the chosen point of high symmetry K/K' or Γ. Because of the mentioned band isotropy close to the points of high symmetry, the shape of the EDC only depends on $\Delta k = |\mathbf{k}-\mathbf{X}|$ within the given range. EDCs at pixel positions of the same color share the same $\Delta k = |\mathbf{k}-\mathbf{X}|$ within an uncertainty $\delta k/2$.

In a second step, we can average over all six K/K'-points (denoted by $\mathbf{X}$) such that

$$I(\Delta k, E) = \frac{1}{6} \sum_{\mathbf{X}\in\{\mathbf{K},\mathbf{K}'\}} I_{\mathbf{X}}(\Delta k, E) \tag{4.4}$$

$$= \frac{1}{6} \sum_{\mathbf{X}\in\{\mathbf{K},\mathbf{K}'\}} \frac{1}{N(\Delta k)} \sum_{\substack{\mathbf{k}, \\ ||\mathbf{k}-\mathbf{X}|-\Delta k|\leq\delta k/2}}^{N(\Delta k)} I(\mathbf{k}, E) \tag{4.5}$$

$$\tag{4.6}$$

The effect of such an averaging is shown in FIGURE 4.9. Here we show the averaging over k-space distances of a) $\Delta k = 0$ px, b) 3 px and c) 5 px for K/K' and in d) to f) for Γ respectively. For $\Delta k = 0$ px we average in total over 6×1 spectra, for $\Delta k = 3$ px over $6 \times 4 = 24$ spectra and for $\Delta k = 5$ px over $6 \times 12 = 72$ spectra. We notice that the signal-to-noise ratio improves rapidly with growing Δk.

4.3.3 Background removal and EDC fitting

Having increased the signal-to-noise ratio in the previous step we now remove the background stemming from electron scattering and attempt to fit the band peaks in the EDCs. In FIGURE 4.9 we see the averaged spectra before and after background removal as well as the determined background for different Δk for K/K' (left) and Γ (right). As we have discussed in section 2.2.2, to our knowledge, there is no consensus on how to remove the inelastic electron scattering background in ARPES spectra for ML-TDMCs. In our method, we opt for a conservative background removal: we try to remove as little signal as possible which does not stem from electron-scattering events. To do so, we define a third-order polynomial spline that passes through the points indicated by black crosses in FIGURE 4.9. We have chosen those points manually at energies where we see a local minimum in photointensity and where we do not expect the presence of any bands. The removal of the spline then results in the photointensity signal labelled ≪ After Removal ≫ for the different Δk.

In the next step we want to fit the photointensity peaks indicating the presence of the band at K as shown in panel a) of FIGURE 4.10. We will first explain our fitting method and then deliver a justification based on recent publications. At K/K' we fit the two expected spin-split bands [97, 118, 121] at the valence band maximum by two Gaussians of the form

$$I(E) = A \cdot \exp\left(\frac{-(E-E_C)^2}{2\sigma^2}\right) \tag{4.7}$$

where A the amplitude, E_C the center of the peak. σ can be related to w the peak full width at half maximum via $\sigma = w/2\sqrt{2\ln(2)}$. In our experiment we should be able to resolve this spin-splitting due to the high spin-splitting of ≈ 500 meV[121] which is higher than our resolution ≈ 200 meV. Finally we add a Gaussian for another ML-WSe_2 band

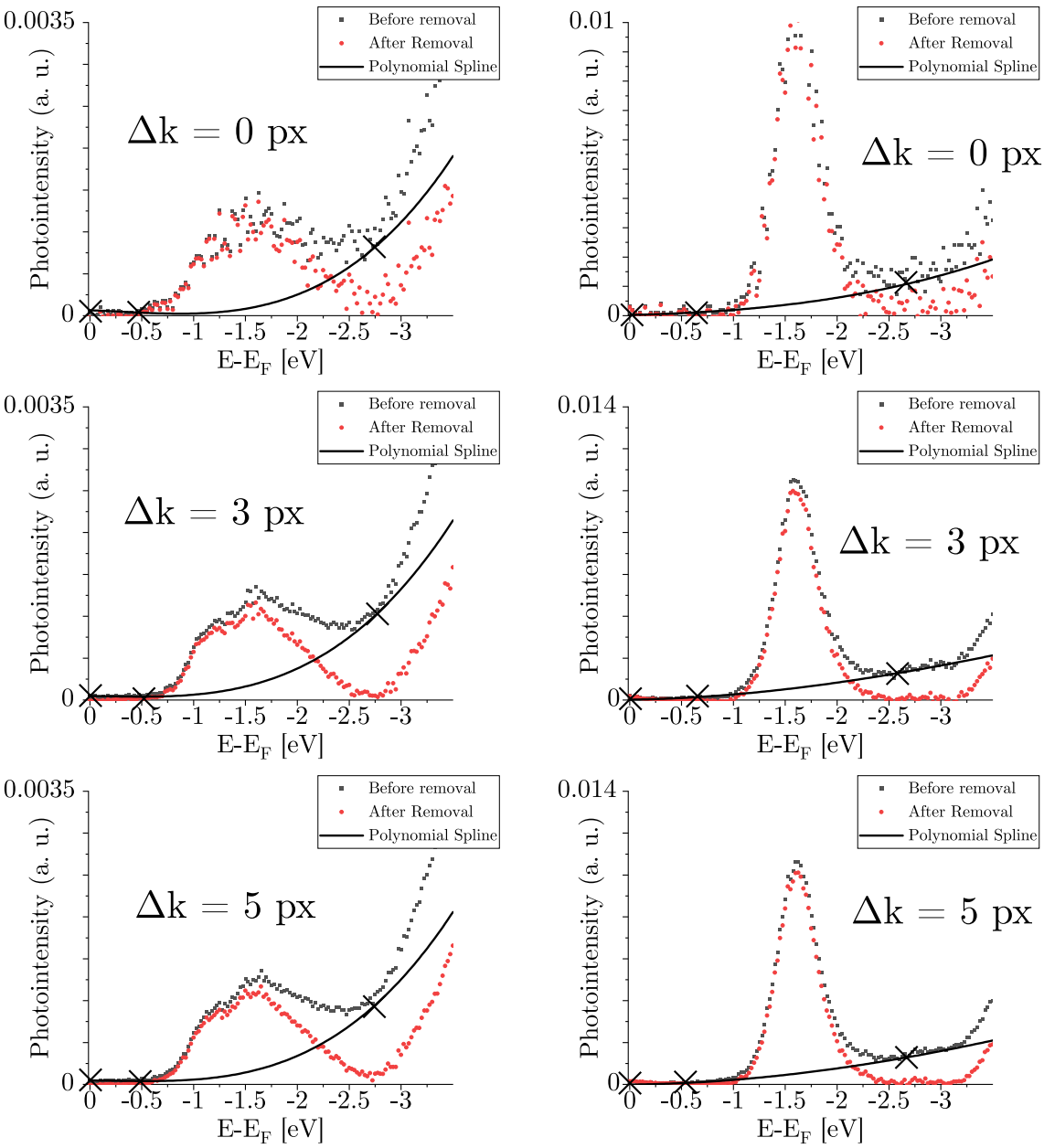

FIGURE *4.9 – Photointensity spectra after averaging over equivalent points of the same Δk in k-space at K/K' (left) and Γ right. We show the spectra for $\Delta k = 0$ px, 3 px and 5 px. The black crosses mark the polynomial spline which is used to remove the background signal. We also show the result of the background removal.*

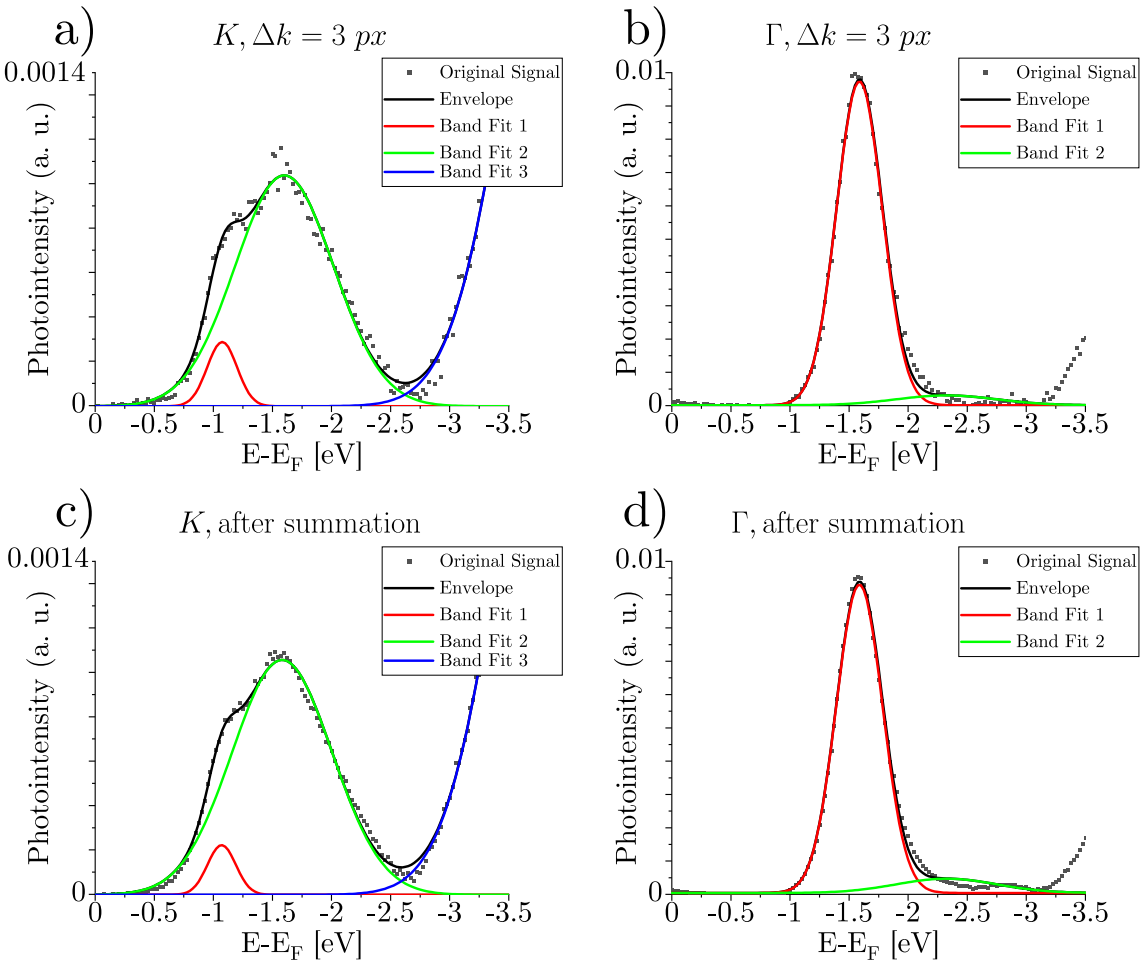

FIGURE *4.10 – Photointensity and fits of the EDCs at K/K' and* Γ *after averaging over equivalent k-space positions for* $\Delta k = 3$ *px* ***(a)*** *and* ***b)****) and after summation as described in the text* ***(c)*** *and* ***d)****). For the fits at K/K', we have included two gaussian curves each for the upper and lower spin-split band, and another band roughly 1 eV below the lower spin-split band. For* Γ *we have included a gaussian curve for the main peak at* $E - E_F = 1.5$ *eV and another band roughly 700 meV below. We have added gaussian curves where we expect band peaks from theory [118].*

roughly 2 eV lower in energy which has been measured and predicted at K/K' [97, 118, 121].

In the resulting fit for EDCs at K/K', shown in panel a) and c) of FIGURE 4.10, the lower spin-split band has a higher FWHM and amplitude than the upper one. We believe that this fitting is correct based on recent literature publications: MAHATHA ET AL.[102] have shown strong electron-phonon coupling between the VBM at Γ and the spin-split bands at K. The coupling broadens the lowest energy peak of the spin-split band energetically closer to the band at Γ which in our case is the lower spin-split band. This electron-phonon coupling is temperature dependent and has been shown to almost double the linewidth of the lower band peak in ML-MoS_2 at room temperature compared to $T < 100$ K (100 meV compared to 60 meV).

We find that the resulting difference in amplitude for the higher and lower spin-split band matches a spin-resolved ARPES measurement of ML-WSe_2 by MO ET AL. [112]. The authors find that the amplitude of the photointensity signal of the lower spin-split band is higher (by a factor of ≥ 2) then for the upper spin-split band. The authors did not quantify the exact ratio of the peaks amplitudes and did not comment on the different amplitudes. A similar observation has been made by [2] for ML-WSe_2 on graphene.

At Γ the signal the signal-to-noise ratio is much stronger as can be seen in panel b) of FIGURE 4.10. Here, we fit the expected photointensity peak at the valence band maximum at Γ by a Gaussian at ≈1.5 eV [97, 118, 121]. We have added a fit for another band at Γ roughly 0.7 and 1.1 eV below the main band peak as expected from theory [118], if the photointensity signal was non-negligible. The fitting of these EDCs yields the dispersion of the bands at K and Γ as shown by FIGURE 4.11. In panel a) we see the band dispersion at K/K' and in b) at Γ.

4.3.4 Nearly free electron band dispersion, dispersion correction and summation of equivalent EDCs

FIGURE 4.11 shows the dispersion of the upper and lower band of the averaged EDCs as a function of Δk. To retrieve the curvature and effective masses of either band, we fit the band using the energy dispersion of the nearly free electron

$$E(\Delta k) = \frac{\hbar^2(\Delta k)^2}{2m_e} + E_0 \tag{4.8}$$

where m_e is the effective mass and E_0 the energetic maximum of the band. We fit in a range from 0 to a maximum of 0.15 $\mathring{A}^{-1}$ for the bands at K/K'. We note that this is beyond the isotropical limit (at $\Delta k = 0.6$ $\mathring{A}^{-1}$) foreseen by KORMÁNYOS ET AL.[79]. However, the extent of the band isotropy is at the limit of our momentum resolution of the NanoEsca $\Delta k_{\parallel} \approx 0.03\mathring{A}^{-1}$. We thus find the given range a good compromise. We fit the parabolic band dispersion up to 0.3 $\mathring{A}^{-1}$ for the band at Γ. To our knowledge the isotropical limit has not yet been calculated for the bands at Γ as it has for K/K' in [78].

The remaining steps are schematically sketched in FIGURE 4.12: (1) We determine the parabolic dispersion of the band $E(\Delta k)$ at K/K' according to the nearly free electron model. (2) We correct the band dispersion by shifting each photointensity spectrum $I(\Delta k, E)$ by the height of the band peak $E(\Delta k)$

$$I'(\Delta k, E) = I(\Delta k, E - E(\Delta k)) \tag{4.9}$$

(3) We can then sum over the spectra $I'(\Delta k, E)$ within the isotropic range for Δk. This « enhanced signal » of the averaged spectra is shown in panel b) for K/K' and d) for Γ

of FIGURE 4.10 where the signal-to-noise ratio is again improved. By summing over these spectra, we lose, however, information about the dispersion. The fits of these enhanced signals at K/K' and Γ are shown in FIGURE 4.10 c) and d) for the other substrates.

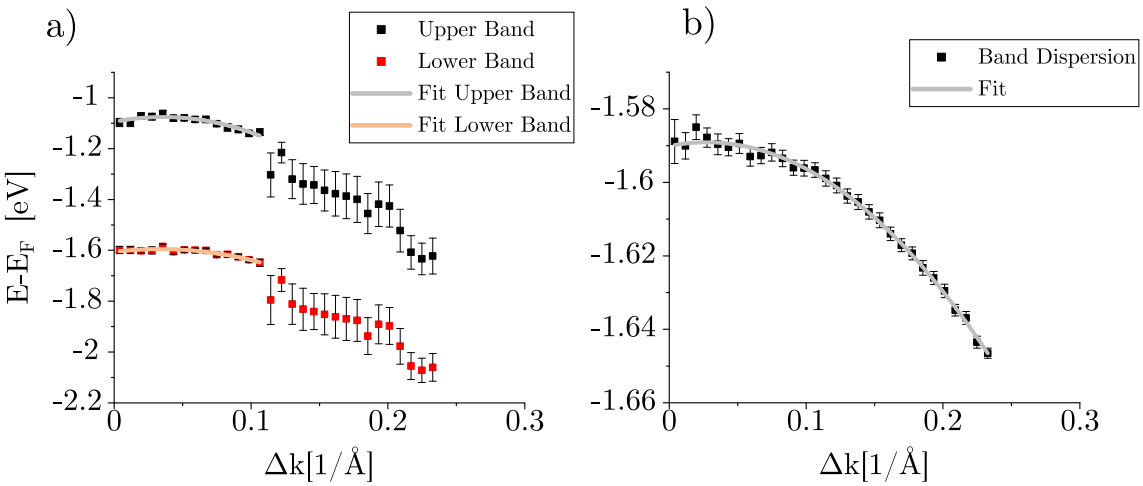

FIGURE *4.11 – Band dispersion at a) K/K' and b) Γ and fit according to the nearly free electron model. In **a)**, we show the band position of the upper and lower spin-split band at K/K' (dotted in black and red) and the corresponding band dispersion fits (gray and red line). In **b)** we show the dispersion of the upper branch of the VBM at Γ (dotted black) and corresponding dispersion fit.*

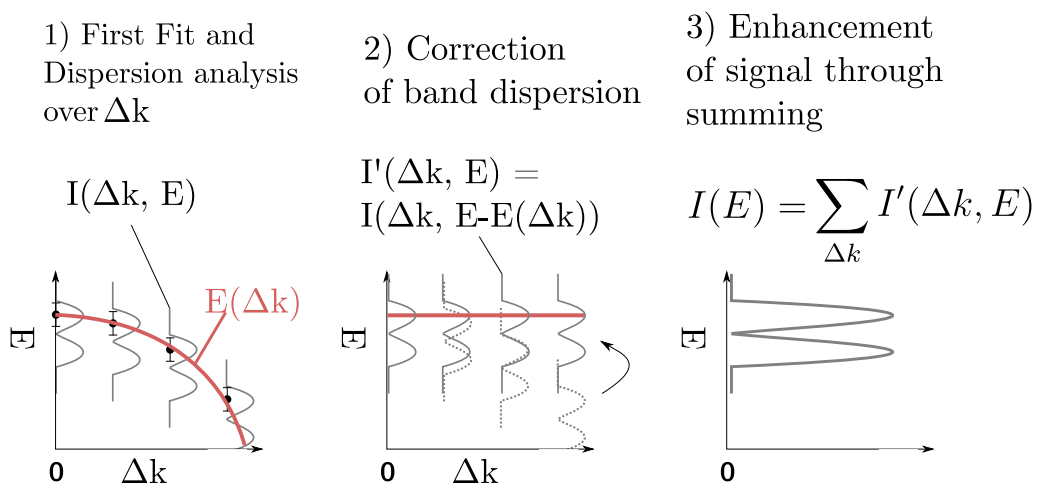

FIGURE *4.12* – *Methodology used to enhance signal quality for the energy distribution curves taken at K/K' and* Γ. *Here we show schematically the spin-orbit splitting at K/K'. After averaging EDCs close to K/K' of same* Δk *and background removal, we are left with EDCs* $I(\Delta k, E)$ *as shown in* ***1)****. These EDCs show schematically the photointensity spectrum of the spin-split bands at a given* Δk*. Fitting these EDCs will determine the dispersion* $E(\Delta k)$ *of the upper spin-split band indicated by the red line. We assume the nearly free electron model for this dispersion.*
In ***2)*** *we use* $E(\Delta k)$ *to correct for this band dispersion. In the corrected EDCs* $I'(\Delta k, E) = I(\Delta k, E - E(\Delta k))$ *the band peak of the upper spin-split band is always at the same energy. In* ***3)*** *we sum over all these EDCs and retrieve a maximally enhanced photointensity distribution* $I(E) = \sum_{\Delta k} I'(\Delta k, E)$ *of the spin-split bands. This maximally enhanced EDC can then again be fitted to retrieve band positions. We show this for the remaining substrates in* FIGURE *4.13. We use the same fitting parameters as shown before. The information about the band dispersion is lost during the summation.*

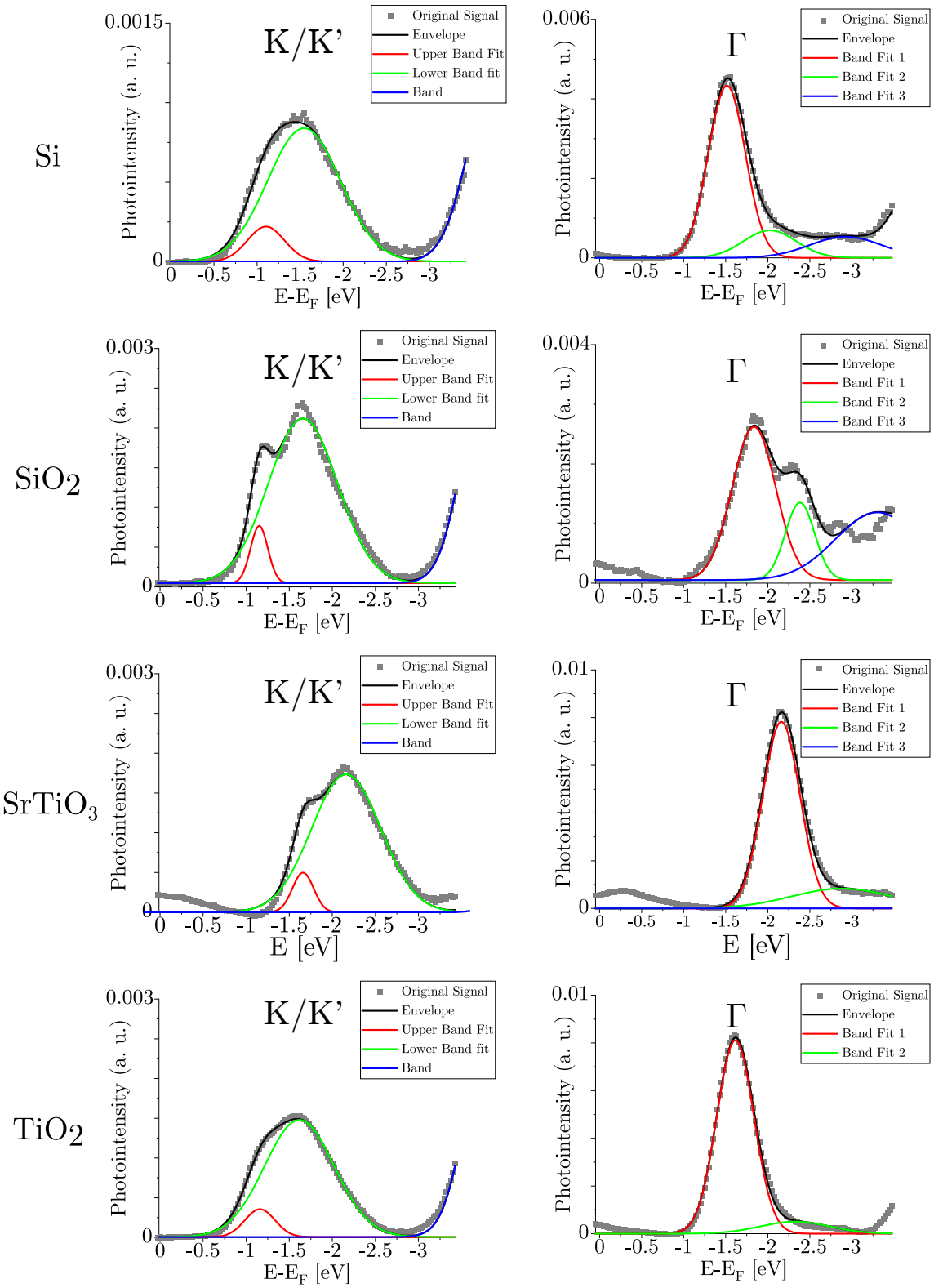

FIGURE *4.13 – Fits of the enhanced spectra of the EDCs at K/K' and Γ on other substrates than hBN after using the methodology in this section.*

4.4 Band structure parameters of ML-WSe_2 and the influence of the dielectric substrate

4.4.1 Measured band structure parameters as a function of the substrate's dielectric constant

We have applied the methodology shown in the previous section to our kPEEM datasets for our different substrates SiO_2, hBN with different twist angles, TiO_2 and $SrTiO_3$. In our study we have used two different WSe_2 crystal sources. On hBN we have measured both monolayer WSe_2 from NIMS (with twist angles 0° and 5°) and « hqgraphene » (named « 3. »). For the 3. hBN sample the signature of the underlying hBN was too weak to determine the twist angle.

Determined band structure parameters as a function of substrate

TABLE 4.1 and TABLE 4.2 show our measured band structure parameters: the effective masses m_e, Δ_{SOC} and $E_{\Gamma K}$ for all presented substrates. For further comparison, we have listed literature values of the band structure parameters in TABLE 4.3.

Most effective masses found in the literature for the upper spin-split band at K are or roughly -0.5 $m_{e,0}$ (for gold or hBN). Here, $m_{e,0}$ is the electron rest mass. Our values for the effective mass are close or below -0.5 $m_{e,0}$ with the effective mass of the upper band being roughly -1 $m_{e,0}$ for all analysed substrates. This is different to [84, 184] who have measured very similar effective masses for the upper as well as the lower branch as can be seen in TABLE 4.3. This discrepancy to the literature is probably due to our larger fitting range around K/K' of approximately $0.15\mathring{A}^{-1}$. At this range we capture a band bending further away from the K/K' point which deviates from the parabolic shape of the nearly free electron dispersion.

ML-WSe_2 on SiO_2 displays a significantly lower effective mass at Γ (-2.37 ± 0.32 $m_{e,0}$) compared to ≈ -4 $m_{e,0}$ for all other substrates. The literature values cover a range from -2.344[184] to -3.5 ± 1.8 $m_{e,0}$ [173] which confirms our range of values.

The right column of TABLE 4.2 compiles the measured values of the spin-orbit splitting Δ_{SOC} between the upper and lower spin-split band at K/K'. These values range from 0.46 eV and 0.51 eV close to literature values on different substrates as shown in TABLE 4.3.

Regarding the difference between the maximum of the valence band at Γ and K/K' $E_{\Gamma K}$, we find notable differences up to approximately 300 meV between the different substrates. $E_{\Gamma K}$ is highest for a substrate of SiO_2 (0.69 ± 0.01 eV) and lowest for Si (0.41 ± 0.02). $E_{\Gamma K}$ remains the same within the margin of uncertainty for all three samples of ML-WSe_2 on hBN (≈ 0.53 eV). These variations are reflected by the literature, where strongly varying values for $E_{\Gamma K}$ can be found (TABLE 4.3). These values range from 0.21 ± 0.01 eV [173] to 0.892 ± 0.02 eV [84].

As pointed out above, we have used two different WSe_2 crystal sources. A comparison shows that the band structure parameters for both sources are similar on hBN: the effective masses are a bit smaller for the 3. sample, (-0.45 ± 0.01 compared to -0.57 ± 0.04 for the 5° sample). $E_{\Gamma K}$ and Δ_{SOC} are roughly 0.53 eV and 0.51 eV for all three samples within a margin of 20 meV and thus similar. We thus conclude that the band structure parameters do not depend on the crystal source. Further, we do not find any significant change of band structure parameters between of the two ML-WSe_2 as a function of twist angle to hBN.

Dielectric constants of the respective substrates

In order to compare the effect of the static dielectric constant of the substrate on the band structure, we assume the following static dielectric constants: For SiO_2 $\epsilon = 3.9$ [50], for hBN $\epsilon \approx 5.9$ after taking the geometric mean $\epsilon = \sqrt{\epsilon_\perp \cdot \epsilon_\parallel}$ where $\epsilon_\parallel = 5$ and $\epsilon_\perp = 7$ [46]. For our amorphous TiO_2 we have measured $\epsilon \approx 34$ using a capacitive low-frequency transport device. For $SrTiO_3$ we assume a high static dielectric constant of $\epsilon \approx 240$ [115]. For Si we assume the bulk dielectric constant $\epsilon \approx 11.7$ [35].

Correlation of the substrate's dielectric constant and band structure parameters

Two competing theoretical works exist to compare with our experimental results: Steinke et al. [151, 164] find that the effect of a dielectric substrate renormalizes the size of the band gap of a ML-TMDC without changing the shape of the valence band. This means that all band structure parameters, except for the size of the band gap E_g, which we did not measure, remain constant over all dielectric substrates. Zibouche et al. [185], however, find that both effective masses and $E_{\Gamma K}$ can be changed: for ML-MoS_2, they find that $E_{\Gamma K}$ decreases by 40(60) meV when comparing the band structure in vaccum ($\epsilon = 1$) to a substrate of hBN(SiO_2) with $\epsilon = 2.6(3.9)$. Hole effective masses increased from 0.42 to 0.45 (0.46). The effect on the effective mass at Γ or the spin-orbit splitting at K/K' was not calculated by Zibouche et al..

In figure 4.14 we present the determined band structure parameters as a function of the static dielectric constant of the substrate. Panel a) shows the effective mass of the upper and lower spin-split band as a function of the static dielectric constant. The changes in effective mass foreseen by Zibouche et al. for ML-MoS_2 and are on the order of 0.01 m_e for changes of the dielectric constant $\Delta\epsilon \approx 1$. These changes are smaller than our error bars for most effective masses.

Panel b) shows the he effective mass at Γ as a function of the substrate's dielectric constant. It changes from SiO_2 ($\epsilon = 3.9$) to hBN ($\epsilon = 5.9$), but remains roughly constant at -4 $m_{e,0}$ for higher dielectric constants $\epsilon > 5.9$.

Panel c) show the spin-orbit splitting Δ_{SOC} as a function of the substrate's dielectric constant. Concerning the Δ_{SOC} we do not see a trend as a function of the substrate's dielectric constant. The values range from 0.46 eV and 0.51 eV. They are similarly high for substrates of a low and very high dielectric constant (SiO_2, hBN and $SrTiO_3$), roughly 0.51 eV. They are lower for Si and TiO_2 (roughly 0.45 eV).

Panel d) of figure 4.14 shows the measured $E_{\Gamma K}$ of ML-WSe_2 as a function of the static dielectric constant of the substrate. Zibouche et al. expect for ML-MoS_2 that $E_{\Gamma K}$ decreases with increasing static dielectric constant. With the assumed static dielectric constants we analyse this behavior for ML-WSe_2: For SiO_2 with $\epsilon = 3.9$ and hBN with $\epsilon = 5.9$ we find that $E_{\Gamma K}$ decreases, in accordance. For the two substrates of hBN we see that the $E_{\Gamma K}$ does not strongly depend on the twist angle. However, we see a minimum of $E_{\Gamma K} \approx 400$ meV for Si at $\epsilon = 11.9$, and then an increase TiO_2 ($\epsilon = 34$, 460 meV) and $SrTiO_3$ ($\epsilon = 240$, 500 meV). The $E_{\Gamma K}$ for high-ϵ-dielectrics (TiO_2 and $SrTiO_3$) remain below the one for hBN.

	m_e **up at K** $[m_{e,0}]$	m_e **low at K** $[m_{e,0}]$	m_e at Γ $[m_{e,0}]$
hBN(5°)	-0.57 ± 0.04	-0.75 ± 0.05	-3.82 ± 0.21
Si	-0.53 ± 0.26	-1.04 ± 0.45	-4.02 ± 0.29
hBN (0°)	-0.66 ± 0.12	-0.93 ± 0.16	-3.99 ± 0.39
hBN (3.)	-0.45 ± 0.01	-0.60 ± 0.03	-3.51 ± 0.14
$SrTiO_3$	-0.62 ± 0.03	-1.14 ± 0.13	-4.35 ± 0.25
TiO_2	-0.63 ± 0.03	-0.74 ± 0.04	-4.26 ± 0.13
SiO_2 (Y., R.)	-0.65 ± 0.04	-1.06 ± 0.06	-2.37 ± 0.32

TABLE *4.1 – Effective masses m_e measured at the upper (up) and lower (low) spin-split band at K/K' and Γ on ML-Wse_2 as a function of dielectric substrate. We use the method laid out in the previous section to measure the effective masses. For two hBN substrates, which is a 2D-material, we have added the twist angle between the crystallographic axes of hBN and ML-WSe_2. The twist is measured between the $\overline{\Gamma K}$ for the monolayer and hBN.*

	$E_{\Gamma K}$ **[eV]**	Δ_{SOC} **[eV]**
hBN(5°)	0.54 ± 0.02	0.51 ± 0.02
Si	0.41 ± 0.02	0.44 ± 0.04
hBN (0°)	0.52 ± 0.01	0.52 ± 0.02
hBN (3.)	0.53 ± 0.01	0.49 ± 0.02
$SrTiO_3$	0.5 ± 0.02	0.5 ± 0.01
TiO_2	0.46 ± 0.02	0.46 ± 0.02
SiO_2 (Y., R.)	0.69 ± 0.01	0.51 ± 0.01

TABLE *4.2 – Measured spin-orbit splitting Δ_{SOC} and the difference in energy between the upper spin-split band at K/K' and upper band at Γ $E_{\Gamma K}$ as a function of substrate. For two hBN substrates, which is a 2D-material, we have added the twist angle between the crystallographic axes of hBN and ML-WSe_2. The twist is measured between the $\overline{\Gamma K}$ for the monolayer and hBN.*

Band Structure Parameter	**Underlying substrate**	**Value and Authors**
m_e at K (Upper Band) [$m_{e,0}$]	Au (amorphous)	-0.529 ± NA [184]
	hBN	-0.42 ± 0.05 [121]
	Si with native SiO_2	-0.35 ± 0.01 [84]; -1.4 ± 0.6 [173] [2]
m_e at K (Lower Band) [$m_{e,0}$]	Au (amorphous)	-0.532 ± NA [184]
	Si with native SiO_2	-0.49 ± 0.05 [84]
m_e at Γ [$m_{e,0}$]	Au (amorphous)	-2.344 ± NA [184]
	Si with native SiO_2	-3.5 ± 1.8 [173]
Δ_{SOC} [eV]	Au (amorphous)	0.46 ± NA [184]
	BLG	0.47 ± NA [112]
	Graphene	0.469 ± 0.008 [118]
	hBN	0.485 ± 0.01 [121]
	Si with native SiO_2	0.513 ± 0.01 [84]
$E_{\Gamma K}$ [eV]	Au (amorphous)	0.68 ± NA [184]
	hBN	0.62 ± 0.01 [121]
	Saphire	0.8 ± 0.1 [124]
	Si with native SiO_2	0.21 ± 0.01 [173]; 0.892 ± 0.02 [84]

TABLE *4.3 – Values for band structure parameters found in the literature for ML-WSe_2 as a function of substrate. We show the difference between the maximum of the valence band between K/K' and Γ $E_{\Gamma K}$, the effective masses for upper, lower spin-split bands at K/K' m_e and Γ and the spin-orbit coupling Δ_{SOC}. When the authors did not specify an error, we noted ≪ NA ≫.*

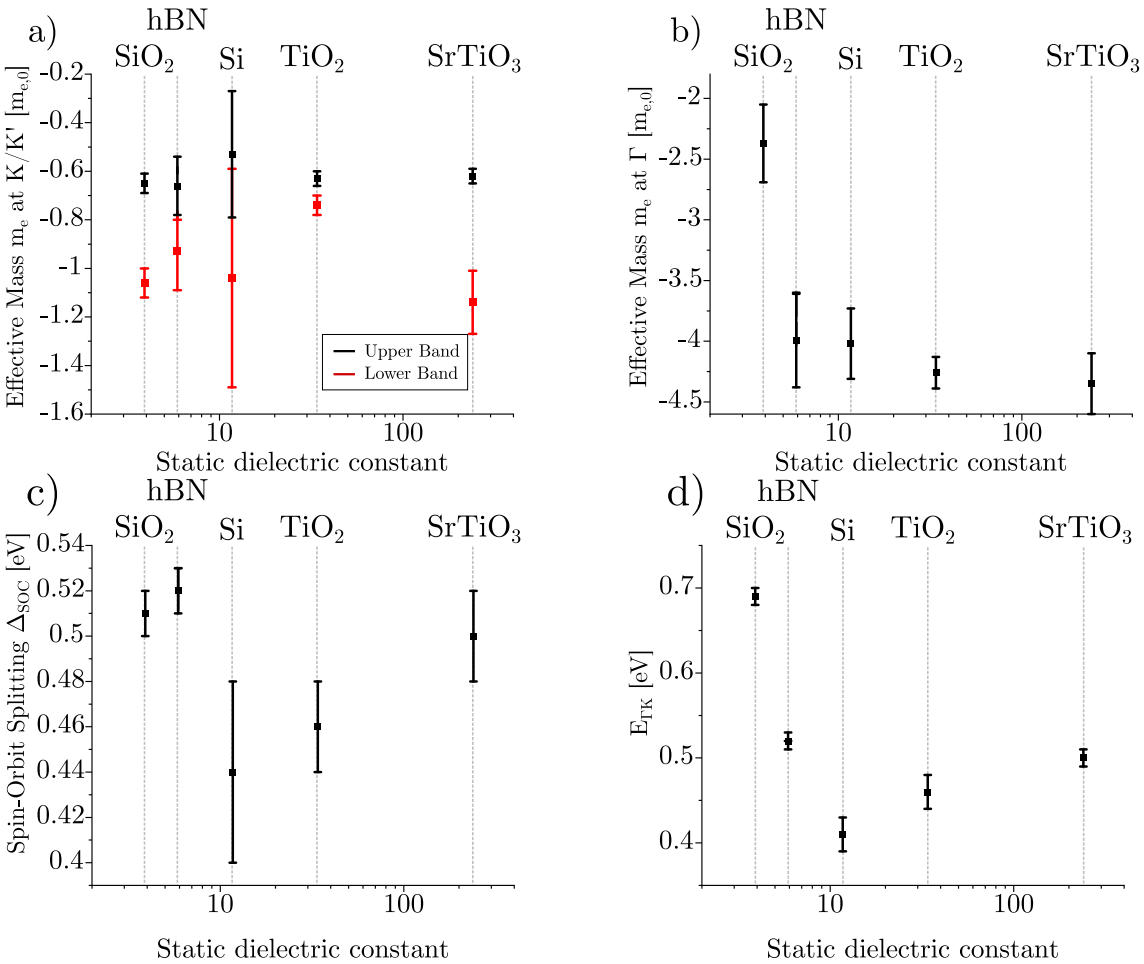

FIGURE *4.14 – Experimentally determined band structure parameters as a function of the dielectric constant of the substrate:*
a) *Effective masses m_e of the upper and lower spin-split band at K/K'*
b) *Effective mass m_e of the valence band maximum at Γ*
c) *Spin-Orbit splitting Δ_{SOC} at K/K'*
d) *Difference between maximum of the valence band at Γ and K/K' $E_{\Gamma K}$*
Here, we show the values only for the hBN sample with a twist angle of $0°$.

SrTiO3

4.4.2 The role of the orbital character in charge screening of ML-TDMCs by the substrate

The dependency of $E_{\Gamma K}$ on the static dielectric constant of the substrate ϵ is not monotonous for our measured samples (smaller $E_{\Gamma K}$ for higher ϵ) as anticipated by Zibouche et al.. Nonetheless we agree with the study that for larger ϵ $E_{\Gamma K}$ seems to be smaller by a few tens of meV. However, this result is in stark contrast to the theoretical work of Steinke et al. [151] and the preceding experimental ARPES study of Waldecker, Steinke et al. [164]. To resolve these discrepancies, we discuss the model assumptions made by Waldecker, Steinke et al. in [164] in the following paragraphs.

Generally, the presence of a charge in the ML-TMDC will be screened by image charges in the substrate. When the local charge distribution in the ML-TMDC is far away from the substrate, the interaction between the charge in the monolayer and the image charge can be modelled by a monopoles. According to Waldecker, Steinke et al., this model is justified when the thickness h of the monolayer is much greater than the spatial extent of the considered electron orbital, d, such that $h \gg d$. We illustrate this case in panel a) of figure 4.15. For a ML-WS_2 Waldecker, Steinke et al. assumed $h = 6.2$ Å [164]. However, h was not compared to an orbital extent d.

The height of a ML-WSe_2 has been measured and predicted to be 6.4 Å [90, 167]. As a first-order approximation, the spatial extent of the electron orbitals d can be assumed to be $d = 2r = 2\sqrt{\langle\psi|\hat{r}^2|\psi\rangle}$. Here, $|\psi\rangle$ is the considered electron orbital and the operator $\hat{r}$ returns the radial component of the position. At Γ the participating orbitals of the valence band maximum are We $5d_{z^2}$ and Se $4p_z$. These orbitals have a strong out-of-plane character [24]. At K/K', on the other hand, the participating orbitals are We $5d_{xy}$, $5d_{x^2-y^2}$ and $4p_{xy}$ with a strong in-plane-character [24, 78]. Waber and Cromer [163] have calculated the maximum $\sqrt{\langle\psi|\hat{r}^2|\psi\rangle}$ for different elemental electron orbitals $|\phi\rangle$. For the orbitals participating in the valence band, namely We 5d and Se 4 p orbitals, they find an $r \approx 0.7$ Å and $r \approx 0.9$ Å respectively. This means that $d = 2r \geq 1.4$ Å is of at least 20 % of h. In that case d becomes comparable to h, as shown in right panel of a) of figure 4.15.

A more rigorous consideration can be made when looking at the charge distribution in a ML-TMDC: Panel a) of figure 4.16 shows the $|\Psi(\mathbf{r})|^2$ of the electron wave function Ψ in ML-MoS_2 as calculated by Naik and Jain [117]. The authors have projected the wave function Ψ on the participating electron orbitals at the valence band maximum of K/K' (left) and Γ (right). We assume the distribution to be similar to the one of ML-WSe_2. The probability was integrated out along the [010] lattice vector direction. z is the out-of-plane direction and x the [100] direction. It is evident from this calculation that the charge distribution has multipole-character and different directional character for Γ and K/K'.

Panel b) of Figure 4.16 shows the the same data as a)[3] but after a second integration along [100] (the x-axis). In the style of [163] one can define a spatial extension d similarly to the mean orbital radius r of [163]

$$d/2 = r = \sqrt{\frac{1}{\int_0^\infty |\phi^2|(z)} \times \int_0^\infty z^2|\phi(z)^2|} \tag{4.10}$$

We thus find that $d_\Gamma = 2.97$Å and $d_{K/K'} = 1.75$Å. The spatial extent d of the electron charge distribution at Γ and K/K' is thus comparable to the height of the monolayer

3. Naik and Jain have amicably shared their data with us in a private communication.

$h = 6.4$ Å [90, 167]. Because of the different directional character and the large spatial extent in comparison to the monolayer height, one thus expects a different effect of charge screening for electrons from Γ and K/K'. We thus expect the assumptions made based on $h \gg d$ to be considerably weakened and the effect of dielectric screening should become k-dependent in the Brillouin zone, as seen by our results.

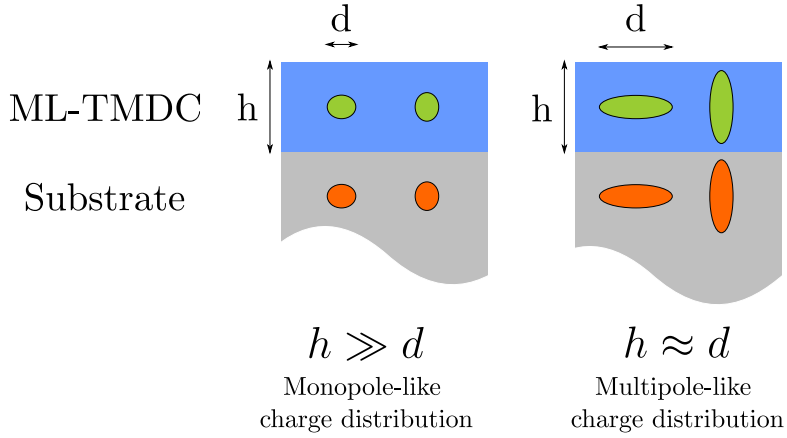

FIGURE *4.15 – Two cases for the effect of dielectric screening of local charges in a ML-TMDC according to* WALDECKER, STEINKE ET AL.*[164]. Left: the spatial extent d of the considered charge distribution is much smaller than the height of the monolayer and thus the distance to the image charges h ≫ d (left). This means that the local charge in the monolayer and the image charge can be modelled as monopoles. Right: the spatial extent becomes comparable to the height of the ML-TMDC h ≈ d such that the charge must be modelled as a multipole with distinct orbital character.*

4.4.3 Supplementary effects aside charge screening and conclusion

From the work of ZIBOUCHE ET AL. we expect a monotonous decrease of $E_{\Gamma K}$ with increasing ϵ of the substrate. We find an opposite trend for $\epsilon > 11.9$ for ML-WSe_2 on Si. Here, we discuss the reasons the trend of decreasing $E_{\Gamma K}$ is not continued for $\epsilon > 11.9$. The main difficulty lies in determining the correct ϵ of the substrate. For Si we have used the macroscopic dielectric constant $\epsilon \approx 11.7$ [35]. But according to the manufacturer, our Si substrate is terminated by a 1 nm thick native oxide layer such that the local dielectric environment may be different from pure Si. In the literature, strongly varying values (0.21 ± 0.01 or 0.892 ± 0.02 eV) for $E_{\Gamma K}$ on SiO_2-terminated Si have been found [84, 173].

$E_{\Gamma K}$ is lower for TiO_2 than for $SrTiO_3$. According to ZIBOUCHE ET AL., one would expect $E_{\Gamma K}$ to be lower for ML-WSe_2 on $SrTiO_3$, where $\epsilon = 240$. One the one hand, this discrepancy could be due to different mean distances between the ML-WSe_2 and the substrate, for instance because of non-negligible surface roughness. On the other hand, we have used buffered hydrofluoric acid to treat our $SrTiO_3$ surface. This acid tends to create TiO_2-terminated sites [68] such that the local dielectric constant underneath the ML-TDMC may be different from the macroscopic one.

Aside from the here analysed dielectric screening, two other effects can potentially modify the band structure: significant charge transfer [17, 181, 184] to the ML-WSe_2 and biaxial strain [5, 118]. In the following sections we thus analyse the contribution of these two effects on our ML-TMDC.

In conclusion we report that the band structure of ML-WSe_2 changes as a function of

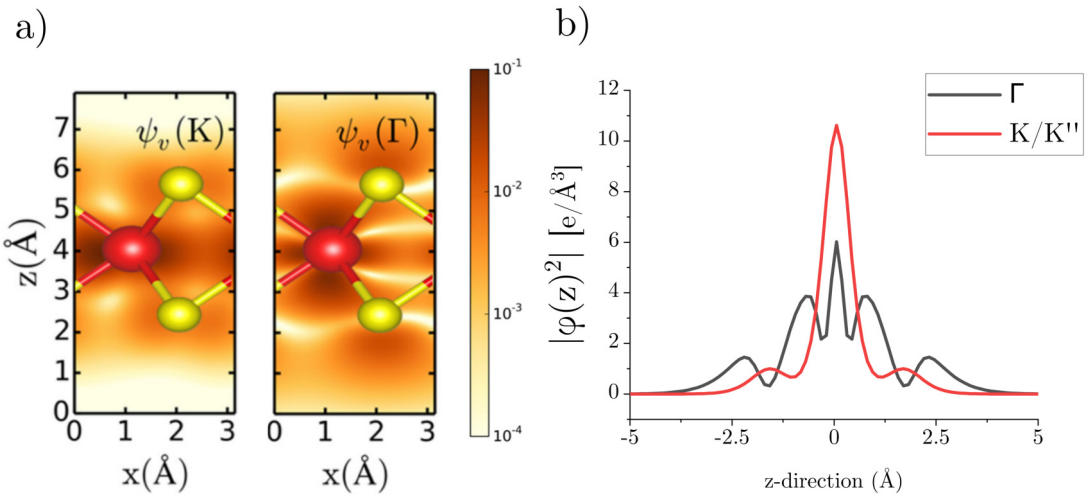

FIGURE *4.16* – ***a)*** *Modulus Square of the wave function in ML-MoS_2 in e/Å^2 as calculated by [117] for electrons stemming from the VBM at Γ and K. In relation to the total height of the monolayer the charge distribution is strongly delocalized. It has very different direction character (in-plane/out-of-plane) for Γ and K respectively.* ***b)*** *Same as a) but integrated along x. One notices that for electrons at K/K', the charge density is strongly localized in plane, whereas for Γ the charge density is localized out-of-plane. We quantify this difference in the main text.*

the dielectric substrate. We find a non-trivial dependency of $E_{\Gamma K}$ with increasing static dielectric constant ϵ of the substrate. This modification of the valence band shape could possibly stem from dielectric screening of the electron charges by the substrate. Because of the spatial extent of the involved electron orbitals such screening becomes orbital-dependent. Because of different orbital characters at Γ and K/K', the modification of the energy of the valence band maximum becomes in turn **k**-dependent. This would explain our change in $E_{\Gamma K}$ as a function of the static dielectric constant of the substrate. $E_{\Gamma K}$ decreases over up to 280 meV from SiO_2 to Si. Changes in the effective mass of the upper band at K/K' $m_{e,0}$ are too small to be resolved with our measurement.

4.5 Analysis of substrate-induced strain in ML-WSe_2 by Raman spectroscopy

From the kPEEM data analysed in the previous section we have seen that the band structure changes as a function of the chosen substrate. In particular, the value $E_{\Gamma K}$ is affected by up to hundreds of meV by the choice of substrate. One possible mechanism which could cause such a modification of the band structure, is biaxial strain. The VBM at Γ and K shift as a function of applied strain. Theoretical studies by multiple authors [5, 116, 118] show that strong biaxial tensile(compressive) strain can increase(decrease) the height of the VBM at Γ in respect to K and thus change the value $E_{\Gamma K}$ on the order of hundreds of meV.

Theoretically it would be possible to measure biaxial strain from our kPEEM data. We could measure the distances in reciprocal space between easily identifiable points, e. g. $\overline{\Gamma K}$, and convert them into values of the lattice parameter (cf. equation (4.1)). However, comparing the angular resolution Δk of our kPEEM setup to this distance $\Delta k/\overline{\Gamma K} = 0.05\mathring{A}^{-1}/1.27\mathring{A}^{-1} \approx 3.9\%$, we find that the changes in reciprocal distance necessary to explain the strain ($\approx 1\%$) are below our resolution.

Another way to detect biaxial strain in ML of TMDCs is through Raman spectroscopy. In the following, we will briefly present the principles of Raman spectroscopy. We then present the setup to measure small strains on ML-WSe_2 and interpret our results.

4.5.1 A short introduction on Raman spectroscopy

We have based the explanations in this paragraph on [120] unless otherwise cited. Raman spectroscopy is a non-destructive spectroscopic techniques which probes the vibrational states of crystal lattices or molecules. In this technique, monochromatic laser light is shone onto a crystal. The incoming photons from the laser source can scatter elastically at the crystal lattice which is called Rayleigh scattering. It can also scatter inelastically, thereby exciting or relaxing vibrational states of the system. The latter process is called Raman scattering. The vibrational states excited during Raman scattering are called **phonons**. During Raman scattering a phonon of energy $h\Delta\nu$ is either created or annihilated in the crystal. In FIGURE 4.17 we show a schematic Raman spectrum. The origin is placed at the energy of the laser light $h\nu$. Photons that scatter inelastically then either lose or gain $h\Delta\nu$ during creation/annihilation of phonon of energy $h\Delta\nu$. The Raman scattering yields two peaks on either side of the main peak at the origin: the stokes peak at $-h\Delta\nu$ for creation of a phonon and the anti-stokes peak at $\Delta\nu$ for the annihilation of a phonon [60, 120].

Because the energy of certain phonon modes is sensitive to the crystal structure, one can quantify uniaxial or biaxial strain in two-dimensional materials by comparing the energies $h\Delta\nu$ of the phonons [127].

4.5.2 Linearly polarized Raman to measure biaxial strain in ML-WSe_2

Raman A/E-Modes dependance on biaxial strain in ML-WSe_2

In ML-WSe_2 the two Raman modes sensitive to biaxial strain are the A- and E-mode which can be found at approximately $\nu = 252\ cm^{-1}$[142, 153]. To our knowledge, the influence of biaxial strain on the A or E-Mode in ML-WSe_2 has not been quantified yet [127]. An estimation of the Raman mode shift per % of biaxial strain can be found elsewhere: According to SAHIN ET AL. [142] biaxial strain on the order of 1 % changes the position of these two modes by $> 1\ cm^{-1}$.

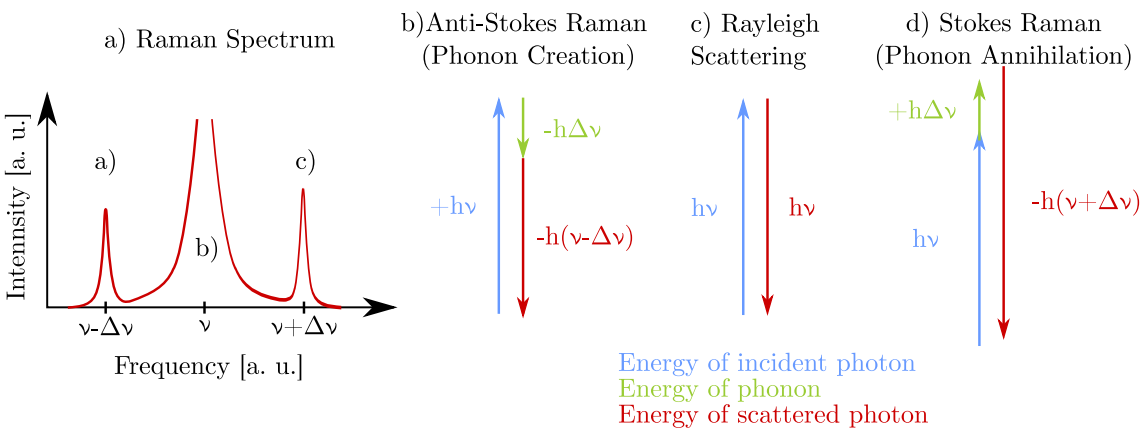

FIGURE *4.17* – *Incident photons of energy $h\Delta\nu$ (blue) scatter with the crystal. The result on the spectrum (left) is a peak at $\nu - \Delta\nu$ where* ***a)*** *a phonon of energy $h\Delta\nu$ is created (Anti-Stokes scattering),* ***b)*** *a peak at ν if the photon scatters elastically (Rayleigh scattering) or* ***c)*** *a peak at $\nu + \Delta\nu$ if a phonon of energy $h\Delta\nu$ is annihilated.*

However, a specific challenge arises: A- and E-Mode in ML-WSe_2 at approximately 252 cm^{-1} are degenerate and are expected to remain degenerate even for strong biaxial strains [142]. The experimental spectral resolution of our setup is 0.5 cm^{-1} and the expected FWHM of the A and E-mode of ML-WSe_2 is at 4-5 cm^{-1} [30]. Using unpolarized optical excitation, we will thus not be able to distinguish a Raman shift of the A or E-Mode of few cm^{-1}.

However, by using linearly polarized light in a special geometrical configuration, which we explain below, the signature of the E-mode is strongly suppressed [30]. This configuration then allows to measure the A-mode only and avoid possible ambiguities caused by the presence of both A and E-Mode in the signal. We have based the explanations in this paragraph on [132] unless otherwise cited. Panel a) of FIGURE 4.18 gives an account of the geometry of our Raman setup, denoted as $Z(YY)\overline{Z}$-orientation. The real-space directions X and Y correspond to the crystallographic axes of index (100) and (010) respectively. The Z-direction has the index (001). In $Z(YY)\overline{Z}$-configuration, the optical excitation is emitted (Z) and collected ($\overline{Z}$) normal to the plane. The incident light is polarised linearly parallel to the (010)-direction, the scattered light is analysed again parallel to the (010)-direction (YY).

The difficulty then lies in aligning polarizer and analyzer such that they coincide with the (010)-axes of the crystal. In a linearly polarized study from DADGAR ET AL. [30] the crystallographic axes can be related to the orientation of the sample flake because of the triangular shape of the CVD-grown TMDC-monolayer. In our study, we have used the previously measured kPEEM band structure data to identify the crystallographic axis. The y-axis chosen by DADGAR ET AL. is parallel to the $\overline{\Gamma K}$ direction in reciprocal space if Γ is centered at the $(x = 0, y = 0)$ origin in real space. We have thus oriented our samples such that the plane of linear polarization is parallel to the $\overline{\Gamma K}$ in reciprocal space. This corresponds to the $Z(YY)\overline{Z}$-direction as suggested by DADGAR ET AL.. This is illustrated in panel b) of FIGURE 4.18.

Linearly polarized Raman experimental parameters

In short we carried out linearly polarized Raman spectroscopy on ML-WSe_2 samples on hBN of thickness 10 nm and 6 nm, on Si and on TiO_2. We used the RAMAN Witec Alpha

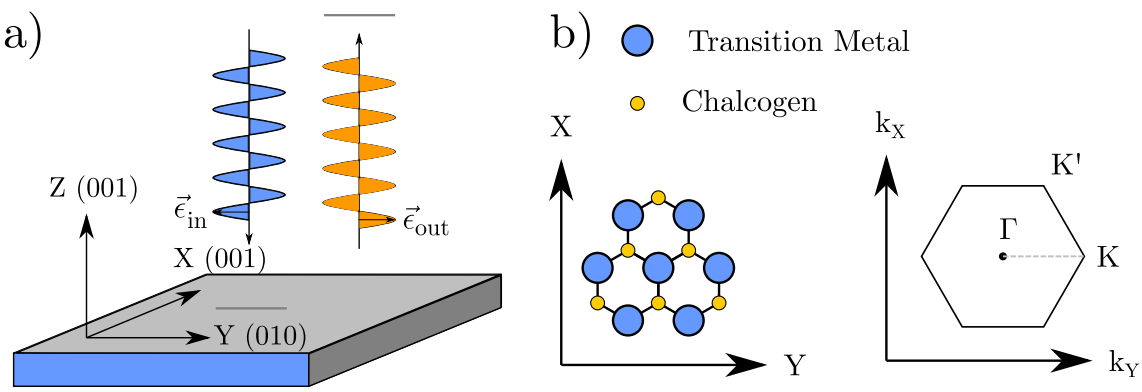

FIGURE *4.18* – ***a)*** *$Z(YY)\overline{Z}$-orientation of the linear plane of polarization according to* DADGAR ET AL. *[30]. We show a schematic of the crystallographic axes and the incident/outbound photon with linear polarization parallel to Y (010).*
b) *Left we show the real space crystal structure of a ML-TMDC from top with transition metal and chalcogen atoms with the two crystallographic axes X and Y.* DADGAR ET AL.*[30] have oriented the plane of linearly polarized incident light such that it is parallel to the real space Y-axis as shown left. Right we show the shape of the Brillouin Zone of ML-TDMC with the points of high symmetry Γ and K/K'. One can see that $\overline{\Gamma K}$ is parallel to the Y-axis on the left. We can thus deduce the correct plane of polarization using the knowledge about the $\overline{\Gamma K}$ from previously taken kPEEM data.*

500 set-up at the Institut Néel of the CNRS in Grenoble, France. We used a custom-built rotational sample holder to align crystallographic Y-axis and plane of polarization according to $Z(YY)\overline{Z}$-configuration used by [30]. The total laser power used in our study was $P = 0.69$ mW. The spot had a diameter of 0.5 μm. The chosen wavelength is at 532 nm ($h\nu = 2.33$ eV). In order to account for sample inhomogenities which can cause locally-dependent biaxial strain, we measured Raman spectra on 3 to 5 different points on the sample. A spectrometer grating of 1800 slits/cm with a resolution of 0.5 cm^{-1} was used. All measurements were carried out under ambient conditions (room temperature and atmospheric pressure).

In order to assign error bars to the measured Raman spectra around the A/E-mode, we use the method suggested by [119]. First we fit the silicon peak at 520.7 cm^{-1} within a range of 480 to 560 cm^{-1} using a Voigt function. We then define the normalized residual at a frequency ν

$$\delta I(\nu) = 100 \cdot \left(\frac{I_{fit}(\nu) - I_{meas}(\nu)}{I_{fit}(\nu)} \right) \tag{4.11}$$

where I_{fit} is the Voigt Fit and I_{meas} is the measured intensity. Using these normalized residuals we can calculate a standard deviation for our Raman spectrum

$$\sigma = \sqrt{\sum_{\nu}^{N} \frac{\delta I(\nu)^2}{N-1}} \tag{4.12}$$

where N the number of all measured points around the Si Peak. We then write the error of our Raman intensity as proportional to measured intensity and standard deviation.

$$\Delta I(\nu) = \sigma \cdot \frac{I_{meas}(\nu)}{100} \tag{4.13}$$

We have fitted using two Voigt functions and a constant offset: one Voigt function at 252 cm^{-1} to account for the A-mode, another one for the 2LA mode at 265 cm^{-1}[30]. We found that the spectral weight of the 2LA mode is often negligible.

4.5.3 The effect of biaxial strain on ML-WSe_2

Table 4.4 shows the mean frequency of the A-mode of our ML-WSe_2 on different spectra. We have calculated the mean over all measured spectra. The values range from 251.1 cm^{-1} for 6 nm thick hBN to 251.8 cm^{-1} for Si. These differences are below 1 cm^{-1} and thus below the expected shift of the A-mode of several cm^{-1} for 1% of biaxial strain. Figure 4.19 shows four representative spectra of a spectral range around the A-mode on the different substrates which reflect the marginal changes of the A-mode position as a function of spectrum. Further, from the kPEEM measurements we know that $E_{\Gamma K} = 0.41$ eV is lowest for Si and highest (0.53 eV) for hBN from the chosen substrates. For a low $E_{\Gamma K}$ we expect high biaxial tensile strain of at least 1%. But high biaxial tensile strain corresponds to a **decrease** of the A-mode frequency [142]. This contradicts the position of the A-modes measured in this study. We thus conclude, that the measured biaxial strain does not to have a measurable effect on the band structure of ML-WSe_2.

Substrate Area	hBN 10 nm	hBN 6 nm	Si	TiO_2
Mean Peak Frequency	251.2 ± 0.03	251.1 ± 0.07	251.8 ± 0.13	251.4 ± 0.05

Table *4.4 – Result of the linearly polarized Raman measurements: The mean peak position of the ML-WSe_2 A-mode as a function of substrate. We calculated the mean value over all measured spectra. For each substrate, between 3-5 spectra were taken to account for sample inhomogenities.*

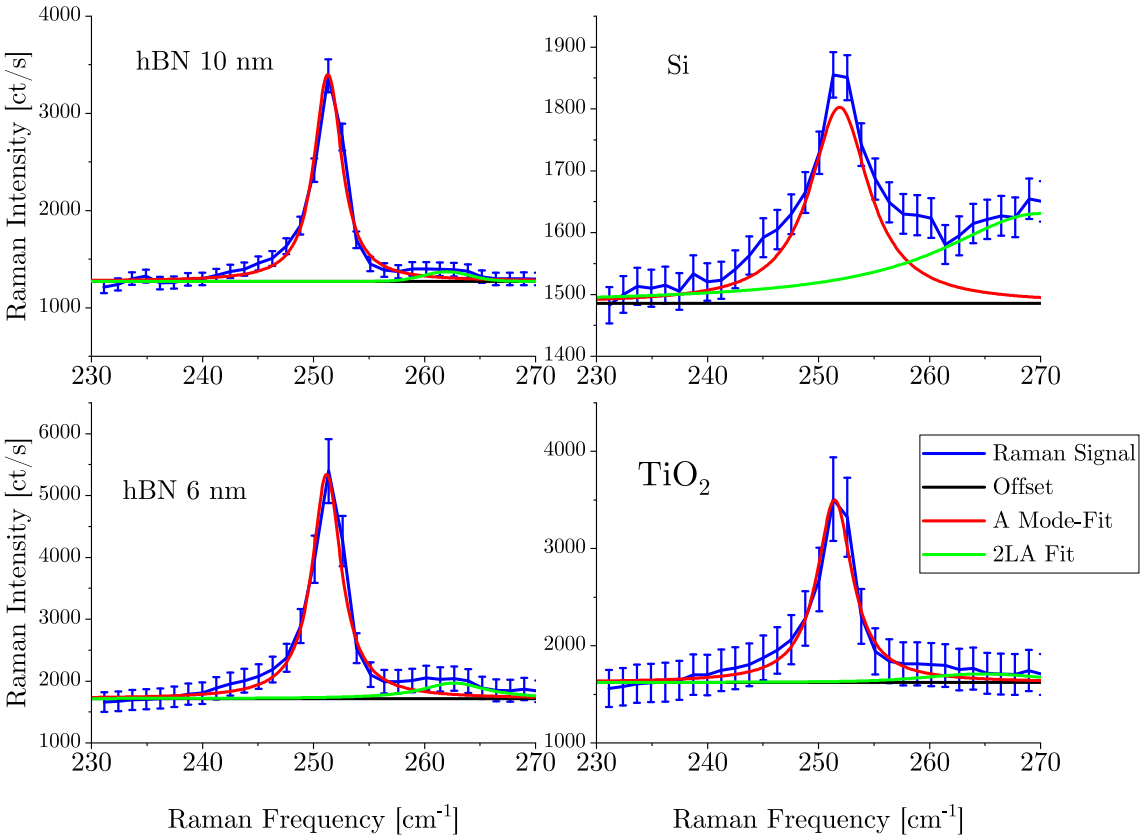

FIGURE *4.19 – Raman intensity spectra of the spectral range around the ML-WSe_2 A-mode as a function of substrate for hBN of thickness 10 nm and 6 nm, Si and amorphous TiO_2. The spectra show that the absolute frequency of the A-mode remains roughly constant over the samples.*

4.6 Work Function Determination of ML-WSe_2 on different substrates

In the previous sections, we have analysed the influence of dielectric screening and biaxial strain on the band structure of ML-WSe_2. Aside from these two effects, charge transfer is suspected to modify the band structure of ML-TMDCs [17, 181, 184]. In order to detect the presence of charges in ML-TMDCs, one can determine the Fermi level position [17, 42] or equivalently the work function $\phi = E_{vac} = -E_F$. In order to verify if charge transfer can have an measurable effect on the band structure of ML-WSe_2, we thus measured the work functions of our samples in EF-PEEM.

4.6.1 Spatially-Resolved Work Function Measurement using EF-PEEM

The measurements of the samples presented in section 4.2 have been carried out at the NanoEsca PEEM setup at the Plateforme Nanocaracterisation of the CEA-LETI in Grenoble. We used a helium discharge lamp of unpolarized light of energy $h\nu = 21.22$ eV. The images were corrected for the non-isochromaticity as described by equation (2.17). The position of the Fermi level was pre-calibrated through a gold metal surface. For the case of ML-WSe_2 on $SrTiO_3$, which is an insulating substrate, the electric connection to the sample flake was lost during the measurement. We were able to retrieve work function data, but not measure the height of the valence band maximum in respect to the Fermi level. The position of the secondary-electron cut-off function is determined by a fit with an error function as explained in section 2.2.3. The resulting work function maps $\phi(x, y)$ are displayed in FIGURE 4.20. In order to extract a value for the work function, we have calculated the mean over the marked areas for the substrate and ML-WSe_2. Mean and standard deviation then give the work function values and uncertainty.

TABLE 4.5 shows the mean work function values for ML-WSe_2 for different substrates. First, we find that the uncertainty of the work function of ML-WSe_2, given by the standard deviation, is low, in the few tens of meV and smaller than the error for the substrate's work function. This shows that local variations of the ML-WSe_2 are small compared to the work function variations of the substrate. The small spatial dependance of the work function is visible in the work function maps in FIGURE 4.20. In panel c) we show a work function map of ML-WSe_2 on hBN and Si. The local variations of the substrate's work functions are low (≈ 10 meV). On $SrTiO_3$ (panel a)) or TiO_2 (panel b)) the local work function variations are much more pronounced (≈ 20 meV). Nonetheless, the work function variation on the monolayer flake retains its homogenity (≈ 10 meV).

	WSe_2 Mean ϕ [eV]	Substrate Mean ϕ [eV]	VBM at K ($E - E_F$) [eV]
Si	5.08 ± 0.01	5.27 ± 0.02	1.14 ± 0.01
hBN	4.74 ± 0.01	4.66 ± 0.01	1.13 ± 0.02
TiO_2	4.64 ± 0.02	4.75 ± 0.04	1.18 ± 0.01
$SrTiO_3$	4.97 ± 0.02	4.78 ± 0.04	
Ni [13]	$4.12 \pm NA$	$4.18 \pm NA$	

TABLE *4.5 – Measured mean work function of ML-WSe_2, mean work function of the substrate and measured valence band maximum at K/K' ($E - E_F$). For $SrTiO_3$ the VBM at K was not measured due to missing electrical contact. We have added a literature value for Nickel [13] measured by Kelvin Probe Force Gradient Microscopy .*

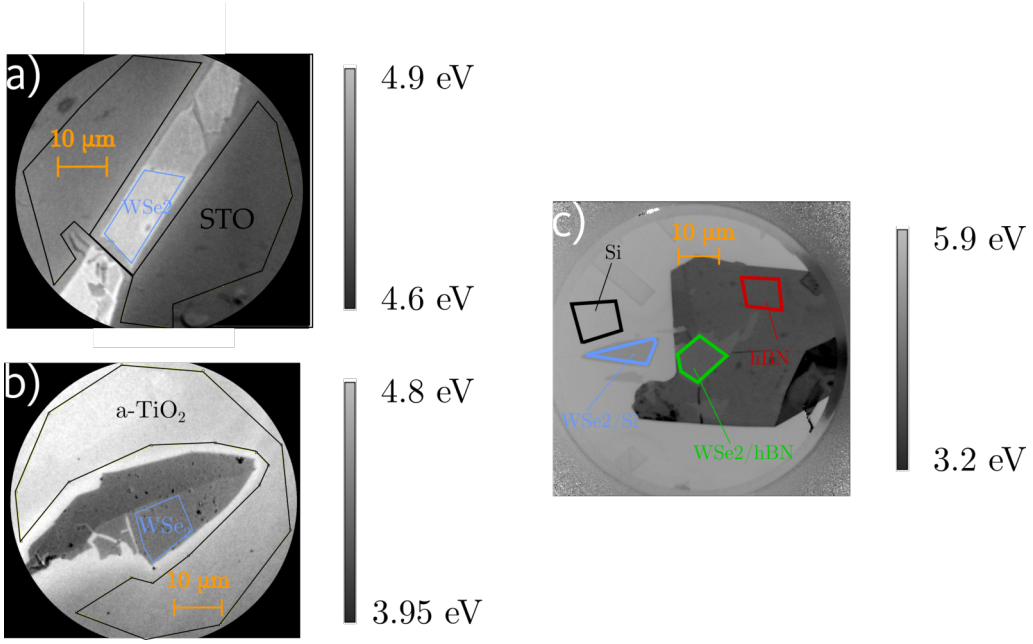

FIGURE *4.20 – Work function maps of WSe_2-flakes on **a)** $SrTiO_3$, **b)** amorphous TiO_2 and **c)** Si and hBN. In order to determine the work function values of substrate and monolayer, we take the mean and standard deviation of the local work function over the shown areas. While the local variation of the substrate's work function is important and up to 100 meV, the local variation over the area of one monolayer is rather small, in the tens of meV.*

4.6.2 Magnitude of charge transfer from substrate to ML-WSe_2 and implications for the band structure

We now turn to the question of charge transfer from these work function values. In ML-TMDCs the Fermi level enters the valence band(conduction band) for charge transfers on the order of 10^{13} to 10^{14} e/cm^2 [17]. From the literature, it is not exactly clear if charge transfer can modify the valence band structure at these doping levels. ARPES studies on K-doped ML-TMDCs find changes in the valence band structure [181, 184] in the tens of meV. NGUYEN ET AL. have measured the modification of the valence band structure at 10^{14} e/cm^2 and find no changes in the shape of the valence band [121].

In the literature, the work function for ML-WSe_2 has been calculated to be in the range from 4.2 to 4.6 eV [14, 49, 71] for the charge-neutral state. Our values are higher than theoretically predicted for ML-WSe_2: on hBN, TiO_2 and $SrTiO_3$ the work function ranges from 4.74 ± 0.01 eV to 4.97 ± 0.02 eV. This is likely due to the influence of the substrate: at the interface of two semi-conductors, one would expect vacuum levels and Fermi levels to align. Because of the high substrates' work functions we thus expect higher ML-WSe_2 work functions. To illustrate this correlation between the substrate's and the monolayer ϕ we have traced the measured mean work function value of the ML-WSe_2 as a function of the substrate's mean work function in FIGURE 4.21. The red line in FIGURE 4.21 thus indicates an alignment of the substrate's and the monolayers ϕ. In the graph, we have added a work function literature value from BORODIN ET AL. for ML-WSe_2 as measured by Kelvin probe force gradient microscopy on Nickel [13]. As can be seen from the red line, the monolayers work function align with the substrate's work function.

A similar alignment between the work function of the substrate and ML-MoS_2 was found by PARK ET AL.[125]. The authors measured the band structure and work function of ML-

MoS_2 on both insulating and metallic substrates. They concluded that the alignment was accompanied by charge transfer between the monolayer and the substrate. The magnitude of the charge transfer was not specified.

However, most of our substrates are dielectric with band gaps greater the band gap of ML-WSe_2 ($E_g \leq 2.6$ eV) [96, 121, 123] : $E_g = 9.1$ eV for amorphous SiO_2 [6], $E_g > 3$ eV for amorphous TiO_2 [129], $E_g \approx 5.4$ eV for hBN [12] and $E_g \approx 3.25$ eV for $SrTiO_3$. With such high band gaps, important charge transfer of the mentioned order of magnitude becomes unlikely. Si is the only substrate with a lower band gap ($E_g = 1.11$ eV [175]). However, as can be seen from TABLE 4.5 the distance between Fermi level and VBM at K remains roughly equal for the different samples, particularly for Si. At the necessary doping levels, the Fermi level should enter either valence or conduction band [17]. This is a strong indication that charge transfer is below the necessary level of 10^{13} e/cm^2.

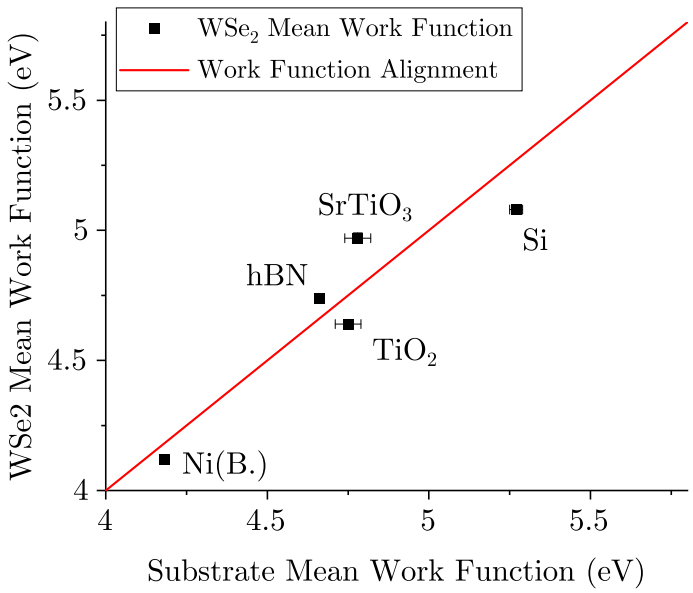

FIGURE *4.21 – Mean Work function of the ML-WSe_2 and the substrate for the measured samples. We have added a literature value from [13] for a substrate of Nickel. The red line of slope one corresponds to an alignment of the two work functions.*

In short, we find that local work function variations of ML-WSe_2 are small (±10 meV) even if the local work function of the substrate varies more strongly (±20 meV). The monolayers work function aligns with the substrate's work function in agreement with recent literature results [125]. This is an indication for charge transfer between substrate and monolayer. The magnitude of the charge transfer is, however, too small to modify the band structure: The relative position of the Fermi level to the valence band maximum at K is > 1 eV and changes only by few tens of meV on the analysed substrates. This indicates that the the charge transfer from the substrate to the monolayer is below the necessary threshold of 10^{13} e/cm^2 to change the band structure. Charge transfer is thus unlikely to modify the valence band structure.

Conclusion and outlook

In this work, we have analyzed the influence of dielectric substrates on the electronic band structure of ML-WSe_2. From our results, we have seen that the choice of the dielectric substrate has a decisive influence on the band structure, and in particular, the parameter $E_{\Gamma K}$, of our ML-TMDC. We find a correlation between the static dielectric constant ϵ of the substrate and the $E_{\Gamma K}$ of the monolayer. The band structure parameter $E_{\Gamma K}$ describes the difference in energy between the valence band maxima at Γ and K/K' and thus parametrizes the direct band gap in ML-TMDCs responsible for the strong light-matter interaction. We have excluded other mechanisms such as biaxial strain and charge transfer, which could alter $E_{\Gamma K}$ and assign the changes in $E_{\Gamma K}$ to the dielectric screening of the substrate as the responsible interaction mechanism.

Nonetheless, the exact nature of the mechanism is still difficult to describe and corresponds to no available theoretical prediction. The parameter $E_{\Gamma K}$ is sensitive to the dielectric constant, unlike predicted in [151, 164]. But the correlation between the assigned static dielectric constant ϵ and the parameter $E_{\Gamma K}$ is not monotonous either [185]. This could be due the difficulty in determining our static dielectric constants of the substrates.

The general lack of literature on dielectric screening by the substrate is probably due to the difficult experimental conditions in which dielectric screening is measured. As we have pointed out in our review (cf. section 4.1), experimental ARPES studies on ML-TMDCs suffer from low signal-to-noise ratio if carried out on non-flat substrates. This is why many studies have not been able to determine a full set of band structure parameters (effective masses at K/K'Γ, spin-orbit splitting Δ_{SOC} and $E_{\Gamma K}$) on certain substrates [52, 62, 63, 67, 160]. In this work we have undergone considerable effort to enhance the signal-to-noise ratio of our EDCs in order to investigate the effect of dielectric substrates onto the band structure. This has allowed us, for the first time, to measure the full set of band structure parameters on a variety of substrates, such as TiO_2 or $SrTiO_3$. This enhancement is done *a posteriori* and the roughness of the sample remains a variable to consider.

Outlook

An *a priori* approach to increase the SNR would consist in fabricating ML-TMDCs on atomically flat substrates. Several groups have shown that it is possible to create dielectric oxides with atomically flat terraces for instance on $SrTiO_3$ [28, 47, 169]. A review on atomically flat oxide substrates has been published by Biswas et al. [11]. These dielectrics have shown extremely high static (bulk) dielectric constants ranging from $\epsilon \approx 25$ ($LaStO_3$) to $\epsilon \approx 4500$ $KTaO_3$ [11]. Whether or not the high ϵ_{bulk} translate to a strong static dielectric constant ϵ_{sur}in the vicinity of the surface, would have to be investigated.

On studies with high resolution and flat substrates the band peaks are usually clearly resolved and the fitting of photointensity peaks is unambiguous. As we have seen for our rough substrates with poor SNR, great care must be taken in the interpretation of the signal. A theoretical model for the treatment of the secondary electron scattering background for ARPES on ML-TMDCs has not yet been formulated. The different heights of the spin-split peaks, as witnessed by [2, 112] remain an open question. Further, there is a report on asymmetric photointensity peaks [18] on non-metallic substrates whose microscopic origin is not exactly clear. These questions can wait if the photoemission signal has high quality, but become relevant in case of more ambiguous signals.

The determination of the precise ϵ remains an open question when the surface properties

such as roughness and passivation layers have to be taken into account. But even without knowing the exact interaction mechanism, band structure parameters could be measured phenomenologically on a larger number of dielectric substrates.

By changing the dielectric substrate, one could then control the excitonic properties: the binding energy of the A and B exciton and thus the energy of the interacting photon. In our study, we have had a particular focus on $E_{\Gamma K}$, the parameter which describes the distance between the valence band maximum at Γ and K/K'. With its direct band gap, the monolayer is efficient at both absorbing and emitting photons at the A exciton energies. If one can induce a direct-to-indirect band gap transition on certain dielectric substrates, i. e. $E_{\Gamma K} \to 0$, the monolayer would continue to absorb photons at the exciton energy levels, but no longer able to emit them efficiently. This flexibility would allow the monolayer to be used both as an emitter and absorber, depending on the context. It would be an example of *substrate tuning* of the band structure.

5

Résumé du travail en français

5.1 Introduction aux monocouches des métaux de transition dichalcogenures

En 2010, les chercheurs André Geim et Kontantin Novoselov furent décorés pour „des expériences révolutionnaires sur le matériau bidimensionel du graphene“. L'extraction d'une monocouche de graphene débuta l'ère des matériaux dits „bidimensionels“ . Malgré leur finesse extrême, à l'échelle de quelques atomes, ces derniers font preuve de propriétés électroniques et optoélectroniques exceptionelles. Les es monocouches des métaux de transition de dichalcogénures (MC-TMD) ont fait leur apparition très vite sur le plan des matériaux bidimensionels après la découverte de graphene. Ces monocouches disposent de propriétés optoelectroniques exceptionnelles qui les rendent intéressantes d'un point de vue scientifique et industriel.

Les propriétés optoélectroniques ou excitoniques des MC-TMD sont déterminées largement par la structure de bandes. Par conséquent, la manipulation de la structure de bandes constitue un moyen de modifier les propriétés optoélectroniques. De différentes méthodes ont été proposées pour changer la structure de bandes. Dans ce travail, nous nous penchons sur une voie très peu étudiée, celle de l'influence diélectrique du substrat. Nous allons donc analyser les liens entre un substrat diélectrique et son effet sur la structure de bande.

Le résumé sur ce travail est constitué comme suit: nous allons d'abord présenter la structure cristalline et électronique des monocouches de TMD, comme anticipée en théorie et mesurée expérimentalement. Ensuite, nous établissons les liens entre la structure de bandes et les propriétés optoélectroniques de la monocouche. Notre méthode expérimentale vise à mesurer la structure de bandes. Elle est basée sur la photoémission et nous en présentons les bases théoriques, l'état de l'art expérimental ainsi que notre dispositif, le ≪ NanoEsca ≫. Nous expliquons notre manière de fabriquer des échantillons à base des monocouches de TMD. Finalement, nous présentons l'état de l'art de la recherche sur l'influence du substrat sur la structure de bandes d'une MC-TMD. Nous résumons nos méthodes et donnons une interprétations basée sur des arguments qualitatifs. Nous démontrons que l'écrantage diélectrique peut avoir un effet important sur la structure de bandes. Nous analysons d'autres influences du substrat et concluons sur nos résultats.

Structure cristalline des TMD

Les informations du paragraphe actuel sont basées sur la/les source(s) [77]. Une molécule singulière d'un TMD est composée de trois atomes selon la formule MX_2. M représente un atome de métal de transition alors que X représente un atome de chalcogène. MoS_2, $MoSe_2$, WS_2 et WSe_2 sont les exemples que l'on va étudier dans ce travail. Les molécules cristallistent dans des couches. Une couche est posée sur une autre couche et liée par des forces van-der-Waals. Dans une couche, les molécules sont liées par liaisons covalentes, relativement fortes par rapport aux forces van-der-Waals. Il est possible de surmonter la cohésion van-der-Waals et, par ainsi, retirer une monocouche du cristal TMD. Les monocouches existent sous différentes configurations cristallines dites « polymorphismes » ($1T$, $2H$, $3R$) comme présenté en sous-figure a) de la FIGURE 5.1. Ils se distinguent entre autre par la coordination de l'atome du métal de transition et leur propriétés électroniques. Pour ce travail-ci, on examinera uniquement le polymorphisme dit $1H_c$, un semi-conducteur avec un band gap direct.

Cellule d'unité et zone de Brillouin

Les informations du paragraphe actuel sont basées sur la/les source(s) [137]. Pour comprendre la structure de bandes il faut avoir connaissance de la zone de Brillouin du cristal qui est basée sur la structure cristalline. La sous-figure b) de la FIGURE 5.1 montre la cellule d'unité d'une monocouche de TMD en polymorphisme $1H_c$. L'atome du métal de transition est placé au centre, les deux atomes de chalcogénes sont déplacés par les vecteurs

$$\delta_{\pm} = d\left(0, \frac{a}{\sqrt{3}}, \pm\frac{a}{2\sqrt{3}}\right) \tag{5.1}$$

où a est le paramètre de maille dans le plan du TMD et d la distance entre l'atome de métal de transition et un des deux chalcogènes. Sous-figure b) de la FIGURE 5.1 montre la monocouche vue du haut. Sa structure et sa cellule d'unité (marquée en gris) sont hexagonales. Les vecteurs de Bravais s'expriment

$$\mathbf{R}_1 = (a, 0, 0) \tag{5.2}$$

$$\mathbf{R}_2 = \left(\frac{a}{2}, \frac{\sqrt{3}a}{2}, 0\right) \tag{5.3}$$

En utilisant la condition de reciprocité $2\pi\delta_{ij} = \mathbf{R}_i \cdot \mathbf{K}_j$ l'on peut déduire les vecteurs de base en espace réciproque

$$\mathbf{K}_1 = \frac{4\pi}{\sqrt{3}a}\left(\frac{\sqrt{3}}{2}, -\frac{1}{2}, 0\right) \tag{5.4}$$

$$\mathbf{K}_2 = \frac{4\pi}{\sqrt{3}a}(0, 1, 0) \tag{5.5}$$

En espace réciproque le caractére hexagonale du cristal s'exprime par une zone de Brillouin hexagonal montré en sous-figure d) de la FIGURE 5.1. Les points de haute symétrie sont

alors

$$\Gamma = (0, 0, 0) \tag{5.6}$$

$$K = \left(\frac{2\pi}{3a}, \frac{-2\pi}{\sqrt{3}a}, 0\right) \tag{5.7}$$

$$K' = \left(\frac{4\pi}{3a}, 0, 0\right) \tag{5.8}$$

$$M = \left(\frac{\pi}{a}, \frac{-\pi}{\sqrt{3}a}, 0\right) \tag{5.9}$$

Ces points sont invariants sous rotations de 120°.

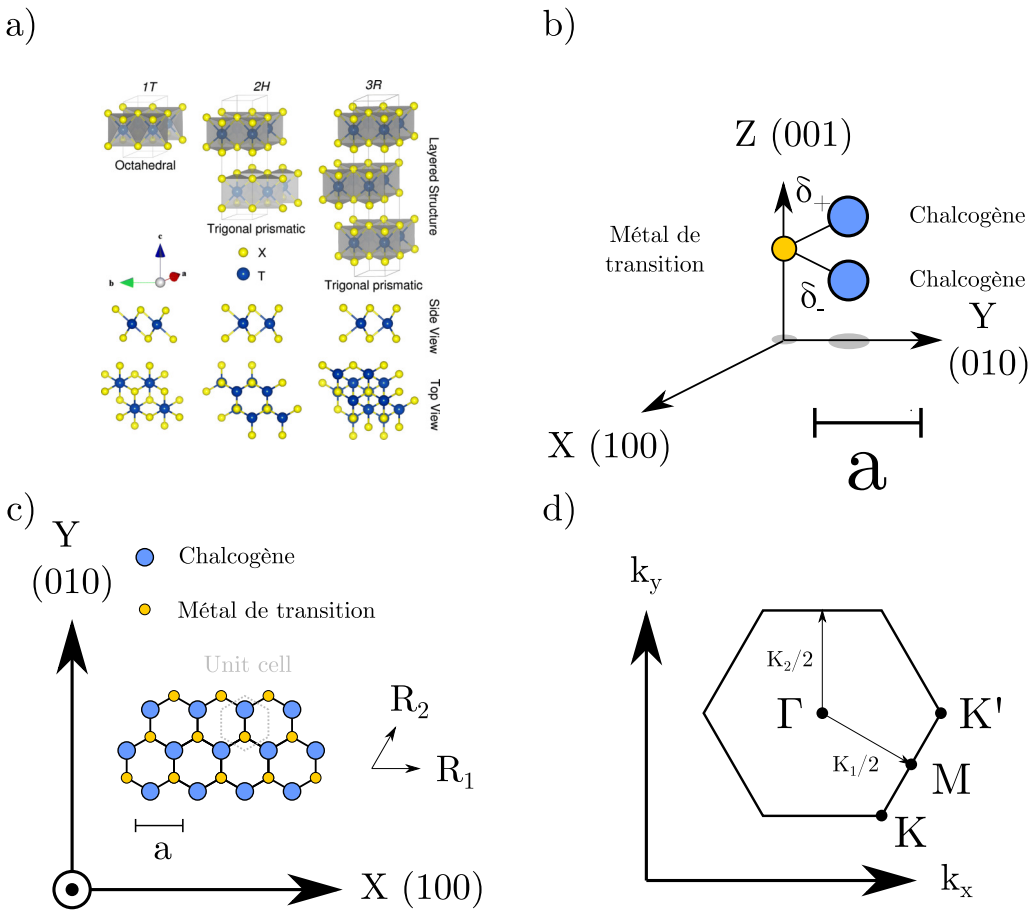

FIGURE 5.1 – ***a)*** *Configurations cristallines des TMDs en polymorphisme 1T, 2H et 3R ainsi que les coordinations de l'atome du métal de transition. Emprunté à [81]* ***b)*** *Cellule d'unité d'un TMD en polymorphisme* $1H_c$*. En bleu, les atomes de chalcogène, en jaune, l'atome de métal de transition. Le métal de transition est placé au centre, alors que les chalogènes sont déplacés par les vecteur* $\pm\delta$*, décrit dans le texte. a est le paramètre de maille dans le plan.* ***c)*** *Structure cristalline d'une monocouche de TMD dans le plan X-Y et les vecteurs de Bravais correspondants* $R_{1/2}$*, a est le paramètre de maille. En gris, la cellule d'unité vue du haut.* ***d)*** *Zone de Brillouin construite à partir des vecteurs de Bravais, les vecteurs réciproques* $\mathbf{K}_{1/2}$*, les points de haute symétrie,* Γ*, K, K' et M.*

Composition orbitale de la bande de valence

Afin de calculer la structure de bandes, il faut avoir connaissance des orbitales électroniques participants. CAPPELUTTI ET AL. [20] ont déterminé la composition orbitale de la bande

de valence de MC-MoS_2: selon les auteurs, les sept bandes de valence sont constituées majoritairement des orbitales 4d de Mo et de six orbitales 3p de S, soit 93 % du poids orbital.

Basé sur ces resultats, Silva et al. [149] ont déterminé la contribution des Mo, $4d_{z^2}$, 4_{xy} We $5d_{z^2}$, $5d_{xy}$, S $3p_{xy}$, $3p_z$ et Se $4p_{xy}$, $4p_z$ pour les 4 MC-TMD MoS_2, $MoSe_2$, WS_2 et WSe_2. La contribution des orbitales reste qualitativement et quantitativement sembable pour tous. A Γ, la bande de valence est composé majoritairement de d_{z^2} et de p_z alors que à K/K' c'est d_{xy} et p_{xy} qui participent. Pour tous les TMDs, le tableau 5.1 compile les compositions orbitales pour les TMDs selon [149].

TMDC	**Orbital**	**K/K'**	Γ	**TMDC**	**Orbital**	**K/K'**	Γ
MoS_2	d_{z^2}	0.0	0.66	**WS_2**	d_{z^2}	0.0	0.64
	d_{xy}	0.76	0.0		d_{xy}	0.74	0.0
	p_{xy}	0.20	0.0		p_{xy}	0.21	0.0
	p_z	0.0	0.28		p_z	0.0	0.28
$MoSe_2$	d_{z^2}	0.0	0.71	**WSe_2**	d_{z^2}	0.0	0.69
	d_{xy}	0.78	0.0		d_{xy}	0.73	0.0
	p_{xy}	0.18	0.0		p_{xy}	0.20	0.0
	p_z	0.0	0.23		p_z	0.0	0.23

Table 5.1 – *Composition orbitale de la bande de valence (VBM à K/K' et à Γ calculé par moyen de DFT par [149] pour une monocouche de MoS_2, $MoSe_2$, WS_2 et WSe_2. Les orbitales d apartiennent au métal de transition, les orbitales p apartiennent aux chalcogénures. Pour tous les TMDs, la bande de valence à K/K' est majoritairement composé de d_{xy} et p_{xy} alors que à Γ elle est composée de d_{z^2} et de p_z*

Comparaison entre les paramètres de la structure de bandes calculés en théorie et mesurés expérimentalement

De différentes méthodes existent afin de calculer la structure de bande d'une monocouche de TMD telles que la Théorie de la fonctionnelle de la densité (« Density Function Theory », DFT) [17, 78, 97, 149], le modèle des liaisons fortes (« tight-binding approximation ») [20, 93, 146, 177] ou encore la théorie $\hat{k} \cdot \hat{p}$ [9, 78, 79]. Dans cette section, nous nous limitons au cas de MC-MoS_2 qui est qualitativement semblable aux autres MC-TMDs. La figure 5.2 montre une structure de bande de MC-MoS_2 mesurée en ARPES et à droite une structure de bandes calculée par moyen de DFT (en gris) et tight-binding (en rouge). Ces deux structures de bandes sont qualitativements similaires à des structures de bandes pour d'autres MC-TMDs. Dans la bande de valence, on trouve un maximum global à K/K' avec une deuxième bande quelques centaines de meV en-dessous. Il s'agit de la même bande séparée par le couplage spin-orbit [96, 112]. A Γ en trouve un maximum local.

Les modèles théoriques arrivent à réproduire la structure de bandes mesurées avec une bonne fidelité. Les masses effectives de la bande supérieure et inférieure à K/K' sont anticipées à -0.54 $m_{e,0}$ [78] et -0.61 $m_{e,0}$[78], pas loin des valeurs mesurées (≈ -0.6 $m_{e,0}$ pour la bande supérieure [65, 121] et -0.84 ± 0.08 $m_{e,0}$ pour la bande inférieure [65].

A Γ, la masse effective est censé être ≈ -2.5 $m_{e,0}$, en accord avec la gamme expérimentale des valeurs allant de -1.85 ± 0.22 $m_{e,0}$ [63] à -2.7 ± 0.1 $m_{e,0}$ [111].

Le couplage spin-orbit est est estimé en théorie à 0.148 eV, confirmé en ARPES (0.145 ± 0.004 eV [111]).

La différence énergétique entre le haut de la bande de valence à Γ et K/K s'appelle $E_{\Gamma K}$. Par rapport à la valeur $E_{\Gamma K}$ il y a moins de clareté: dans la même étude de différentes valeurs (0.07 et 0.46 eV) ont été anticipées théoriquement [78]. Les valeurs en ARPES vont de 0.14 ± 0.04 eV [121] à 0.36 ± 0.06 [15].

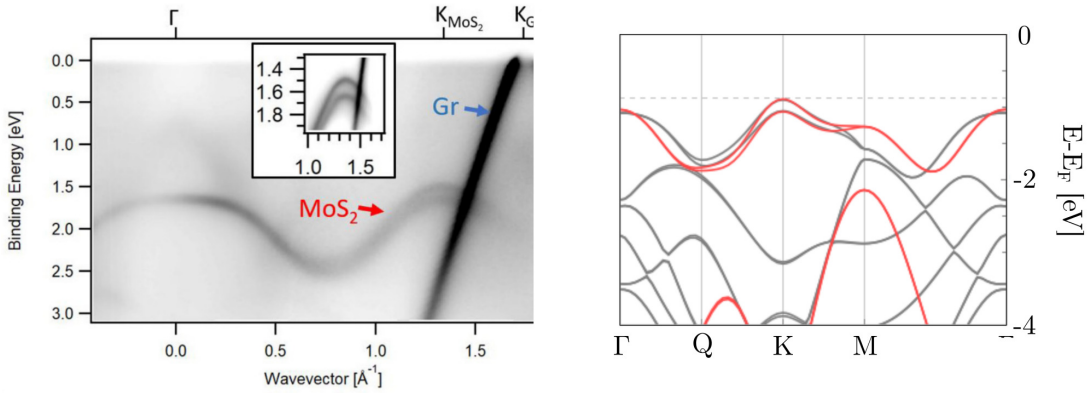

FIGURE 5.2 – *A gauche la structure de bandes de MC-MoS_2 sur graphene mesurée en ARPES par [36]. A droite deux structures de bandes de [149] calculés par moyen de DFT (en gris) et tight-binding (en rouge). Les deux structures de bandes sont qualitativement semblables, avec un maximum globale à K/K' et un maximum local à* Γ. *A K/K' on trouve aussi deux bandes séparées, lié au couplage spin-orbit.*

L'influence de la structure de bandes sur les propriétés optoélectroniques

Les informations du paragraphe actuel sont basées sur la/les source(s) [165]. Maintenant que nous avons connaissance de la structure de bandes en monocouches de TMD, il s'agit de lier cette dernière à ses propriétés optoélectroniques exceptionelles. En monocouches de TMD, les interactions lumière-matière sont dominées par la création et l'extinction d'« excitons ». En excitant un électron de la bande de valence à la bande de conduction, ce dernier peut entrer en liaison avec le trou qui demeure dans la bande de valence. La paire électron-trou couplée qui en résulte s'appelle « exciton ».

L'énergie nécessaire pour dissocier l'exciton en un électron et un trou libre s'appelle l'énergie excitonique de liaison E_B. En monocouches de TMD, les excitons disposent d'une énergie de liaison à l'échelle de plusieurs centaines de meV[165] , deux ordres de grandeur plus grands que dans les semiconducteurs de GaAs [108]. Grâce à cette augmentation importante de E_B, les excitons en monocouches sont stable même à température ambiente.

Le sous-figure a) de la FIGURE 5.3 montre des spectres de photoluminescence pour des différentes monocouches de TMD. Le fait que les excitons relaxent sous émission d'un photon est aussi grâce à leur énergie de liaison. La valeur de l'énergie de liaison s'explique par un modèle simplifié. On emprunte le modèle de l'atome hydrogène en deux dimensions qui approxime la liaison électron-trou dans une monocouche. Selon ce modèle, l'énergie de liaison s'écrit à l'aide des niveaux $n = 1$ et $n = \infty$

$$E_B = E^{n=\infty} - E^{n=1} \approx \frac{4 \cdot E_{Ryd} \cdot \mu}{m_e \cdot \epsilon_{eff}^2} \tag{5.10}$$

où E_{Ryd} est l'énergie de Rydberg, m_e la masse de l'électron immobil, ϵ_{eff} la constante de l'écrantage effectif de l'environnement et la masse réduite μ du système electron-trou dans le modèle du centre de masse. La masse réduite s'exprime à partir les masses effectives des bandes qu'occupent l'électron et le trou: $m_e \approx m_h \approx 0.5\ m_{e,0} \rightarrow \mu \approx 0.25\ m_{e,0}$. En prenant une constante $\epsilon = 5$ on obtient $E_{bin} = 500$ meV.

Une deuxième transition excitonique, denommée « exciton B », est affichée dans les spectres de réflectivité différentielle en sous-figure a) de la FIGURE 5.3. Son origine est expliquée dans la sous-figure b) de la FIGURE 5.3. L'exciton couple un électron et un trou du même spin dans la bande de conduction et la bande de valence. Le trou peut provenir de la bande supérieure à K/K' ou de la bande inférieure, séparées par le couplage spin-orbit. Cela donne lieu à deux excitons, séparées en énergie par la valeur de couplage spin-orbit.

Les informations du paragraphe actuel sont basées sur la/les source(s) [7, 21, 78, 80]. La troisième excitation excitonique, appelée « exciton C », est directement liée à la courbure de la structure de bandes proche de Γ. Elle peut, en approximation, être paramétrisée par la masse effective m_e à Γ et la différence entre le haut de la bande de valence à K/K' et à Γ $E_{\Gamma K}$. Au-delà du point K et K', il existe des domaines dans la zone de Brillouin ou la courbure de la bande de conduction et celle de la bande de valence sont quasi parallèles. Cela entraine une divergence de la densité jointe d'états, responsable pour la forte absorption au niveau de l'exciton C en sous-figure a) de la FIGURE 5.3.

Nous concluons que les paramètres de la structure de bandes, les masses effectives m_e à K/K' et Γ, le couplage spin-orbit Δ_{SOC} et $E_{\Gamma K}$ sont liés aux propriétés optoélectroniques. En modifiant ces paramètres, on peut alors modifier la physique des excitons en monocouches de TMD, un moyen intéressant de contrôler ses propriétés optoélectroniques.

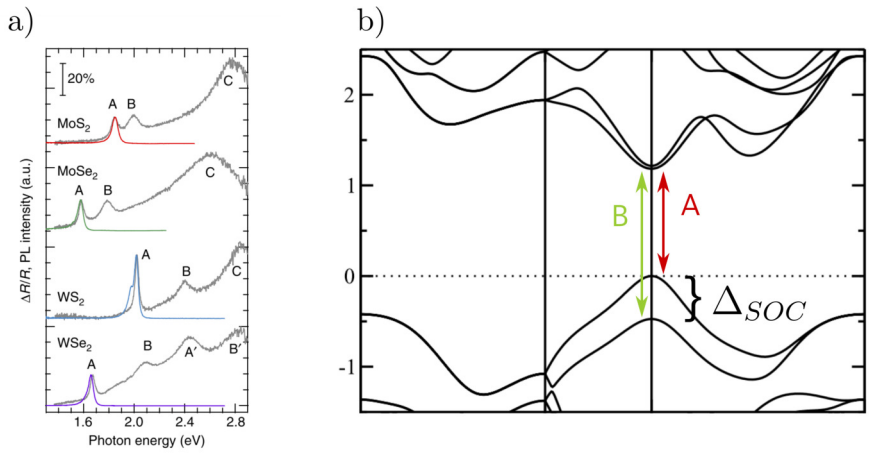

FIGURE 5.3 – *Spectre de photoluminescence (coloré) et spectres de réflectivité différentielle sur des monocouches de MoS_2, $MoSe_2$, WS_2 et WSe_2 de [80]. Les auteurs ont indiqué l'énergie de l'exciton A, B et C. Ils ont aussi marqué deux autres transitions dénommées A' et B' pour MC-WSe_2 sans préciser leurs origines.* ***b)*** *Structure de bandes de MC-WSe_2, modifiée et empruntée à [17]. Les flèches rouge et vertes indiquent les états électrons(trous) dans le bande de conduction(valence) qui participent à la formation d'un exciton. Les excitons A et B sont séparées approximativement par le couplage spin-orbit Δ_{SOC} dans la bande de valence.*

5.2 Principes de la photoémission et de l'ARPES

5.2.1 Principe de photoémission, effet photoélectrique et cinématique de la photoémission

Les informations du paragraphe actuel sont basées sur la/les source(s) [31, 55]. Notre méthode pour mesurer la structure de bandes d'une monocouche de TMD est basée sur la photoémission et l'effet photoélectrique. En 1887, HEINRICH HERTZ découvra l'effet photoélectrique qui fut expliqué par EINSTEIN. Ce dernier a obtenu le prix Nobel en 1921 pour la déscription physique de l'éffet photoélectrique. Selon la déscription d'EINSTEIN, un matériau émet des photoélectrons avec une énergie cinétique maximale de

$$E_{kin,max} = h\nu - \phi \tag{5.11}$$

sous absorption des photons. Dans cette équation h est la constante de Planck, ν la fréquence de la lumière et ϕ une constante spécifique au matériau appelé « travail de sortie ». Afin de déterminer la structure de bandes d'un cristal, il faut connaitre la liaison entre l'énergie E des bandes et le vecteur $\mathbf{k}_{in}$ à l'intérieur du cristal. Equation (5.11) donne accès à l'énergie. On trouve pour un photoélectron après sa sortie du cristal les relations suivantes entre l'énergie cinétique et $\mathbf{k}_{out}$ hors du cristal

$$E_{kin} = h\nu - \phi - E_{bin} \tag{5.12}$$

$$k_{out,\parallel} = \frac{\sqrt{2mE_{kin}}}{\hbar} \cdot \sin(\theta) \tag{5.13}$$

$$k_{out,\perp} = = \frac{\sqrt{2mE_{kin}}}{\hbar} \cdot \cos(\theta) \tag{5.14}$$

où E_{kin} l'énergie cinétique du photoélectron, ϕ le travail de sortie, θ l'angle par rapport à la normale à la surface. E_{bin} est l'énergie de liaison du photoélectron par rapport au niveau

de Fermi, m la masse d'électron au repos. La composante parallèle du $\mathbf{k}$ du photoélectron à l'intérieur reste inchangée après la traversée de la surface

$$k_{\parallel,out} = k_{\parallel,in} \tag{5.15}$$

Tel n'est pas forcément le cas pour la composante $\mathbf{k}_\perp$. Mais comme on considère que des matériaux bidimensionels il n'existe pas de dispersion hors-du-plan.

5.2.2 Principe d'ARPES

La structure de bande d'un cristal peut être déterminée en « Angle-resolved Photoemission Spectroscopy » (ARPES). En sous-figure a) et b) de la FIGURE 5.4 nous présentons le principe d'ARPES dans deux configurations. En a), des photoélectrons de différents énergies cinétiques $E_{kin,1/2/3}$ sont acceptés sous angle petit $\approx 1°$ à l'entrée de la colonne ARPES. Ils sont transférés vers l'analyseur d'électrons où un champ électrique les disperse selon l'énergie cinétique. Les photoélectrons à l'énergie cinétique calibrée passeront l'analyseur par une fente et seront détectés par un détecteur.

Un dispositif plus avancé est présenté en sous-figure b). Des photoélectrons de différentes énergies cinétiques et de différentes angles $\pm 15°$ sont acceptés. Dans l'image, on montre que des électrons de même énergie cinétique mais de différentes θ. Ensuite, dans l'analyseur, ils sont dispersés à la fois selon l'angle et l'énergie cinétique. Un écran bidimensionel et un detecteur d'image permettent d'enregistrer les deux informations E_{kin} et θ à la fois. Cette approche permet une détection plus rapide et s'appelle « ARPES conventionel ».

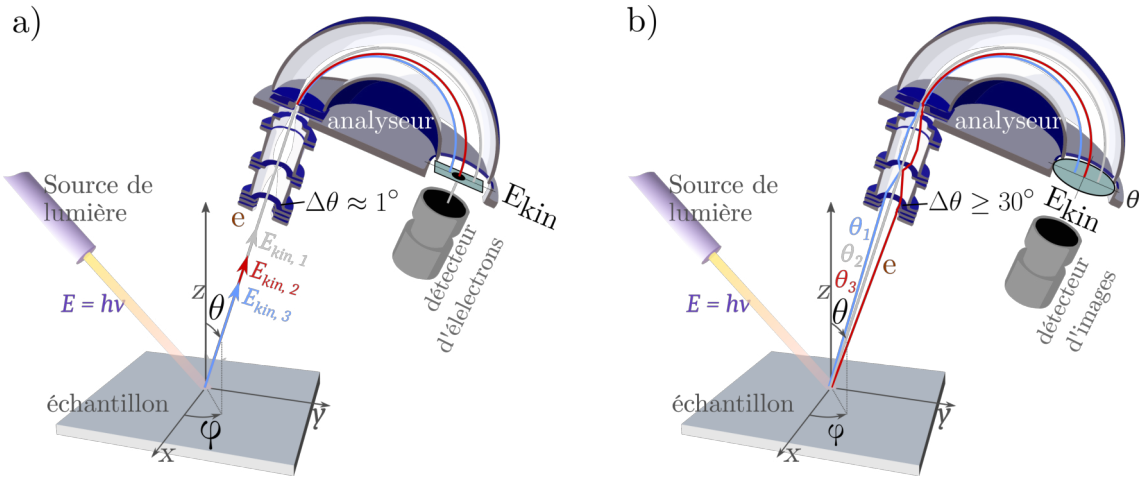

FIGURE 5.4 – *Le principe de base d'un dispositif ARPES en configuration originale* ***a)*** *et plus avancée* ***b)****. Dans les deux cas, l'échantillon est illuminé par une source de lumière avec des photons d'énergie $E = h\nu$. Le courant de photoélectron résultant est mesuré par le dispositif en fonction de l'énergie cinétique E_{kin} et des angles ϕ et θ par rapport à l'échantillon. Les photoélectrons sont dispersés par un champ électrique au sein de l'analyseur. Dans la configuration de a), l'analyseur disperse les photoélectrons uniquement selon leurs énergies cinétiques E_{kin}. Une fente à la sortie de l'analyseur permet de sélectionner les photoélectrons à 'énergie considérée. En b) les photoélectrons ne sont pas seulement dispersés en énergie E_{kin} mais aussi par rapport à l'angle θ. En b) nous ne montrons que la dispersion par rapport à θ pour plus de clareté. Un détecteur d'image bidimensionel à la sortie de l'analyseur permet de capturer les deux informations E_{kin} et θ à la fois. Cela permet un enregistrement plus rapide qu'en a). Pris et modifié de l'article Wikipedia Spectroscopie photoelectronique resolue en angle, 19/11/2021 à 17:00*

Les informations du paragraphe actuel sont basées sur la/les source(s) [99, 126, 150]. Un échantillon porteur d'une monocouche de TMD doit unir certaines conditions pour l'analyse en ARPES. La monocouche devrait mesurer plusieurs microns en taille. La surface doit être propre est libre de contaminants. Elle doit être plane, pour prévenir un signal diffus et inhomogène. Avant de passer à l'analyse en ARPES, un recuit thermique s'impose pour dégager des films d'eau et d'autres contaminants présents sur la surface. Les expériences sont conduites sous ultra-vide (10^{-10} Torr).

Les informations du paragraphe actuel sont basées sur la/les source(s) [23, 56]. Actuellement, il existe deux approches différentes en photoémission pour mesurer la structure de bandes:

— μ- or *nano-ARPES*: Les deux sont souvent effectués au synchrotron. La lumière est focalisée sur un spot de taille micrométrique, voire en dessous [54, 57, 76, 121, 168]. Une translation de l'échantillon en espace permet d'analyser une région spécifique. La résolution en $\mathbf{k}_{\|}$ atteint les $0.01\mathring{A}^{-1}$ [67, 121, 168], la résolution énergétique figure dans les dizaines de meV [54, 67, 162].

— *Photoemission Electron Microscopy (PEEM)*: Au lieu d'illuminer un spot de taille microscopique, tout l'échantillon est irradié. Une tension est appliquée entre l'échantillon et une anode appelée « extracteur ». Cette tension de plusieurs kV accélère tous les électrons vers une colonne composée de lentilles électriques et magnétiques. Les photoélectrons sont finalement être projetés sur un plan bidimensionel. L'aire d'intérêt est sélectionnée à l'aide d'un iris. La colonne de PEEM ne dispose pas de filtre en énergie, souvent un analyseur hémisphérique accomplit cette tâche. Après filtrage, les photoélectrons sont enregistrés en images isoénergétiques par un détecteur bidimensionels d'images.

  Les résolutions en énergie atteignent les 100 meV en énergie et $0.1\mathring{A}^{-1}$ en $\mathbf{k}_{\|}$. L'un des avantages du kPEEM par rapport à d'autres dispositif est sa capacité de basculer rapidement entre imagerie en espace réel et réciproque. Il est disponible au laboratoire est ainsi très accessible à l'expérimentateur, contrairement à l'ARPES au synchrotron.

Nous avons résumé les aspects techniques des deux dispositifs dans le tableau 2.1. Récemment, les deux techniques ont été surpassés par un nouveau développement au « Advanced Light Source » synchrotron à Berkeley (USA). Après une mise à jour, il est possible de détecter toute la zone de Brillouin sans bouger l'échantillon [67, 159]. Cela assure une acquisition stable et rapide (souvent pendant quelques minutes).

5.2.3 Notre dispositif expérimental: le NanoEsca I

Dans la section actuelle, nous détaillons le fonctionnement de notre dispositif ARPES, le « NanoEsca ». Il permet de mesurer la structure de bandes de nos monocouches de TMD.

Étant sortis du cristal, les photoélectrons sont accélérés vers la colonne PEEM par un champ électrique entre l'échantillon et une anode dans la colonne PEEM. Dans la colonne, ils passent à travers plusieurs lentilles électriques et magnétiques. La colonne permet ainsi de corriger des aberrations d'images, d'aggrandir l'image et de basculer d'une imagerie en espace réèlle en espace réciproque.

A la sortie de la colonne PEEM, les électrons de l'énergie cinétique considérée auront une energie cinétique $E_{kin} = E_{pass}$ avec E_{pass} « l'énergie de passage » de l'analyseur hémisphérique. Ils passent ensuite par l'analyseur hémisphérique, ou tous électrons $E_{kin} \neq E_{pass}$ seront filtrés. Nous détailons par la suite la capacité du NanoEsca de filtrer des photoélectrons en énergie.

	μ- or nanoARPES	Notre dispositif: kPEEM
Source de lumière	Synchrotron	Lampe à décharge d'hélium
Énergies accessibles	10 eV à keV [150]	21.22 eV (He I), 40.8 eV (He II)
Résolution en $k_{\parallel}$	< 0.01 à $0.03 \AA^{-1}$ [67, 121, 168]	$\approx 0.03 \AA^{-1}$
Résolution énergétique	Dizaines de meV [54, 67, 162]	200 meV
Taille minimale du cristal pour analyse de la structure de bandes	jusqu'à $< 1\ \mu m$ [54, 57, 76, 121, 168]	5 x 5 $(\mu m)^2$
Accessibilité	difficile	Disponibles en laboratoires, très accessible
Exemples d'instruments pour l'analyse des MC-TMDCs	ALS MAESTRO (USA) [67, 76, 140, 162], Diamond I05 Beamline (UK) [54, 57, 58] , SOLEIL (France) [52, 130], Elettra (Italy) [102, 121, 168]	PFNC du CEA-LETI à Grenoble [72, 135] IRAMIS/SPEC/LENSIS au CEA-Saclay NanoESCA/Nanospectroscopy beamline à Elettra (Italie) University of Linköping, Suède University of Bristol, Royaume-Uni

TABLE *5.2 – Comparaison des techniques utilisées pour l'analyse de la structure des bandes. On compare $\mu-$ ou nanoArpes au synchrotron à notre dispositif de la Plateforme Nanocaractérisation du CEA-LETI à Grenoble.*

Ajustement des potentiels électrostatiques des anodes

Les informations du paragraphe actuel sont basées sur la/les source(s) [43, 126]. Après la sortie du cristal, les photoélectrons sont porteurs d'une énergie cinétique donné par l'équation 5.11. Ils sont accélérés vers la colonne PEEM par une anode accélératrice, appelée « extracteur » du potentiel électrostatique V_{ext}. Ils obtiendront une énergie $E_{kin,col}$ après l'entrée dans la colonne.

Pour sélectionner des photoélectrons à l'énergie cinétique $E_{kin,out}$ après sortie du cristal, le potentiel V_{sample} de l'échantillon est fixé à

$$e \cdot V_{sample} = E_{kin,out} \tag{5.16}$$

Ensuite les photoélectrons sont accélérés par un champ électrique de tension $V_{ext} - V_{sample}$ vers la colonne PEEM. La nouvelle énergie cinétique du photoélectron dans la colonne s'écrit

$$E_{kin,col} = E_{kin,out} + e \cdot (V_{ext} - V_{sample}) = e \cdot V_{ext} \tag{5.17}$$

où V_{ext} et V_{sample} sont les potentiels électrostatiques de l'extracteur et de l'échantillon. Ensuite, les photoélectrons sont freinés par une anode à potentiel V_{dec} pour correspondre à l'énergie de passage

$$E_{pass} = E_{kin,col} - e \cdot V_{dec} - \phi_{hsa} = e \cdot V_{ext} - e \cdot V_{dec} - \phi_{hsa} \tag{5.18}$$

où V_{ext}, V_{dec} and ϕ_{hsa} sont les potentiels électrostatiques du décélérateur et le travail de sortie de l'analyseur hémisphérique[126]. L'analyseur hémisphérique renvoie tous les photoélectrons $E_{kin} \notin [E_{pass} - \Delta E, E_{pass} + \Delta E]$. ΔE est la résolution énergétique de l'analyseur.

Fonctionnement de l'analyseur hémisphérique

Les informations du paragraphe actuel sont basées sur la/les source(s) [113, 126]. L'analyseur hémisphérique est un dispositif pour filtrer les photoélectrons en énergie. La figure 5.5 montre une coupe à travers un analyseur hémisphérique. Les deux côtés à R_i et à R_a résident à des potentiels électrostatiques différents ce qui entraine un champ électrique à l'intérieur de l'analyseur. Les lignes grises indiquent la direction du champ électrique.

A gauche le photoélectron d'énergie cinétique E_{kin} entre par la fente d'entrée de longueur d_{entr}. Il peut être décrit par les coordonnées α_0, β_0, r_0, z_0, E_{kin}: les angles, le rayon et la

hauteur d'entrée et l'énergie cinétique du photoélectron. Les cordonnées de sortie par la fente de sortie de longueur d_{exit} s'expriment

$$r_\pi = (\frac{2}{2 - \frac{r_0}{R_0}\frac{E_{pass}}{E_{kin}} \cdot \cos^2\alpha_0} - 1) \cdot r_0 \tag{5.19}$$

$$\alpha_\pi = -\alpha_0 \tag{5.20}$$

$$z_\pi = -z_0 \tag{5.21}$$

$$\beta_\pi = -\beta_0 \tag{5.22}$$

où $E_{pass} = -U/2$ appelée l'énergie de passage avec U la tension entre les murs à R_i et R_a. On constate que l'équation 5.19 dépend de plusieurs paramètres: de l'énergie cinétique E_{kin}, de l'angle d'entrée α_0 et le rayon d'entrée r_0. Cela signifie que des photoélectrons outre ceux dont $E_{kin} = E_{pass}$ passeront l'analyseur tant que l'equation (5.19) est remplie. Les électrons qui arrivent à la fente de sortie seront dispersés le long de R selon leur énergie cinétique E_{kin}. Pourtant, ils seront également dispersés selon r_0 et α_0. Pour un photoélectron les informations de ces trois paramètres seront mélangées à la sortie de l'analyseur.

Pour résoudre ce problème, les informations spatiales sont traduites en coordonnées angulaires par une lentille de Fourier devant l'entrée de l'analyseur. Après le transfert des informations spatiales (x, y) en information angulaires (α, β) on sait depuis equation (5.20) et equation (5.22) que les angles sont conservés à part pour l'inversement de signe. Une deuxième lentille Fourier derrière la sortie de l'analyseur permet de récupérer les informations spatiales depuis les coordonnées angulaires.

On peut montrer que pour la résolution énergétique ΔE_{ana} d'un analyseur hémisphérique vaut

$$\frac{\Delta E_{ana}}{E_{pass}} = \frac{1}{2}\left(\frac{d_{entr} + d_{exit}}{2} + \alpha_{0,max}^2\right) \approx \frac{1}{2}\left(\frac{d_{entr} + d_{exit}}{2}\right) \tag{5.23}$$

5.2.4 Théorie de la photoémission

Les informations du paragraphe actuel sont basées sur la/les source(s) [31, 113]. Dans la section actuelle, nous présentons une déscription du processus quantique de la photoémission qui permet d'enregistrer la structure de bandes. En fin de la section nous allons voir comment nous en arrivons à un spectre qui affichent les énergies des bandes.

De manière rigoureuse, le méchanisme de photoémission doit être traité dans le cadre du « one-step-model » (modèle à un étape) où toutes les interactions de photoélectron avec son environnement lors de la photoémission sont pris en compte. Pourtant, le modèle à trois étapes « three-step model » s'est avéré adapté pour décrire le processus:

1. L'atome est ionisé sous absorption d'un photon. Nous traitons le procéssus de photoionisation dans le cadre du modèle électron-dipole.
2. Le photoélectron se propage vers la surface en interagissant avec le cristal. Il est susceptible de diffracter.
3. Le photoélectron traverse la surface.

Le photocourant provenant de l'échantillon est proportionel au taux de photoionisation. Celui-ci s'écrit à l'aide de la règle d'or de Fermi

$$I_0 = -e \cdot \sum_{f,i} w_{f,i} = -e \cdot \sum_{f,i} \frac{2\pi}{\hbar}\left|\langle\Psi_f^N|\hat{H}_{int}|\Psi_i^N\rangle\right|^2 \delta(E_f^N - E_i^N - h\nu) \tag{5.24}$$

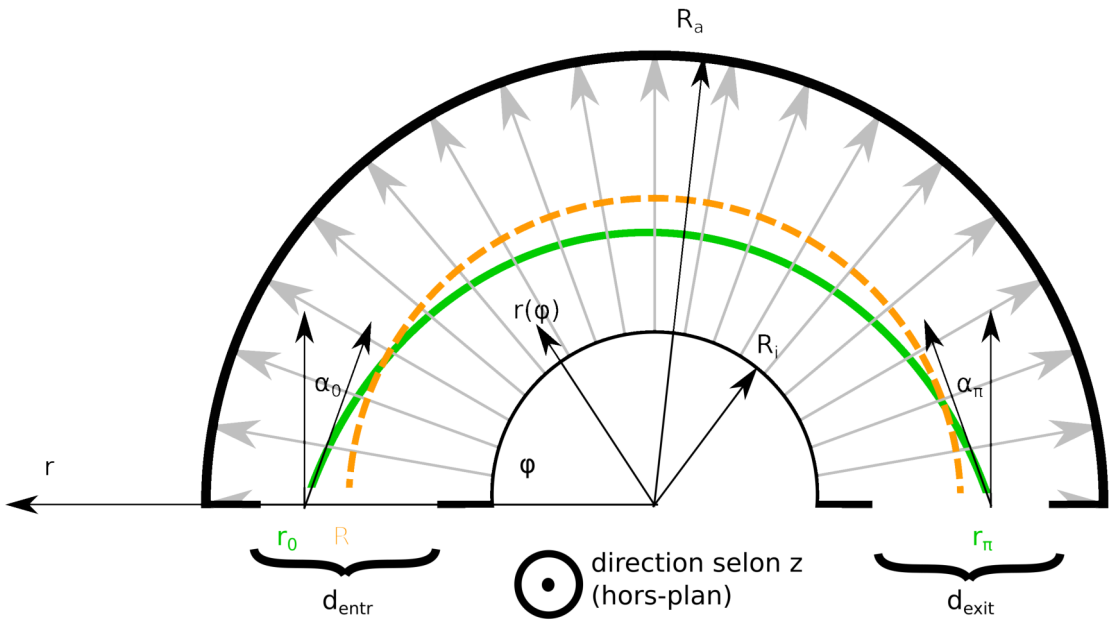

FIGURE 5.5 – *Coupe à travers l'analyseur hémisphérique selon le plan dispersif* (r, ϕ). *Les lignes grises indiquent la direction du champ électrique. Le mur extérieur à* R_a *réside à un potentiel électrostatique plus haut que celui de l'intérieur à* R_i. *L'électron entre dans la fente de longueur* d_{entr} *à* r_0 *sous l'angle d'entrée* α_0 *et suit la trajectoire schématique (non exacte). Il sort de l'analyseur à la fente de sortie avec longueur* d_{exit} *à la position* r_π *sous l'angle* α_π.

ou e la charge élémentaire, $\omega_{f,i}$ est le taux de transition de photoionisation, $E^N_{f/i}$ est l'énergie du système à l'état final/initial $\langle\Psi^N_f|\,,|\Psi^N_i\rangle$, et $h\nu$ est l'énergie du photon absorbé. Nous mettons la gauge $\Psi = 0$ à l'infini. Nous abondonnons les termes au-délà de l'approximation linéaire. Si la longueur d'onde du photon est grande devant l'échelle atomique (ce qui est le cas dans l'UV) on peut écrire l'hamiltonien d'interaction dans le cadre l'approximation électron-dipole

$$\hat{H}_{int} = \frac{e}{2mc}\Big(\mathbf{A}(\mathbf{r})\cdot\hat{p} + \hat{p}\cdot\mathbf{A}(\mathbf{r})\Big) \approx \frac{e}{mc}\mathbf{A}\cdot\hat{p} = \frac{2}{mc^2}\epsilon\cdot e^{i\mathbf{k}_{h\nu}\mathbf{r}}\hat{p} \tag{5.25}$$

où m la masse de l'électron au repos, $\hat{p}$ l'opérateur d'impulsion, c la vitesse de la lumière et $\mathbf{A}$ le potentiel vecteur du champ magnétique et ϵ le vecteur de polarisation. Pour écrire l'état initial et final pendant la photoémission, on considère que le photoélectron sera enlévé du système à N électrons en laissant derrière lui un système à (N-1) électrons. La photoionisation est suffisamment rapide pour que les interactions entre le photoélectron est le système à (N-1) sont négligables (« sudden approximation »). Les états initial et final s'écrivent alors

$$\Psi^N_{f,m} = \mathcal{A}\phi^{\mathbf{k}_f}_f(\mathbf{r})\Psi^{N-1}_{(f,m)}(\mathbf{r}) \tag{5.26}$$

$$\Psi^N_i = \mathcal{A}\phi^{\mathbf{k}_i}_i(\mathbf{r})\Psi^{N-1}_i(\mathbf{r}) \tag{5.27}$$

où $\mathcal{A}$ est un opérateur qui antisymmetrise la fonction d'onde afin de satisfaire à la condition de Pauli. $\phi^{\mathbf{k}}_{i/f}$ sont les états initial/final de l'électron. $\Psi^{N-1}_{i/(f,m)}$ sont les états initial/final du système à N électrons. Nous définissons par la suite les produits scalaires

$$M^{\mathbf{k}_i,\mathbf{k}_f}_{f,i} = \langle\phi^{\mathbf{k}_f}_f(\mathbf{r})|\hat{H}_{int}|\phi^{\mathbf{k}_i}_i(\mathbf{r})\rangle \tag{5.28}$$

$$c_{(f,m),i} = \langle\Psi^{N-1}_{f,m}(\mathbf{r})|\Psi^{N-1}_i(\mathbf{r})\rangle \tag{5.29}$$

A priori, il y a plusieurs états finaux $\Psi^{N-1}_{(f,m)}$ disponibles que nous énumérons par l'index m. Le taux total de transition est donné par la somme sur tous les m. On obtient ainsi pour le produit scalaire

$$\langle\Psi^N_f|\hat{H}_{int}|\Psi^N_i\rangle = \underbrace{\langle\phi^{\mathbf{k}_f}_f(\mathbf{r})|\hat{H}_{int}|\phi^{\mathbf{k}_i}_i(\mathbf{r})\rangle}_{M^{\mathbf{k}_i,\mathbf{k}_f}_{f,i}}\underbrace{\langle\Psi^{N-1}_{f,m}(\mathbf{r})|\Psi^{N-1}_i(\mathbf{r})\rangle}_{c_{(f,m),i}} \tag{5.30}$$

où nous avons défini les élements de matrice $M^{\mathbf{k}_i,\mathbf{k}_f}_{i,f}$ and $c_{(m,i)}$. Le premier produit scalaire décrit la photoionisation, le deuxième décrit l'overlap entre l'état initial et final du système à N électrons. Insérant l'équation 5.25 en 5.24 on obtient

$$I_0(\mathbf{k}_f,\mathbf{k}_i,E_{kin}) = -e\cdot\sum_{f,i} w_{f,i} \tag{5.31}$$

$$= -e\cdot\frac{2\pi}{\hbar}\sum_{(f,m),i}\left|M^{\mathbf{k}_i,\mathbf{k}_f}_{i,f}\right|^2\sum_m |c_{m,i}|^2\delta(E_{kin}+E^{N-1}_m-E^N_i-h\nu) \tag{5.32}$$

pour un ensemble d'états finaux $\langle\Psi^{N-1}_m|$ énuméré par l'index m. $w_{f,i}$ est le taux de transition d'une photoexcitation pour un système selon la règle d'or de Fermi pour d'un état initial (i) à un étal final (f)'. On constate que le spectre de photoémission sera peuplé de pic-delta qui représente la présence d'une bande à l'énergie du peak.

5.2.5 Influence de la géometrie expérimentale sur l'élément de matrice de photoionisation

En section 5.1 nous avons discuté la composition orbitale de là bande de valence d'un TMD. A Γ la bande de valence est majoritairement composée de d_{z^2} et p_z alors qu'à K/K' les orbitales sont $d_{x^2-y^2}, d_{xy}$ et p_x, p_y [95]. Les orbitales d_{z^2} et p_z disposent d'une directionalité hors-plan contrairement à d_{xy} et p_{xy} qui sont localisées dans le plan. L'élement de matrice de la photoionisation peut être exprimé par

$$|M_{f,i}^{k_\parallel}|^2 \propto |\langle \phi_f^{\mathbf{k}_f} | \epsilon \cdot \hat{x} | \phi_i^{\mathbf{k}_i} \rangle| \tag{5.33}$$

ou $\hat{x}$ est l'opérateur de position et ϵ le vecteur de polarisation de la lumière incidente. A un angle d'incidence normale à la surface $|M_{f,i}^{k_\parallel}|^2$ sera petit pour les orbitales hors-plan, grand pour les orbitales planaires. Cette tendance est inversée en augmentant l'angle par rapport à la normale. Pour notre expérience, avec un angle d'incidence de 65° par rapport à la normale, cela veut dire que le signal provenant des orbitales à Γ (hors-plan) sera exalté alors que le signal provenant de K/K' sera attenué.

Diffraction de photoélectrons et fond d'électrons sécondaires

Après photoionisation de l'atome, un photoélectron est susceptible d'interagir avec des atomes ou électrons jusqu'à sa sortie du cristal. Le « libre parcours moyen » λ_{IMFP} indique la distance moyenne sur laquelle l'électron est exempté d'interagir avec son environnement [56, 150]. Généralement, la quantité dépend du matériau et de l'énergie cinétique du photoélectron. Cependant, elle est la plus petite dans la gamme de 10 eV $< h\nu <$ 100 eV avec $\lambda_{IMFP} \approx 5$ Å, c'est-à-dire proche de l'épaisseur des TMD [90, 167]. A cette λ_{IMFP} on favorise le photosignal provenant de la monocouche et non du substrat, indispensable pour son analyse en ARPES.

Néanmoins, certains photoélectrons diffractent de manière inélastique pendant la photoémission. Par conséquent, ils perdent en énergie et adoptent un **k** et nombre spin **s** aléatoire. Dans le spectre de photoémission, les interactions inélastiques se manifestent par un fond de photosignal important. A notre connaissance, il n'existe pas de modèle théorique qui décrit la forme de ce fond. De nombreuses approches ont été utilisées pour enlever le fond du signal appartenant à la présence des bandes: des fonds linéaires [67, 118, 181], polynomial [32, 65, 102] et la méthode « Shirley » (expliqué en [38]) [18, 184]. Nous avons opté pour un fond polynomial qui nous décrivons en section 5.4.1.

Travail de sortie en photoémission

A part les paramètres de la structure de bandes des MC-TMDs(m_e, Δ_{SOC}, $E_{\Gamma K}$) il existe encore un autre paramètre important pour décrire l'état de la monocouche, le « travail de sortie ». La définition la plus générale du travail de sortie s'écrit

$$\phi = E_{vac} - E_F \tag{5.34}$$

où E_{vac} est le niveau du vide et E_F est l'énergie de Fermi. Dans le domaine des matériaux bidimensionels, le travail de sortie est une valeur importante: elle permet de déduire, approximativement, l'alignement des bandes dans une hétérostructures faite de plusieurs monocouches à l'aide de règle d'Anderson [26, 49, 85].

La photoémission permet de mesurer le travail de sortie. Pour sortir du cristal, les photoélectrons doivent atteindre le niveau du vide. Puisque l'énergie de la lumière incidente est finie à $h\nu$, il existe un niveau énergétique minimale d'électrons qui peuvent être arrachés au cristal.

Ce niveau s'appelle E_{SECO} « Secondary Electron Cut-Off ». Le signal disparait en-dessous de ce niveau. Il disparait également au-délà du niveau de Fermi E_F. La connaissance des deux niveaux permet de déduire le travail de sortie ϕ.

En FIGURE 5.6 on montre des spectres de photoémission après illumination de $h\nu = 21.22$ eV pour un métal et un sémiconducteur typiques. Quant au métal, le signal disparait au niveau de Fermi $= E_F$, c'est-à-dire au signal des photoélectrons avec la plus grande énergie cinétique $E_{kin,max}$. Il permet alors de calibrer E_F pour tout matériau suivant. A l'autre extremité des spectres, le signal disparait en-dessous de E_{SECO} qui correspond aux électrons d'énergie cinétique la moins importante $E_{kin,min}$.

De ces valeurs on peut déduire le travail de sortie

$$\phi = h\nu - |E_F - E_{SECO}| = h\nu - |E_{kin,max} - E_{kin,min}| \tag{5.35}$$

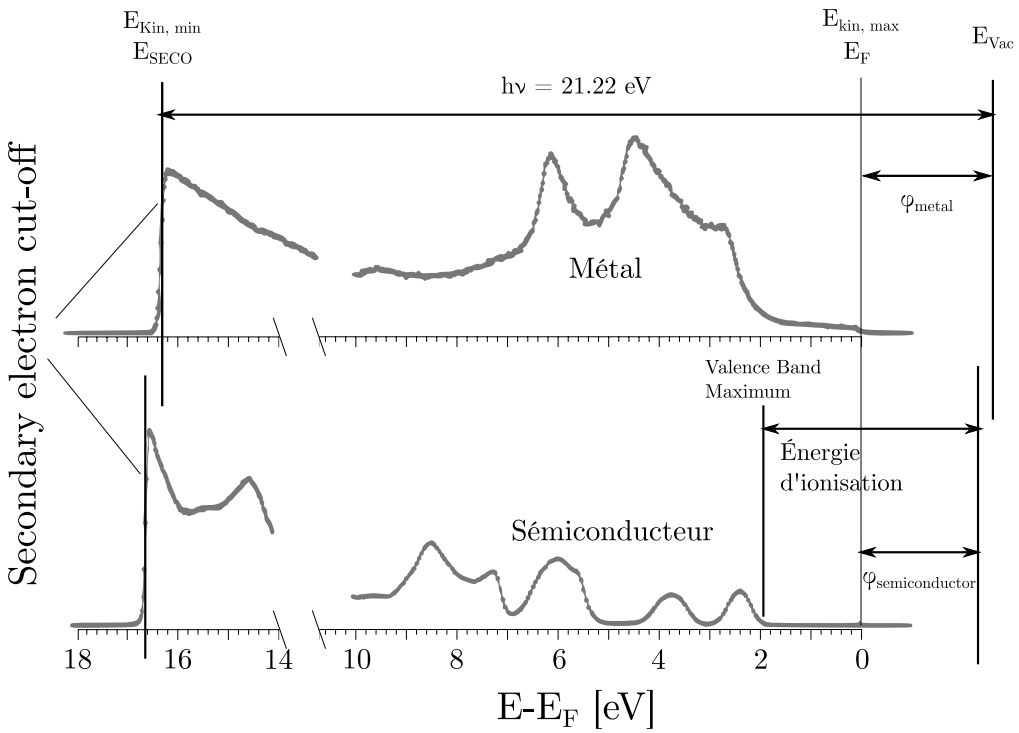

FIGURE 5.6 – *Spectre de photoémission après illumination de $h\nu = 21.22$ eV pour un métal typique et un sémiconducteur typique. Emprunté à [73]. Les auteurs n'ont pas précisé les matériaux examinés. Quant au métal, l'énergie cinétique maximale $E_{kin,max}$ avec un signal fini provient des photoélectrons au niveau de Fermi E_F. La chute en photointensité à $E_{kin,max}$ permet de calibrer le niveau de Fermi pour des semiconducteurs. L'énergie cinétique la plus basse $E_{kin,min}$ correspond à la chute du signal des électrons sécondaires à E_{SECO}. La connaissance des énergies cinétiques permet de déduire le travail de sortie ϕ.*

5.3 Fabrication d'échantillons de monocouches de TMD pour mesure en kPEEM

Le but de notre étude est d'analyser des monocouches de TMD mesurés sur différents substrats. Pour cela, il existe plusieurs techniques telles que le dépôt chimique en phase vapeur [2, 102] et l'épitaxie à jet moléculaire [102, 181]. Les deux permettent de créer des monocouches de taille assez grande (dans les dizaines de μm) pour une analyse en ARPES [36, 65, 111, 118, 131, 160, 181]. Par contre, le choix de substrats est généralement restreints à graphene [2, 36, 66, 111, 118, 181], Au(111) [15, 53, 102] ou SiO_2 [65]. Un technique plus flexible est l'exfoliation mécanique en combinaison avec la technique du stamping.

Tout d'abord, les substrats sont dôtés de flèches indicatrices par lithographie de laser est évaporation métalique. Ces flèches servent d'orientation dans l'expérience PEEM. Dans la FIGURE 5.7 nous présentons les étapes d'exfoliation et de stamping pour déposer une MC-TMD sur le substrat visé.

1. Le cristal est placé sur un film de scotch.
2. Le cristal est couvert de scotch des deux côtés et le film est rétiré.
3. Un certain nombre de monocouches et de multicouches sont produits ainsi.
4. Les flocons de TMD sont posés sur une lame de verre couverte de polydiméthylsiloxane (PDMS [89]) et doivent être localisés sous microscope optique.
5. et 6. Une plateforme controllable en trois dimensions est employée pour déposer la monocouche sur le substrat visé.

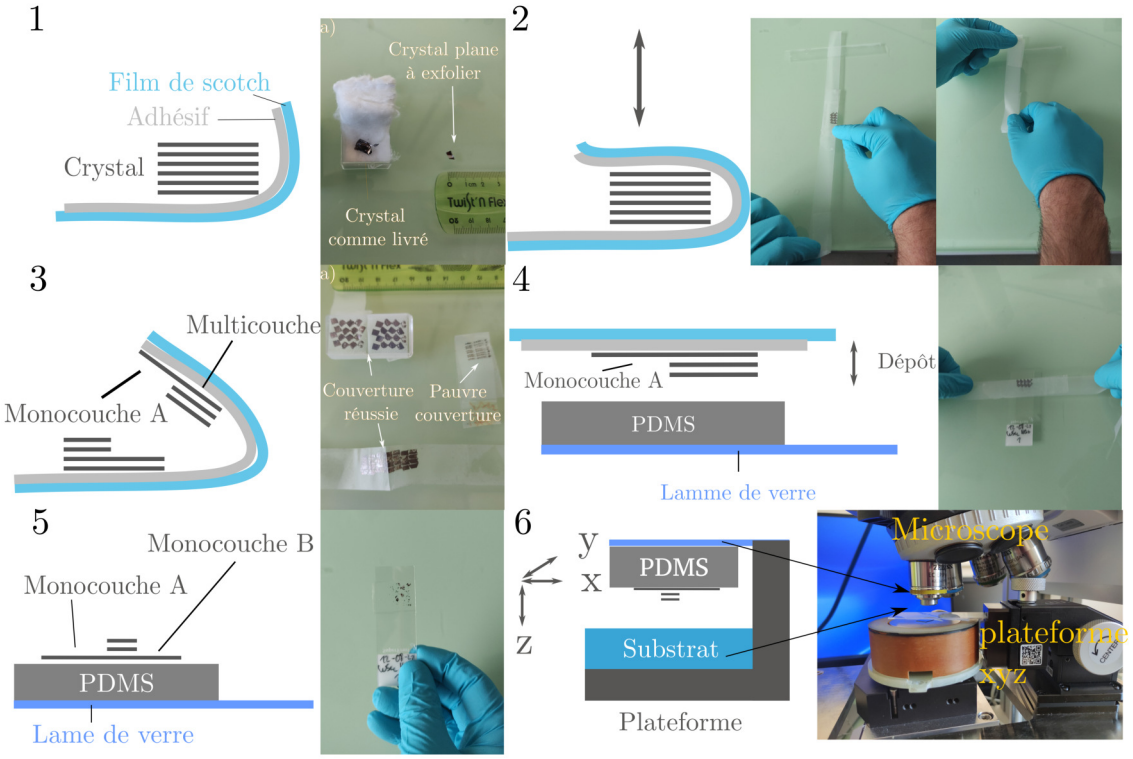

FIGURE 5.7 – *Les étapes de création d'un échantillon MC-TMD par moyen d'exfoliation mécanique: (1) Le cristal est placé sur un film de scotch est exfolié en couvrant et retirant le scotch de manière répétée (2). (3) Il en résulte un certain nombre de flocons de différentes épaisseurs (monocouches et multicouches) du TMD. (4) Les flocons sont déposés sur une lame de verre couverte de polydiméthylsiloxane (PDMS). (5) La monocouche réside sur le PDMS et doit être localisée par un microscope optique. (6) La monocouche peut être déposée par la plateforme controllable en trois dimensions.*

5.4 L'impact du substrat diélectrique sur la structure électronique d'une monocouche en TMD

L'état de l'art: l'influence du substrat diélectrique sur la structure de bandes en monocouches de TMD

La question de l'influence d'un substrat diélectrique sur la structure de bandes d'une MC-TMD a été posée par deux groupes de théoricien.ne.s. Pourtant, les réponses divergent: Steinke et al. [151] trouvent que le substrat diélectrique conduit à une renormalisation du band gap sans changer la forme de bandes. En MC-MoS_2, par exemple, le bandgap est réduit de 300 à 350 meV en passant de $\epsilon = 1$ à $\epsilon = 5$ dans toutes les MC-TMD. Voici, ϵ désigne la constante diélectrique statique du substrat. Ainsi, les masses effectives, Δ_{SOC} et $E_{\Gamma K}$ demeurent inchangés.

En revanche, l'étude théorique de Zibouche et al. [185] prédit un changement de structure de bandes d'une monocouche de MoS_2. En passant d'une monocouche dans le vide ($\epsilon = 1$) à un substrat de hBN ($\epsilon = 2.6$) à un substrat de SiO_2 ($\epsilon = 3.9$) , les masses effectives dans la bande de valence de K changent de $0.42m_{e,0}$ à $0.45m_{e,0}$ à $0.46m_{e,0}$. $E_{\Gamma K}$ change de 0.23 eV à 0.19 eV à 0.17 eV.

Pour éclairer cette question de l'influence du substrat diélectrique, nous avons résumé l'état de l'art des études ARPES quant à l'influence d'un substrat diélectrique. Pour l'analyse des structures de bandes en ARPES, on emploie typiquement un de trois substrats suivant: de l'or [15, 32, 41, 65, 102, 111, 124, 184], graphene [1, 2, 36, 44, 66, 110, 118, 130, 131, 176] et multicouches du graphene [18, 19, 112, 128, 155, 164, 168, 178, 181], ou hBN [25, 64, 67, 121, 164]. A l'exception de hBN, ces substrats sont conducteurs, une qualité qui empêche des effets de chargement [143]. Ils sont d'ailleurs atomiquement plans ce qui assure un signal homogène en ARPES.

A part les substrats typiques, il existe aussi un certain nombre d'études ARPES sur des substrats non-typiques: Si [62, 63, 84, 173], GaN [52], Nb−$SrTiO_3$ [160], Nb−TiO_2 [67, 160], et des monocouches suspendues [63] ont été analysées en ARPES.

Il y a plusieurs études qui mentionnent l'influence du substrat diélectrique [15, 19, 25, 111, 160, 173, 184]. Cependant, nous n'avons trouvé qu'une seule étude qui analyse l'influence du substrat diélectrique en comparant plusieurs substrats [164]. En général, on rencontre les problèmes suivants en consultant la littérature:

- **Ambiguité des mécanismes impliqués**: Certaines études comparent les structures de bandes mesurées en ARPES à des structures de bandes calculées [19, 25, 62, 72, 173]. De quelconques différences sont attribuées à l'écrantage diélectrique du substrat. Pourtant, il existe d'autres mécanismes provenant du substrat qui peuvent entrainer un changement de structure de bandes: stress mécanique [5, 118], transfert de charges [17, 178, 184] ou hybridisation orbitale [15, 111].
- **Manque de comparaisons cohérentes**: Certaines études comparent leurs paramètres de structure de bande à des valeurs expérimentales ARPES obtenues par un autre groupe [19], par moyen de spectroscopie de photoluminescence [111] ou par microscopie à effet tunnel [184]. De telles comparaison à des résultats externes et, en particuliers, à d'autres types d'expérience posent problèmes: rien ne n'assure que la fabrication des échantillons, l'exécution de l'expérience et l'analyse des données soient comparables. Il y a très peu d'études qui comprennent plusieurs substrats différents, et elles se limitent à deux substrats différents [63, 67, 160, 164].
- **Signal-sur-bruit faible sur des substrats rugueux**: Les monocouches de TMD

analysées en ARPES doivent être posées sur des substrats atomiquement plans. Sinon, le signal de photoémission sera inhomogène et fortement élargi [52, 62, 63, 67, 160]. Les études citées dans la phrase précédente n'ont pas réussi à obtenir l'ensemble de paramètres de structures de bandes sur de tels substrats (Δ_{SOC}, $E_{\Gamma K}$, masses effectives m_e).

Les informations collectées dans cette revue nous pousse à entamer une étude qui devrait réunir les conditions suivantes:

— Notre étude devrait comparer la structure de bande de valence sur de différents substrats diélectriques, avec un band gap de $E_g > 2$ eV afin d'exclure tout transfert de charge et hybridisation orbitale. Il faudrait aussi tenir compte d'un possible stress mécanique sur la monocouche.

— L'étude devrait comprendre plusieurs environnements diélectriques et déterminer l'ensemble de paramètres de structure de bandes (Δ_{SOC}, $E_{\Gamma K}$ et masses effectives m_e) en liaison avec les propriétés diélectriques du substrat.

Mesures kPEEM et données brutes de photoémission

Nous avons mesuré plusieurs échantillons de MC-WSe_2 sur de différents substrats en utilisant le « NanoEsca » PEEM à la Plateforme Nanocaractérisation (PFNC) du CEA-LETI à Grenoble. Nous avons créé les échantillons suivants:

— Si et hBN: des flocons de hBN d'une épaisseur de 6 et 10 nm, fournie par K. Watanabe et T. Taniguchi du « National Institute of Material Sciences » (NIMS, Japon), ont été deposés sur des substrats Si(100) fournis par « Siltronix ». Les substrats sont terminés par une couche SiO_2. Nous avons déposé des monocouches de WSe_2 synthétique fournie par NIMS sur ces substrats.

— TiO_2: Nous avons fabriqués des substrats de TiO_2 en Atomic layer deposition. 10nm de TiO_2 amorphe ont été déposé sur des substrats Si(100) de Siltronix. Nous avons également déterminé la constante diélectrique statique de la couche à $\epsilon \approx 34$. Nous avons déposé des monocouches de TMD de WSe_2 synthétique fournie par « hqgraphene » (Pays-Bas) sur ce substrat.

— $SrTiO_3$: des monocrystaux de $SrTiO_3$ ont été acheté chez « Neyco » (Vanves, France). Nous avons enlevé la surface terminé par TiO_2 avec un acide hydrofluorique. Nous avons déposé des monocouches de TMD de WSe_2 synthétique fournie par « hqgraphene » (Pays-Bas) sur ce substrat.

— SiO_2: 10 nm de SiO_2 ont été deposé sur Si par Yashiyuki YAMASHITA du NIMS et mesuré par Olivier RENAULT au NanoEsca de la PFNC.

Toutes les mesures ont été effectuées avec une lampe à décharge d'hélium dont la raie la plus brillante se situe à $h\nu = 21.22$ eV. Les mesures ont été conduites à température ambiante et sous vide de $< 10^{-8}$ mbar. Avant chaque mesure les échantillons sont soumis à un recuit thermique de 300° pendant 2-4 h.

Les données brutes peuvent être consultées à section 4.2. De manière générale, on constate que les données souffrent d'un mauvais rapport signal-sur-bruit. Dans la section suivante, nous allons tenter d'améliorer ce signal-sur-bruit.

5.4.1 Notre approche pour le traitement et l'analyse des spectres de photointensité en kPEEM

Augmenter le signal-sur-bruit en ARPES en exploitant les symétries de la zone de Brillouin

L'objectif de notre étude consiste à déterminer les paramètres de la structure de bandes: Δ_{SOC}, les masses effectives m_e et $E_{\Gamma K}$. Or, les données prises sur certains substrats souffrent d'un faible signal-sur-bruit et des lignes élargies. Le même constat a été fait par d'autres groupes sur des substrats rugueux [52, 62, 63, 67, 160]. Nous abordons brièvement notre stratégie pour améliorer le rapport signal-sur-bruit qui sera détaillée dans la section suivante.

Afin d'améliorer le rapport signal-sur-bruit, nous proposons d'exploiter les symétries de la zone de Brillouin: en monocouches de TMD, la structure de bandes dispose d'une symétrie hexagonale. La structure de bande au point $\mathbf{k}$ est invariante sous rotation de 60°. Pour un spectre $I(\mathbf{k}, E)$ pour un $\mathbf{k}$ dans la zone de Brillouin, il existe alors 5 autres spectres après rotation de 60° qui devraient être équivalents.

En outre, proche d'un point de haute symétrie Γ ou K/K', que l'on désigne par $\mathbf{K}_i$, la structure de bandes est isotropique: elle ne dépend pas de $\mathbf{k}$, mais de $\Delta k = |\mathbf{k} - \mathbf{K}_i|$. Pour les points K et K', cela est vrai tant que $\Delta k \leq 5\% \times \overline{\Gamma K}$ [78]. Pour Γ nous n'avons pas connaissance d'un chiffre exact.

En tenant compte des deux symétries (hexagonalité et isotropie), il existe alors un ensemble $\{\mathbf{k}\}$ pour un certain Δk dont tous les $I(E, \mathbf{k})$ sont physiquement « équivalents ». En moyennant sur tous les spectres $I(\mathbf{k}, E)$, où $\mathbf{k} \in \{\mathbf{k}\}$ on devrait alors gagner en signal-sur-bruit. Le résultat s'appelle $I(\Delta k, E)$.

De ces spectres $I(\Delta k, E)$ on peut extraire des dispersions $E(\Delta k)$ pour chaque bande. Ensuite, $E(\Delta k)$ sera la dispersion de la bande la plus haute en énergie. Cette dispersion permet de déduire la masse effective selon le modèle de l'électron quasi-libre. Cependant, il nous permet d'aller encore plus loin dans le moyennage.

En tenant compte de la dispersion $E(\Delta k)$, on peut moyenner $I(\Delta k, E)$ sur tous les Δk (dans la gamme d'isotropie). Ainsi, nous obtenons un spectre de photointensité $I(E)$ avec un très bon rapport signal-sur-bruit dont on peut déduire la position des bandes avec une certitude réduite. Cependant, ce spectre $I(E)$ ne comprend plus aucune information sur la dispersion.

Moyennage sur points équivalents en espace réciproque

Il faut d'abord déterminer les positions des points de haute symétries en espace k, c'est-à-dire K/K' et Γ. Ces derniers sont indiqués dans l'image de photointensité isoénergétique en sous-figure a) de la FIGURE 5.8. Peu en dessous du haut de la bande de valence (environ 100 meV), les maxima des bandes au point K/K' s'expriment par des domaines de haute photointensité. Au centre de ces domaines, nous trouvons les points K/K'. On agit de même pour Γ (pas montré dans ce chapitre).

Nos données kPEEM sont discretisées en énergie E par pas de 25 meV et discretisées en $\mathbf{k}$ en pixel. La largueur d'un pixel $\delta k \approx 0.008 \mathring{A}^{-1}$. Cette discretisation sur des différents $\mathbf{k}$ dans le plan isoénergétique est montrée en sous-figure b) de la FIGURE 5.8. Le schema est centré sur un point de haute symétrie $\mathbf{K}_i$ (Γ ou K/K'). Les pixels de même couleurs, appartenant au même « anneau », remplissent la condition

$$||\mathbf{k} - \mathbf{K}_i| - \Delta k| \leq \delta k/2 \tag{5.36}$$

pour un Δk fixé en pixel. Ici, δk correspond à la largeur d'un pixel en espace réciproque. On peut alors définir un ensemble de spectres

$$S_{\Delta k,\mathbf{K}_i} = \{I(E,\mathbf{k}) : ||\mathbf{k}-\mathbf{K}_i| - \Delta k| \leq \delta k/2\} \tag{5.37}$$

pour un Δk en pixel et un point de haute symétrie $\mathbf{K}_i$. Pour les $\mathbf{K}_i = \mathbf{K}, \mathbf{K}'$ vaut: tant que $\Delta k < 5\% \times \overline{\Gamma K}$, la dispersion des bandes à K/K' est isotropique. Pour $\mathbf{K}_i = \Gamma$ nous n'avons pas connaissance d'un chiffre exact pour l'isotropie. On s'attend alors à ce que tous les spectres en $S_{\Delta k,\mathbf{K}_i}$ pour un Δk soient semblables. Cela permet de prendre la moyenne sur tous les membres de $S_{\Delta k,\mathbf{K}_i}$ pour augmenter le signal-sur-bruit.

$$I_{\mathbf{K}_i}(\Delta k, E) = \frac{1}{N(\Delta k)} \sum_{\substack{\mathbf{k} \\ ||\mathbf{k}-\mathbf{K}_i|-\Delta k| \leq \delta k/2}}^{N(\Delta k)} I(\mathbf{k}, E) \tag{5.38}$$

pour un point $\mathbf{K}_i$. $N(\Delta k)$ est le nombre de pixels qui remplissent la condition 5.36 pour le même Δk. Dans un deuxième pas, on peut moyenner aussi sur tous les $\mathbf{K}_i$ (les autres points K/K'), indiqués par l'ensemble $\{\mathbf{K}, \mathbf{K}'\}$. Cela donne le spectre moyenné

$$\begin{aligned} I(\Delta k, E) &= \frac{1}{6} \sum_{\mathbf{K}_i \in \{\mathbf{K},\mathbf{K}'\}} I_{\mathbf{K}_i}(\Delta k, E) \\ &= \frac{1}{6} \sum_{\mathbf{K}_i \in \{\mathbf{K},\mathbf{K}'\}} \frac{1}{N(\Delta k)} \sum_{\substack{\mathbf{k} \\ ||\mathbf{k}-\mathbf{K}_i|-\Delta k| \leq \delta k/2}}^{N(\Delta k)} I(\mathbf{k}, E) \end{aligned} \tag{5.39}$$

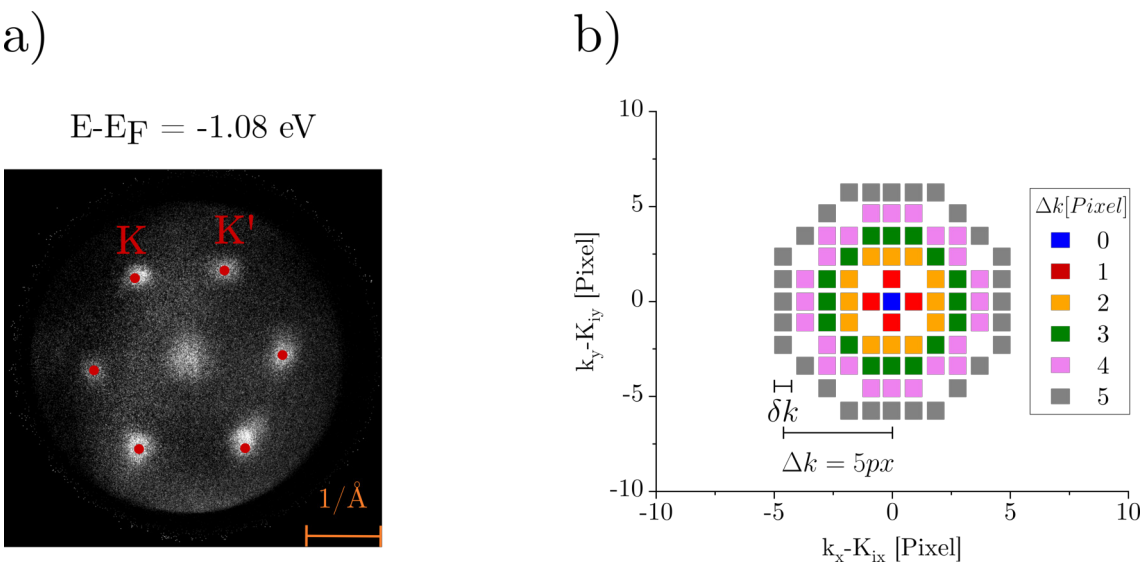

FIGURE 5.8 – ***a)*** *Coupe isoénergétique à travers la zone de Brillouin pour une MC-WSe_2 sur hBN à $E - E_F = 1.08$ eV, c'est-à-dire peu dessous le haut de la bande de valence. A cette énergie, des domaines de haute photointensité apparaissent. Leurs centres marquent les positions des points K et K'.* ***b)*** *Positions de spectres « équivalents » dans l'espace réciproque autour d'un point de haute symétrie K/K' ou Γ qui est placé au centre. Les valeurs du* $\mathbf{k}$ *sont discrétisées en pixels. Grâce à l'isotropie autour d'un point de haute symétrie, les spectres qui remplissent $||\mathbf{k}-\mathbf{K}_i| - \Delta k| \leq \delta k/2$ pour le même Δk devraient avoir la même forme (ils sont « équivalents »). Ici, δk est la largeur réciproque d'un pixel. Cette condition est valable pour $\Delta k \leq \overline{\Gamma K}$ [78].*

Traitement du fond d'électrons secondaires

En sous-figure a) et b) de FIGURE 5.9 nous avons mis en oeuvre l'équation 5.38: le spectre est le résultat d'un moyennage sur tous les spectres qui remplissent la condition 5.36 avec $\Delta k = 3$ px à K/K' (c) et Γ (d). Au signal de photoémission s'ajoute un fond d'électrons sécondaires. Nous enlévons ce fond un utilisant une fonction polynomiale comme indiquée. En rouge, nous montrons le signal de photoémission obtenue après enlèvement du fond.

Ajustement des courbes pour obtenir la position des bandes

A la prochaine étape nous ajustons les pics dans les spectres de photointensité par des courbes gaussiennes. Les pics représentent la présence d'une bande (voir 5.31). Pour cela, dans les spectres moyennés nous modélisons chaque pic par une gaussienne de forme

$$I(E) = A \cdot \exp\left(\frac{-(E - E_C)^2}{2\sigma^2}\right) \tag{5.40}$$

où A est l'amplitude, E_C le centre du pic. σ est lié à la largeur w à mi-hauteur du pic $\sigma = w/2\sqrt{2\ln(2)}$.

A K/K' nous cherchons a fitter les deux bandes séparées par le couplage spin-orbit $\Delta_{SOC} \approx$ 500 meV[121]. Δ_{SOC} est au-delà de notre résolution $\Delta E \approx 200$ meV. L'ajustement des courbes n'était pas restreint en largueur des raies w, amplitude A ou position des pics E_C. Nous avons ajouté une troisième gaussienne pour une bande environ 2 eV en dessous du haut de la bande de valence [97, 118, 121].

A Γ nous avons ajouté jusqu'à 3 gaussiennes: une en haut de la bande de valence, et deux gaussiennes 700 meV et 1100 meV en-dessous pour des bandes correspondants [118] s'il y avait un signal de photointensité non-négligable .

Les sous-figures c) et d) de la FIGURE 5.9 montrent le résultat de nos ajustements pour K/K' et Γ pour le cas de MC-WSe_2 sur hBN. Pour les bandes à K/K' on remarque que l'amplitude et la largeur de la bande inférieure sont visiblement plus importantes que celles de la bande supérieure. Deux études expliquent ces observations: la bande inférieure à K/K' est énergétiquement plus proche de celle à Γ que la bande supérieure. La bande inférieure et la bande à Γ sont alors liées par couplage électron-phonon qui peut fortement élargir la raie inférieur par rapport à la raie supérieure (100 meV contre 60 meV dans le cas de MC-MoS_2) [101]. Une étude ARPES résolue en spin montre que l'amplitude de la bande inférieure dispose d'une amplitude plus importante que celle de la bande supérieure sans que les auteurs détaillent l'origine de ce phénomène [112]. Le pic de la bande inférieure étant plus large et plus important en amplitude, en accord avec nos fits.

Mesure de la dispersion, correction de dispersion et moyennage

Les étapes suivants sont dessinés en FIGURE 5.10 pour l'exemple des spectres autour de K/K' avec un couplage spin-orbit important. Nous extrayons la dispersion de la bande supérieure et inférieure $E(\Delta k)$ obtenues dans l'étape précédente en ajustant la courbe suivante

$$E(\Delta k) = \frac{\hbar^2 \Delta k^2}{2m} + E_0 \tag{5.41}$$

qui correspond à la dispersion d'un électron quasi-libre. m est sa masse effective. Nous notons que ce modèle n'est valable que lors que $\Delta k \leq 5\% \cdot \Gamma K \approx 0.06 \mathring{A}^{-1}$ [78]. Mais cette valeur est très proche de notre résolution $\Delta k_{\|} \approx 0.03 \mathring{A}^{-1}$. Comme compromis, nous avons ajusté la dispersion jusqu'à $0.15 \mathring{A}^{-1}$ pour toutes nos courbes à K/K'. A Γ nous avons ajusté jusqu'à $0.3 \mathring{A}^{-1}$.

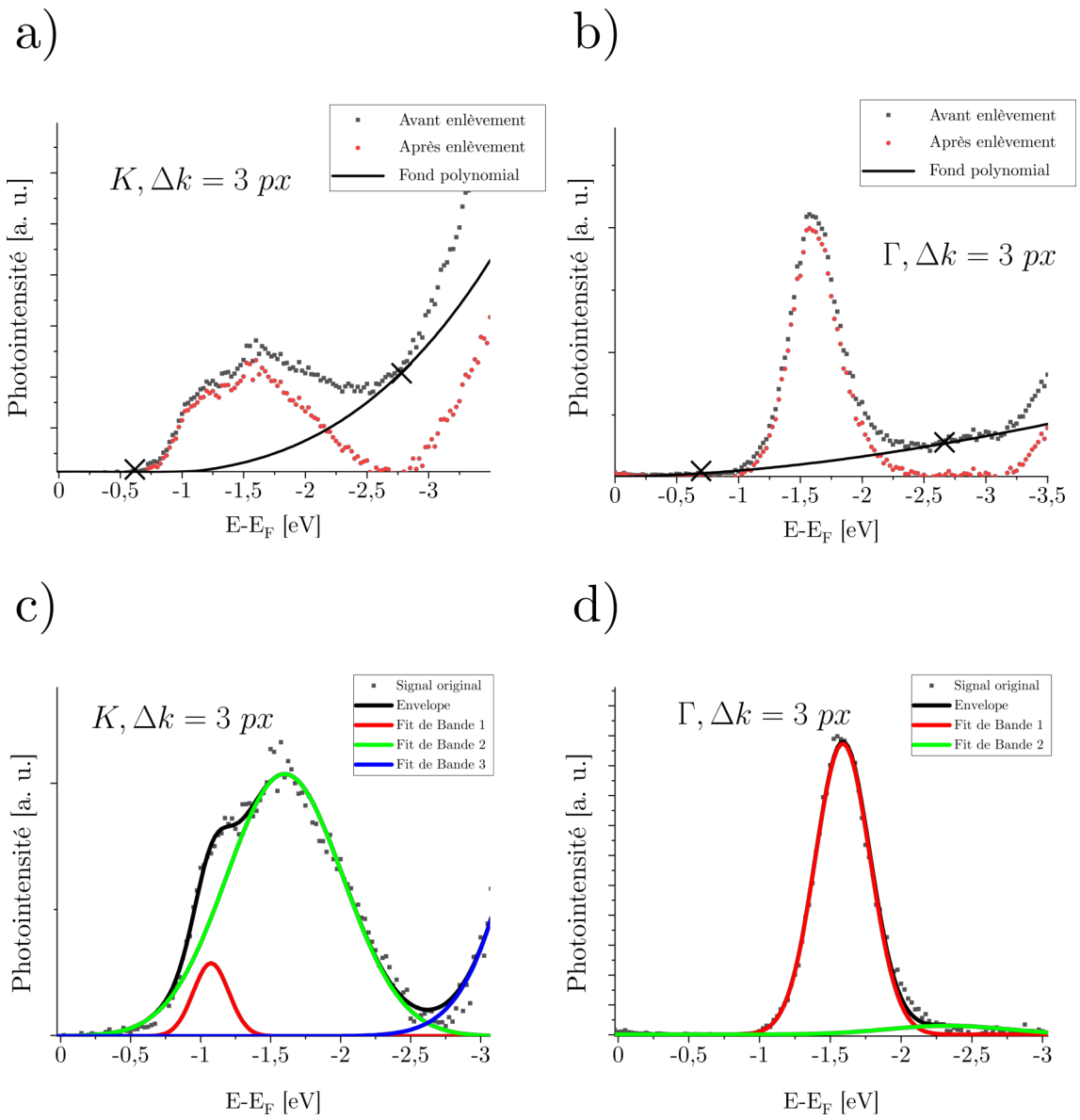

FIGURE 5.9 – ***a)*** *et* ***b)*** *Spectres de photointensité après moyennage pour un* $\Delta k = 3\ px$ *à K/K' (c) et* Γ *(d) en noir. Nous enlevons un fond d'électrons sécondaires polynomial indiqué par la ligne, il en resulte le spectre en rouge.* ***c)*** *et* ***d)*** *Les spectres de a) et b) après ajustement des courbes avec des gaussiennes. Chaque gaussienne correspond à une bande anticipée par la théorie [118].*

Pour augmenter encore davantage le signal, nous voudrions moyenner sur tous les $I(\Delta k, E)$. Pourtant, ces spectres ne sont pas équivalents en espace k car parce la position des pics va être déplacée par la dispersion des bandes respectives. Nous montrons cette situation et la méthode en FIGURE 5.10. Nous créons de nouveaux spectres compte tenu de la dispersion de la bande supérieure $E(\Delta k)$

$$I'(\Delta k, E) = I(\Delta k, E - E(\Delta k)) \tag{5.42}$$

Ensuite, nous moyennons sur tous les spectres

$$I(E) = \frac{1}{N} \sum_{\Delta k} I'(\Delta k, E) \tag{5.43}$$

ou N est le nombre des spectres. Le spectre résultant aura un signal-sur-bruit maximal et la position des bandes déterminées par des gaussiennes de la même manière que décrit en haut. Pourtant, ce nouveau spectre ne comprend plus l'information sur la dispersion.

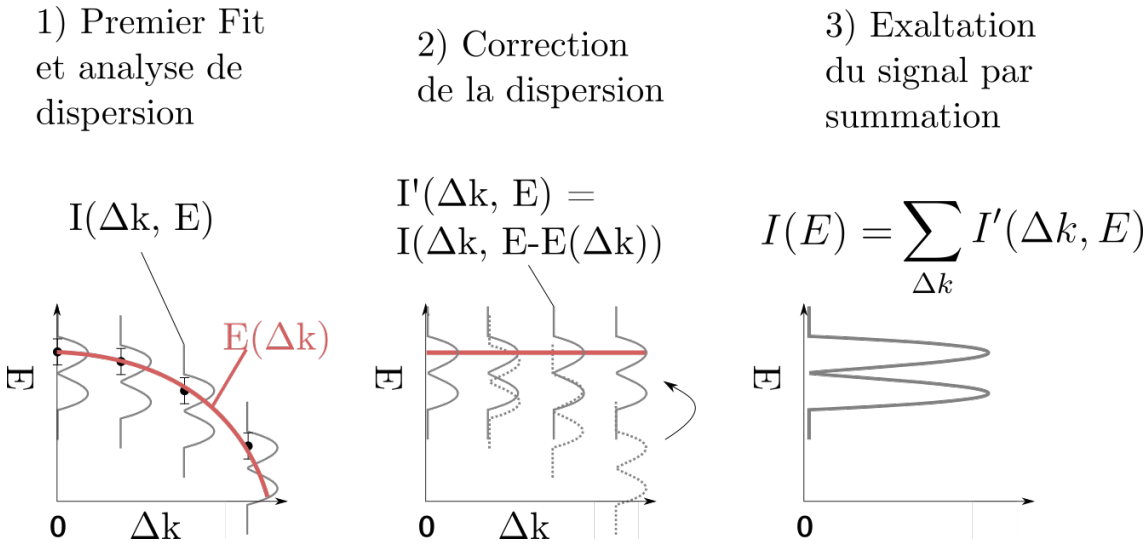

FIGURE *5.10 – Étapes supplémentaires pour une augmentation maximale du rapport signal-sur-bruit pour des spectres pris autour de K/K'. On a schématisé le couplage spin-orbit dans les spectres. 1) en analysant les spectres $I(\Delta k, E)$ on obtient une dispersion des bandes $E(\Delta k)$. En 2) nous corrigons cette dispersion en créant de nouveaux spectres $I'(\Delta k, E) = I(\Delta k, E - E(\Delta k))$, avant de moyenner sur tous ces spectres en 3). Le résultat est une augmentation maximale du signal-sur-bruit.*

5.4.2 Description des résultats

Les valeurs des paramètres de la structure de bandes sont présentées au tableau 5.3. Pour les deux substrats de hBN nous avons précisé l'écart angulaire entre les axes cristallographiques du hBN et de la monocouche. Les masses effectives de la bande supérieure sont autour de -0.5 $m_{e,0}$, celles de la bande inférieure à environ 1 $m_{e,0}$. Une valeur de $\approx 0.5 m_{e,0}$ pour la bande supérieure correspond aux valeurs de la littérature [84, 121, 184].

La masse effective de la bande inférieure est deux fois plus grande que celles en littérature ($\approx -0.5 m_e$ [84, 184]). Cette déviation peut être expliquée par le fait que nous ajustions la courbe sur une gamme assez large dans l'espace réciproque de 0.15 $\mathring{A}^{-1}$ que d'autres études.

Nos valeurs pour la masse effective à Γ sont atour de -4 $m_{e,0}$ pour tous les substrats excepté sur SiO_2 ($-2.37 \pm 0.332 m_{e,0}$). Dans la littérature, la gamme pour la masse effective à Γ

s'étend de $-2.344m_{e,0}$ [184] à $-3.5 \pm 1.8m_{e,0}$ [173]. Nos valeurs correspondent donc à cette gamme sur tous les substrats.

Nos valeurs de Δ_{SOC} s'étendent de 0.44 ± 0.04 sur Si eV à 0.51 ± 0.01 sur SiO_2 et dans la gamme des résultats de la littérature (0.46 eV [184] à 0.51 ± 0.01 [84]).

Concernant la différence entre le haut de la bande de valence à K/K' et à Γ nous constatons des différences notables d'environ 300 meV sur les différents substrats. $E_{\Gamma K}$ est le moins important sur SiO_2 (-0.69 ± 0.01 eV) et plus grand sur Si (-0.41 ± 0.02). La valeur reste invariant au twist angle sur hBN à environ ≈ -0.53 eV. Dans la littérature, $E_{\Gamma K}$ a été mesuré de -0.21 ± 0.01 [173] à -0.892 ± 0.02 eV [84].

5.4.3 Relation entre les paramètres de la structure de bandes et la constante diélectrique statique du substrat

Afin de comparer l'influence de la constante diélectrique du substrat, nous avons utilisé les valeurs suivantes: pour SiO_2 $\epsilon = 3.9$ [50], pour hBN nous avons pris la moyenne géométrique $\epsilon = \sqrt{\epsilon_\perp \cdot \epsilon_\parallel} \approx 5.9$ ou $\epsilon_\parallel = 5$ et $\epsilon_\perp = 7$ [46]. Pour TiO_2 amorphe nous avons mesuré une constante diélectrique de $\epsilon \approx 34$ à l'aide d'une structure capacitive microscopique à basse fréquence. Pour $SrTiO_3$ nous avons supposé la constante diélectrique $\epsilon = 300$ selon le fournisseur. Pour Si nous prenons la valeur macroscopique $\epsilon = 11.7$ [35].

Nous avons tracé les paramètres de la structure de bandes en fonction de la constante diélectrique statique du substrat en figure 5.11. Pour les masses effectives à K/K' an sous-figure a) nous ne voyons pas de corrélation hors de la barre d'erreur.

En b) quant à la masse effective de Γ, elle est plus petite sur SiO_2 (-2.37 ± 0.32 $m_{e,0}$) que sur les autres substrats qui sont autour de la même valeur (≈ -4.2 $m_{e,0}$).

Le couplage spin-orbit Δ_{SOC} semble quelques dizaines de meV plus petits que pour Si et TiO_2, dans la gamme de $\epsilon = 11.9$ à 34, mais elle remonte à environ 500 meV pour $SrTiO_3$ à $\epsilon = 300$.

La correlation la plus importante peut être trouvée pour $E_{\Gamma K}$. Elle augmente de -0.69 ± 0.01 eV pour SiO_2 à autour de -0.43 eV pour hBN à $\epsilon = 5.9$. Elle continue à augmenter avec un maximum de 0.41 ± 0.02 pour Si à $\epsilon = 11.9$. Ensuite elle diminue encore pour TiO_2 à 0.46 ± 0.02 ($\epsilon = 34$) et diminue encore pour $SrTiO_3$ $\epsilon = 300$.

Le rôle des orbitales dans l'influence du substrat diélectrique

Selon les résultats présentés, nous voyons une correlation non-triviale entre ϵ et $E_{\Gamma K}$. Notre $E_{\Gamma K}$ n'augmente pas de manière monotone comme le prédisent Zibouche et al.. Cependant, nous constatons un changement important de $E_{\Gamma K}$ selon le substrat. Cette modification contredit les travaux théorique de Steinke et al. [151] qui prédit que $E_{\Gamma K} = const.$ peu importe la constante diélectrique du substrat. Pour resoudre cette problèmatique, nous analysons un argument de modelisation de Steinke, Waldecker et al. utilisé en [164].

De manière générale, une charge dans une monocouche de TMD sera écrantée par les charges images dans le substrat. Si la distribution locale de la charge est loin du substrat, les interactions entre charge et charge image peuvent être modelisées par des distributions monopoles Ce scénario est modelisé en sous-figure a) de la figure 5.12. Selon Steinke, Waldecker et al. c'est le cas si $h \gg d$ où h est la hauteur de la monocouche et d l'extension spatiale de la distribution de charges.

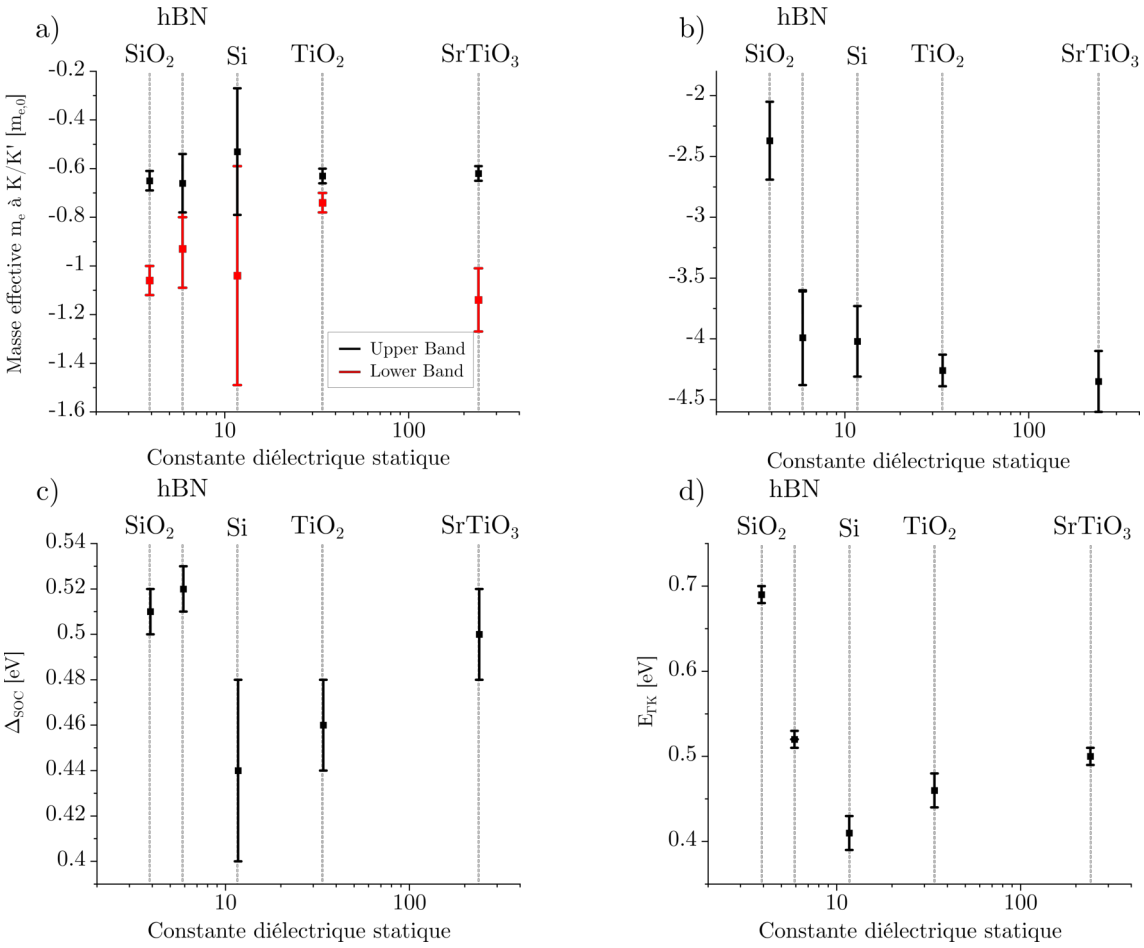

FIGURE *5.11 – Les paramètres de structures de bandes en fonction de la constante diélectrique statique du substrat.* ***a)*** *Masse effective des bandes à K/K',* ***b)*** *Masse effective de la bande à* Γ*,* ***c)*** *Couplage spin-orbit* Δ_{SOC} *et différence entre le haut de la bande de valence à* Γ *et à K/K'* $E_{\Gamma K}$*. Au cas de hBN, un matériaux bidimensionel, nous avons ajouté la différence en angle entre les axes cristallographiques de hBN et MC-*WSe_2*.*

	m_e **(s)** $[m_{e,0}]$	m_e **(i)** $[m_{e,0}]$	m_e Γ $[m_{e,0}]$	$E_{\Gamma K}$ **[eV]**	Δ_{SOC} **[eV]**
hBN(5°)	-0.57 ± 0.04	-0.75 ± 0.05	-3.82 ± 0.21	-0.54 ± 0.02	-0.51 ± 0.02
Si	-0.53 ± 0.26	-1.04 ± 0.45	4.02 ± 0.29	-0.41 ± 0.02	-0.44 ± 0.04
hBN (0°)	-0.66 ± 0.12	-0.93 ± 0.16	-3.99 ± 0.39	-0.52 ± 0.01	-0.52 ± 0.02
hBN (3.)	-0.45 ± 0.01	-0.6 ± 0.03	-3.51 ± 0.14	-0.53 ± 0.01	-0.49 ± 0.02
$SrTiO_3$	-0.62 ± 0.03	-1.14 ± 0.13	-4.35 ± 0.25	-0.5 ± 0.02	-0.5 ± 0.01
TiO_2	-0.63 ± 0.03	-0.74 ± 0.04	-4.26 ± 0.13	-0.46 ± 0.02	-0.46 ± 0.02
SiO_2 (Y., R.)	-0.65 ± 0.04	-1.06 ± 0.06	-2.37 ± 0.32	-0.69 ± 0.01	-0.51 ± 0.01

TABLE *5.3 – Masses effectives m_e mesurées à la bande supérieur (s) et inférieure (i) des bandes à K/K et à Γ sur MC-WSe_2 en fonction du substrat. Nous avons employé la méthode utilisée dans la section précédente. Au cas de hBN, un matériaux bidimensionel, nous avons ajouté la différence en angle entre les axes cristallographiques de hBN et MC-WSe_2. La différence entre la bande supérieure et inférieure à K/K' due au couplage spin-orbit Δ_{SOC} et la différence entre la bande supérieure à K/K' et à Γ $E_{\Gamma K}$ en fonction du substrat. Au cas de hBN, un matériau bidimensionel, nous avons ajouté la différence en angle entre les axes cristallographiques de hBN et MC-WSe_2.*

La hauteur d'une monocouche de WSe_2 s'élève à 6.4 Å [90, 167]. L'extension spatiale d peut être approximée par l'extension des orbitales électroniques r. L'extension spatiale devient alors $d = 2r = 2\sqrt{\langle\Psi|\hat{r}^2|\Psi\rangle}$ ou $\hat{r}$ retourne la coordonnée radiale. Pour les orbitales qui participent à la bande de valence We $5d_{xy}$ $5d_{z^2}$, $4p_{xy}$, $4p_z$, $r \geq 0.7$Å. Cela signifie que $d = 2r = 1.4$Å devient comparable à h et la condition de modélisation de STEINKE, WALDECKER ET AL. est affaiblie. Comme expliqué dans une partie précédente, les orbitales ont une directionalité hors-plan (dans le plan) à Γ (K/K'). L'effet de l'écrantage diélectrique devrait désormais dépendre de **k** dans la zone de Brillouin.

Conclusion

Nous avons constaté une correlation non-triviale entre $E_{\Gamma K}$ et ϵ, la constante diélectrique statique du substrat. Si $E_{\Gamma K}$ n'est pas constant comme le prédisent STEINKE, WALDECKER ET AL. [151, 164], il n'augmente pas non plus de manière monotone par rapport à ϵ comme anticipé par ZIBOUCHE ET AL. [185]. Au dela d'une valeur de $\epsilon = 11.9$ pour Si, les valeurs de $E_{\Gamma K}$ baissent encore.

Une difficulté dans l'expérience consiste à déterminer la constante diélectrique statique du substrat. Notre fabrication et la rugosité de la surface peuvent influencer l'environnement diélectrique effectif. Par exemple, le traitement avec une acide hydrofluorique créent des sites terminé par TiO_2 sur notre substrat de $SrTiO_3$ [68].

Contrairement à ce qui est prévu dans la littérature théorique [151, 185], la correlation entre la constante diélectrique statique du substrat et $E_{\Gamma K}$ est non-trivial. Pourtant, il existent d'autres méchanismes qui peuvent influencer la structure de bandes. Ils sont à écarter pour confirmer l'influence de l'écrantage diélectrique. Pour confirmer ou infirmer l'existence d'autres méchanismes, nous étudions par la suite la présence de stress mécanique et des quantité de charges importantes dans la monocouche.

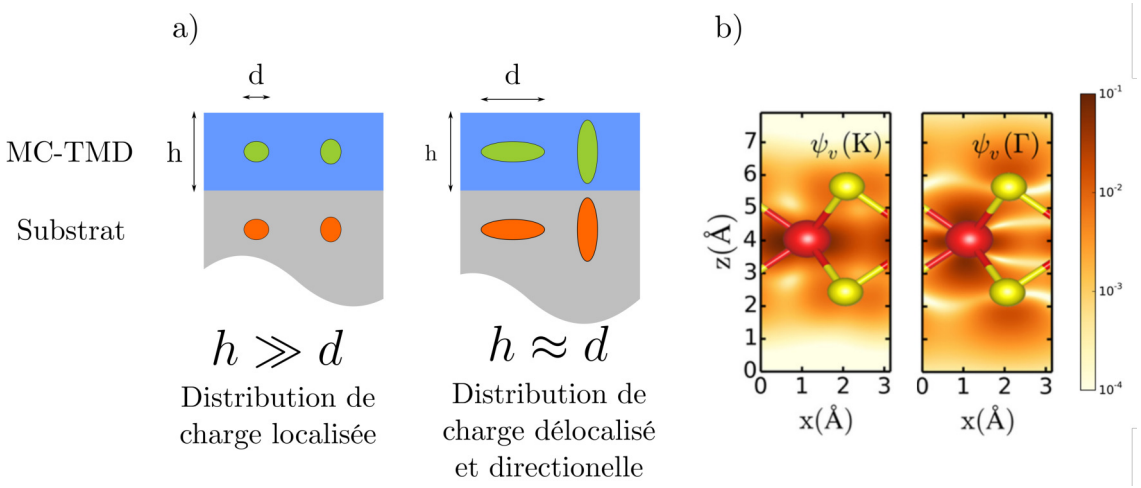

FIGURE 5.12 – ***a)*** *Deux régimes de validité pour l'écrantage diélectrique d'une charge locale dans une MC-TMD selon* WALDECKER, STEINKE ET AL. *[151, 164]. A gauche: L'extension spatiale d de la distribution de la charge est beaucoup moins importante que la hauteur h de la monocouche $h \gg d$. Dans ce cas, la distribution de charge ainsi que la charge image dans le substrat peuvent être modelisées en tant que monopoles. A droite, le cas $h \approx d$: Les distributions de la charge locale et sa charge image sont délocalisées, directionnelles et doivent être modelisées par des multipoles. Le caractère orbitale doit alors être pris en compte.* ***b)*** *$|\Psi(\mathbf{r})|^2$ de la fonction d'onde $\Psi(\mathbf{r})$ d'une monocouche de MoS_2, calculée par [117], pour des électrons provénant du haut de la bande de valence à K/K' (gauche) et à Γ (droite). Par rapport à la hauteur totale de la monocouche, la distribution de charge est visiblement très délocalisée et directionnelle: elle semble pointé hors-du-plan à Γ et dans-le-plan à K/K'.*

5.4.4 Mesures Raman pour vérifier la présence de stress mécanique

Dans la partie précédente nous avons constaté que la structure de bandes, en particulier, le paramètre $E_{\Gamma K}$ est susceptible de changer en fonction du substrat. Un mécanisme capable de changer la structure de bandes est le stress mécanique biaxial. Des études théoriques montrent qu'un stress mécanique biaxial de l'ordre de plusieurs % est capable de changer $E_{\Gamma K}$ de quelques centaines de meV [5, 116, 118]. Une manière de détecter la présence de stress mécanique exercé par le substrat est par spectroscopie Raman.

En MC-WSe_2 les deux modes Raman sensible au stress mécanique sont le mode A et E à environ 252 cm^{-1} [142, 153]. On estime que la fréquence des modes devrait changer de quelques cm^{-1} par % de stress mécanique biaxial [142]. Toutefois, les deux modes sont censés rester dégénérés en dépit du stress. Cela pose problème sur le plan de résolution car les deux modes ont une une largeur de 4-5 cm^{-1} [30] et la résolution de notre dispositif Raman est de $0.5cm^{-1}$.

Pour minimiser les ambiguités causé par la largueur des modes et notre résolution, nous menons une expérience de Raman polarisée: en utilisant de la lumière linéairement polarisée, nous arrivons à supprimer le mode E. Les positions du mode A seront alors plus facile à modéliser. Pour y parvenir, nous utilisons une configuration de Raman appelée $Z(YY)\overline{Z}$ proposée par [30] et montrée en sous-figure a) de la FIGURE 5.13. Les informations du paragraphe actuel sont basées sur la/les source(s) [132]. Les photons sont incidents et collectés parallèlement à la normale (Z et $\overline{Z}$). La lumière est linéairement polarisée est analysée avec une polarisation parallele à l'axe Y (direction cristaline (010)). En b) la direction Y peut être déterminé à l'aide des mesures kPEEM ou la direction Y est parallèle à $\overline{\Gamma K}$.

Au tableau 5.4 nous présentons les positions du mode A de MC-WSe_2 mésurés sur de différents substrats. Les valeurs représentent la moyenne sur positions de tous les spectres. Les valeurs vont de 251.1 cm^{-1} pour un substrat de hBN de 6 nm d'épaisseur à 251.8 cm^{-1} pour le substrat de Si. Les différences sont en dessous de 1 cm^{-1} et donc en dessous du seuil requis pour une modification importante de la structure de bandes. Ces résultats nous permettent d'écarter le stress mécanique comme mécanisme responsable du changement de $E_{\Gamma K}$ dans les mesures précédentes.

Aire de la surface	hBN 10 nm	hBN 6 nm	Si	TiO_2
Fréquence moyenne	251.2 ± 0.03	251.1 ± 0.07	251.8 ± 0.13	251.4 ± 0.05

TABLE *5.4 – Positions du mode A de MC-WSe_2 sur de différents substrats. Les différences sont trop petites pour un stress mécanique qui influence $E_{\Gamma K}$ dans les centaines de meV.*

5.4.5 Mesures de travail de sortie

Dans les parties précédentes nous avons analysé l'écrantage diélectrique et le stress mécanique comme mécanisme possible pour changer la structure de bandes de MC-WSe_2. La présence de charges est débatue comme mécanisme capable de changer la structure de bandes [17, 181, 184]. Afin de déterminer la présence de charges on peut mesurer la position du niveau de Fermi ou le travail de sortie $\phi = E_{vac} - E_F$.

Nous avons effectué nos experiences au dispositif NanoEsca PEEM setup du PFNC au CEA-LETI à Grenoble. Les échantillons analysés sont illuminés d'une lampe à décharge d'hélium avec une énergie de photon de $h\nu = 21.22$ eV. Le tableau 5.5 montre le travail de sortie de la monocouche en fonction du travail de sortie du substrat. Les valeurs sont moyennées sur l'aire totale de la monocouche et une aire importante (plusieurs centaines

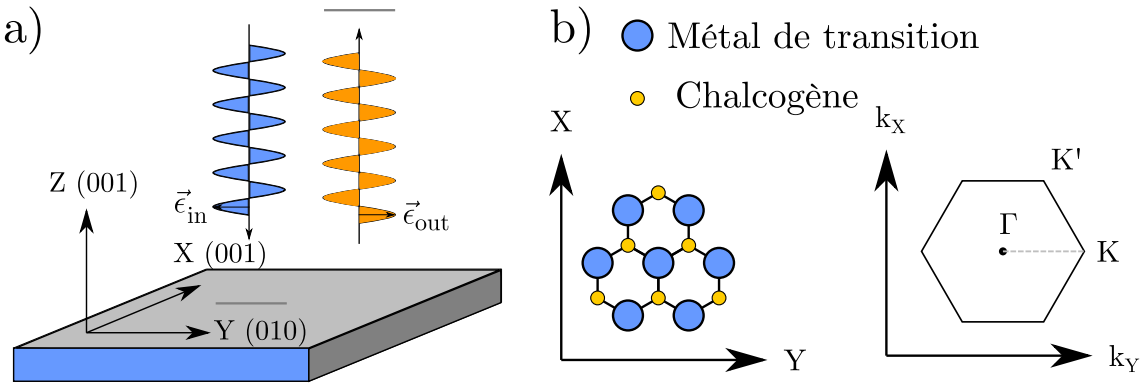

FIGURE 5.13 – ***a)*** *Configuration du Raman linéairement polarisé selon [30, 132]. Le faisceau de lumière arrive parallèle à la normale (Z), il est polarisé et analysé selon Y, et collecté selon la normale $(\overline{Z}$. Cela donne $Z(YY)\overline{Z}$.* ***b)*** *A l'aide de nos mesures kPEEM précédentes nous pouvons récupérer la direction Y qui correspond à la direction de ΓK dans la zone de Brillouin.*

de μm^2) du substrat. Les incertitudes correspondent à la deviation standard. En rouge, on a tracé l'alignement des deux travaux de sorties.

Qu'un transfert de charge puisse modifier la structure de bande fait objet d'une controverse dans la littérature. Des mesures ARPES sur des MC-TMDs dopé par du potassium ont montré des changements importants de $E_{\Gamma K}$ de quelques dizaines de meV [181, 184]. Une étude menée par NGUYEN ET AL. avec une grille électrique ne constate pas de changement de $E_{\Gamma K}$ [121].

Le travail de sortie de MC-WSe_2 a été estimé dans une gamme de 4.2 eV à 4.6 eV [14, 49, 71] pour l'état sans charge. Nos valeurs sont plus importantes que les prédictions théoriques: sur hBN, TiO_2 et $SrTiO_3$ les valeurs vont de 4.74 ± 0.01 à 4.97 ± 0.02 eV. Nous nous attendons à ce que le niveau de Fermi de la monocouche s'aligne à celui du substrat, ainsi les travaux de sorties du substrat et de la monocouche vont s'aligner. Dans la FIGURE 5.14 nous présentons la corrélation entre le travail de sortie du substrat et de la monocouche. Nous avons ajouté une valeur mesurée en KPFM par [13] sur Ni. Les points de données sont proche de la ligne rouge ce qui correspond à un alignement des travaux de sortie de la monocouche et du substrat.

Un tel alignement a été constaté dans une étude menée par PARK ET AL. [125]. Les auteurs ont mesurée le travail de sortie de MC-MoS_2 sur des substrats métalliques et isolants. Ils ont conclu que l'alignement devrait être accompagné d'un transfert de charge important sans quantifier la valeur. Cependant, nos substrats sont diélectriques avec des band gaps plus importants que celui de MC-WSe_2 ($E_g < 2.6$ eV [96, 121, 123]. $E_g > 3$ eV pour TiO_2 amorphe, $E_g \approx 5.4$ eV pour hBN [12] et $E_g \approx 3.25$ eV pour $SrTiO_3$. Étant donné les hauteurs du band gap, un transfert de charge semble improbable. Seul Si dispose d'un band gap moins important $E_g = 1.11$ eV [175].

Si la quantité des charges est suffisament importante pour modifier $E_{\Gamma K}$, elle doit être de l'ordre 10^{13} à 10^{14} e/cm^2. A cette quantité, le niveau de Fermi entre dans la bande de valence ou bande de conduction [17]. Pour confirmer cela, nous avons ajouté les valeurs du haut de la bande de valence à K/K' par rapport au niveau de Fermi dans le tableau 5.5. Nous voyons que pour les trois substrats Si, hBN et TiO_2 le niveau de Fermi est loin (> 1 eV) de la bande de valence. Elle est proche de la moitié de la valeur du band gap $E_g \approx 2.4$ eV [34, 88, 133] comme attendue pour un semi-conducteur non-dopé.

Comme conclusion, nous constatons que les variations locales du travail de sortie sont petites (±10 meV) devant les variations locales du substrat (±20 meV). Le travail de sortie de la monocouche s'aligne avec celui du substrat. Un transfert de charge important nous semble improbable à cause des band gaps supérieurs à MC-WSe_2 à part pour le substrat de Si. Pour Si la position du haut de la bande de valence à K/K' n'est pas modifié. Cela nous amène à exclure un transfert de charge comme mécanisme responsable de changer la structure de bandes comme vue dans les mesures kPEEM.

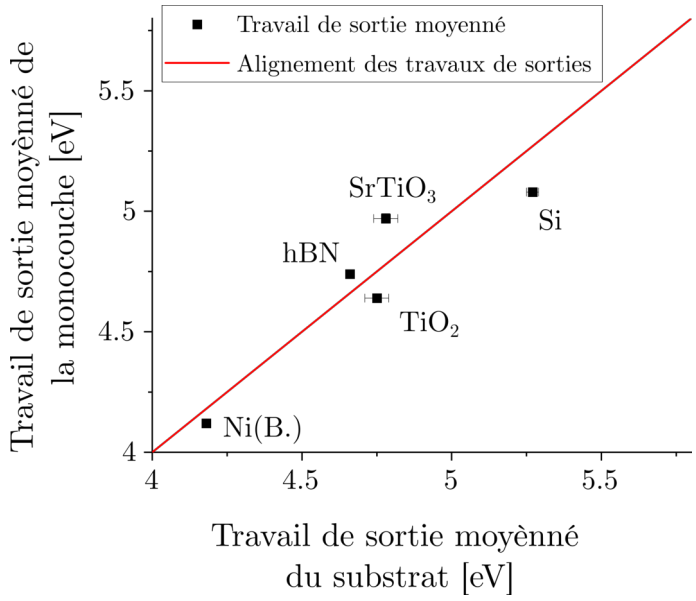

FIGURE *5.14 – Travail de sortie ϕ de la monocouche de WSe_2 en fonction du travail de sortie du substrat. Nous avons ajouté une valeur mesurée par [13] sur un substrat de Ni. Les valeurs sont proches de la ligne rouge qui indique un alignement des travaux de sortie de la monocouche et du substrat. Nous avons ajouté une valeur externe prises par [13] d'une MC-WSe_2 sur Ni avec la méthode Kelvin-Probe.*

	MC-WSe_2 ϕ moyenné [eV]	ϕ moyenné du substrat[eV]	Haut VBM à K/K' $E - E_F$ [eV]
Si	5.08 ± 0.01	5.27 ± 0.02	1.14 ± 0.01
hBN	4.74 ± 0.01	4.66 ± 0.01	1.13 ± 0.02
TiO_2	4.64 ± 0.02	4.75 ± 0.04	1.18 ± 0.01
$SrTiO_3$	4.97 ± 0.02	4.78 ± 0.04	
Ni [13]	$4.12 \pm NA$	$4.18 \pm NA$	

TABLE *5.5 – Travail de sortie moyenné de la monocouche de WSe_2, travail de sortie moyenné du substrat et position énergétique du haut de la bande de valence à K/K'. Pour l'échantillon de $SrTiO_3$ la position du haut de la bande de valence n'a pas été mésurée suite à rupture de la connexion électrique. Nous avons ajouté une valeur en littérature de [13] pour un substrat de nickel mésuré en Kelvin Probe Force Gradient Microscopy .*

5.4.6 Conclusions et perspectives

Dans ce travail, nous avons analysé l'influence des substrats diélectriques sur la structure de bandes électronique dans une monocouche de WSe_2. De nos résultats, nous avons vu que le choix du substrat diélectrique a une influence déterminante sur la structure de bande,

et en particulier, le paramètre $E_{\Gamma K}$. Nous trouvons une corrélation entre la constante diélectrique statique ϵ du substrat et la $E_{\Gamma K}$ de la monocouche. Le paramètre de structure de bande $E_{\Gamma K}$ décrit la différence d'énergie entre les maxima de la bande de valence à Γ et K/K' et paramétrise ainsi le band gap direct dans les MC-TMDC responsables de la forte interaction lumière-matière. Nous avons exclu d'autres mécanismes tels que le stress mécanique biaxial et le transfert de charges, qui pourraient modifier $E_{\Gamma K}$ et nous attribuons les changements de $E_{\Gamma K}$ à l'écrantage diélectrique du substrat comme mécanisme d'interaction responsable.

La dépendance que nous avons établie n'est pas monotone. Cela peut être dû à notre manière d'attribuer des constantes diélectriques statiques aux substrats utilisés. Nous nous sommes basés sur les constantes du bulk. Cependant, le vrai environnement diélectrique peut être plus compliqué à cause des propriétés de la surface.

De manière générale, l'influence du substrat diélectrique n'a pas très souvent été étudiée dans la littérature. Cela est problement dû aux conditions difficiles dans lesquelles il doit être mésuré. Nous avons montré que le rapport signal-sur-bruit est très faible sur des substrats rugueux. C'est pour cela que plusieurs études n'ont pas été en mésure de mésurer l'ensemble des paramètres de la structure de bandes (m_e, Δ_{SOC}, $E_{\Gamma K}$) [52, 62, 63, 67, 160]. Dans ce travail, nous avons fait un effort considérable afin d'améliorer le rapport signal sur bruit. Nous sommes parvenus à déterminer, pour la première fois, des paramètres de la structure de bandes sur certains substrats tels que TiO_2 ou $SrTiO_3$.

Perspectives

Une possibilité d'améliorer le signal-sur-bruit en analysant l'éffet de l'écrantage diélectrique consiste à déposer des monocouches de TMD sur des oxides atomiquement plans avec une constante diélectrique statique très élévée. Une revue sur de tels oxides a été publiée par Biswas et al. [11]. Il faudrait pourtant analyser si une constante diélectrique élévée du bulk correspond à une constante diélectrique statique élévée à proximité de la monocouche.

Nous avons montré que le choix du substrat influence fortement le paramètre $E_{\Gamma K}$ qui décrit l'état du band gap dans la monocouche de TMD (direct/indirecte). Si l'influence du substrat diélectrique sur $E_{\Gamma K}$ par écrantage diélectrique est avéré, on pourrait passer d'un band gap direct à un band gap indirect tout en changeant de substrat. Cela permettrait de transformer une monocouche émettrice de photons une monocouche absorbante de photons. Cela serait un exemple de modifier la structure de bandes par le substrat.

Bibliography

[1] S. Aeschlimann et al. "Direct evidence for efficient ultrafast charge separation in epitaxial WS2/graphene heterostructures". In: *Sci. Adv.* 6.20 (2020), pp. 2–7. ISSN: 23752548. DOI: 10.1126/sciadv.aay0761. arXiv: 1904.01379.

[2] S. Agnoli et al. "Unraveling the Structural and Electronic Properties at the WSe 2 –Graphene Interface for a Rational Design of van der Waals Heterostructures". In: *ACS Appl. Nano Mater.* 1.3 (2018), pp. 1131–1140. ISSN: 2574-0970. DOI: 10.1021/acsanm.7b00315. URL: https://pubs.acs.org/doi/10.1021/acsanm.7b00315.

[3] E. M. Alexeev et al. "Resonantly hybridized excitons in moiré superlattices in van der Waals heterostructures". In: *Nature* 567.7746 (2019), pp. 81–86. ISSN: 0028-0836. DOI: 10.1038/s41586-019-0986-9. URL: http://www.nature.com/articles/s41586-019-0986-9.

[4] M. Amani et al. "Near-unity photoluminescence quantum yield in MoS2". In: *Science (80-.).* 350.6264 (2015), pp. 1065–1068. ISSN: 10959203. DOI: 10.1126/science.aad2114.

[5] B. Amin, T. P. Kaloni, and U. Schwingenschlögl. "Strain engineering of WS 2 , WSe 2 , and WTe 2". In: *RSC Adv.* 4.65 (2014), p. 34561. ISSN: 2046-2069. DOI: 10.1039/C4RA06378C. URL: http://xlink.rsc.org/?DOI=C4RA06378C.

[6] V. Astašauskas, A. Bellissimo, P. Kuksa, C. Tomastik, H. Kalbe, and W. S. Werner. "Optical and electronic properties of amorphous silicon dioxide by single and double electron spectroscopy". In: *J. Electron Spectros. Relat. Phenomena* 241.October 2018 (2020), p. 146829. ISSN: 03682048. DOI: 10.1016/j.elspec.2019.02.008. URL: https://doi.org/10.1016/j.elspec.2019.02.008.

[7] F. Bassani, G. P. Parravicini, and R. A. Ballinger. *Electronic States and Optical Transitions in Solids.* Pergamon Press, 1975.

[8] M. M. Beerbom, B. Lägel, A. J. Cascio, B. V. Doran, and R. Schlaf. "Direct comparison of photoemission spectroscopy and in situ Kelvin probe work function measurements on indium tin oxide films". In: *J. Electron Spectros. Relat. Phenomena* 152.1-2 (2006), pp. 12–17. ISSN: 03682048. DOI: 10.1016/j.elspec.2006.02.001.

[9] K. Beiranvand, A. G. Dezfuli, and M. Sabaeian. "A two-band spinful k.p Hamiltonian of monolayer MoS2 from a nine-band model based on group theory". In: *Superlattices Microstruct.* 120 (2018), pp. 812–823. ISSN: 10963677. DOI: 10.1016/j.spmi.2018.06.033. URL: https://doi.org/10.1016/j.spmi.2018.06.033.

[10] R. Bian, C. Li, Q. Liu, G. Cao, Q. Fu, P. Meng, J. Zhou, F. Liu, and Z. Liu. "Recent progress in the synthesis of novel two-dimensional van der Waals materials". In: *Natl. Sci. Rev.* April 2021 (2021). ISSN: 2095-5138. DOI: 10.1093/nsr/nwab164.

[11] A. Biswas, C. H. Yang, R. Ramesh, and Y. H. Jeong. "Atomically flat single terminated oxide substrate surfaces". In: *Prog. Surf. Sci.* 92.2 (2017), pp. 117–141. ISSN: 00796816. DOI: 10.1016/j.progsurf.2017.05.001. arXiv: 1705.03436. URL: http://dx.doi.org/10.1016/j.progsurf.2017.05.001.

[12] X. Blase, A. Rubio, S. G. Louie, and M. L. Cohen. "Quasiparticle band structure of bulk hexagonal boron nitride and related systems". In: *Phys. Rev. B* 51.11 (1995), pp. 6868–6875. ISSN: 01631829. DOI: 10.1103/PhysRevB.51.6868.

[13] B. R. Borodin, F. A. Benimetskiy, I. A. Nyapshaev, and P. A. Alekseev. "Kelvin probe force gradient microscopy of WSe2 monolayers on Ni". In: *J. Phys. Conf. Ser.* 1400.5 (2019). ISSN: 17426596. DOI: 10.1088/1742-6596/1400/5/055012.

[14] L Britnell et al. "Strong Light-Matter Interactions Thin Films". In: *Science (80-.).* 340.June (2013), pp. 1311–1315.

[15] A. Bruix et al. "Single-layer <math> <msub> <mtext>MoS</mtext> <mn>2</mn> </msub> </math> on Au(111): Band gap renormalization and substrate interaction". In: *Phys. Rev. B* 93.16 (2016), p. 165422. ISSN: 2469-9950. DOI: 10.1103/PhysRevB.93.165422. arXiv: 1601.00095. URL: https://link.aps.org/doi/10.1103/PhysRevB.93.165422http://arxiv.org/abs/1601.00095http://dx.doi.org/10.1103/PhysRevB.93.165422.

[16] I. E. Brumboiu, O. Eriksson, and P. Norman. "Atomic photoionization cross sections beyond the electric dipole approximation". In: *J. Chem. Phys.* 150.4 (2019). ISSN: 00219606. DOI: 10.1063/1.5083649. arXiv: 1810.08542. URL: http://dx.doi.org/10.1063/1.5083649.

[17] T. Brumme, M. Calandra, and F. Mauri. "First-principles theory of field-effect doping in transition-metal dichalcogenides: Structural properties, electronic structure, Hall coefficient, and electrical conductivity". In: *Phys. Rev. B* 91.15 (2015), p. 155436. ISSN: 1098-0121. DOI: 10.1103/PhysRevB.91.155436. arXiv: 1501.07223. URL: https://link.aps.org/doi/10.1103/PhysRevB.91.155436.

[18] F. Bussolotti, J. Yang, H. Kawai, J. Y. Chee, and K. E. J. Goh. "Influence of many-body effects on hole quasiparticle dynamics in a <math> <mrow> <msub> <mi mathvariant="normal">WS</mi> <mn>2</mn> </msub> </mrow> </math> monolayer". In: *Phys. Rev. B* 103.4 (2021), p. 045412. ISSN: 2469-9950. DOI: 10.1103/PhysRevB.103.045412. URL: https://link.aps.org/doi/10.1103/PhysRevB.103.045412.

[19] F. Bussolotti et al. "Electronic properties of atomically thin MoS2 layers grown by physical vapour deposition: Band structure and energy level alignment at layer/substrate interfaces". In: *RSC Adv.* 8.14 (2018), pp. 7744–7752. ISSN: 20462069. DOI: 10.1039/c8ra00635k.

[20] E. Cappelluti, R. Roldán, J. A. Silva-Guillén, P. Ordejón, and F. Guinea. "Tight-binding model and direct-gap/indirect-gap transition in single-layer and multilayer MoS2". In: *Phys. Rev. B - Condens. Matter Mater. Phys.* 88.7 (2013), pp. 1–18. ISSN: 10980121. DOI: 10.1103/PhysRevB.88.075409. arXiv: 1304.4831.

[21] A. Carvalho, R. M. Ribeiro, and A. H. Castro Neto. "Band nesting and the optical response of two-dimensional semiconducting transition metal dichalcogenides". In: *Phys. Rev. B - Condens. Matter Mater. Phys.* 88.11 (2013), pp. 1–6. ISSN: 10980121. DOI: 10.1103/PhysRevB.88.115205. arXiv: 1305.6672.

[22] A. Castellanos-Gomez, M. Buscema, R. Molenaar, V. Singh, L. Janssen, H. S. Van Der Zant, and G. A. Steele. "Deterministic transfer of two-dimensional materials by all-dry viscoelastic stamping". In: *2D Mater.* 1.1 (2014). ISSN: 20531583. DOI: 10.1088/2053-1583/1/1/011002. arXiv: 1311.4829.

[23] M. Cattelan and N. Fox. "A Perspective on the Application of Spatially Resolved ARPES for 2D Materials". In: *Nanomaterials* 8.5 (2018), p. 284. ISSN: 2079-4991. DOI: 10.3390/nano8050284. URL: http://www.mdpi.com/2079-4991/8/5/284.

[24] C.-h. Chang, X. Fan, S.-H. Lin, and J.-L. Kuo. "Orbital analysis of electronic structure and phonon dispersion in MoS <math display="inline"> <msub> <mrow/> <mn>2</mn> </msub> </math> , MoSe <math display="inline"> <msub> <mrow/> <mn>2</mn> </msub> </math> , WS <math display="inline"> <msub> <mrow/> <m". In: *Phys. Rev. B* 88.19 (2013), p. 195420. ISSN: 1098-0121. DOI: 10.1103/PhysRevB.88.195420. URL: https://link.aps.org/doi/10.1103/PhysRevB.88.195420.

[25] M.-W. Chen et al. "Electronic Properties of Transferable Atomically Thin MoSe 2 /h-BN Heterostructures Grown on Rh(111)". In: *ACS Nano* 12.11 (2018), pp. 11161–11168. ISSN: 1936-0851. DOI: 10.1021/acsnano.8b05628. URL: https://pubs.acs.org/doi/10.1021/acsnano.8b05628.

[26] M.-H. Chiu. "Band Alignment Determination of Two-Dimensional Heterojunctions and Their Electronic Applications". In: (2018). URL: https://repository.kaust.edu.sa/bitstream/handle/10754/627889/Ming-HuiChiu-Dissertation-FinalDraft.pdf?sequence=1{\&}isAllowed=y.

[27] T. H. Choudhury, X. Zhang, Z. Y. Al Balushi, M. Chubarov, and J. M. Redwing. *Epitaxial Growth of Two-Dimensional Layered Transition Metal Dichalcogenides.* Vol. 50. 2020, pp. 155–177. ISBN: 0000000305891. DOI: 10.1146/annurev-matsci-090519-113456.

[28] J. G. Connell, B. J. Isaac, G. B. Ekanayake, D. R. Strachan, and S. S. Seo. "Preparation of atomically flat SrTiO3 surfaces using a deionized-water leaching and thermal annealing procedure". In: *Appl. Phys. Lett.* 101.25 (2012), pp. 2012–2015. ISSN: 00036951. DOI: 10.1063/1.4773052.

[29] H. Coy Diaz, J. Avila, C. Chen, R. Addou, M. C. Asensio, and M. Batzill. "Direct Observation of Interlayer Hybridization and Dirac Relativistic Carriers in Graphene/MoS 2 van der Waals Heterostructures". In: *Nano Lett.* 15.2 (2015), pp. 1135–1140. ISSN: 1530-6984. DOI: 10.1021/nl504167y. URL: https://pubs.acs.org/doi/10.1021/nl504167y.

[30] A. M. Dadgar, D. Scullion, K. Kang, D. Esposito, E. H. Yang, I. P. Herman, M. A. Pimenta, E.-J. G. Santos, and A. N. Pasupathy. "Strain Engineering and Raman Spectroscopy of Monolayer Transition Metal Dichalcogenides". In: *Chem. Mater.* 30.15 (2018), pp. 5148–5155. ISSN: 0897-4756. DOI: 10.1021/acs.chemmater.8b01672. URL: https://pubs.acs.org/doi/10.1021/acs.chemmater.8b01672.

[31] A. Damascelli. "Probing the Electronic Structure of Complex Systems by ARPES". In: *Phys. Scr.* T109 (2004), p. 61. ISSN: 0031-8949. DOI: 10.1238/Physica.Topical.109a00061. arXiv: 0307085v1 [arXiv:cond-mat]. URL: https://iopscience.iop.org/article/10.1238/Physica.Topical.109a00061.

[32] M. Dendzik, M. Michiardi, C. Sanders, M. Bianchi, J. A. Miwa, S. S. Grønborg, J. V. Lauritsen, A. Bruix, B. Hammer, and P. Hofmann. "Growth and electronic structure of epitaxial single-layer <math> <msub> <mtext>WS</mtext> <mn>2</mn> </msub> </math> on Au(111)". In: *Phys. Rev. B* 92.24 (2015), p. 245442. ISSN: 1098-0121. DOI: 10.1103/PhysRevB.92.245442. arXiv: 1509.05133. URL: https://link.aps.org/doi/10.1103/PhysRevB.92.245442.

[33] H. C. Diaz, Y. Ma, S. Kolekar, J. Avila, C. Chen, M. C. Asensio, and M. Batzill. "Substrate dependent electronic structure variations of van der Waals heterostructures of MoSe 2 or MoSe 2(1- x) Te 2 x grown by van der Waals epitaxy". In: *2D Mater.* 4.2 (2017), p. 025094. ISSN: 2053-1583. DOI: 10.1088/2053-1583/aa6e6a. URL: https://iopscience.iop.org/article/10.1088/2053-1583/aa6e6a.

[34] Y. Ding, Y. Wang, J. Ni, L. Shi, S. Shi, and W. Tang. "First principles study of structural, vibrational and electronic properties of graphene-like MX2 (M=Mo, Nb, W, Ta; X=S, Se, Te) monolayers". In: *Phys. B Condens. Matter* 406.11 (2011), pp. 2254–2260. ISSN: 09214526. DOI: 10.1016/j.physb.2011.03.044. URL: http://dx.doi.org/10.1016/j.physb.2011.03.044.

[35] W. C. Dunlap and R. L. Watters. "Direct Measurement of the Dielectric Constants of Silicon and Germanium". In: *Phys. Rev.* 92.6 (1953), pp. 1396–1397. ISSN: 0031-899X. DOI: 10.1103/PhysRev.92.1396. URL: https://link.aps.org/doi/10.1103/PhysRev.92.1396.

[36] N. Ehlen et al. "Narrow photoluminescence and Raman peaks of epitaxial MoS 2 on graphene/Ir(1 1 1)". In: *2D Mater.* 6.1 (2018), p. 011006. ISSN: 2053-1583. DOI: 10.1088/2053-1583/aaebd3. URL: https://iopscience.iop.org/article/10.1088/2053-1583/aaebd3.

[37] T. Eknapakul et al. "Electronic Structure of a Quasi-Freestanding MoS 2 Monolayer". In: *Nano Lett.* 14.3 (2014), pp. 1312–1316. ISSN: 1530-6984. DOI: 10.1021/nl4042824. URL: https://linkinghub.elsevier.com/retrieve/pii/S0038109812000889https://pubs.acs.org/doi/10.1021/nl4042824.

[38] M. H. Engelhard, D. R. Baer, A. Herrera-Gomez, and P. M. A. Sherwood. "Introductory guide to backgrounds in XPS spectra and their impact on determining peak intensities". In: *J. Vac. Sci. Technol. A* 38.6 (2020), p. 063203. ISSN: 0734-2101. DOI: 10.1116/6.0000359. URL: http://avs.scitation.org/doi/10.1116/6.0000359.

[39] I. Epstein et al. "Near-unity light absorption in a monolayer WS2 van der Waals heterostructure cavity". In: (2019). DOI: 10.1021/acs.nanolett.0c00492. arXiv: 1908.07598. URL: http://arxiv.org/abs/1908.07598.

[40] M. Escher et al. "Nanoelectron spectroscopy for chemical analysis: a novel energy filter for imaging x-ray photoemission spectroscopy". In: *J. Phys. Condens. Matter* 17.16 (2005), S1329–S1338. ISSN: 0953-8984. DOI: 10.1088/0953-8984/17/16/004. URL: https://iopscience.iop.org/article/10.1088/0953-8984/17/16/004.

[41] M. Ewert et al. "The Transition From MoS2 Single-Layer to Bilayer Growth on the Au(111) Surface". In: *Front. Phys.* 9.June (2021), pp. 1–9. ISSN: 2296-424X. DOI: 10.3389/fphy.2021.654845. URL: https://www.frontiersin.org/articles/10.3389/fphy.2021.654845/full.

[42] A. Faridi, D. Culcer, and R. Asgari. "Quasiparticle band-gap renormalization in doped monolayer <math> <msub> <mi>MoS</mi> <mn>2</mn> </msub> </math>". In: *Phys. Rev. B* 104.8 (2021), p. 085432. ISSN: 2469-9950. DOI: 10.1103/PhysRevB.104.085432. arXiv: 2108.10599. URL: https://link.aps.org/doi/10.1103/PhysRevB.104.085432.

[43] Focus GmbH. *NanoESCA Technical Reference Manual : Instrument*. Vol. 49. November. Taunusstein, 2014, pp. 1–62.

[44] S. Forti et al. "Electronic properties of single-layer tungsten disulfide on epitaxial graphene on silicon carbide". In: *Nanoscale* 9.42 (2017), pp. 16412–16419. ISSN: 2040-3364. DOI: 10.1039/C7NR05495E. URL: http://xlink.rsc.org/?DOI=C7NR05495E.

[45] L. Gao, J. Souto-Casares, J. R. Chelikowsky, and A. A. Demkov. "Orientation dependence of the work function for metal nanocrystals". In: *J. Chem. Phys.* 147.21 (2017), p. 214301. ISSN: 0021-9606. DOI: 10.1063/1.4991725. URL: http://dx.doi.org/10.1063/1.4991725http://aip.scitation.org/doi/10.1063/1.4991725.

[46] R. Geick, C. H. Perry, and G. Rupprecht. "Normal modes in hexagonal boron nitride". In: *Phys. Rev.* 146.2 (1966), pp. 543–547. ISSN: 0031899X. DOI: 10.1103/PhysRev.146.543.

[47] F. Gellé, R. Chirita, D. Mertz, M. V. Rastei, A. Dinia, and S. Colis. "Guideline to atomically flat TiO2-terminated SrTiO3(001) surfaces". In: *Surf. Sci.* 677.001 (2018), pp. 39–45. ISSN: 00396028. DOI: 10.1016/j.susc.2018.06.001.

[48] S. M. Goldberg, C. S. Fadley, and S. Kono. "Photoionization cross-sections for atomic orbitals with random and fixed spatial orientation". In: *J. Electron Spectros. Relat. Phenomena* 21.4 (1981), pp. 285–363. ISSN: 03682048. DOI: 10.1016/0368-2048(81)85067-0.

[49] C. Gong, H. Zhang, W. Wang, L. Colombo, R. M. Wallace, and K. Cho. "Band alignment of two-dimensional transition metal dichalcogenides: Application in tunnel field effect transistors". In: *Appl. Phys. Lett.* 103.5 (2013). ISSN: 00036951. DOI: 10.1063/1.4817409.

[50] P. R. Gray, P. J. Hurst, S. H. Lewis, R. G. Meyer, and J. Wiley. *ANALYSIS AND DESIGN OF ANALOG INTEGRATED CIRCUITS*. Wiley, 2009. ISBN: 978-0470245996. DOI: 10.1.1.692.1567.

[51] G. Gupta, S. Kallatt, and K. Majumdar. "Direct observation of giant binding energy modulation of exciton complexes in monolayer MoS e2". In: *Phys. Rev. B* 96.8 (2017), pp. 1–5. ISSN: 24699969. DOI: 10.1103/PhysRevB.96.081403. arXiv: 1703.07057.

[52] H. Henck et al. "Direct observation of the band structure in bulk hexagonal boron nitride". In: *Phys. Rev. B* 95.8 (2017), p. 085410. ISSN: 2469-9950. DOI: 10.1103/PhysRevB.95.085410. URL: https://link.aps.org/doi/10.1103/PhysRevB.95.085410.

[53] N. F. Hinsche et al. "Spin-dependent electron-phonon coupling in the valence band of single-layer <math> <msub> <mi>WS</mi> <mn>2</mn> </msub> </math>". In: *Phys. Rev. B* 96.12 (2017), p. 121402. ISSN: 2469-9950. DOI: 10.1103/PhysRevB.96.121402. arXiv: 1706.05484. URL: https://link.aps.org/doi/10.1103/PhysRevB.96.121402.

[54] M. Hoesch et al. "A facility for the analysis of the electronic structures of solids and their surfaces by synchrotron radiation photoelectron spectroscopy". In: *Rev. Sci. Instrum.* 88.1 (2017). ISSN: 10897623. DOI: 10.1063/1.4973562. arXiv: 1612.08634. URL: http://dx.doi.org/10.1063/1.4973562.

[55] S. Hüfner. *Photoelectron Spectroscopy.* Springer, 1996.

[56] H. Iwasawa. "High-resolution angle-resolved photoemission spectroscopy and microscopy". In: *Electron. Struct.* 2.4 (2020), p. 043001. ISSN: 2516-1075. DOI: 10.1088/2516-1075/abb379. URL: https://iopscience.iop.org/article/10.1088/2516-1075/abb379.

[57] H. Iwasawa, P. Dudin, K. Inui, T. Masui, T. K. Kim, C. Cacho, and M. Hoesch. "Buried double CuO chains in YBa2Cu4 O8 uncovered by nano-ARPES". In: *Phys. Rev. B* 99.14 (2019), pp. 1–6. ISSN: 24699969. DOI: 10.1103/PhysRevB.99.140510. arXiv: 1902.08322.

[58] H. Iwasawa, E. F. Schwier, M. Arita, A. Ino, H. Namatame, M. Taniguchi, Y. Aiura, and K. Shimada. "Development of laser-based scanning µ-ARPES system with ultimate energy and momentum resolutions". In: *Ultramicroscopy* 182 (2017), pp. 85–91. ISSN: 18792723. DOI: 10.1016/j.ultramic.2017.06.016.

[59] A. Jain, P. Bharadwaj, S. Heeg, M. Parzefall, T. Taniguchi, K. Watanabe, and L. Novotny. "Minimizing residues and strain in 2D materials transferred from PDMS". In: *Nanotechnology* 29.26 (2018), p. 265203. ISSN: 0957-4484. DOI: 10.1088/1361-6528/aabd90. arXiv: 1801.02971. URL: https://iopscience.iop.org/article/10.1088/1361-6528/aabd90.

[60] U. A. Jayasooriya and R. D. Jenkins. "Introduction to Raman Spectroscopy". In: *An Introd. to Laser Spectrosc.* Boston, MA: Springer US, 2002, pp. 77–104. ISBN: 9781461352136. DOI: 10.1007/978-1-4615-0727-7_3. URL: http://link.springer.com/10.1007/978-1-4615-0727-7{_}3.

[61] C. Jin et al. "Observation of moiré excitons in WSe2/WS2 heterostructure superlattices". In: *Nature* 567.7746 (2019), pp. 76–80. ISSN: 0028-0836. DOI: 10.1038/s41586-019-0976-y. URL: http://dx.doi.org/10.1038/s41586-019-0976-yhttp://www.nature.com/articles/s41586-019-0976-y.

[62] W. Jin et al. "Direct Measurement of the Thickness-Dependent Electronic Band Structure of <math display="inline"> <msub> <mi>MoS</mi> <mn>2</mn> </msub> </math> Using Angle-Resolved Photoemission Spectroscopy". In: *Phys. Rev. Lett.* 111.10 (2013), p. 106801. ISSN: 0031-9007. DOI: 10.1103/PhysRevLett.111.106801. URL: https://link.aps.org/doi/10.1103/PhysRevLett.111.106801.

[63] W. Jin et al. "Substrate interactions with suspended and supported monolayer <math> <mrow> <mi>Mo</mi> <msub> <mi mathvariant="normal">S</mi> <mn>2</mn> </msub> </mrow> </math> : Angle-resolved photoemission spectroscopy". In: *Phys. Rev. B* 91.12 (2015), p. 121409. ISSN: 1098-0121. DOI: 10.1103/PhysRevB.91.121409. URL: https://link.aps.org/doi/10.1103/PhysRevB.91.121409.

[64] A. J. H. Jones et al. "Visualizing band structure hybridization and superlattice effects in twisted MoS$_2$/WS$_2$ heterobilayers". In: (2021), pp. 1–31. arXiv: 2106.00403. URL: http://arxiv.org/abs/2106.00403.

[65] S. W. Jung et al. "Spectral functions of CVD grown MoS2 monolayers after chemical transfer onto Au surface". In: *Appl. Surf. Sci.* 532.July (2020), p. 147390. ISSN: 01694332. DOI: 10.1016/j.apsusc.2020.147390. URL: https://doi.org/10.1016/j.apsusc.2020.147390.

[66] C. Kastl et al. "Multimodal spectromicroscopy of monolayer WS2 enabled by ultra-clean van der Waals epitaxy". In: *2D Mater.* 5.4 (2018), p. 045010. ISSN: 20531583. DOI: 10.1088/2053-1583/aad21c. URL: https://iopscience.iop.org/article/10.1088/2053-1583/aad21c.

[67] J. Katoch et al. "Giant spin-splitting and gap renormalization driven by trions in single-layer WS2/h-BN heterostructures". In: *Nat. Phys.* 14.4 (2018), pp. 355–359. ISSN: 1745-2473. DOI: 10.1038/s41567-017-0033-4. arXiv: 1705.04866. URL: http://www.nature.com/articles/s41567-017-0033-4.

[68] M. Kawasaki, K. Takahashi, T. Maeda, R. Tsuchiya, M. Shinohara, O. Ishiyama, T. Yonezawa, M. Yoshimoto, and H. Koinuma. "Atomic Control of the SrTiO3 Crystal Surface". In: *Science (80-.).* 266.5190 (1994), pp. 1540–1542. ISSN: 0036-8075. DOI: 10.1126/science.266.5190.1540. URL: https://www.sciencemag.org/lookup/doi/10.1126/science.266.5190.1540.

[69] R. Kershaw, M. Vlasse, and A. Wold. "The preparation of and electrical properties of niobium selenide and tungsten selenide". In: *Inorg. Chem.* 6.8 (1967), pp. 1599–1602. ISSN: 0020-1669. DOI: 10.1021/ic50054a043. URL: https://pubs.acs.org/doi/abs/10.1021/ic50054a043.

[70] C. K. Kim, I. K. Drozdov, K. Fujita, J. C. Davis, I. Božović, and T. Valla. "In-situ angle-resolved photoemission spectroscopy of copper-oxide thin films synthesized by molecular beam epitaxy". In: *J. Electron Spectros. Relat. Phenomena* May (2018). ISSN: 03682048. DOI: 10.1016/j.elspec.2018.07.003. arXiv: 1805.04811.

[71] H.-g. Kim and H. J. Choi. "Thickness dependence of work function, ionization energy, and electron affinity of Mo and W dichalcogenides from DFT and GW calculations". In: *Phys. Rev. B* 103.8 (2021), p. 085404. ISSN: 2469-9950. DOI: 10.1103/PhysRevB.103.085404. arXiv: 2103.07858. URL: https://link.aps.org/doi/10.1103/PhysRevB.103.085404.

[72] H. Kim, D. Dumcenco, M. Frégnaux, A. Benayad, M.-W. Chen, Y.-C. Kung, A. Kis, and O. Renault. "Free-standing electronic character of monolayer <math> <msub> <mi>MoS</mi> <mn>2</mn> </msub> </math> in van der Waals epitaxy". In: *Phys. Rev. B* 94.8 (2016), p. 081401. ISSN: 2469-9950. DOI: 10.1103/PhysRevB.94.081401. URL: https://link.aps.org/doi/10.1103/PhysRevB.94.081401.

[73] J. W. Kim and A. Kim. "Absolute work function measurement by using photoelectron spectroscopy". In: *Curr. Appl. Phys.* 31.August (2021), pp. 52–59. ISSN: 15671739. DOI: 10.1016/j.cap.2021.07.018. URL: https://doi.org/10.1016/j.cap.2021.07.018.

[74] K. Kinoshita, R. Moriya, M. Onodera, Y. Wakafuji, S. Masubuchi, K. Watanabe, T. Taniguchi, and T. Machida. "Dry release transfer of graphene and few-layer h-BN by utilizing thermoplasticity of polypropylene carbonate". In: *npj 2D Mater. Appl.* 3.1 (2019), pp. 4–6. ISSN: 23977132. DOI: 10.1038/s41699-019-0104-8. URL: http://dx.doi.org/10.1038/s41699-019-0104-8.

[75] A. Knapp. "Surface potentials and their measurement by the diode method". In: *Surf. Sci.* 34.2 (1973), pp. 289–316. ISSN: 00396028. DOI: 10.1016/0039-6028(73)90120-9. URL: https://linkinghub.elsevier.com/retrieve/pii/0039602873901209.

[76] R. J. Koch, C. Jozwiak, A. Bostwick, B. Stripe, M. Cordier, Z. Hussain, W. Yun, and E. Rotenberg. "Nano focusing of soft x-rays by a new capillary mirror optic". In: *Synchrotron Radiat. News* 31.4 (2018), pp. 50–52. ISSN: 19317344. DOI: 10.1080/08940886.2018.1483660.

[77] A. V. Kolobov and J. Tominaga. "Two-Dimensional Transition Metal Dichalcogenides". In: Springer, 2016. DOI: 10.1007/978-3-319-31450-1_1. URL: http://link.springer.com/10.1007/978-3-319-31450-1{_}1.

[78] A. Kormányos, G. Burkard, M. Gmitra, J. Fabian, V. Zólyomi, N. D. Drummond, and V. Fal'ko. "k · p theory for two-dimensional transition metal dichalcogenide semiconductors". In: *2D Mater.* 2.2 (2015), p. 022001. ISSN: 2053-1583. DOI: 10.1088/2053-1583/2/2/022001. arXiv: 1410.6666. URL: https://iopscience.iop.org/article/10.1088/2053-1583/2/2/022001.

[79] A. Kormányos, V. Zólyomi, N. D. Drummond, P. Rakyta, G. Burkard, and V. I. Fal'ko. "Monolayer MoS <math display="inline"> <msub> <mrow/> <mn>2</mn> </msub> </math> : Trigonal warping, the <math display="inline"> <mi>Γ</mi> </math> valley, and spin-orbit coupling effects". In: *Phys. Rev. B* 88.4 (2013), p. 045416. ISSN: 1098-0121. DOI: 10.1103/PhysRevB.88.045416. arXiv: 1304.4084. URL: https://link.aps.org/doi/10.1103/PhysRevB.88.045416.

[80] D. Kozawa et al. "Photocarrier relaxation pathway in two-dimensional semiconducting transition metal dichalcogenides". In: *Nat. Commun.* 5 (2014), pp. 1–7. ISSN: 20411723. DOI: 10.1038/ncomms5543.

[81] A. Kuc. "Low-dimensional transition-metal dichalcogenides". In: *Chem. Model.* Vol. 11. 2014, pp. 1–29. ISBN: 9781849739542. DOI: 10.1039/9781782620112-00001. URL: http://ebook.rsc.org/?DOI=10.1039/9781782620112-00001.

[82] A. Kumar and P. K. Ahluwalia. "A first principle Comparative study of electronic and optical properties of 1H – MoS2 and 2H – MoS2". In: *Mater. Chem. Phys.* 135.2-3 (2012), pp. 755–761. ISSN: 0254-0584. DOI: 10.1016/J.MATCHEMPHYS.2012.05.055.

[83] A. Kumara and P. K. Ahluwalia. "Electronic structure of transition metal dichalcogenides monolayers 1H-MX2 (M = Mo, W; X = S, Se, Te) from ab-initio theory: new direct band gap semiconductors". In: *Eur. Phys. J. B 2012 856* 85.6 (2012), pp. 1–7. ISSN: 1434-6036. DOI: 10.1140/EPJB/E2012-30070-X. URL: https://link.springer.com/article/10.1140/epjb/e2012-30070-x.

[84] D. Le, A. Barinov, E. Preciado, M. Isarraraz, I. Tanabe, T. Komesu, C. Troha, L. Bartels, T. S. Rahman, and P. A. Dowben. "Spin-orbit coupling in the band structure of monolayer WSe2". In: *J. Phys. Condens. Matter* 27.18 (2015), pp. 1–6. ISSN: 1361648X. DOI: 10.1088/0953-8984/27/18/182201. URL: https://iopscience.iop.org/article/10.1088/0953-8984/27/18/182201https://iopscience-iop-org.gaelnomade-1.grenet.fr/article/10.1088/0953-8984/27/18/182201/pdfhttp://stacks.iop.org/0953-8984/27/i=18/a=182201?key=crossref.9afef45ca37b4ce9230a36795c6330a3.

[85] C. Lei, Y. Ma, X. Xu, T. Zhang, B. Huang, and Y. Dai. "Broken-Gap Type-III Band Alignment in WTe2/HfS2 van der Waals Heterostructure". In: *J. Phys. Chem. C* 123.37 (2019), pp. 23089–23095. ISSN: 19327455. DOI: 10.1021/acs.jpcc.9b07862.

[86] W. Li and D. Y. Li. "On the correlation between surface roughness and work function in copper". In: *J. Chem. Phys.* 122.6 (2005), p. 064708. ISSN: 0021-9606. DOI: 10.1063/1.1849135. URL: http://aip.scitation.org/doi/10.1063/1.1849135.

[87] Y. Li, A. Chernikov, X. Zhang, A. Rigosi, H. M. Hill, A. M. Van Der Zande, D. A. Chenet, E. M. Shih, J. Hone, and T. F. Heinz. "Measurement of the optical dielectric function of monolayer transition-metal dichalcogenides: MoS2, Mo S e2, WS2, and WS e2". In: *Phys. Rev. B - Condens. Matter Mater. Phys.* 90.20 (2014), pp. 1–6. ISSN: 1550235X. DOI: 10.1103/PhysRevB.90.205422.

[88] Y. Liang, S. Huang, R. Soklaski, and L. Yang. "Quasiparticle band-edge energy and band offsets of monolayer of molybdenum and tungsten chalcogenides". In: *Appl. Phys. Lett.* 103.4 (2013). ISSN: 00036951. DOI: 10.1063/1.4816517. arXiv: 1306.0620.

[89] M. Liao et al. "Precise control of the interlayer twist angle in large scale MoS2 homostructures". In: *Nat. Commun.* 11.1 (2020), pp. 1–8. ISSN: 20411723. DOI: 10.1038/s41467-020-16056-4. URL: http://dx.doi.org/10.1038/s41467-020-16056-4.

[90] Y. C. Lin et al. "Atomically thin heterostructures based on single-layer tungsten diselenide and graphene". In: *Nano Lett.* 14.12 (2014), pp. 6936–6941. ISSN: 15306992. DOI: 10.1021/nl503144a.

[91] F. Liu, Q. Li, and X. Zhu. "Direct determination of momentum resolved electron transfer in the photo-excited MoS2/WS2 van der Waals heterobilayer by TR-ARPES". In: (2019). DOI: 10.1103/PhysRevB.101.201405. arXiv: 1909.07759. URL: http://arxiv.org/abs/1909.07759http://dx.doi.org/10.1103/PhysRevB.101.201405.

[92] F. Liu, M. E. Ziffer, K. R. Hansen, J. Wang, and X. Zhu. "Direct Determination of Band-Gap Renormalization in the Photoexcited Monolayer MoS2". In: *Phys. Rev. Lett.* 122.24 (2019), p. 246803. ISSN: 10797114. DOI: 10.1103/PhysRevLett.122.246803. arXiv: 1902.07124. URL: https://doi.org/10.1103/PhysRevLett.122.246803.

[93] G. B. Liu, W. Y. Shan, Y. Yao, W. Yao, and D. Xiao. "Three-band tight-binding model for monolayers of group-VIB transition metal dichalcogenides". In: *Phys. Rev. B - Condens. Matter Mater. Phys.* 88.8 (2013), pp. 1–10. ISSN: 10980121. DOI: 10.1103/PhysRevB.88.085433. arXiv: 1305.6089.

[94] G. B. Liu, W. Y. Shan, Y. Yao, W. Yao, and D. Xiao. "Three-band tight-binding model for monolayers of group-VIB transition metal dichalcogenides". In: *Phys. Rev. B - Condens. Matter Mater. Phys.* 88.8 (2013), pp. 1–10. ISSN: 10980121. DOI: 10.1103/PhysRevB.88.085433. arXiv: 1305.6089.

[95] G. B. Liu, D. Xiao, Y. Yao, X. Xu, and W. Yao. "Electronic structures and theoretical modelling of two-dimensional group-VIB transition metal dichalcogenides". In: *Chem. Soc. Rev.* 44.9 (2015), pp. 2643–2663. ISSN: 14604744. DOI: 10.1039/c4cs00301b.

[96] H. J. Liu, L. Jiao, L. Xie, F. Yang, J. L. Chen, W. K. Ho, C. L. Gao, J. F. Jia, X. D. Cui, and M. H. Xie. "Molecular-beam epitaxy of monolayer and bilayer WSe2: A scanning tunneling microscopy/spectroscopy study and deduction of exciton binding energy". In: *2D Mater.* 2.3 (2015), p. 034004. ISSN: 20531583. DOI: 10.1088/2053-1583/2/3/034004. URL: https://iopscience.iop.org/article/10.1088/2053-1583/2/3/034004.

[97] H. Liu, P. Lazzaroni, and C. Di Valentin. "Nature of excitons in bidimensional WSe2 by hybrid density functional theory calculations". In: *Nanomaterials* 8.7 (2018), p. 481. ISSN: 20794991. DOI: 10.3390/nano8070481. URL: http://www.mdpi.com/2079-4991/8/7/481.

[98] R.-Y. Liu et al. "Femtosecond to picosecond transient effects in WSe 2 observed by pump-probe angle-resolved photoemission spectroscopy". In: *Sci. Rep.* 7.1 (2017), p. 15981. ISSN: 2045-2322. DOI: 10.1038/s41598-017-16076-z. URL: http://www.nature.com/articles/s41598-017-16076-z.

[99] Y. Liu. "ANGLE-RESOLVED PHOTOEMISSION STUDIES OF TWO-DIMENSIONAL ELECTRON SYSTEMS". PhD thesis. Urbana, Illinois, 2010, p. 125. ISBN: 9789968663038. DOI: 10.1088/1751-8113/44/8/085201. arXiv: 1011.1669.

[100] J. Madéo et al. "Directly visualizing the momentum-forbidden dark excitons and their dynamics in atomically thin semiconductors". In: *Science (80-.).* 370.6521 (2020), pp. 1199–1204. ISSN: 0036-8075. DOI: 10.1126/science.aba1029. arXiv: 2005.00241. URL: http://arxiv.org/abs/2005.00241http://dx.doi.org/10.1126/science.aba1029https://www.science.org/doi/10.1126/science.aba1029.

[101] S. K. Mahatha, K. D. Patel, and K. S. Menon. "Electronic structure investigation of MoS 2 and MoSe 2 using angle-resolved photoemission spectroscopy and abinitio band structure studies". In: *J. Phys. Condens. Matter* 24.47 (2012), pp. 0–5. ISSN: 09538984. DOI: 10.1088/0953-8984/24/47/475504.

[102] S. K. Mahatha et al. "Electron–phonon coupling in single-layer MoS2". In: *Surf. Sci.* 681 (2019), pp. 64–69. ISSN: 00396028. DOI: 10.1016/j.susc.2018.11.012. arXiv: 1811.07297. URL: https://linkinghub.elsevier.com/retrieve/pii/S0039602818308082.

[103] K. F. Mak, C. Lee, J. Hone, J. Shan, and T. F. Heinz. "Atomically thin MoS2: A new direct-gap semiconductor". In: *Phys. Rev. Lett.* 105.13 (2010), pp. 2–5. ISSN: 00319007. DOI: 10.1103/PhysRevLett.105.136805. arXiv: 1004.0546.

[104] G. Margaritondo, ed. *Electronic Structure of Semiconductor Heterojunctions.* Vol. 1. Perspectives in Condensed Matter Physics. Dordrecht: Springer Netherlands, 1988. ISBN: 978-90-277-2824-1. DOI: 10.1007/978-94-009-3073-5. URL: http://link.springer.com/10.1007/978-94-009-3073-5.

[105] C. Mathieu, N. Barrett, J. Rault, Y. Y. Mi, B. Zhang, W. A. de Heer, C. Berger, E. H. Conrad, and O. Renault. "Microscopic correlation between chemical and electronic states in epitaxial graphene on SiC <math display="inline"> <mrow> <mo stretchy="false">(</mo> <mn>000</mn> <mover accent="true"> <mrow> <mn>1</mn> </mrow> <mrow> <mo>¯</mo> </mrow> </mover> <mo stre". In: *Phys. Rev. B* 83.23 (2011), p. 235436. ISSN: 1098-0121. DOI: 10.1103/PhysRevB.83.235436. arXiv: 1104.1359. URL: https://link.aps.org/doi/10.1103/PhysRevB.83.235436.

[106] J. D. McIntyre and D. E. Aspnes. "Differential reflection spectroscopy of very thin surface films". In: *Surf. Sci.* 24.2 (1971), pp. 417–434. ISSN: 00396028. DOI: 10.1016/0039-6028(71)90272-X.

[107] N. W. A. N. D. Mermin. *SOLID STATE PHYSICS*. Ed. by R. Holt and Winston. New York, 1976.

[108] R. Miller and D. Kleinman. "Excitons in GaAs quantum wells". In: *J. Lumin.* 30.1-4 (1985), pp. 520–540. ISSN: 00222313. DOI: 10.1016/0022-2313(85)90075-4. URL: https://linkinghub.elsevier.com/retrieve/pii/0022231385900754.

[109] J. Minár, J. Braun, S. Mankovsky, and H. Ebert. "Calculation of angle-resolved photo emission spectra within the one-step model of photo emission—Recent developments". In: *J. Electron Spectros. Relat. Phenomena* 184.3-6 (2011), pp. 91–99. ISSN: 03682048. DOI: 10.1016/j.elspec.2011.01.009. URL: https://linkinghub.elsevier.com/retrieve/pii/S0368204811000156.

[110] J. A. Miwa, M. Dendzik, S. S. Grønborg, M. Bianchi, J. V. Lauritsen, P. Hofmann, and S. Ulstrup. "Van der Waals Epitaxy of Two-Dimensional MoS2-Graphene Heterostructures in Ultrahigh Vacuum". In: *ACS Nano* 9.6 (2015), pp. 6502–6510. ISSN: 1936086X. DOI: 10.1021/acsnano.5b02345.

[111] J. A. Miwa, S. Ulstrup, S. G. Sørensen, M. Dendzik, A. G. Čabo, M. Bianchi, J. V. Lauritsen, and P. Hofmann. "Electronic Structure of Epitaxial Single-Layer <math display="inline"> <msub> <mrow> <mi>MoS</mi> </mrow> <mn>2</mn> </msub> </math>". In: *Phys. Rev. Lett.* 114.4 (2015), p. 046802. ISSN: 0031-9007. DOI: 10.1103/PhysRevLett.114.046802. arXiv: 1410.0615. URL: https://link.aps.org/doi/10.1103/PhysRevLett.114.046802.

[112] S. K. Mo, C. Hwang, Y. Zhang, M. Fanciulli, S. Muff, J. Hugo Dil, Z. X. Shen, and Z. Hussain. "Spin-resolved photoemission study of epitaxially grown MoSe2 and WSe2 thin films". In: *J. Phys. Condens. Matter* 28.45 (2016), p. 454001. ISSN: 1361648X. DOI: 10.1088/0953-8984/28/45/454001. URL: http://stacks.iop.org/0953-8984/28/i=45/a=454001?key=crossref.e365825162e68544a77eb38d513163a8.

[113] S. Moser. "An experimentalist's guide to the matrix element in angle resolved photoemission". In: *J. Electron Spectros. Relat. Phenomena* 214 (2017), pp. 29–52. ISSN: 03682048. DOI: 10.1016/j.elspec.2016.11.007. URL: http://dx.doi.org/10.1016/j.elspec.2016.11.007https://linkinghub.elsevier.com/retrieve/pii/S0368204816301724.

[114] M.P.Seah and W.A.Dench. "Quantitative Electron Spectroscopy of Surface". In: *Surf. Interface Anal.* 1.1 (1979), p. 2.

[115] N. F. Muhamad, R. A. Maulat Osman, M. S. Idris, and M. N. Mohd Yasin. "Physical and electrical properties of SrTiO3 and SrZrO3". In: *EPJ Web Conf.* 162 (2017), pp. 2–5. ISSN: 2100014X. DOI: 10.1051/epjconf/201716201052.

[116] D. Muoi, N. V. N. Hieu, H. T. Phung, H. V. Phuc, B. Amin, B. D. Hoi, N. V. N. Hieu, L. C. Nhan, C. V. Nguyen, and P. T. Le. "Electronic properties of WS2 and WSe2 monolayers with biaxial strain: A first-principles study". In: *Chem. Phys.* 519.November 2018 (2019), pp. 69–73. ISSN: 03010104. DOI: 10.1016/j.chemphys.2018.12.004. URL: https://linkinghub.elsevier.com/retrieve/pii/S0301010418312904.

[117] M. H. Naik and M. Jain. "Origin of layer dependence in band structures of two-dimensional materials". In: *Phys. Rev. B* 95.16 (2017), p. 165125. ISSN: 2469-9950. DOI: 10.1103/PhysRevB.95.165125. arXiv: 1703.00257. URL: http://link.aps.org/doi/10.1103/PhysRevB.95.165125.

[118] H. Nakamura et al. "Spin splitting and strain in epitaxial monolayer WSe2 on graphene". In: *Phys. Rev. B* 101.16 (2020), p. 165103. ISSN: 24699969. DOI: 10.1103/PhysRevB.101.165103. arXiv: 1912.04770. URL: https://doi.org/10.1103/PhysRevB.101.165103https://link.aps.org/doi/10.1103/PhysRevB.101.165103.

[119] G. Nayak et al. "Cathodoluminescence enhancement and quenching in type-I van der Waals heterostructures: Cleanliness of the interfaces and defect creation". In: *Phys. Rev. Mater.* 3.11 (2019), pp. 1–8. ISSN: 24759953. DOI: 10.1103/PhysRevMaterials.3.114001.

[120] G. Nayak. "Enhancing physical properties of low dimensional materials by engineering its environment in composite Van der Waals heterostructures Goutham Nayak To cite this version : HAL Id : tel-02269239 dimensional materials by engineering its". In: (2019).

[121] P. V. Nguyen et al. "Visualizing electrostatic gating effects in two-dimensional heterostructures". In: *Nature* 572.7768 (2019), pp. 220–223. ISSN: 14764687. DOI: 10.1038/s41586-019-1402-1. arXiv: 1904.07301. URL: http://arxiv.org/abs/1904.07301http://www.nature.com/articles/s41586-019-1402-1.

[122] Y. Niu et al. "Thickness-dependent differential reflectance spectra of monolayer and few-layer MoS2, MoSe2, WS2 and WSe2". In: *Nanomaterials* 8.9 (2018). ISSN: 20794991. DOI: 10.3390/nano8090725.

[123] J. H. Park et al. "Scanning Tunneling Microscopy and Spectroscopy of Air Exposure Effects on Molecular Beam Epitaxy Grown WSe2 Monolayers and Bilayers". In: *ACS Nano* 10.4 (2016), pp. 4258–4267. ISSN: 1936086X. DOI: 10.1021/acsnano.5b07698. URL: https://pubs.acs.org/doi/10.1021/acsnano.5b07698.

[124] S. Park, N. Mutz, T. Schultz, S. Blumstengel, A. Han, A. Aljarb, L.-J. Li, E. J. W. List-Kratochvil, P. Amsalem, and N. Koch. "Direct determination of monolayer MoS 2 and WSe 2 exciton binding energies on insulating and metallic substrates". In: *2D Mater.* 5.2 (2018), p. 025003. ISSN: 2053-1583. DOI: 10.1088/2053-1583/aaa4ca. URL: https://iopscience.iop.org/article/10.1088/2053-1583/aaa4ca.

[125] S. Park et al. "The Schottky–Mott Rule Expanded for Two-Dimensional Semiconductors: Influence of Substrate Dielectric Screening". In: *ACS Nano* (2021), acsnano.1c04825. ISSN: 1936-0851. DOI: 10.1021/acsnano.1c04825. URL: https://pubs.acs.org/doi/10.1021/acsnano.1c04825.

[126] M. C. Patt. *Bulk and surface sensitive energy-filtered photoemission microscopy using synchrotron radiation for the study of resistive switching memories.* Vol. 122. 2016. ISBN: 9783958061309.

[127] Z. Peng, X. Chen, Y. Fan, D. J. Srolovitz, and D. Lei. "Strain engineering of 2D semiconductors and graphene: from strain fields to band-structure tuning and photonic applications". In: *Light Sci. Appl.* 9.1 (2020). ISSN: 20477538. DOI: 10.1038/s41377-020-00421-5. URL: http://dx.doi.org/10.1038/s41377-020-00421-5.

[128] C. Pettenkofer, A. Klein, W. Jaegermann, S. Tiefenbacher, and V. Eyert. "Electronic band structure of single-crystal and single-layer (formula presented) Influence of interlayer van der Waals interactions". In: *Phys. Rev. B - Condens. Matter Mater. Phys.* 64.20 (2001), pp. 1–14. ISSN: 1550235X. DOI: 10.1103/PhysRevB.64.205416.

[129] H. H. Pham and L. W. Wang. "Oxygen vacancy and hole conduction in amorphous TiO2". In: *Phys. Chem. Chem. Phys.* 17.1 (2015), pp. 541–550. ISSN: 14639076. DOI: 10.1039/c4cp04209c.

[130] D. Pierucci et al. "Band Alignment and Minigaps in Monolayer MoS 2 -Graphene van der Waals Heterostructures". In: *Nano Lett.* 16.7 (2016), pp. 4054–4061. ISSN: 1530-6984. DOI: 10.1021/acs.nanolett.6b00609. URL: https://pubs.acs.org/doi/10.1021/acs.nanolett.6b00609.

[131] D. Pierucci et al. "Large area molybdenum disulphide- epitaxial graphene vertical Van der Waals heterostructures". In: *Sci. Rep.* 6.June (2016). ISSN: 20452322. DOI: 10.1038/srep26656. URL: http://dx.doi.org/10.1038/srep26656.

[132] V. V. Poborchii, A. V. Kolobov, and K. Tanaka. "An in situ Raman study of polarization-dependent photocrystallization in amorphous selenium films". In: *Appl. Phys. Lett.* 72.10 (1998), pp. 1167–1169. ISSN: 00036951. DOI: 10.1063/1.121002.

[133] A. Ramasubramaniam. "Large excitonic effects in monolayers of molybdenum and tungsten dichalcogenides". In: *Phys. Rev. B - Condens. Matter Mater. Phys.* 86.11 (2012), pp. 1–6. ISSN: 10980121. DOI: 10.1103/PhysRevB.86.115409.

[134] E. Razzoli et al. "Selective Probing of Hidden Spin-Polarized States in Inversion-Symmetric Bulk MoS2". In: *Phys. Rev. Lett.* 118.8 (2017), pp. 1–6. ISSN: 10797114. DOI: 10.1103/PhysRevLett.118.086402. arXiv: 1701.07109.

[135] O. Renault, H. Kim, D. Dumcenco, D. Unuchek, N. Chevalier, M. Gay, A. Kis, and N. Fairley. "Correlating chemical and electronic states from quantitative photoemission electron microscopy of transition-metal dichalcogenide heterostructures". In: *J. Vac. Sci. Technol. A* 39.5 (2021), p. 053210. ISSN: 0734-2101. DOI: 10.1116/6.0001135.

[136] M. Repoux. "Comparison of background removal methods for XPS". In: *Surf. Interface Anal.* 18.7 (1992), pp. 567–570. ISSN: 10969918. DOI: 10.1002/sia.740180719.

[137] E. Ridolfi. "Electronic structure, transport and optical properties of MoS2 monolayers and nanoribbons". PhD thesis. Universidade Federal Fluminense, Niterói, 2017.

[138] A. F. Rigosi, H. M. Hill, K. T. Rim, G. W. Flynn, and T. F. Heinz. "Electronic band gaps and exciton binding energies in monolayer M ox W1-x S2 transition metal dichalcogenide alloys probed by scanning tunneling and optical spectroscopy". In: *Phys. Rev. B* 94.7 (2016), pp. 1–6. ISSN: 24699969. DOI: 10.1103/PhysRevB.94.075440.

[139] T. Roman and A. Groß. "Periodic Density-Functional Calculations on Work-Function Change Induced by Adsorption of Halogens on Cu(111)". In: *Phys. Rev. Lett.* 110.15 (2013), p. 156804. ISSN: 0031-9007. DOI: 10.1103/PhysRevLett.110.156804. URL: https://link.aps.org/doi/10.1103/PhysRevLett.110.156804.

[140] E. Rotenberg and A. Bostwick. "Microarpes and nanoarpes at diffraction-limited light sources: Opportunities and performance gains". In: *J. Synchrotron Radiat.* 21.5 (2014), pp. 1048–1056. ISSN: 16005775. DOI: 10.1107/S1600577514015409.

[141] J. A. Rothschild and M. Eizenberg. "Work function calculation of solid solution alloys using the image force model". In: *Phys. Rev. B* 81.22 (2010), p. 224201. ISSN: 1098-0121. DOI: 10.1103/PhysRevB.81.224201. URL: https://link.aps.org/doi/10.1103/PhysRevB.81.224201.

[142] H. Sahin, S. Tongay, S. Horzum, W. Fan, J. Zhou, J. Li, J. Wu, and F. M. Peeters. "Anomalous Raman spectra and thickness-dependent electronic properties of WSe2". In: *Phys. Rev. B - Condens. Matter Mater. Phys.* 87.16 (2013), p. 165409. ISSN: 10980121. DOI: 10.1103/PhysRevB.87.165409. arXiv: 1303.5861. URL: https://link.aps.org/doi/10.1103/PhysRevB.87.165409.

[143] C. M. Schneider and G. Schönhense. "Investigating surface magnetism by means of photoexcitation electron emission microscopy". In: *Reports Prog. Phys.* 65.12 (2002). ISSN: 00344885. DOI: 10.1088/0034-4885/65/12/202.

[144] J. Scofield. *Theoretical photoionization cross sections from 1 to 1500 keV.* Tech. rep. U.S. Atomic Energy Commission: Divison of Technical Information Extension, 1973. DOI: 10.2172/4545040. URL: http://www.osti.gov/servlets/purl/4545040/.

[145] K. L. Seyler, P. Rivera, H. Yu, N. P. Wilson, E. L. Ray, D. G. Mandrus, J. Yan, W. Yao, and X. Xu. "Signatures of moiré-trapped valley excitons in MoSe2/WSe2 heterobilayers". In: *Nature* 567.7746 (2019), pp. 66–70. ISSN: 0028-0836. DOI: 10.1038/s41586-019-0957-1. URL: http://www.nature.com/articles/s41586-019-0957-1.

[146] K. V. Shanavas and S. Satpathy. "Effective tight-binding model for MX2 under electric and magnetic fields". In: *Phys. Rev. B - Condens. Matter Mater. Phys.* 91.23 (2015), pp. 1–9. ISSN: 1550235X. DOI: 10.1103/PhysRevB.91.235145.

[147] P. M. Sherwood. "The use and misuse of curve fitting in the analysis of core X-ray photoelectron spectroscopic data". In: *Surf. Interface Anal.* 51.6 (2019), pp. 589–610. ISSN: 0142-2421. DOI: 10.1002/sia.6629. URL: https://onlinelibrary.wiley.com/doi/abs/10.1002/sia.6629.

[148] D. A. Shirley. "High-resolution x-ray photoemission spectrum of the valence bands of gold". In: *Phys. Rev. B* 5.12 (1972), pp. 4709–4714. ISSN: 01631829. DOI: 10.1103/PhysRevB.5.4709.

[149] J. á. Silva-Guillén, P. San-Jose, and R. Roldán. "Electronic band structure of transition metal dichalcogenides from ab initio and slater-koster tight-binding model". In: *Appl. Sci.* 6.10 (2016). ISSN: 20763417. DOI: 10.3390/app6100284. arXiv: 1611.04512.

[150] J. A. Sobota, Y. He, and Z.-X. Shen. "Angle-resolved photoemission studies of quantum materials". In: *Rev. Mod. Phys.* 93.2 (2021), p. 025006. ISSN: 0034-6861. DOI: 10.1103/RevModPhys.93.025006. URL: https://link.aps.org/doi/10.1103/RevModPhys.93.025006.

[151] C Steinke, T. O. Wehling, and M Rösner. "Coulomb-engineered heterojunctions and dynamical screening in transition metal dichalcogenide monolayers". In: *Phys. Rev. B* 102.11 (2020), p. 115111. ISSN: 2469-9950. DOI: 10.1103/PhysRevB.102.115111. URL: https://link.aps.org/doi/10.1103/PhysRevB.102.115111.

[152] I. Tanabe et al. "The symmetry-resolved electronic structure of 2H-WSe2(0 0 0 1)". In: *J. Phys. Condens. Matter* 28.34 (2016), p. 345503. ISSN: 1361648X. DOI: 10.1088/0953-8984/28/34/345503. URL: http://stacks.iop.org/0953-8984/28/i=34/a=345503?key=crossref.a4466993b4bcb4dfee70cfc013473150.

[153] H. Terrones et al. "New First Order Raman-active Modes in Few Layered Transition Metal Dichalcogenides". In: *Sci. Rep.* 4 (2014), pp. 1–9. ISSN: 20452322. DOI: 10.1038/srep04215.

[154] S. Tougaard. "Quantitative analysis of the inelastic background in surface electron spectroscopy". In: *Surf. Interface Anal.* 11.9 (1988), pp. 453–472. ISSN: 10969918. DOI: 10.1002/sia.740110902.

[155] D. J. Trainer et al. "Inter-Layer Coupling Induced Valence Band Edge Shift in Mono- to Few-Layer MoS 2". In: *Sci. Rep.* 7.August 2016 (2017), pp. 1–11. ISSN: 20452322. DOI: 10.1038/srep40559.

[156] C. Tusche, Y. J. Chen, C. M. Schneider, and J. Kirschner. "Imaging properties of hemispherical electrostatic energy analyzers for high resolution momentum microscopy". In: *Ultramicroscopy* 206.July (2019), p. 112815. ISSN: 18792723. DOI: 10.1016/j.ultramic.2019.112815. URL: https://doi.org/10.1016/j.ultramic.2019.112815.

[157] C. Tusche, A. Krasyuk, and J. Kirschner. "Spin resolved bandstructure imaging with a high resolution momentum microscope". In: *Ultramicroscopy* 159 (2015), pp. 520–529. ISSN: 18792723. DOI: 10.1016/j.ultramic.2015.03.020. URL: http://dx.doi.org/10.1016/j.ultramic.2015.03.020https://linkinghub.elsevier.com/retrieve/pii/S0304399115000698.

[158] M. M. Ugeda et al. "Giant bandgap renormalization and excitonic effects in a monolayer transition metal dichalcogenide semiconductor". In: *Nat. Mater.* 13.12 (2014), pp. 1091–1095. ISSN: 14764660. DOI: 10.1038/nmat4061. URL: http://www.nature.com/articles/nmat4061.

[159] S. Ulstrup et al. "Direct observation of minibands in a twisted graphene/WS2 bilayer". In: *Sci. Adv.* 6.14 (2020), pp. 1–7. ISSN: 23752548. DOI: 10.1126/sciadv.aay6104.

[160] S. Ulstrup et al. "Spatially Resolved Electronic Properties of Single-Layer WS 2 on Transition Metal Oxides". In: *ACS Nano* 10.11 (2016), pp. 10058–10067. ISSN: 1936-0851. DOI: 10.1021/acsnano.6b04914. URL: https://pubs.acs.org/doi/10.1021/acsnano.6b04914.

[161] S. Ulstrup et al. "Ultrafast Band Structure Control of a Two-Dimensional Heterostructure". In: *ACS Nano* 10.6 (2016), pp. 6315–6322. ISSN: 1936-0851. DOI: 10.1021/acsnano.6b02622. arXiv: 1606.03555. URL: https://pubs.acs.org/doi/10.1021/acsnano.6b02622.

[162] M. I. B. Utama et al. "Visualization of the flat electronic band in twisted bilayer graphene near the magic angle twist". In: *Nat. Phys.* (2020), pp. 2–8. ISSN: 1745-2473. DOI: 10.1038/s41567-020-0974-x. arXiv: 1912.00587. URL: http://arxiv.org/abs/1912.00587http://dx.doi.org/10.1038/s41567-020-0974-xhttp://www.nature.com/articles/s41567-020-0974-x.

[163] J. T. Waber and D. T. Cromer. "Orbital radii of atoms and ions". In: *J. Chem. Phys.* 42.12 (1965), pp. 4116–4123. ISSN: 00219606. DOI: 10.1063/1.1695904.

[164] L. Waldecker et al. "Rigid Band Shifts in Two-Dimensional Semiconductors through External Dielectric Screening". In: *Phys. Rev. Lett.* 123.20 (2019), p. 206403. ISSN: 0031-9007. DOI: 10.1103/PhysRevLett.123.206403. arXiv: 1907.05535. URL: https://doi.org/10.1103/PhysRevLett.123.206403http://arxiv.org/abs/1907.05535https://link.aps.org/doi/10.1103/PhysRevLett.123.206403.

[165] G. Wang, A. Chernikov, M. M. Glazov, T. F. Heinz, X. Marie, T. Amand, and B. Urbaszek. "Colloquium: Excitons in atomically thin transition metal dichalcogenides". In: *Rev. Mod. Phys.* 90.2 (2018), p. 21001. ISSN: 15390756. DOI: 10.1103/RevModPhys.90.021001. arXiv: 1707.05863. URL: https://doi.org/10.1103/RevModPhys.90.021001.

[166] J. J. White, J. Liu, J. J. Hinsch, and Y. Wang. "Theoretical understanding of the properties of stepped iron surfaces with van der Waals interaction corrections". In: *Phys. Chem. Chem. Phys.* 23.4 (2021), pp. 2649–2657. ISSN: 1463-9076. DOI: 10.1039/D0CP05977C. URL: http://xlink.rsc.org/?DOI=D0CP05977C.

[167] J. A. Wilson and A. D. Yoffe. "The transition metal dichalcogenides discussion and interpretation of the observed optical, electrical and structural properties". In: *Adv. Phys.* 18.73 (1969), pp. 193–335. ISSN: 14606976. DOI: 10.1080/00018736900101307.

[168] N. R. Wilson et al. "Determination of band offsets, hybridization, and exciton binding in 2D semiconductor heterostructures". In: *Sci. Adv.* 3.2 (2017), pp. 1–8. ISSN: 2375-2548. DOI: 10.1126/sciadv.1601832. URL: https://www.science.org/doi/10.1126/sciadv.1601832.

[169] S. Woo, H. Jeong, S. A. Lee, H. Seo, M. Lacotte, A. David, H. Y. Kim, W. Prellier, Y. Kim, and W. S. Choi. "Surface properties of atomically flat poly-crystalline SrTiO 3". In: *Sci. Rep.* 5 (2015), pp. 1–7. ISSN: 20452322. DOI: 10.1038/srep08822.

[170] A. Yan, J. Velasco, S. Kahn, K. Watanabe, T. Taniguchi, F. Wang, M. F. Crommie, and A. Zettl. "Direct Growth of Single- and Few-Layer MoS 2 on h-BN with Preferred Relative Rotation Angles". In: *Nano Lett.* 15.10 (2015), pp. 6324–6331. ISSN: 1530-6984. DOI: 10.1021/acs.nanolett.5b01311. URL: https://pubs.acs.org/doi/10.1021/acs.nanolett.5b01311.

[171] J. Yeh and I Lindau. "Atomic subshell photoionization cross sections and asymmetry parameters: 1 Z 103". In: *At. Data Nucl. Data Tables* 32.1 (1985), pp. 1–155. ISSN: 0092640X. DOI: 10.1016/0092-640X(85)90016-6. URL: http://linkinghub.elsevier.com/retrieve/pii/0092640X85900166https://linkinghub.elsevier.com/retrieve/pii/0092640X85900166.

[172] P.-C. Yeh et al. "Direct Measurement of the Tunable Electronic Structure of Bilayer MoS 2 by Interlayer Twist". In: *Nano Lett.* 16.2 (2016), pp. 953–959. ISSN: 1530-6984. DOI: 10.1021/acs.nanolett.5b03883. URL: https://pubs.acs.org/doi/10.1021/acs.nanolett.5b03883.

[173] P.-C. Yeh et al. "Layer-dependent electronic structure of an atomically heavy two-dimensional dichalcogenide". In: *Phys. Rev. B* 041407.4 (2015), pp. 1–6. ISSN: 1098-0121. DOI: 10.1103/PhysRevB.91.041407. URL: https://link.aps.org/doi/10.1103/PhysRevB.91.041407.

[174] H. K. Yoo, S. I. Hyun, Y. J. Chang, L. Moreschini, C. H. Sohn, H. D. Kim, A. Bostwick, E. Rotenberg, J. H. Shim, and T. W. Noh. "Thickness-dependent electronic structure in ultrathin LaNiO3 films under tensile strain". In: *Phys. Rev. B* 93.3 (2016), pp. 1–7. ISSN: 24699969. DOI: 10.1103/PhysRevB.93.035141.

[175] P. Y. Yu and M. Cardona. *Fundamentals of Semiconductors*. Graduate Texts in Physics. Berlin, Heidelberg: Springer Berlin Heidelberg, 2005. ISBN: 978-3-540-25470-6. DOI: 10.1007/b137661. URL: http://link.springer.com/10.1007/b137661.

[176] H. Yuan et al. "Evolution of the Valley Position in Bulk Transition-Metal Chalcogenides and Their Monolayer Limit". In: *Nano Lett.* 16.8 (2016), pp. 4738–4745. ISSN: 15306992. DOI: 10.1021/acs.nanolett.5b05107.

[177] F. Zahid, L. Liu, Y. Zhu, J. Wang, and H. Guo. "A generic tight-binding model for monolayer, bilayer and bulk MoS 2". In: *AIP Adv.* 3.5 (2013), p. 052111. ISSN: 21583226. DOI: 10.1063/1.4804936. arXiv: 1304.0074. URL: http://aip.scitation.org/doi/10.1063/1.4804936.

[178] M. Zhang et al. "Two-dimensional molybdenum tungsten diselenide alloys: Photoluminescence, Raman scattering, and electrical transport". In: *ACS Nano* 8.7 (2014), pp. 7130–7137. ISSN: 1936086X. DOI: 10.1021/nn5020566.

[179] X. Zhang, X.-f. Qiao, W. Shi, J.-b. Wu, D.-s. Jiang, and P.-h. Tan. "Phonon and Raman scattering of two-dimensional transition metal dichalcogenides from monolayer, multilayer to bulk material". In: *Chem. Soc. Rev.* 44.9 (2015), pp. 2757–2785. ISSN: 0306-0012. DOI: 10.1039/C4CS00282B. URL: http://dx.doi.org/10.1039/c4cs00282bhttp://xlink.rsc.org/?DOI=C4CS00282B.

[180] Y. Zhang et al. "Direct observation of the transition from indirect to direct bandgap in atomically thin epitaxial MoSe2". In: *Nat. Nanotechnol.* 9.2 (2014), pp. 111–115. ISSN: 1748-3387. DOI: 10.1038/nnano.2013.277. arXiv: 1401.3386. URL: http://www.nature.com/articles/nnano.2013.277.

[181] Y. Zhang et al. "Electronic Structure, Surface Doping, and Optical Response in Epitaxial WSe2 Thin Films". In: *Nano Lett.* 16.4 (2016), pp. 2485–2491. ISSN: 15306992. DOI: 10.1021/acs.nanolett.6b00059. URL: https://pubs.acs.org/doi/10.1021/acs.nanolett.6b00059.

[182] Y. Zhang et al. "Electronic Structure, Surface Doping, and Optical Response in Epitaxial WSe2 Thin Films". In: *Nano Lett.* 16.4 (2016), pp. 2485–2491. ISSN: 15306992. DOI: 10.1021/acs.nanolett.6b00059.

[183] Y. Zhang, Y. Gao, and D. Xiao. "Topological charge pumping in twisted bilayer graphene". In: 041410 (2019), pp. 1–5. ISSN: 24699969. DOI: 10.1103/PhysRevB.101.041410. arXiv: 1910.09001. URL: http://arxiv.org/abs/1910.09001.

[184] W. Zhao et al. "Electronic structure of exfoliated millimeter-sized monolayer WSe2 on silicon wafer". In: *Nano Res.* 12.12 (2019), pp. 3095–3100. ISSN: 19980000. DOI: 10.1007/s12274-019-2557-7. URL: https://doi.org/10.1007/s12274-019-2557-7.

[185] N. Zibouche, M. Schlipf, and F. Giustino. "GW band structure of monolayer <math> <msub> <mrow> <mi>MoS</mi> </mrow> <mn>2</mn> </msub> </math> using the SternheimerGW method and effect of dielectric environment". In: *Phys. Rev. B* 103.12 (2021), p. 125401. ISSN: 2469-9950. DOI: 10.1103/PhysRevB.103.125401. URL: https://link.aps.org/doi/10.1103/PhysRevB.103.125401.

[186] K. Zollner, P. E. Junior, and J. Fabian. "Strain-tunable orbital, spin-orbit, and optical properties of monolayer transition-metal dichalcogenides". In: *Phys. Rev. B* 100.19 (2019), pp. 1–10. ISSN: 24699969. DOI: 10.1103/PhysRevB.100.195126. arXiv: 1909.10763.

List of Figures

1.1 **a)** The crystal structure of a TMDC in 1T, 2H and 3R-polymorphism. In the first row, a side view of the layered structure, the second row a side, and third row a top view of the monolayer. The metal atom coordination (trigonal prismatic or octahedral) is indicated. The number of the polymorphism (1, 2, 3) refers to the number of layers in the unit cell, the letter stands for **t**etrahedral, **h**exagonal or **r**homohedral structure. Taken from [81] **b)** Unit cells of 2H-TMDCs in the H_a and H_c-configuration. Here, the blue dots represent chalcogen atoms whereas the gold dots represent transition metal atoms. Taken and adapted from [77]. The lattice parameters c (out-of-plane) and a (in-plane) are related by $c = 1.816 \times a$ [167]. 14

1.2 **a)** Unit cell of $1H_c$-MX_2 with a transition metal atom M and two chalcogen atoms X at lattice constant a. The chalcogen atoms (blue) are separated from the transition metal atom (gold) by the vectors $\delta_\pm$ as defined in the text.
b) Top view on the $1H_c$-MX_2-structure with real space lattice vectors R_1 and R_2. The hexagonal unit cell is marked by a gray dashed line. **c)** Resulting planar hexagonal Brillouin zone with reciprocal lattice vectors K_1 and K_2 and the points of high symmetry Γ, K, K' and M as defined in the text. All figures adapted from [137]. 16

1.3 **a)-d)** Band structure measurements by ARPES on ML-TMDCS (left side; multiple authors) and corresponding theoretical band structures from [149] (on the right side) by DFT (in grey) and tight-binding calculations (red). MoS_2 on graphene [36], $MoSe_2$ on hBN [25], WS_2 on hBN [164], WSe_2 on hBN [121]. We have mirrored the calculations of [149] to correspond to the experimental graphs. For all ML-TMDCs there is good qualitative agreement between the theory and the experimental band structures. A local maximum of the valence band can be found at Γ, the global maximum of the valence band is found at K/K' with a split-off band. 19

1.4 Spin-polarized photoemission spectra at K' (left) and K right showing the different spin-split states for ML-WSe_2 at approximately $E - E_F = -1.2$ eV and -1.7 eV. The sign of the spin switches from K to K', but the energies of the bands remain the same. Taken and adapted from [112] 20

1.5 **a)** Photoluminescence (colored) and differential reflectance spectra on monolayers of MoS_2, $MoSe_2$, WS_2 and WSe_2 taken from [80]. The authors have indicated the transitions of the A, B and C exciton. For ML-WSe_2 two peaks labelled A' and B' are marked by the authors. Their origin was not elucidated, the background partially attributed to the C exciton seen in the other ML-TMDCs. **b)** Band structure of ML-WSe_2 taken and modified from [17]. The red and green arrow indicate the bound electron (hole) states in the conduction (valence) band which participate in forming an exciton. Because of the large spin-orbit splitting, the energy of the B exciton is ≈ 0.5 eV higher than of the A exciton, as can be seen for ML-WSe_2 in panel a). . 23

1.6 Band structures calculated by [80]. The green arrows indicate electronic transition at parallel band curvatures where the joint density of states (jDOS) diverges. In differential reflectance spectra, the electronic transitions at the indicated areas contribute to the « C exciton » transition as seen in panel a) of FIGURE 1.5. 25

2.1 Number of electrons as a function of internal energy $N(E)$ and the measured photointensity spectrum $I(E_{kin})$ as a function of kinetic energy E_{kin} after photoexcitation of energy $h\nu$. Core levels are mapped onto single peaks, the valence band is found as a broad band. Taken and adapted from [55]. . . . 29

2.2 The basic principle of an ARPES setup in the **a)** original and more advanced configuration **b)**. For both configurations the sample is illuminated by photons of energy $E = h\nu$ from a light source. The resulting photoelectrons are measured using the detection and imaging system as a function of their kinetic energy E_{kin} and their polar φ and azimuthal θ angle. In **a)** the electron analyzer disperses photoelectrons only by their kinetic energy E_{kin} along the radial axis for a fixed φ and θ. The slits at the entrance and exit of the analyzer determine the energy resolution. Photoelectrons are then measured by an electron detector. In **b)** photoelectrons are dispersed according to their θ and E_{kin} simultaneously. For clarity, we only show electrons of different θ, not E_{kin}. Both variables are recorded on a two-dimensional image detector. This allows faster measurement. All measured parameters E_{kin}, φ, θ are crucial to determine the band structure $E(\mathbf{k})$ of the electron before excitation. Taken and modified from Wikipedia *Spectroscopie photoélectronique résolue en angle*, 19/11/2021 at 17:00 31

2.3 Schematic of the NanoEsca I energy-filtered PEEM system as described in the text. The NanoEsca I consists of the PEEM objetive column, the double hemispherical analyzer (HSA) and its electron detection system. We have added the electrostatic potentials at the height of the V_{sample}, extractor anode V_{ext} and decelerating projective lens V_{dec}. Elements of the microscope which are relevant to our work are written in bold and colored. For completeness, we have also noted other elements in gray. Taken and modified from [126] 37

2.4 Schematic of the NanoEsca I energy-filtered PEEM column as described in the text. We show the different modes and the trajectory of some photoelectron paths for real space EF-PEEM (standard), real space EF-PEEM (in telescopic mode) and Fourier Space EF-PEEM (kPEEM, in telescopic mode). For the latter two, the transfer lens is activated which moves the back fourier plane of the image. At the contrast aperture the image is always in reciprocal space, at the iris it is always in real space. We have noted the electrostatic potential at the sample V_{sample}, the extractor V_{ext} and the decelerating projective lens 1 V_{dec}. Elements of the microscope relevant to our work are written in bold and colored. For completeness, we have also noted other elements in gray. Taken from [126] 39

2.5 Schematic cross-section through a hemispherical analyzer along the dispersive (r, ϕ) plane. The grey lines indicate the direction of the electric field. The outter wall is of radius R_a whereas the inner wall is of radius R_i set at a higher electrostatic potential. An electron enters within the slit width d_{entr} at position r_0 under entrance angle α_0 (β_0, out-of-plane, not shown), follows the schematic trajectory in green (not exact) and leaves at position r_π at exit angle α_π ($\beta_p i$ not shown) within the slit width d_{exit}. Taken and adapted from [157] 40

2.6 Electronic orbitals with in-plane character along x/y, (red, blue: for $d_{x^2-y^2}, d_{xy}$ and p_x, p_y) and out-of-plane along z (green: for d_{z^2} and p_z-orbitals). We show different experimental configurations of incident light, their angle and polarization. **b)** Disappearing signal at Γ for ARPES on ML-MoS_2 [62] because of the normal photon incidence. 45

2.7 Photoemission spectra after excitation with the He-I α line at 21.22 eV for a typical metal and semiconductor. For the metal, the highest kinetic energy $E_{kin,max}$ that can be measured stems from photoelectrons that originate from the Fermi level E_F. The drop in photointensity at $E_{kin,max}$ then allows to calibrate the Fermi level position for semiconductors where the Fermi level is somewhere in the band gap. The lowest kinetic energy of photoelectrons is $E_{kin,min}$ measured by E_{SECO}. The exact materials were not specified by the authors. Δ refers to the work function difference between the metal and the semiconductor. The picture was modified.
Taken under license from [73] [Creative Commons Attribution 4.0 International (CC BY 4.0)]. 49

3.1 Complete steps from creation of a monolayer-TMDC flake via mechanical exfoliation to deposition using our stamping setup: **(1)** The bulk crystal is placed onto scotch tape and exfoliated through repeated covering and pulling **(2)**. In **(3)** we end up with mono- to multilayer flakes on the scotch tape which can then be deposited onto a transparent glass stripe covered with polydimethylsiloxane (PDMS) (**4**). Having pulled off the scotch tape we obtain mono- and multilayer flakes on the PDMS **(5)**. The monolayer must now be localized under the microscope, before the glass slide can then be transferred. This is done using a microscope and an an xyz-controllable stage **(6)**. 53

3.2 Standardized procedure to confirm monolayer character of thin layer flakes under an optical microscope. In **a)** we show a possible monolayer as photographed under a microscope. **b)** shows a WSe_2-flake with confirmed monolayer thinness. Both pictures have been taken with different lighting conditions. In order to compare the two images, we use the green, blue and red channels histogramms provided in most microscopic photography or graphic editing software as shown next to the picture. These histogramms are created based on the areas without flakes, delimited by the orange rectangles. Using Automatic White Balancing and changing the exposure time we then calibrate the RGB-channels such that they align with a signal prototypical to **f)**. This procedure is applied for both flakes in **a)** and **b)**. The resulting images are shown in **c)** and **d)** where the suspected monolayer displays a similar color to the confirmed monolayer. 55

3.3 **a)** Fabricated stamp of double-layered PDMS with a target monolayer flake on top. Scalpel blade for size comparison. **b)** View under the microscope during lowering of the ML-TDMC-stamp. The monolayer flake is deposited in the target area demarked by microscopic arrow structures (microscopic markers). The dark area marks the contact surface between PDMS and substrate and is delimited by a fine line called « meniscus ». When the meniscus reaches the monolayer, said monolayer comes into contact with the substrate. Upon increasing the distance between substrate and PDMS glass stripe, the meniscus moves back and the monolayer remains on the substrate, provided the adhesive forces of the substrate are stronger than those of the PDMS. 56

3.4 **1)** Pristine substrate. **2)** Deposition of an optical resine on top. **3)** Exposure to UV laser light according to the recipe in the text. The laser light induces a chemical reaction which makes the resine susceptible to being washed away by the presence of a developer liquid as shown in **4)**. In **5)** 15 nm of Titanium and 30 nm of Gold or Platinum are evaporated onto the substrate. Using acetone **6)** the developped areas can be removed (« lift-off »). 58

3.5 **a)** Microscopic markers for orientation as shown by computer lithography software. **a)** Microscopic markers structure with a deposited hBN-flake after finished laser lithography, development, evaporation and lift-off. The microscopic markers enable quick localization of the TMDC-based structure on the substrate despite the limited field of view of the kPEEM setup. 58

4.1 Measured ARPES bandstructures of MoS_2/Au(111) from Bruix et al. [15] through the high symmetry points M, Γ and K of the Brillouin zone. **a)** and **b)** show the complete measured band structures at $h\nu = 70$ eV and $h\nu = 49$ eV excitation energy . In **c)** the authors show the data of b). The edges of the Au band continuums (orange lines) and the MoS_2 band structure of the theoretical MoS_2 band structure (yellow lines) have been superposed. « Gap » and « continuum » refer to the absence of bands from gold at K or to the band continuum of gold around the Γ-Point. At Γ strong hybridization between gold and MoS_2 bands blurrs the signal. The $E_{\Gamma K}$ between the VBM at K and the strongly hybridized band at K is ≈ 0.31 eV. Taken from [15].
. 64

4.2 Measured band structure of monolayer MoS_2 on Graphene as measured by Ehlen et al. The annotation MoS_2 refers to the upper valence band edge of the MoS_2 bands, Gr refers to the graphene $\pi-$bands at K. No avoided crossings, indications of orbital hybridization, can be found between Graphene and MoS_2 bands close to K. K_{MoS2} and K_{Gr} refer to the K-Points of either MoS_2 or graphene layer. The Fermi level is situated at the Dirac point of Graphene. Taken from [36]. 64
4.3 Measured ARPES spectrum of ML-WS_2 on hBN. Taken and modified from [67]. The two hexagons indicate the cross-section through reciprocal space with the Brillouin zone of hBN (violet) and ML-WS_2 (green). At around $E - E_F = 2$ eV one can see the valence band edge of ML-WS_2, at around $E - E_F = 4$ eV the maxima of the hBN-π-bands. The valence band maxima of either ML-WS_2 and hBN are separated by roughly 2 eV and do not intersect. 66
4.4 Raw photointensity data after normalization of our kPEEM measurements of ML-WSe_2 on a) hBN, b) silicon, c) amorphous TiO_2 and d) $SrTiO_3$. We describe the normalization in section 2.1.8. For each substrate, we show a slice through the Brillouin zone from K to Γ (left). We also show energy distribution curves taken at K and Γ (right). In some cases we have increased the photointensity spectra after normalization by a factor of $\times 2$ or $\times 3$. For each $\mathbf{k}$ the photointensity has been normalized over the integrated signal $I_{norm}(E) = I(E, \mathbf{k}) / \int I(E, \mathbf{k})\, \mathrm{d}E$. In the case of $SrTiO_3$, which is insulating, our sample was electrically decoupled from the microscope such that we could not reliably determine the Fermi level position. For the hBN substrate we only show the data from the sample with 0° twist angle. . . . 71
4.5 Same as figure 4.4 but for a substrate of SiO_2 as measured by Renault and fabricated by Yamashita. 72
4.6 Isoenergetic slice of photoelectron intensity through the first Brillouin zone of ML-WSe_2 by kPEEM for two different samples **a)** and **b)**. Left column at $E - E_F = -1$ eV and middle column at $E - E_F = -2.9$ eV. The energies are chosen such that they lie roughly 100 meV below the valence band maximum at K/K' for ML-WSe_2 and hBN respectively. At these energies, the valence band maxima at K/K' of either material translate to small areas of high photointensity. The centers of these areas determine the approximate positions of the K/K'-points of either material. Comparing the angle between such two areas for either material allows us to determine the twist angle φ. The two hexagons in the right column thus indicate the extent of the first hexagonal Brillouin zones of either material. We find that in **a)**, there is a twist angle of 5° whereas in **b)** are roughly aligned at 0°. 73
4.7 Isoenergetic slice of a measured ML-WSe_2 on hBN at $E - E_F = -1.13$ eV for Γ (left) and $E - E_F = -1.08$ eV for K/K' (right) in kPEEM. The cuts are taken roughly 200 meV below the VBM at K. At these energies, the valence band maxima at K/K' of either material translate to small areas of high photointensity. The centers of these areas determine the approximate positions of the K/K'-points of either material. The determined K/K' and Γ points are indicated by red and blue dots. 75
4.8 Map of equivalent k-Space positions by pixel for different $\Delta k = |\mathbf{k} - \mathbf{X}|$ for a point of high symmetry $\mathbf{X}$ (K/K' or Γ): The center of the map is placed at one of the points $\mathbf{X}$. δk is the length of a pixel. For $\Delta k = |\mathbf{k} - \mathbf{X}| \leq 5\% \times \overline{\Gamma K}$ the bands are approximately isotropic as described in the text. Points of the same color are at the same Δk and indicate positions at which the energy distribution curve should have similar shape. 76

4.9 Photointensity spectra after averaging over equivalent points of the same Δk in k-space at K/K' (left) and Γ right. We show the spectra for $\Delta k = 0$ px, 3 px and 5 px. The black crosses mark the polynomial spline which is used to remove the background signal. We also show the result of the background removal. 78

4.10 Photointensity and fits of the EDCs at K/K' and Γ after averaging over equivalent k-space positions for $\Delta k = 3$ px (**a)** and **b)**) and after summation as described in the text (**c)** and **d)**). For the fits at K/K', we have included two gaussian curves each for the upper and lower spin-split band, and another band roughly 1 eV below the lower spin-split band. For Γ we have included a gaussian curve for the main peak at $E - E_F = 1.5$ eV and another band roughly 700 meV below. We have added gaussian curves where we expect band peaks from theory [118]. 79

4.11 Band dispersion at a) K/K' and b) Γ and fit according to the nearly free electron model. In **a)**, we show the band position of the upper and lower spin-split band at K/K' (dotted in black and red) and the corresponding band dispersion fits (gray and red line). In **b)** we show the dispersion of the upper branch of the VBM at Γ (dotted black) and corresponding dispersion fit. 81

4.12 Methodology used to enhance signal quality for the energy distribution curves taken at K/K' and Γ. Here we show schematically the spin-orbit splitting at K/K'.
After averaging EDCs close to K/K' of same Δk and background removal, we are left with EDCs $I(\Delta k, E)$ as shown in **1)**. These EDCs show schematically the photointensity spectrum of the spin-split bands at a given Δk. Fitting these EDCs will determine the dispersion $E(\Delta k)$ of the upper spin-split band indicated by the red line. We assume the nearly free electron model for this dispersion.
In **2)** we use $E(\Delta k)$ to correct for this band dispersion. In the corrected EDCs $I'(\Delta k, E) = I(\Delta k, E - E(\Delta k))$ the band peak of the upper spin-split band is always at the same energy. In **3)** we sum over all these EDCs and retrieve a maximally enhanced photointensity distribution $I(E) = \sum_{\Delta k} I'(\Delta k, E)$ of the spin-split bands. This maximally enhanced EDC can then again be fitted to retrieve band positions. We show this for the remaining substrates in FIGURE 4.13. We use the same fitting parameters as shown before. The information about the band dispersion is lost during the summation. 82

4.13 Fits of the enhanced spectra of the EDCs at K/K' and Γ on other substrates than hBN after using the methodology in this section. 83

4.14 Experimentally determined band structure parameters as a function of the dielectric constant of the substrate:
a) Effective masses m_e of the upper and lower spin-split band at K/K'
b) Effective mass m_e of the valence band maximum at Γ **c)** Spin-Orbit splitting Δ_{SOC} at K/K' **d)** Difference between maximum of the valence band at Γ and K/K' $E_{\Gamma K}$ Here, we show the values only for the hBN sample with a twist angle of 0°. 88

4.15 Two cases for the effect of dielectric screening of local charges in a ML-TMDC according to Waldecker, Steinke et al.[164]. Left: the spatial extent d of the considered charge distribution is much smaller than the height of the monolayer and thus the distance to the image charges $h \gg d$ (left). This means that the local charge in the monolayer and the image charge can be modelled as monopoles. Right: the spatial extent becomes comparable to the height of the ML-TMDC $h \approx d$ such that the charge must be modelled as a multipole with distinct orbital character. 90

4.16 **a)** Modulus Square of the wave function in ML-MoS_2 in $e/\text{Å}^2$ as calculated by [117] for electrons stemming from the VBM at Γ and K. In relation to the total height of the monolayer the charge distribution is strongly delocalized. It has very different direction character (in-plane/out-of-plane) for Γ and K respectively. **b)** Same as a) but integrated along x. One notices that for electrons at K/K', the charge density is strongly localized in plane, whereas for Γ the charge density is localized out-of-plane. We quantify this difference in the main text. 91

4.17 Incident photons of energy $h\Delta\nu$ (blue) scatter with the crystal. The result on the spectrum (left) is a peak at $\nu - \Delta\nu$ where **a)** a phonon of energy $h\Delta\nu$ is created (Anti-Stokes scattering), **b)** a peak at ν if the photon scatters elastically (Rayleigh scattering) or **c)** a peak at $\nu + \Delta\nu$ if a phonon of energy $h\Delta\nu$ is annihilated. 93

4.18 **a)** $Z(YY)\overline{Z}$-orientation of the linear plane of polarization according to Dadgar et al. [30]. We show a schematic of the crystallographic axes and the incident/outbound photon with linear polarization parallel to Y (010).
b) Left we show the real space crystal structure of a ML-TMDC from top with transition metal and chalcogen atoms with the two crystallographic axes X and Y. Dadgar et al.[30] have oriented the plane of linearly polarized incident light such that it is parallel to the real space Y-axis as shown left. Right we show the shape of the Brillouin Zone of ML-TDMC with the points of high symmetry Γ and K/K'. One can see that $\overline{\Gamma K}$ is parallel to the Y-axis on the left. We can thus deduce the correct plane of polarization using the knowledge about the $\overline{\Gamma K}$ from previously taken kPEEM data. . . 94

4.19 Raman intensity spectra of the spectral range around the ML-WSe_2 A-mode as a function of substrate for hBN of thickness 10 nm and 6 nm, Si and amorphous TiO_2. The spectra show that the absolute frequency of the A-mode remains roughly constant over the samples. 96

4.20 Work function maps of WSe_2-flakes on **a)** $SrTiO_3$, **b)** amorphous TiO_2 and **c)** Si and hBN. In order to determine the work function values of substrate and monolayer, we take the mean and standard deviation of the local work function over the shown areas. While the local variation of the substrate's work function is important and up to 100 meV, the local variation over the area of one monolayer is rather small, in the tens of meV. 98

4.21 Mean Work function of the ML-WSe_2 and the substrate for the measured samples. We have added a literature value from [13] for a substrate of Nickel. The red line of slope one corresponds to an alignment of the two work functions. 99

5.1 **a)** Configurations cristallines des TMDs en polymorphisme 1T, 2H et 3R ainsi que les coordinations de l'atome du métal de transition. Emprunté à [81] **b)** Cellule d'unité d'un TMD en polymorphisme $1H_c$. En bleu, les atomes de chalcogène, en jaune, l'atome de métal de transition. Le métal de transition est placé au centre, alors que les chalogènes sont déplacés par les vecteur $\pm\delta$, décrit dans le texte. a est le paramètre de maille dans le plan. **c)** Structure cristalline d'une monocouche de TMD dans le plan X-Y et les vecteurs de Bravais correspondants $R_{1/2}$, a est le paramètre de maille. En gris, la cellule d'unité vue du haut. **d)** Zone de Brillouin construite à partir des vecteurs de Bravais, les vecteurs réciproques $\mathbf{K}_{1/2}$, les points de haute symétrie, Γ, K, K' et M. 105

5.2 A gauche la structure de bandes de MC-MoS_2 sur graphene mesurée en ARPES par [36]. A droite deux structures de bandes de [149] calculés par moyen de DFT (en gris) et tight-binding (en rouge). Les deux structures de bandes sont qualitativement semblables, avec un maximum globale à K/K' et un maximum local à Γ. A K/K' on trouve aussi deux bandes séparées, lié au couplage spin-orbit. 107

5.3 Spectre de photoluminescence (coloré) et spectres de réflectivité différentielle sur des monocouches de MoS_2, $MoSe_2$, WS_2 et WSe_2 de [80]. Les auteurs ont indiqué l'énergie de l'exciton A, B et C. Ils ont aussi marqué deux autres transitions dénommées A' et B' pour MC-WSe_2 sans préciser leurs origines. **b)** Structure de bandes de MC-WSe_2, modifiée et empruntée à [17]. Les flèches rouge et vertes indiquent les états électrons(trous) dans le bande de conduction(valence) qui participent à la formation d'un exciton. Les excitons A et B sont séparées approximativement par le couplage spin-orbit Δ_{SOC} dans la bande de valence. 109

5.4 Le principe de base d'un dispositif ARPES en configuration originale **a)** et plus avancée **b)**. Dans les deux cas, l'échantillon est illuminé par une source de lumière avec des photons d'énergie $E = h\nu$. Le courant de photoélectron résultant est mesuré par le dispositif en fonction de l'énergie cinétique E_{kin} et des angles ϕ et θ par rapport à l'échantillon. Les photoélectrons sont dispersés par un champ électrique au sein de l'analyseur. Dans la configuration de a), l'analyseur disperse les photoélectrons uniquement selon leurs énergies cinétiques E_{kin}. Une fente à la sortie de l'analyseur permet de sélectionner les photoélectrons à 'énergie considérée. En b) les photoélectrons ne sont pas seulement dispersés en énergie E_{kin} mais aussi par rapport à l'angle θ. En b) nous ne montrons que la dispersion par rapport à θ pour plus de clareté. Un détecteur d'image bidimensionel à la sortie de l'analyseur permet de capturer les deux informations E_{kin} et θ à la fois. Cela permet un enregistrement plus rapide qu'en a). Pris et modifié de l'article Wikipedia *Spectroscopie photoelectronique resolue en angle*, 19/11/2021 à 17:00 . . . 110

5.5 Coupe à travers l'analyseur hémisphérique selon le plan dispersif (r, ϕ). Les lignes grises indiquent la direction du champ électrique. Le mur extérieur à R_a réside à un potentiel électrostatique plus haut que celui de l'intérieur à R_i. L'électron entre dans la fente de longueur d_{entr} à r_0 sous l'angle d'entrée α_0 et suit la trajectoire schématique (non exacte). Il sort de l'analyseur à la fente de sortie avec longueur d_{exit} à la position r_π sous l'angle α_π. 114

5.6 Spectre de photoémission après illumination de $h\nu = 21.22$ eV pour un métal typique et un sémiconducteur typique. Emprunté à [73]. Les auteurs n'ont pas précisé les matériaux examinés. Quant au métal, l'énergie cinétique maximale $E_{kin,max}$ avec un signal fini provient des photoélectrons au niveau de Fermi E_F. La chute en photointensité à $E_{kin,max}$ permet de calibrer le niveau de Fermi pour des semiconducteurs. L'énergie cinétique la plus basse $E_{kin,min}$ correspond à la chute du signal des électrons sécondaires à E_{SECO}. La connaissance des énergies cinétiques permet de déduire le travail de sortie ϕ. 117

5.7 Les étapes de création d'un échantillon MC-TMD par moyen d'exfoliation mécanique: (1) Le cristal est placé sur un film de scotch est exfolié en couvrant et retirant le scotch de manière répétée (2). (3) Il en résulte un certain nombre de flocons de différentes épaisseurs (monocouches et multicouches) du TMD. (4) Les flocons sont déposés sur une lame de verre couverte de polydiméthylsiloxane (PDMS). (5) La monocouche réside sur le PDMS et doit être localisée par un microscope optique. (6) La monocouche peut être déposée par la plateforme controllable en trois dimensions. 119

5.8 **a)** Coupe isoénergétique à travers la zone de Brillouin pour une MC-WSe_2 sur hBN à $E - E_F = 1.08$ eV, c'est-à-dire peu dessous le haut de la bande de valence. A cette énergie, des domaines de haute photointensité apparaissent. Leurs centres marquent les positions des points K et K'. **b)** Positions de spectres « équivalents » dans l'espace réciproque autour d'un point de haute symétrie K/K' ou Γ qui est placé au centre. Les valeurs du $\mathbf{k}$ sont discrétisées en pixels. Grâce à l'isotropie autour d'un point de haute symétrie, les spectres qui remplissent $||\mathbf{k} - \mathbf{K}_i| - \Delta k| \leq \delta k/2$ pour le même Δk devraient avoir la même forme (ils sont « équivalents »). Ici, δk est la largueur réciproque d'un pixel. Cette condition est valable pour $\Delta k \leq \overline{\Gamma K}$ [78]. 123

5.9 **a)** et **b)** Spectres de photointensité après moyennage pour un $\Delta k = 3$ px à K/K' (c) et Γ (d) en noir. Nous enlevons un fond d'électrons sécondaires polynomial indiqué par la ligne, il en resulte le spectre en rouge. **c)** et **d)** Les spectres de a) et b) après ajustement des courbes avec des gaussiennes. Chaque gaussienne correspond à une bande anticipée par la théorie [118]. . 125

5.10 Étapes supplémentaires pour une augmentation maximale du rapport signal-sur-bruit pour des spectres pris autour de K/K'. On a schématisé le couplage spin-orbit dans les spectres. 1) en analysant les spectres $I(\Delta k, E)$ on obtient une dispersion des bandes $E(\Delta k)$. En 2) nous corrigons cette dispersion en créant de nouveaux spectres $I'(\Delta k, E) = I(\Delta k, E - E(\Delta k))$, avant de moyenner sur tous ces spectres en 3). Le résultat est une augmentation maximale du signal-sur-bruit. 126

5.11 Les paramètres de structures de bandes en fonction de la constante diélectrique statique du substrat. **a)** Masse effective des bandes à K/K', **b)** Masse effective de la bande à Γ, **c)** Couplage spin-orbit Δ_{SOC} et différence entre le haut de la bande de valence à Γ et à K/K' $E_{\Gamma K}$. Au cas de hBN, un matériaux bidimensionel, nous avons ajouté la différence en angle entre les axes cristallographiques de hBN et MC-WSe_2. 128

5.12 **a)** Deux régimes de validité pour l'écrantage diélectrique d'une charge locale dans une MC-TMD selon Waldecker, Steinke et al. [151, 164]. A gauche: L'extension spatiale d de la distribution de la charge est beaucoup moins importante que la hauteur h de la monocouche $h \gg d$. Dans ce cas, la distribution de charge ainsi que la charge image dans le substrat peuvent être modelisées en tant que monopoles. A droite, le cas $h \approx d$: Les distributions de la charge locale et sa charge image sont délocalisées, directionnelles et doivent être modelisées par des multipoles. Le caractère orbitale doit alors être pris en compte. **b)** $|\Psi(\mathbf{r})|^2$ de la fonction d'onde $\Psi(\mathbf{r})$ d'une monocouche de MoS_2, calculée par [117], pour des électrons provénant du haut de la bande de valence à K/K' (gauche) et à Γ (droite). Par rapport à la hauteur totale de la monocouche, la distribution de charge est visiblement très délocalisée et directionnelle: elle semble pointé hors-du-plan à Γ et dans-le-plan à K/K'. 130
5.13 **a)** Configuration du Raman linéairement polarisé selon [30, 132]. Le faisceau de lumière arrive parallèle à la normale (Z), il est polarisé et analysé selon Y, et collecté selon la normale ($\overline{Z}$. Cela donne $Z(YY)\overline{Z}$. **b)** A l'aide de nos mesures kPEEM précédentes nous pouvons récupérer la direction Y qui correspond à la direction de ΓK dans la zone de Brillouin. 132
5.14 Travail de sortie ϕ de la monocouche de WSe_2 en fonction du travail de sortie du substrat. Nous avons ajouté une valeur mesurée par [13] sur un substrat de Ni. Les valeurs sont proches de la ligne rouge qui indique un alignement des travaux de sortie de la monocouche et du substrat. Nous avons ajouté une valeur externe prises par [13] d'une MC-WSe_2 sur Ni avec la méthode Kelvin-Probe. 133
5.15 Slices through the kPEEM raw data of the different substrates from K over M to K' point. 165

List of Tables

1.1 Orbital composition of the valence band maximum (VBM) at K/K' and Γ as calculated by DFT from [149] for ML-MoS_2, $MoSe_2$, WS_2 and WSe_2. d-orbitals belong to the transition metal atom, p-orbitals stem from the two chalcogen atoms. For all ML-TMDCs holds that the valence band maximum at K/K' is made up of mostly d_{xy} and p_{xy} orbitals, whereas at Γ mostly d_{z^2} and p_z contribute. 18

1.2 Band structure parameters as measured by ARPES (expt.) and from theoretical calculations (theory) for ML-MoS_2 and ML-WS_2. The band structure parameters are the effective masses m_e of the upper and lower spin-split band at K/K', the effective mass of the band at Γ, the spin-orbit splitting at K/K' Δ_{SOC} and the difference between the upper spin-split band at K/K' and Γ. m_e is the electron rest mass. 21

1.3 Same table as TABLE 1.2 but for ML-$MoSe_2$ and ML-WSe_2. m_e is the electron rest mass. 22

2.1 Comparison of currently used techniques for band structure analysis. Here, we compare μ- or nanoArpes with synchrotron light to our setup at the Plateforme Nanocaractérisation of the CEA-LETI in Grenoble. 36

4.1 Effective masses m_e measured at the upper (up) and lower (low) spin-split band at K/K' and Γ on ML-Wse_2 as a function of dielectric substrate. We use the method laid out in the previous section to measure the effective masses. For two hBN substrates, which is a 2D-material, we have added the twist angle between the crystallographic axes of hBN and ML-WSe_2. The twist is measured between the $\overline{\Gamma K}$ for the monolayer and hBN. 86

4.2 Measured spin-orbit splitting Δ_{SOC} and the difference in energy between the upper spin-split band at K/K' and upper band at Γ $E_{\Gamma K}$ as a function of substrate. For two hBN substrates, which is a 2D-material, we have added the twist angle between the crystallographic axes of hBN and ML-WSe_2. The twist is measured between the $\overline{\Gamma K}$ for the monolayer and hBN. 86

4.3 Values for band structure parameters found in the literature for ML-WSe_2 as a function of substrate. We show the difference between the maximum of the valence band between K/K' and Γ $E_{\Gamma K}$, the effective masses for upper, lower spin-split bands at K/K' m_e and Γ and the spin-orbit coupling Δ_{SOC}. When the authors did not specify an error, we noted « NA ». 87

4.4 Result of the linearly polarized Raman measurements: The mean peak position of the ML-WSe_2 A-mode as a function of substrate. We calculated the mean value over all measured spectra. For each substrate, between 3-5 spectra were taken to account for sample inhomogenities. 95

4.5 Measured mean work function of ML-WSe_2, mean work function of the substrate and measured valence band maximum at K/K' ($E - E_F$). For $SrTiO_3$ the VBM at K was not measured due to missing electrical contact. We have added a literature value for Nickel [13] measured by Kelvin Probe Force Gradient Microscopy 97

5.1 Composition orbitale de la bande de valence (VBM à K/K' et à Γ calculé par moyen de DFT par [149] pour une monocouche de MoS_2, $MoSe_2$, WS_2 et WSe_2. Les orbitales d apartiennent au métal de transition, les orbitales p apartiennent aux chalcogénures. Pour tous les TMDs, la bande de valence à K/K' est majoritairement composé de d_{xy} et p_{xy} alors que à Γ elle est composée de d_{z^2} et de p_z 106

5.2 Comparaison des techniques utilisées pour l'analyse de la structure des bandes. On compare $\mu-$ ou nanoArpes au synchrotron à notre dispositif de la Plateforme Nanocaractérisation du CEA-LETI à Grenoble. 112

5.3 Masses effectives m_e mesurées à la bande supérieur (s) et inférieure (i) des bandes à K/K et à Γ sur MC-WSe_2 en fonction du substrat. Nous avons employé la méthode utilisée dans la section précédente. Au cas de hBN, un matériaux bidimensionel, nous avons ajouté la différence en angle entre les axes cristallographiques de hBN et MC-WSe_2. La différence entre la bande supérieure et inférieure à K/K' due au couplage spin-orbit Δ_{SOC} et la différence entre la bande supérieure à K/K' et à Γ $E_{\Gamma K}$ en fonction du substrat. Au cas de hBN, un matériau bidimensionel, nous avons ajouté la différence en angle entre les axes cristallographiques de hBN et MC-WSe_2. . 129

5.4 Positions du mode A de MC-WSe_2 sur de différents substrats. Les différences sont trop petites pour un stress mécanique qui influence $E_{\Gamma K}$ dans les centaines de meV. 131

5.5 Travail de sortie moyenné de la monocouche de WSe_2, travail de sortie moyenné du substrat et position énergétique du haut de la bande de valence à K/K'. Pour l'échantillon de $SrTiO_3$ la position du haut de la bande de valence n'a pas été mésurée suite à rupture de la connexion électrique. Nous avons ajouté une valeur en littérature de [13] pour un substrat de nickel mésuré en Kelvin Probe Force Gradient Microscopy 133

5.5 Appendix

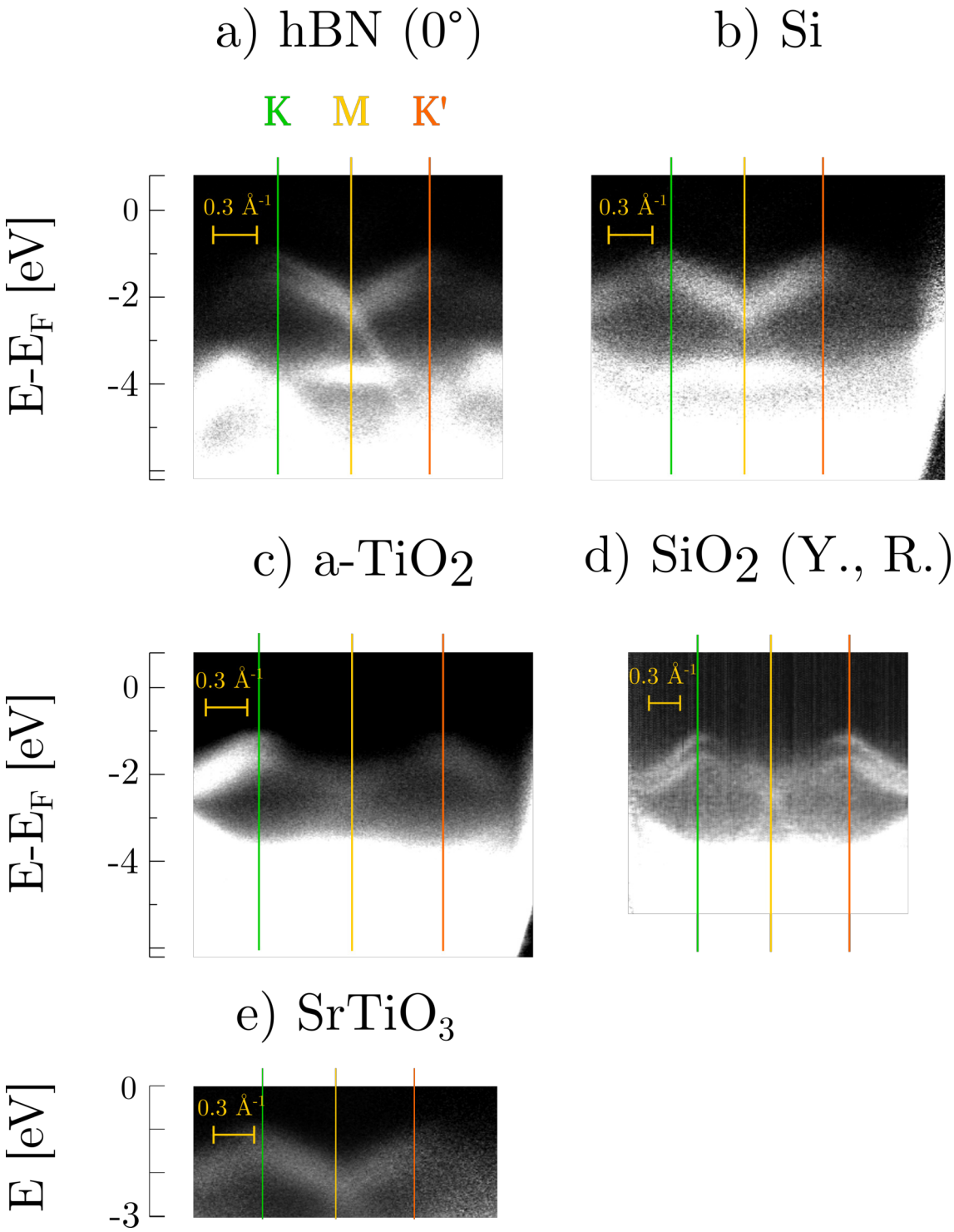

FIGURE 5.15 – *Slices through the kPEEM raw data of the different substrates from K over M to K' point.*